Angle resolved Mueller polarimetry, applications to periodic structures

Clément Fallet

Thèse

présentée pour obtenir le grade de

Docteur de l'École polytechnique

Spécialité : Physique

présentée par

Clément Fallet

Angle resolved Mueller polarimetry, applications to periodic structures

Directeur de thèse : **Antonello De Martino**

Date de soutenance : Mardi 18 Octobre 2011

Jury

Cattelan Denis	Horiba Jobin Yvon	Examinateur
De Martino Antonello	École Polytechnique	Directeur de thèse
Deumié Carole	Institut Fresnel	Rapporteur
Järrendahl Kenneth	Linköping University	Président du Jury
Vannuffel Cyril	CEA-LETI	Examinateur
Zallat Jihad	LSIIT	Rapporteur

Laboratoire de Physique des Interfaces et Couches Minces,

Contents

Introduction

This manuscript is the result of three years of research in the Laboratory of Physics of Interfaces and Thin Films in the group of optical characterization led by Prof. Antonello de Martino. It directly follows the work of Sami Ben Hatit who defended in thesis in december 2008. More than just a addition to his work, this thesis actually was a reengineering process. Whereas Ben Hatit's work was more a proof of concept and the assessment of the basic possibilities of the instrument in critical dimension metrology, this work was more instrument oriented with the constant will to make it as close to a first prototype as possible, yet driven by an application: the metrology of overlay defects in microelectronics industry. Due to my background in optical design and instrumentation, I tried to be as accurate and thorough as possible in my design to be able to help Horiba Jobin-Yvon in the making of the first pre-industrial prototype. However, things are always more complicated than one might expect and unfortunately some choices in the design of the instrument, though driven by experimental evidences, can still not be explained.

This manuscript is divided in four chapters.

The first chapter of this dissertation will focus on polarization and its formalism. We will explicitly introduce all the concepts and notations and how to deal with them. The different choices we made in terms of representation of polarization states and the conventions will be justified. Therefore this chapter is a prerequisite for everything that follows and will serve as a toolbox for th rest of our study. A discussion about non-conventional Mueller matrices, namely Stokes non-diagonalizable matrices, which were part of my research during my first year in the laboratory will conclude this chapter. Tough their construction and their mathematical properties may seem very abstract, we will see that they are quite simple indeed to generate and have some directly interpretable physical properties.

The second chapter will focus on the instrument itself. After reviewing the basic specifications of the system, we will thoroughly dissect each part of it to fully described it. After explaining the design of the instrument, we will then introduce the calibration methods we use in the laboratory and how we manage to accurately characterize the microscope objective contribution and even calibrate the first element of the Mueller matrix, m_{11} so we can quantitatively use it for fit purposes.

The third chapter will be dedicated to our collaboration with the group of Prof. Hans Arwin from the University of Linköping, Sweden. Through this collaboration, we were able to measure some very interesting and complex structures, yet very com-

mon and accessible to everyone : the exoskeleton of shiny beetles. The possible use of the system to characterize samples in the real space had already been briefly discussed by Sami Ben Hatit in the last part of his dissertation. But it is only through a very close collaboration with the group of Hans Arwin who provided us with a lot of specimen to measure and a lot of good advice that we have been able to obtain qualitative and quantitative results on the beetles. After a review of current results and thoughts about the exoskeleton of beetles, we will compare our spatially resolved Mueller matrices with the spectroscopic data from Linköping. Different ways to extract the useful information inspired by image processing and Mueller matrix decomposition theory will be introduced.

The last chapter will describe the main project I worked on during these three years. As I began my thesis, a new project called MuellerFourier and involving the group of optical characterization of LPICM, Horiba Jobin Yvon and the CEA-LETI began too. Angle resolved Mueller polarimetry in the back focal plane of a high numerical aperture objective has already demonstrated a good potential for CD metrology. The purpose of MuellerFourier was to demonstrate the ability of angle resolved Mueller polarimetry for measurements of the overlay error between two gratings at different levels. This approach has the advantages of traditional optical methods (speed, low-cost, non-destructive) and could alone provide all data needed for reliable characterization.

The final part of this manuscript will be a global conclusion and a reflection on these three years of research.

Chapter 1

General Principles of Polarization

This introductory chapter is not intended to be exhaustive and consists only of clarification of concepts and notations that will be used throughout this manuscript. We will handle the Jones and Stokes vectors as well as the Jones and Mueller matrices. We will see the different representations for the state of polarization of an electromagnetic wave. We will focus only on monochromatic plane waves.

1.1 Polarization of a wave

An electromagnetic wave is fully characterized by two fields, the electric field $\mathbf{E}$ and the magnetic field $\mathbf{B}$. The vectorial product $\mathbf{E} \wedge \mathbf{B}$, also known as the Poynting vector, defines the wave propagation. It then appears clearly that the fields $\mathbf{E}$ and $\mathbf{H}$ are always in the plane orthogonal to the wave propagation direction. If the wave is propagating along the z axis, then the electric field is confined in the xOy plane. Let us define the polarization of the wave as the curve described by the vector $\mathbf{E}$ through time. It is useless to also focus on the magnetic field, its components and behavior can be calculated from the Maxwell equations knowing the electric field.

1.1.1 Totally polarized light

Let $\mathbf{E}$ be the complex electric field. $\mathbf{E}$ can be expressed as:

$$\mathbf{E}(\mathbf{r},t) = [\mathbf{E_x}(\mathbf{r},t)\mathbf{e_x} + \mathbf{E_y}(\mathbf{r},t)\mathbf{e_y}]e^{-i\omega t} \tag{1.1}$$

with :

- $\mathbf{e_x}$ and $\mathbf{e_y}$, unitary orthogonal vectors
- $\mathbf{r}$ and t, space and time coordinates
- $\omega = 2\pi f$ is the angular frequency in radians per second

The deterministic vector

$$\begin{bmatrix} \mathbf{E_x}(\mathbf{r},t) \\ \mathbf{E_y}(\mathbf{r},t) \end{bmatrix} \tag{1.2}$$

is called Jones vector. One can see emerging the elliptic trajectory of the electric field vector whose parameters are fully and explicitly given by the Jones vector.

$$\Re(\mathbf{E}(\mathbf{r},t)) = \begin{bmatrix} E_{0x}\cos(\omega t - kz - \Phi_x) \\ E_{0y}\cos(\omega t - kz - \Phi_y) \end{bmatrix} \tag{1.3}$$

with E_{0x} and E_{0y}, amplitudes of the field; $k = \frac{2\pi}{\lambda}$, norm of the wave vector and Φ_x and Φ_y phases.

The light polarization state, defined as the trajectory of the electric field, can be easily seen, only in the case of a fully polarized wave, as an ellipse whose equation has been previously given(1.3). We can thus extract a first graphic representation of the polarization by plotting this ellipse and extract from it the first interesting parameters of the polarization.

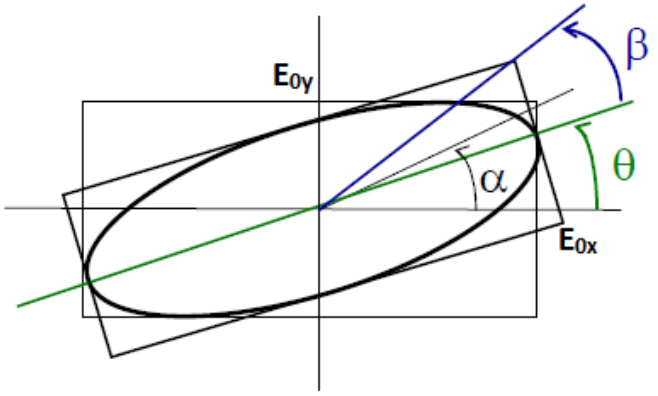

Figure 1.1: Representation of the polarization ellipse and its corresponding polarimetric angles

α, orientation of the rectangle surrounding the ellipse, takes value in $[0; \pi/2]$ such as $\tan\alpha = \frac{E_{Oy}}{E_{Ox}}$

Φ, the phase difference between the x and the y components. $\Phi = \Phi_x - \Phi_y$

We can also extract the relationships between the mathematical expression of the ellipse and its geometrical form.

$$\begin{aligned} \sin 2\varepsilon &= \sin 2\alpha \sin\Phi \\ \tan 2\theta &= \tan 2\alpha \cos\Phi \\ \tan 2\varepsilon &= \sin 2\theta \tan\Phi \end{aligned} \tag{1.4}$$

θ, orientation of the ellipse takes value in $[0; \pi/2]$
ε, ellipticity, takes value in $[0; \pi/4]$ with
$\varepsilon = 0 \rightarrow$ linear polarization
$\varepsilon = \pm\pi/4 \rightarrow$ circular polarization. in this particular case, α is not uniquely defined.

The Jones vectors of some classical polarization states are listed in appendixes.

1.1.2 Partially polarized light

In the case of a partially polarized wave, the electric field can be characterized in a deterministic way: the Jones vector is considered a random vector with zero mean. The electric field vector is then the realization of a random field with zero mean. We therefore characterize **E** by its coherency matrix (for a classical random variable, it

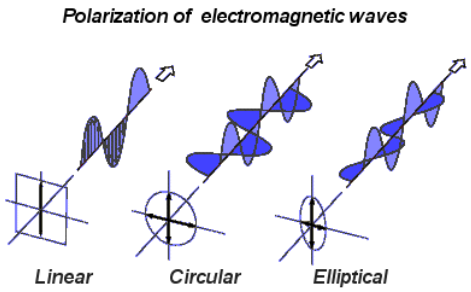

Figure 1.2: Possible polarization states of a totally polarized wave

would be called covariance matrix) defined as

$$\Gamma = \begin{bmatrix} < |\mathbf{E}_\mu{}^{\mathbf{x}}(\mathbf{r},t)|^2 > & < \mathbf{E}_\mu{}^{\mathbf{x}}(\mathbf{r},t)\mathbf{E}_\mu{}^{\mathbf{y}*}(\mathbf{r},t) > \\ < \mathbf{E}_\mu{}^{\mathbf{x}*}(\mathbf{r},t)\mathbf{E}_\mu{}^{\mathbf{y}}(\mathbf{r},t) > & < |\mathbf{E}_\mu{}^{\mathbf{y}}(\mathbf{r},t)|^2 > \end{bmatrix} \tag{1.5}$$

Note that to satisfy the conditions of homogeneity and stationarity, Γ must be independent of both $\mathbf{r}$ and t.

The complete polarization state of the wave is described by Γ. Any covariance matrix is symmetric, positive definite, we can decompose it into eigen values and eigen vectors.

$$\Gamma = U\Delta U^\dagger \quad \text{with U unitary matrix} \quad UU^\dagger = I \quad U^\dagger, \text{conjugate transpose}$$
$$\text{and} \qquad \Delta = \begin{bmatrix} \lambda_1 & 0 \\ 0 & \lambda_2 \end{bmatrix} \tag{1.6}$$

We can now define the degree of polarization as

$$P = \frac{\lambda_1 - \lambda_2}{\lambda_1 + \lambda_2} \text{ with } \lambda_1 \geqslant \lambda_2 \tag{1.7}$$

If $P = 1 \Rightarrow \lambda_2 = 0$, totally polarized light, the two components $\mathbf{E}_\lambda{}^{\mathbf{x}}$ and $\mathbf{E}_\lambda{}^{\mathbf{y}}$ are totally correlated. The eigen vector corresponding to the eigen value λ_1 is the Jones vector representing the polarization state.

if $P = 0 \Rightarrow \lambda_1 = \lambda_2$, totally depolarized light: the two conponents $\mathbf{E}_\lambda{}^{\mathbf{x}}$ and $\mathbf{E}_\lambda{}^{\mathbf{y}}$ are totally decorrelated.

if $0 < P < 1$, the light is partially polarized and the polarization state corresponding to the eigen vector with the eigen value λ_1 is called the principal polarization state.

To represent a partially polarized light, the Jones vector is not enough, the number of available parameters is no longer sufficient: we need a new model.

We introduce the Stokes vector, $\mathbf{S}$ defined bijectively by the coherency matrix Γ.

$$\mathbf{S} = A\overrightarrow{\gamma} \qquad A = \begin{bmatrix} 1 & 0 & 0 & 1 \\ 1 & 0 & 0 & -1 \\ 0 & 1 & 1 & 0 \\ 0 & i & -i & 0 \end{bmatrix} \tag{1.8}$$

$$\overrightarrow{\gamma} = [\Gamma_{XX}; \Gamma_{XY}; \Gamma_{YX}; \Gamma_{YY}]$$

Due to the bijective nature of the relationship between them, Γ and $\mathbf{S}$ contain exactly the same information. However, we note that $\mathbf{S}$ has real coefficients and its four

components have a physical meaning.

$$\mathbf{S} = \begin{bmatrix} < |\mathbf{E}_\mu{}^{\mathbf{x}}|^2 + |\mathbf{E}_\mu{}^{\mathbf{y}}|^2 > \\ < |\mathbf{E}_\mu{}^{\mathbf{x}}|^2 - |\mathbf{E}_\mu{}^{\mathbf{y}}|^2 > \\ < \mathbf{E}_\mu{}^{\mathbf{x}}\mathbf{E}_\mu{}^{\mathbf{y}*} + \mathbf{E}_\mu{}^{\mathbf{x}*}\mathbf{E}_\mu{}^{\mathbf{y}} > \\ < i(\mathbf{E}_\mu{}^{\mathbf{x}}\mathbf{E}_\mu{}^{\mathbf{y}*} - \mathbf{E}_\mu{}^{\mathbf{x}*}\mathbf{E}_\mu{}^{\mathbf{y}}) > \end{bmatrix} \tag{1.9}$$

What emerges in the equation (1.9) is the expression of sums and differences of electric field intensities. We can then rewrite (1.9) as

$$\mathbf{S} = \begin{bmatrix} I \\ Q \\ U \\ V \end{bmatrix} = \begin{bmatrix} I_x + I_y \\ I_x - I_y \\ I_{45^\circ} - I_{-45^\circ} \\ I_{\text{circ left}} - I_{\text{circ right}} \end{bmatrix} \tag{1.10}$$

It is easier to use the normalized Stokes vector.

$$\mathbf{S_{norm}} = \mathbf{S}/I = \begin{bmatrix} 1 \\ Q/I \\ U/I \\ V/I \end{bmatrix} = \begin{bmatrix} 1 \\ S_1/S_0 \\ S_2/S_0 \\ S_3/S_0 \end{bmatrix} \tag{1.11}$$

Just like we have defined the degree of polarization in 1.7, we introduce a new definition of the degree of polarization for a Stokes Vector [1, 2, 3] :

$$P = \frac{\sqrt{Q^2 + U^2 + V^2}}{I} \leq 1 \tag{1.12}$$

The Stokes vector can be represented in the 3 dimension space (we don't take into account the absolute intensity I). Because the degree of polarization is always less or equal to 1, a point representing a physical Stokes vector is always confined in a sphere in this space. The sphere is called the Poincaré sphere. An illustration is given in fig. 1.3. In this sphere, the cartesian coordinates are [S_1/S_0 S_2/S_0 S_3/S_0] and the spherical coordinates are [P 2θ 2ε].

The Poles of the Poincaré sphere represent the circular states, the equator represents the linear states. Every other point represents an elliptical state. On a meridian, the azimuth θ is constant. On a parallel, the ellipticity ε is constant. The surface of the sphere represents the totally polarized states. One can notice that two orthogonal states are diametrally opposed on the sphere. We will see in a next section how the Poincaré sphere can be useful to illustrate the transformation of a polarization state by a medium.

1.2 Interaction between polarized light and a medium

1.2.1 Totally polarized light

We have seen previously that the Jones formalism described in a simple and complete manner the totally polarized light, we then use this formalism to analyse the interaction between a totally polarized wave and a medium.

An homogeneous medium linearly interacting with a totally polarized wave can be described by a 2x2 matrix T called the Jones Matrix.

$$\mathbf{J_{out}} = T \times \mathbf{J_{in}} \tag{1.13}$$

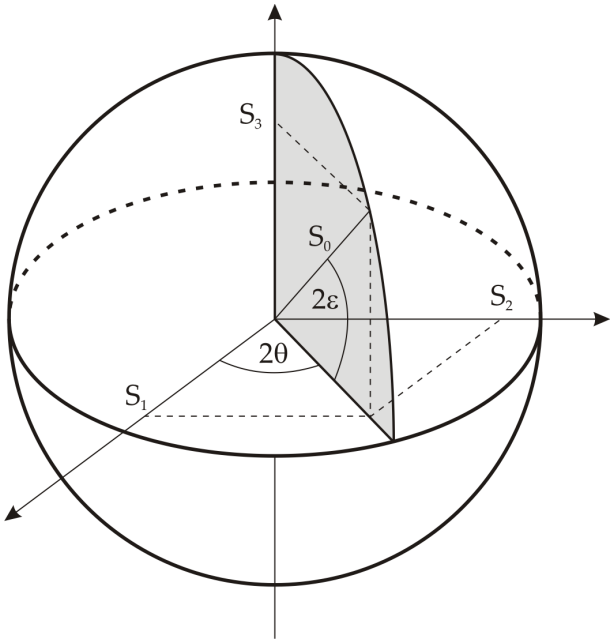

Figure 1.3: Poincaré Sphere

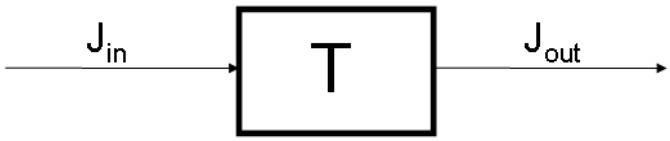

Figure 1.4: Interaction of a totally polarized wave with a medium

$$T = \begin{bmatrix} T_{XX} & T_{XY} \\ T_{YX} & T_{YY} \end{bmatrix} \tag{1.14}$$

It should be noted that both the input and the output states must be totally polarized for this formalism to be adapted. If the medium induces a loss of degree of polarization (depolarization effect), the output polarization state cannot be represented by a Jones vector and thus the medium cannot be represented by a Jones matrix. The matrical formalism is well-adapted to polarization: if polarized light passes through N media of Jones matrices given by T_i, the light will have a global change given by the product $\prod T_i$.

This matrix has complex coefficients, the total phase is of no interest, only 7 parameters are to be considered for this matrix. These parameters can be extracted from the Jones matrix using its decomposition in eigenvalues and eigenvectors. Let be $\upsilon_{\mathbf{1}}$ and $\upsilon_{\mathbf{2}}$ the eigenvectors of T associated to the eigenvalues λ_1 and λ_2. T satisfies the following equations.

$$\begin{cases} T\upsilon_{\mathbf{1}} = \lambda_1 \upsilon_{\mathbf{1}} \\ T\upsilon_{\mathbf{2}} = \lambda_2 \upsilon_{\mathbf{2}} \end{cases} \tag{1.15}$$

$\upsilon_{\mathbf{1}}$ and $\upsilon_{\mathbf{2}}$ represents two Jones vectors associated to two polarization states we will

call the eigen states of the medium. These eigen states pass through the medium without any deformation. The eigenvalue λ_i is complex and its modulus $|\lambda_i|$ expresses the attenuation of the eigen state $\upsilon_\mathbf{i}$ and its argument ϕ_i gives its dephasing.

We can now define two scalar parameters

$$D = \frac{|\lambda_1| - |\lambda_2|}{|\lambda_1| + |\lambda_2|} \quad \text{(Diattenuation)} \tag{1.16}$$

$$R = |\phi_1| - |\phi_2| \quad \text{(Retardance)} \tag{1.17}$$

If $\upsilon_\mathbf{1}$ and $\upsilon_\mathbf{2}$ are orthogonal, the Jones Matrix is said to be homogeneous and the matrix U whose columns are the eigen vectors $\upsilon_\mathbf{1}$ and $\upsilon_\mathbf{2}]$ is unitary. Otherwise, the Jones matrix is said to be inhomogeneous.

The Jones matrices of some classical polarization components are listed in appendices.

1.2.2 Partially polarized light

We have briefly noticed in the previous section that in the case of a medium exhibiting a depolarization effect, the Jones formalism cannot be used to model the medium.

We have defined the Stokes vector starting from the coherency matrix $\Gamma =< \mathbf{E}_\mu.\mathbf{E}_\mu^\dagger >$

By definition of the Jones matrix T, we have [4] :

$$\mathbf{E_{out},}_\mu = T \cdot \mathbf{E_{in},}_\mu \Rightarrow < \mathbf{E_{out},}_\mu.\mathbf{E}^\dagger_{\mathbf{out},\mu} >= T_\mu \cdot < \mathbf{E_{in},}_\mu.\mathbf{E}^\dagger_{\mathbf{in},\mu} > \cdot T_\mu^\dagger \tag{1.18}$$

$$\Gamma_{out} =< T_\mu \cdot \Gamma_{in} \cdot T_\mu^\dagger > \tag{1.19}$$

$$\Gamma_{out,ij} = \sum_{k=X,Y} \sum_{l=X,Y} < T_{\mu,ik} \cdot T^*_{\mu,jl} > \cdot \Gamma_{in,kl} \tag{1.20}$$

Let us define $\gamma = [\Gamma_{XX}; \Gamma_{XY}; \Gamma_{YX}; \Gamma_{YY}]$. We have a linear relationship between $\gamma_\mathbf{in}$ and $\gamma_\mathbf{out}$

$$\gamma_\mathbf{out} = N \cdot \gamma_\mathbf{in} \tag{1.21}$$

with N = $\begin{bmatrix} < T_{\mu,XX} \cdot T^*_{\mu,XX} > & < T_{\mu,XX} \cdot T^*_{\mu,XY} > & < T_{\mu,XY} \cdot T^*_{\mu,XX} > & < T_{\mu,XY} \cdot T^*_{\mu,XY} > \\ < T_{\mu,XX} \cdot T^*_{\mu,YX} > & < T_{\mu,XX} \cdot T^*_{\mu,YY} > & < T_{\mu,XY} \cdot T^*_{\mu,YX} > & < T_{\mu,XY} \cdot T^*_{\mu,YY} > \\ < T_{\mu,YX} \cdot T^*_{\mu,XX} > & < T_{\mu,YX} \cdot T^*_{\mu,XY} > & < T_{\mu,YY} \cdot T^*_{\mu,XX} > & < T_{\mu,YY} \cdot T^*_{\mu,XY} > \\ < T_{\mu,YX} \cdot T^*_{\mu,YX} > & < T_{\mu,YX} \cdot T^*_{\mu,YY} > & < T_{\mu,YY} \cdot T^*_{\mu,YX} > & < T_{\mu,YY} \cdot T^*_{\mu,YY} > \end{bmatrix}$

$=< T_\mu \bigotimes T_\mu^\dagger >$

with $\bigotimes$ being the Kronecker product.

In equation 1.8, we have seen the linear relationship between $\mathbf{S}$ and γ. By combining 1.8 and 1.21, we have :

$$\mathbf{S_{out}} = A \cdot N \cdot A^{-1} \cdot \mathbf{S_{in}} \tag{1.22}$$

We then introduce the Mueller matrix M defined as [5]

$$M = A \cdot N \cdot A^{-1} \tag{1.23}$$

$$\mathbf{S_{out}} = M \times \mathbf{S_{in}} \tag{1.24}$$

$$\begin{bmatrix} S_{out,1} \\ S_{out,2} \\ S_{out,3} \\ S_{out,4} \end{bmatrix} = \begin{bmatrix} M_{11} & M_{12} & M_{13} & M_{14} \\ M_{21} & M_{22} & M_{23} & M_{24} \\ M_{31} & M_{32} & M_{33} & M_{34} \\ M_{41} & M_{42} & M_{43} & M_{44} \end{bmatrix} \times \begin{bmatrix} S_{in,1} \\ S_{in,2} \\ S_{in,3} \\ S_{in,4} \end{bmatrix} \tag{1.25}$$

In the following of this manuscript, except if the contrary is clearly specified, we will use the normalized Mueller matrix defined as:

$$\begin{bmatrix} M_{11} & M_{12}/M_{11} & M_{13}/M_{11} & M_{14}/M_{11} \\ M_{21}/M_{11} & M_{22}/M_{11} & M_{23}/M_{11} & M_{24}/M_{11} \\ M_{31}/M_{11} & M_{32}/M_{11} & M_{33}/M_{11} & M_{34}/M_{11} \\ M_{41}/M_{11} & M_{42}/M_{11} & M_{43}/M_{11} & M_{44}/M_{11} \end{bmatrix} \tag{1.26}$$

Due to the equation 1.12, it is clear that $M_{11} > 0$ and that $|M_{ij} \leq M_{11}|, \forall(i,j)$, which means that the elements of the normalized Mueller matrix are always between -1 and 1.

Because this formalism is only useful for a medium exhibiting depolarization, it is interesting to focus on where this depolarization effect comes from. Let $\mathbf{J} = \begin{bmatrix} J_\mu^X(t) \\ J_\mu^Y(t) \end{bmatrix}$ the Jones vector representing the polarization state of the wave at the instant t, so we can define an instantaneous Stokes vector $\mathbf{S}_\mu(t) = \begin{bmatrix} |J_\mu^X(t)|^2 + |J_\mu^Y(t)|^2 \\ |J_\mu^X(t)|^2 - |J_\mu^Y(t)|^2 \\ J_\mu^X(t) \cdot J_\mu^{Y*}(t) + J_\mu^Y(t) \cdot J_\mu^{X*}(t) \\ i \cdot [J_\mu^X(t) \cdot J_\mu^{Y*}(t) - J_\mu^Y(t) \cdot J_\mu^{X*}(t)] \end{bmatrix}$. The mean polarization state of the wave is defined by the average of the random Stokes vector previously defined $< \mathbf{S}_\mu(t) >$. We can either have time average (t) or space average (μ) depending on the source of the wave we are considering. For example, if the light source is thermal light, the depolarization effect comes from the time fluctuations of the wave emitted. If a laser beam is reflected on a rough surface, each speckle pattern is totally polarized but with fluctuating polarization and then depolarization arises.

The Mueller matrices of some classical polarization components are listed in the appendixes.

1.3 Analysis of a Mueller matrix

As seen in the previous section, a Mueller matrix enables us to model the interaction of a totally or partially polarized wave with a medium. The Mueller matrices being at the very core of this dissertation, we will focus more on how to deal with them and how to understand them.

1.3.1 Physically realizable Mueller matrices

One must be very careful when dealing with Mueller matrices: contrary to Jones vector, Stokes vectors are not a vector space which means that every 4×1 vector is not a physically realizable Stokes vector. A Stokes vector must satisfy the condition defined in 1.12 thus imposing the same kind of condition for the Mueller matrix. Mueller matrices are not a subalgebra of the 4×4 real matrices algebra because multiplying a Mueller matrix by a negative scalar is a physical non-sense. However, multiplying (respectively adding) two Mueller matrices corresponds to add (respectively incoherently superimpose) two media.

We have seen in 1.23 that the Mueller matrix comes from the coherency matrix N. Any coherency matrix must be positive-definite, we can then define a necessary and sufficient condition for a Mueller matrix to be a physically realizable one [3, 6] :

$$\begin{aligned} \text{M , physically realizable} &\Leftrightarrow \text{N, coherency matrix,positive-definite} \\ &\Leftrightarrow \text{all eigenvalues of N positive} \end{aligned} \tag{1.27}$$

Though this condition is necessary and sufficient, some of the measured matrices we are going to deal with in this manuscript will be physically non-realizable. This is a non-sense because we measured them from a physical sample. This problem may arise when noise becomes predominant. A very thorough study of conditions for a matrix to be a Mueller matrix for non-plane waves can be found in reference [7]. We have then made the choice to present the filtered Mueller matrices.

Filtering of a Mueller matrix

We use the approach introduced by Cloude in [8] based on a sum decomposition of the Mueller matrix. This decomposition is based on the coherency matrix associated to the Mueller matrix. An analysis of the eigenvalue λ_i of the coherency matrix gives us all the information on the different non-depolarizing contributions the Mueller matrix contains. We will not explicitly detail how to obtain the elements of the coherency matrix from the Mueller matrix as it can be easily found in [8].

The coherency matrix is positive semidefinite and therefore should have 4 real non-negative eigenvalues λ_i. Any physically realizable Mueller matrix can be written as :

$$M = \lambda_1 \cdot M_1 + \lambda_2 \cdot M_2 + \lambda_3 \cdot M_3 + \lambda_4 \cdot M_4 \tag{1.28}$$

with M_i being a Jones-Mueller matrices whose elements are derived from the eigenvectors of the coherency matrix.

A non depolarizing Mueller matrix will have only one non-zero eigenvalue and the Jones-Mueller matrix associated to this eigenvalue will be the non-depolarizing Mueller matrix. Any negative or imaginary eigenvalue λ_1 is set to zero. The filtered Mueller matrix is obtained by replacing the corrected eigenvalues in eq. 1.28.

1.3.2 Change of Reference planes

The Jones and Stokes vectors clearly depends on the chosen reference system . It can be helpful to be able to express the Stokes and the Mueller matrix in different planes of reference.

For a Jones matrix, the change of reference is easily described by classical transformation matrices in algebra. However, for Mueller matrices, this transformation is more complex because the Stokes vector is defined via an intensity-based approach.

Rotation of the reference

Let $\mathbf{S}$ be a Stokes vector. A rotation of the reference planes by an angle θ transforms $\mathbf{S}$ in $\mathbf{S}'$.

$$\mathbf{S}' = R(\theta) \cdot \mathbf{S} \tag{1.29}$$

with $R(\theta)$, the rotation matrix given by the following expression

$$R(\theta) = \begin{bmatrix} 1 & 0 & 0 & 0 \\ 0 & cos(2\theta) & sin(2\theta) & 0 \\ 0 & -sin(2\theta) & cos(2\theta) & 0 \\ 0 & 0 & 0 & 1 \end{bmatrix} \tag{1.30}$$

We can now deduce the effect of a rotation on the Mueller matrix. After a rotation of the reference planes by θ, the resulting Mueller matrix is given by

$$M(\theta) = R(\theta) \cdot M(0^\circ) \cdot R(-\theta) \tag{1.31}$$

Reflection on a dielectric surface at normal incidence

The conditions of continuity of the electric field require that at any time the field of the incident wave and reflected wave are proportional.

So the temporal evolution of these two fields, for any point near the mirror is identical. However, the components of the Stokes vector describing the state depend on the choice of reference for both waves. This reference, called xyz for the incident wave, is supposed to be direct and the propagation is along the axis z. For the reflected wave, the reference becomes x'y'z' with z' = -z. We shall define the axes x'y' in the plane where the electric field evolves.

Then we shall have to consider the two following choices:

- x'=x and y'=-y. This is the most common choice because in this case, x'y'z' is direct. The Mueller matrix of the mirror is then $M_{mirror} = \begin{bmatrix} 1 & 0 & 0 & 0 \\ 0 & 1 & 0 & 0 \\ 0 & 0 & -1 & 0 \\ 0 & 0 & 0 & -1 \end{bmatrix}$
- x'=x and y'=y. This is not that common because x'y'z' is not direct. However, **we will use this reference throughout this manuscript** because it enables us to directly compare the M_{22} and M_{33} elements which is very convenient for mirror and back scattering given that these elements will be equal and not opposed. The Mueller matrix of the mirror is then considered to be the same as in vacuum. $M_{mirror} = \begin{bmatrix} 1 & 0 & 0 & 0 \\ 0 & 1 & 0 & 0 \\ 0 & 0 & 1 & 0 \\ 0 & 0 & 0 & 1 \end{bmatrix}$

It is of course very easy to switch from one convention to the other: we just have to multiply the last two rows by -1.

1.3.3 Polarimetric properties of a Mueller matrix

We will investigate in this section the different properties of a Mueller matrix. We have defined in equations 1.16 ans 1.17 the polarimetric properties for a Jones matrix. The same quantities can be defined for the Mueller matrix as we will see in the following.

Diattenuation

As seen in 1.16, the diattenuation (also called dichroism, both terms will be used indifferently) characterizes the change in amplitude of the components of the electric field.

We define the scalar diattenuation D characterizing the transmission of light with respect to the incident polarization state.

$$D = \frac{T_{max} - T_{min}}{T_{max} + T_{min}} \tag{1.32}$$

T_{max} and T_{min} are maximal and minimal transmissions. However, to completely characterize diattenuation, we have to introduce the diattenuation vector because two different diattenuators can have the same scalar diattenuation.

The direction of the vector is given by the orientation of the polarization state with the highest transmission T_{max}. Let $[1; d_1; d_2; d_3]$ be the normalized Stokes vector of this state.

D is defined as :

$$\mathbf{D} = D \cdot \begin{bmatrix} d_1 \\ d_2 \\ d_3 \end{bmatrix} = \begin{bmatrix} D_{horizontal} \\ D_{45^\circ} \\ D_{circular} \end{bmatrix} \tag{1.33}$$

The three components of the diattenuation vector **D** define respectively the horizontal, the 45° and the circular diattenuation. We also introduce the linear diattenuation D_{linear} defined as:

$$D_{linear} = \sqrt{D^2_{horizontal} + D^2_{45^\circ}} \tag{1.34}$$

Being defined by the relationship between the intensity of the beam exiting the system and the input polarization state, the diattenuation can be read straightforwardly from the Mueller matrix by just looking at its first row.

$$\mathbf{D} = \begin{bmatrix} M_{12}/M_{11} \\ M_{13}/M_{11} \\ M_{14}/M_{11} \end{bmatrix} \tag{1.35}$$

The Mueller matrix of a pure diattenuator is:

$$\begin{gathered} M_D = T_{unpol} \cdot \begin{bmatrix} 1 & \mathbf{D^t} \\ \mathbf{D} & m_D \end{bmatrix} \\ m_D = \sqrt{1 - D^2} \cdot Id + \frac{(1-\sqrt{1-D^2})\mathbf{D}\cdot\mathbf{D^t}}{D^2} \end{gathered} \tag{1.36}$$

T_{unpol} stands for the transmission of the unpolarized light and Id is the identity matrix. m_D is a symmetric 3×3 matrix with 3 degrees of freedom: the 3 components of the diattenuation vector . The diattenuator Mueller matrix thus has 4 degrees of freedom.

Polarizance

If we consider an unpolarized beam coming on a medium characterized by its Mueller matrix M, the polarization state emerging from the medium is entirely defined by the first column of M: $S_{out} = \begin{bmatrix} M_{11} \\ M_{21} \\ M_{31} \\ M_{41} \end{bmatrix}$. The degree of polarization of this Stokes vector is called the scalar polarizance.

$$P = \frac{\sqrt{M_{21}^2 + M_{31}^2 + M_{41}^2}}{M_{11}} \tag{1.37}$$

By analogy with the diattenuation, we also define the polarizance vector given by:

$$\mathbf{P} = \frac{1}{M_{11}} \cdot \begin{bmatrix} M_{21} \\ M_{31} \\ M_{41} \end{bmatrix} = \begin{bmatrix} P_{horizontal} \\ P_{45^\circ} \\ P_{circular} \end{bmatrix} \tag{1.38}$$

For a non-depolarizing system, one can demonstrate that $D = P$ so the following equality is true:

$$M_{21}^2 + M_{31}^2 + M_{41}^2 = M_{12}^2 + M_{13}^2 + M_{14}^2 \tag{1.39}$$

One can also demonstrate that a necessary and sufficient condition for a non-depolarizing Mueller matrix to be homogeneous is to satisfy $\mathbf{D} = \mathbf{P}$.

Birefringence

A retarder is characterized by the phase shift it induces between its two eigen states. Its eigen states are orthogonal. A pure retarder does not change the amplitude of its eigen states: the transmission is independent of the incident polarization state. We can define R the retardation as the phase delay between both eigen states.

$$R = |\delta_1 - \delta_2| \text{ , } 0 \leq R \leq \pi \tag{1.40}$$

With δ_1 and δ_2 being the phase shift of the eigen states. The fast axis of the retarder is defined as the orientation of the eigen mode first emerging from the retarder. Let $\mathbf{r} = [1; r_1; r_2; r_3]$ be the Stokes vector representing the fast axis of the retarder. Given that a retarder does not change the amplitude we have:

$$\sqrt{r_1^2 + r_2^2 + r_3^2} = 1 \tag{1.41}$$

Just like we introduced the diattenuation vector in eq. 1.33, we introduce the retardation vector $\mathbf{R}$.

$$\mathbf{R} = R \cdot \begin{bmatrix} r_1 \\ r_2 \\ r_3 \end{bmatrix} = \begin{bmatrix} R_{horizontal} \\ R_{45^\circ} \\ R_{circular} \end{bmatrix} \tag{1.42}$$

The linear retardation can be defined as:

$$R_{linear} = \sqrt{R_{horizontal}^2 + R_{45^\circ}} \tag{1.43}$$

The Mueller matrix of a retarder is a unitary matrix, it is fully characterized by the retardation vector **R**.

$$M_R = \begin{pmatrix} 1 & 0 \\ 0 & m_R \end{pmatrix} \tag{1.44}$$

m_R is a rotation matrix in $\Re^3$, its full expression can be found in many references. The retarder Mueller matrix has three degrees of freedom, the three components of the retardation vector.

Finding the scalar retardance R from the Mueller matrix is straightforward.

$$R = arccos\frac{tr(M_R)}{2} - 1 \tag{1.45}$$

The expression of the components of the retardation components can be found in [9].

Depolarization

We introduce the quadratic depolarization $\Delta_{quadratic}$ characterizing the mean depolarization when integrating on all the Poincaré sphere.

$$\Delta_{quadratic} = 1 - \sqrt{\frac{Tr(M^t \cdot M) - M_{11}^2}{3M_{11}^2}} \tag{1.46}$$

One should note that this definition is different from the one introduced by Gil and Bernabeu in [10]. However, this definition is more convenient and better described depolarization: for a non-depolarizing Mueller matrix, the quadratic depolarization is null and is equal to 1 for a totally depolarizing Mueller matrix.

From the definition we have introduced, we can obtain a necessary and sufficient condition for M to be a non-depolarizing Mueller matrix and thus to be equivalent to a Jones matrix.

$$\text{M, non-depolarizing} \Leftrightarrow Tr(M^t \cdot M) = 4M_{11}^2 \tag{1.47}$$

A pure depolarizer can be expressed by its Mueller matrix

$$M_\Delta = \begin{bmatrix} 1 & 0 \\ 0 & m_\Delta \end{bmatrix} \tag{1.48}$$

m_Δ is a symmetric 3×3 matrix. It can then be diagonalized in an orthonormal base. This matrix has 9 degrees of freedom and can be represented after the proper change of reference by a diagonal matrix.

$$M_\Delta = \begin{bmatrix} 1 & 0 & 0 & 0 \\ 0 & a & 0 & 0 \\ 0 & 0 & b & 0 \\ 0 & 0 & 0 & c \end{bmatrix} \tag{1.49}$$

a,b,c $\in [-1, 1]$ define the depolarization along the eigen states of the depolarizer. We can now introduce the principal depolarization ρ.

$$\rho = 1 - \frac{|a| + |b| + |c|}{3} = 1 - \frac{Tr(|M_\Delta|) - M_{11}}{3M_{11}} \tag{1.50}$$

The trace being similarity-invariant, the last definition of the principal depolarization is valid no matter what base the matrix is expressed in.

The definitions listed above are not the only estimators for the depolarization effects and many others exist and remain to be defined [11, 12].

1.3.4 Decomposition of a Mueller matrix

In the previous sections we have presented some polarimetric properties of pure Mueller matrices. However, an experimental Mueller matrix is never a pure polarimetric component, all properties are mixed and one need a mean to extract these properties [13, 14, 15]. We have previously stated that the diattenuation can be read directly from the first row of the Mueller matrix an that polarizance can be read from the first column. We then need to find a way to extract birefringence and depolarization. Various kinds of decompositions of Mueller matrices have been proposed throughout the years whether they involve product decompositions [16] or sum decompositions [8, 15]

Polar decomposition, Lu-Chipman algorithm

Introduced by Lu and Chipman in [9] the polar decomposition is probably the most common and its understanding is quite easy. Lu and Chipman proved that any Mueller matrix M can be decomposed according to the following form:

$$M = M_\Delta \cdot M_R \cdot M_D \tag{1.51}$$

M_Δ, M_R and M_D stand for respectively a depolarizer, a retarder and a diattenuator. M can be expressed by the following expression :

$$M = \begin{bmatrix} 1 & \mathbf{D^T} \\ P^T & \mathbf{m} \end{bmatrix} \tag{1.52}$$

with $\mathbf{D}$ the diattenuation and $\mathbf{P}$ the polarizance.

The first step of this decomposition is to extract the diattenuation vector $\mathbf{D}$ as the first row of the Mueller matrix. M_D can be constructed according to 1.36. If the matrix M_D is invertible (i.e. if M_D is not singular), we then define an intermediate matrix M' as $M' = M \times M_D^{-1}$. This matrix has a null diattenuation but contains polarizance, depolarization and birefringence.

It is important to note that the depolarization matrix has a non-null polarizance: the depolarizer is not a diagonal one.

$$M' = \begin{bmatrix} 1 & 0^T \\ \mathbf{P_\Delta} & \mathbf{m'} \end{bmatrix} \tag{1.53}$$

$\mathbf{P_\Delta}$ is defined by :

$$\mathbf{P_\Delta} = \frac{\mathbf{P} - m \cdot \mathbf{D}}{1 - D^2} \tag{1.54}$$

The sub-matrix m' is a mix between the sub-matrix m_Δ from the polarizance matrix and the sub-matrix m_R from the retardation part of the matrix.

The sub-matrix m_Δ can easily be recovered from the global sub-matrix m' and its eigenvalues as described in [9].

Once M_Δ has been reconstructed, one can easily extract the retardation matrix M_R using

$$M_R = M_\Delta^{-1} \cdot M' \tag{1.55}$$

Several extensions of the original algorithm have been introduced to enlarge the scope of applications and be able to process more and more data. In [17], Ossikovski et al extended the possibilities to experimental data exhibiting a negative determinant. In [18], Arteaga and Canillas introduced a pseudo-polar decomposition $M = M_R \cdot M_D \cdot M_{1C} \cdot M_{2C}$ with M_{1C} and M_{2C} two corrections factors which arise from the noncommutativity of the polarization properties.

Reverse decomposition

The matrix multiplication being not commutative, the Lu-Chipman decomposition may seem quite reductive. In [19] , Morio and Goudail showed that the six possible decomposition with a diattenuator, a retarder and a depolarizer can be reduced in only two families of decomposition : the forward one (forward respect to Lu-Chipman definition) and the reverse one (with components in the reverse order). In the reverse decomposition, the depolarizer has a non-null diattenuation but a null polarizance.

Ossikovski introduced in [20] the method to retrieve the reverse decomposition.

$$M = M_D \cdot M_R \cdot M_\Delta \tag{1.56}$$

This decomposition is very useful for the case where depolarization occurs before the diattenuation as showed in [21] Although, in the most general case, the physical interpretability of the outputs of these decompositions is not ensure due to this noncommutativity. No one should take for granted the results of a polar decomposition, either Lu-Chipman or reverse, without further investigation of the physical properties of the sample [22].

Normal decomposition

However, in the most general case, the Lu-Chipman decomposition involves a depolarizer with non-zero polarizance, while for the reverse decomposition this element may have nonzero diattenuation, which is somewhat at odds with respect to "real" depolarizers.

The symmetric decomposition was first introduced for Mueller matrices derived from a Jones matrix [23, 24] but then the method has been extended to any input matrix M.

$$M = M_{D2} \cdot M_{R2} \cdot M_\Delta \cdot M_{R1}^T \cdot M_{D1} \tag{1.57}$$

where and are the matrices of diattenuators and retarders, while the depolarizer is actually diagonal as in eq 1.48. One should notice and be aware that eq 1.57 only holds for Stockes diagonalizable matrices whereas this symmetric decomposition theory still needs to be extended for Stokes non-diagonalizable matrices as stated in and will be developed in another article yet to be published. This is a special case of the normal form of Mueller matrices described previously in refs [25] and [26].

$$M = M_2 \cdot M_\Delta \cdot M_1 \tag{1.58}$$

where M_1 and M_2 are two non-depolarizing (i.e. which do not reduce the degree of polarization of any totally polarized Stokes vector) Mueller matrices bracketing the diagonal depolarizer matrix. Each of these non-depolarizing matrices can then be decomposed using a polar decomposition. We introduce the symmetric decomposition of a Mueller matrix by applying Lu-Chipman decomposition to M_1 and reverse decomposition to M_2. Equation 1.58 can now be transformed in eq. 1.57 .

The central position of the depolarizer in the symmetric decomposition can be very useful when trying to localize the various effects of the sample without any a priori modeling, as most depolarizers occurring in practice are diagonal indeed. However as stated in [27], a prior modeling of the medium can be useful: this decomposition can only recover successfully all the constitutive elements if the depolarizer is not degenerate, i.e. if all the diagonal coefficients are different enough. If the depolarizer is degenerate (e.g. a back-scattering medium whose Mueller matrix would have two equal elements), only the diattenuators and the global retarder (product of M_{R1} and M_{R2}) would be correctly extracted using this decomposition. Therefore, this decomposition is best intended for media with a strong depolarization effect.

1.4 Particular case of a depolarizer: example of a non Stokes diagonalizable depolarizer

1.4.1 Theoretical background

We have previously seen that any non-depolarizing Mueller matrix preserves the degree of polarization of the input polarization state whereas a depolarizing matrix decreases it. Any depolarizing matrix can be regarded as the average of two or more non-depolarizing matrices [28]. Any Mueller matrix can be factored using the equation 1.58. We can separate the Mueller matrix space into two groups depending on the form of the central depolarizer and more precisely depending on whether this central depolarizer is diagonal or not. We define the auxiliary matrix $N = GM^TGM$, where $G = diag(1, -1, -1, -1)$, and compute its eigenvalue. If the eigenvector associated to the highest eigenvalue corresponds to a partially polarized polarization state, then the central depolarizer is diagonal, if it corresponds to a totally polarized state, the depolarizer cannot be diagonalized. These two groups are referred to as type I and type II matrices [29, 30, 31] We renamed these groups with more physical-sense appealing denominations, respectively Stokes diagonalizable and Stokes non-diagonalizable matrices [32]. Although encountering Stokes diagonalizable matrices in experiments is quite common (eg. depolarization arising with back scattering events), an experimental realization of Stokes non-diagonalizable matrices had not been proposed until recently when Sudha et al. [33] proposed their experimental proof from quantum measurement theory able to generate both Stokes diagonalizable and nondiagonalizable Mueller matrices. Nevertheless, their set-up is very complicated and we thought that a simpler scheme must be feasible. We then built a very simple optical set-up comprising only two non-depolarizing samples allowing us to generate a complete family of Stokes non-diagonalizable Mueller matrices.

If we consider the weighted average M of an inhomogeneous [34] ideal polarizer

M_{IP} and void M_v :

$$\begin{aligned} M &= \alpha \cdot M_{IP} + \beta \cdot M_v \\ &= \alpha/2 \begin{bmatrix} 1 & 1 & 0 & 0 \\ -1 & -1 & 0 & 0 \\ 0 & 0 & 0 & 0 \\ 0 & 0 & 0 & 0 \end{bmatrix} + \beta \begin{bmatrix} 1 & 0 & 0 & 0 \\ 0 & 1 & 0 & 0 \\ 0 & 0 & 1 & 0 \\ 0 & 0 & 0 & 1 \end{bmatrix} \\ &= \begin{bmatrix} \alpha/2+\beta & \alpha/2 & 0 & 0 \\ -\alpha/2 & -\alpha/2+\beta & 0 & 0 \\ 0 & 0 & \beta & 0 \\ 0 & 0 & 0 & \beta \end{bmatrix} \end{aligned} \tag{1.59}$$

with α and β are the corresponding weights.

It is straightforward to notice that the N matrix has a unique eigenvalue, fourfold degenerate, associated to the Stokes vector S=[1 -1 0 0] which represents a totally polarized state. This matrix is thus of type II, Stokes non-diagonalizable. By varying the weights α and β, we can generate a family of Stokes non-diagonalizable matrices.

1.4.2 Experimental realization

The first step of this experimental realization of a family of Stokes non-diagonalizable Mueller matrices is to create the inhomogeneous polarizer. This is easily done by combining an horizontal polarizer and an half-wave plate whose fast axis is oriented at 45° respect to the orientation of the polarizer.

$$M_{IP} = \begin{bmatrix} 1 & 0 & 0 & 0 \\ 0 & -1 & 0 & 0 \\ 0 & 0 & 1 & 0 \\ 0 & 0 & 0 & -1 \end{bmatrix} \frac{1}{2} \begin{bmatrix} 1 & 1 & 0 & 0 \\ 1 & 1 & 0 & 0 \\ 0 & 0 & 0 & 0 \\ 0 & 0 & 0 & 0 \end{bmatrix} \tag{1.60}$$

The second step is to "add" the inhomogeneous polarizer and void to generate our Stokes non-diagonalizable matrix. If multiplying two Mueller matrices is easily done and straightforward, the addition of two media is more subtle, it requires an incoherent superposition of two media. We include the inhomogeneous polarizer in the aperture plane of a Kohler illumination set-up. The illuminating beam cross section is larger than the polarizer clear aperture, so due to the fundamental property of telecentric systems (collimation of chief rays for all points across the image), the CCD pixels gather the sum of the response of void and our inhomogeneous polarizer.

The experimental set-up used is described in figure 1.5. On this figure, PSG (resp. PSA) stands for Polarization State Generator (resp. Polarization State Analyser), BFP (Back Focal Plane). The two pairs of lenses L1-L2 and L2-L3 form telecentric systems. The diaphragm placed in the back focal plane BFP1 enables us to control the beam cross section diameter of the sample and thus adjust β in eq. 1.59 and generate a family of Stokes non-diagonalizable matrices. More about this set-up can be found in [21, 27].

We measured some realizations of matrices belonging to this family with our device. The Mueller matrices obtained for two different void fractions are shown in figure 1.6. These matrices are clearly of the form shown in eq. 1.59. Each element of the Mueller matrix is a 256×256 image which enables us to extract more accurately the void fraction. To assess the quality of our measurements, we can compute some very simple estimators. We have selected the two following :

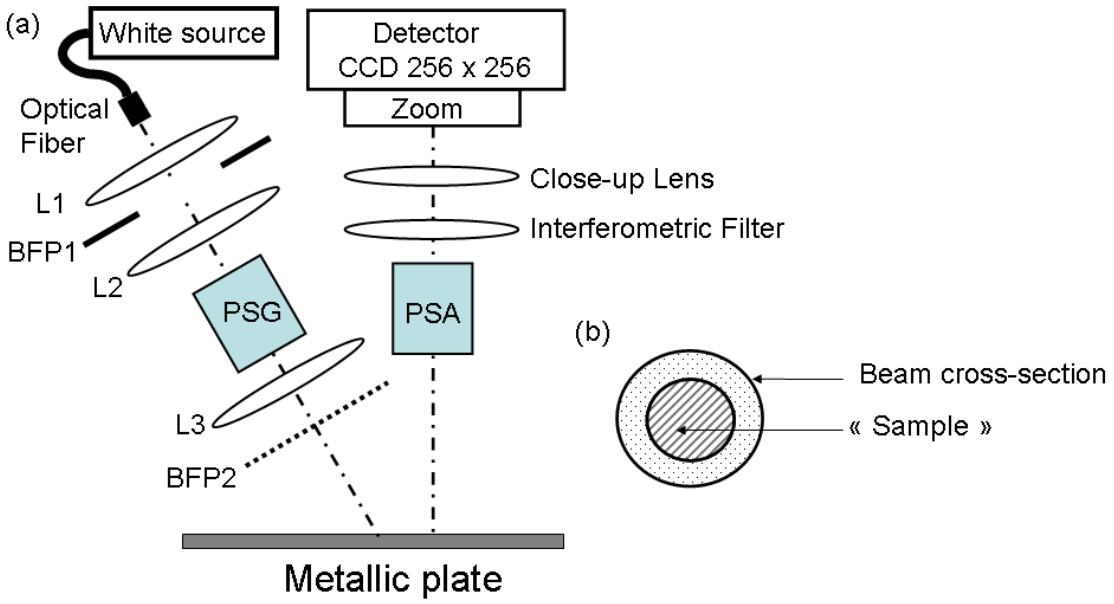

Figure 1.5: (a) : experimental set-up (b) : cross section of the back focal plane BFP2 where the sample is introduced

- $E_1 = M_{12} + M_{21}$: should be equal to 0
- $E_2 = M_{21} + M_{33} - M_{22}$:should be equal to 0

The results of these estimators for one of the measurements are shown in figure 1.7. The estimators are very inhomogeneous and display a clear deviation toward the positive values. However, the mean values for both estimators is quite close to zero ($\overline{E_1} = 0.02$, $\overline{E_2} = 0.03$) as well as standard deviation ($\sigma_1 = 0.01$, $\sigma_2 = 0.02$). The measurements can then be used to recover the void fraction using the M_{33} element which directly equal to β and M_{12} which is equal to $\alpha/2$. The graphes in figure 1.8 show the mueller matrix elements evolution versus the void fraction. We notice that the evolution of the matrix elements respect to the void fraction is nearly linear.

If you look closer at the algebraic properties of this family of matrices, we notice

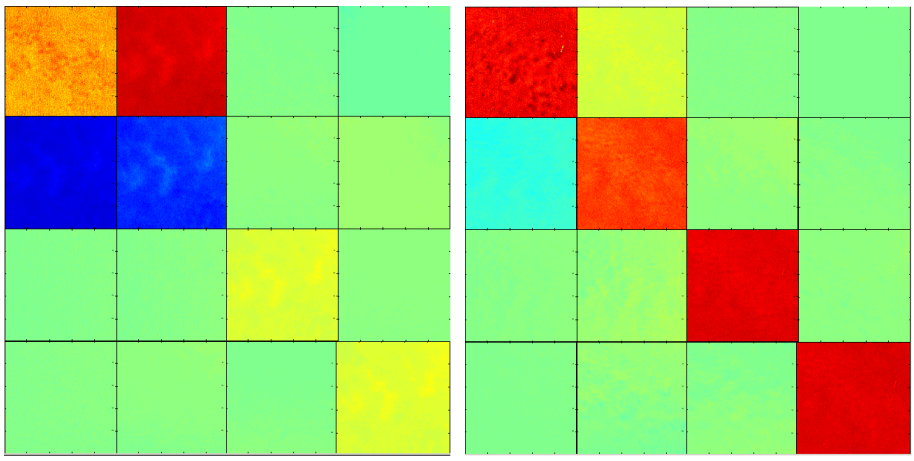

Figure 1.6: Mueller matrices measured using our imaging polarimeter for two different void fractions

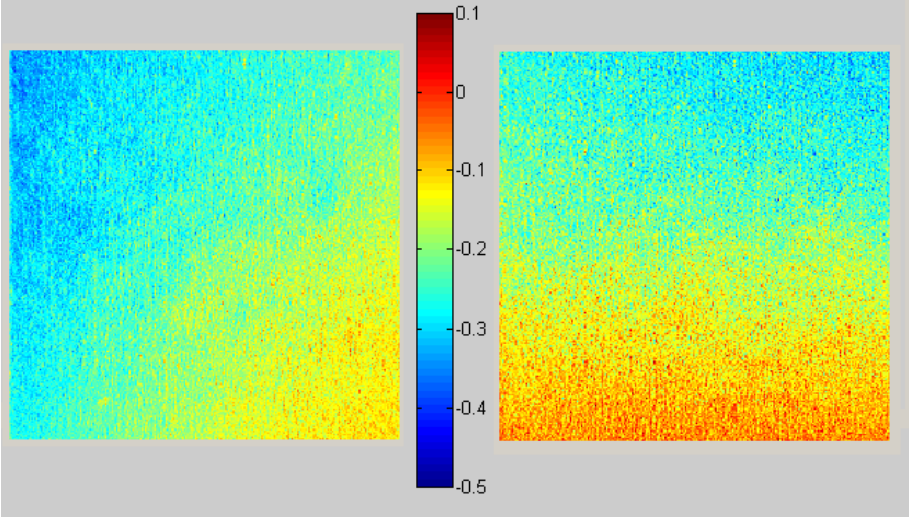

Figure 1.7: left : $M_{12} + M_{21}$ - right : $M_{21} + M_{33} - M_{22}$

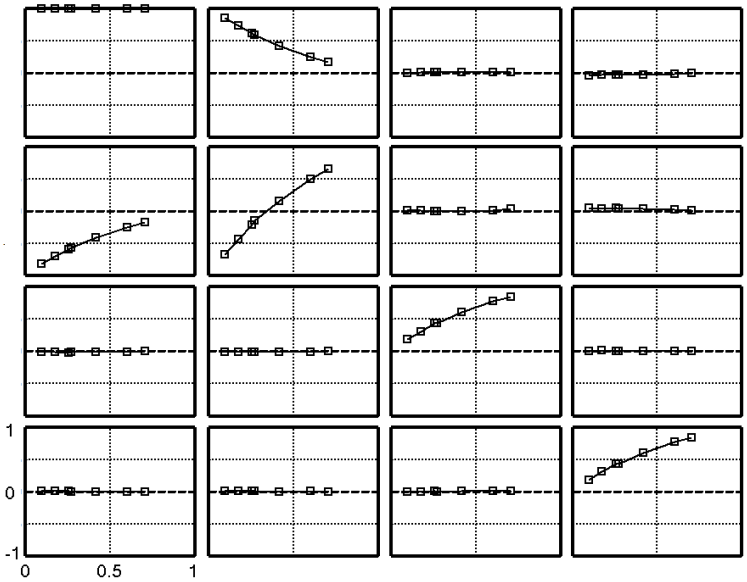

Figure 1.8: Experimental elements of the normalized Mueller matrix versus the void fraction. The experimental errors is smaller than the size of the square. The solid line is a guide for the eye. All x axis between 0 and 1, all y axis between -1 and 1

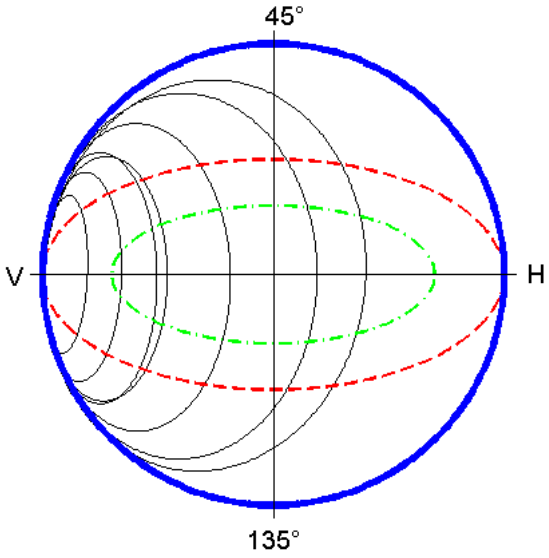

Figure 1.9: Equatorial cut of the Poincaré sphere. Blue line : equator (non-depolarizing Mueller matrix); black solid lines : experimental Stokes non-diagonalizable matrices; dashed red and green lines : diagonal depolarizer

that the totally polarized eigen vector of the auxiliary matrix N is the only Stokes vector which is not depolarized by the medium. We can state it differently by saying that a Stokes non-diagonalizable matrix decreases the degree of polarization of all the input Stokes vectors except the one associated to the eigenvalue of the auxiliary matrix N. This general property of the type II matrices can be demonstrated geometrically by plotting the output ellipsoid of degree of polarization for our experimental matrices. If the matrix is a non-depolarizing one, it means that any totally polarized state is transformed into a totally polarized state: the Poincaré sphere is mapped onto itself. In fig. 1.9, we only plot the equatorial cut of the Poincaré sphere because the polarization states of interest are the linearly polarized ones.

We can now characterize the Stokes non-diagonalizable matrices using the number of contacts between the Poincaré Sphere and the DOP ellipsoid. If the ellipsoid has zero, two or more than two contact points with the Poincaré sphere, then the Mueller matrix can be reduced to a Stokes diagonalizable matrix. On the other hand, if the ellipsoid has only one contact point with the Poincaré sphere, the Mueller matrix belongs to the Stokes non-diagonalizable family and the contact point corresponds to the totally polarized eigenvector of the auxiliary matrix N.

Chapter 2

Mueller Microscope

This chapter aims at describing the experimental configuration chosen for implementation in the laboratory always keeping in mind the commercial purpose of the instrument through its development by the company Horiba Jobin Yvon. We shall justify the technical choices we made and the key points of design.

2.1 Experimental configuration of the microscope

We want to be as close as possible to a conventional microscope configuration. Abundance of literature on this topic and commercial availability of blocks that can be assembled oriented us toward this path. However, one quickly realizes that there is not a conventional microscope, but a huge variety of designs [35, 36]. This number of designs can be reeduced given that for the intended applications, only the inspections in reflection are to be considered. It should be noted therefore that this is a reduction of the possibilities of the instrument originally developed in our group by Sami Ben Hatit [37]. In the original version, the inspection of samples in double-pass transmission was also studied [38].

The constraint of the study imposes a reflection microscope in epi-illumination: under such arrangement, the microscope objective plays the dual role of condenser in the illumination part and objective in the imaging part.

2.1.1 Illumination part

The illumination part has been designed like a Köhler illumination, this kind of illumination system is widely used in traditional microscopy [35] due to the total decoupling it enables between the field and the aperture. In our system, this decoupling is crucial because we need to be able to control the field we enlighten without changing the numerical aperture.

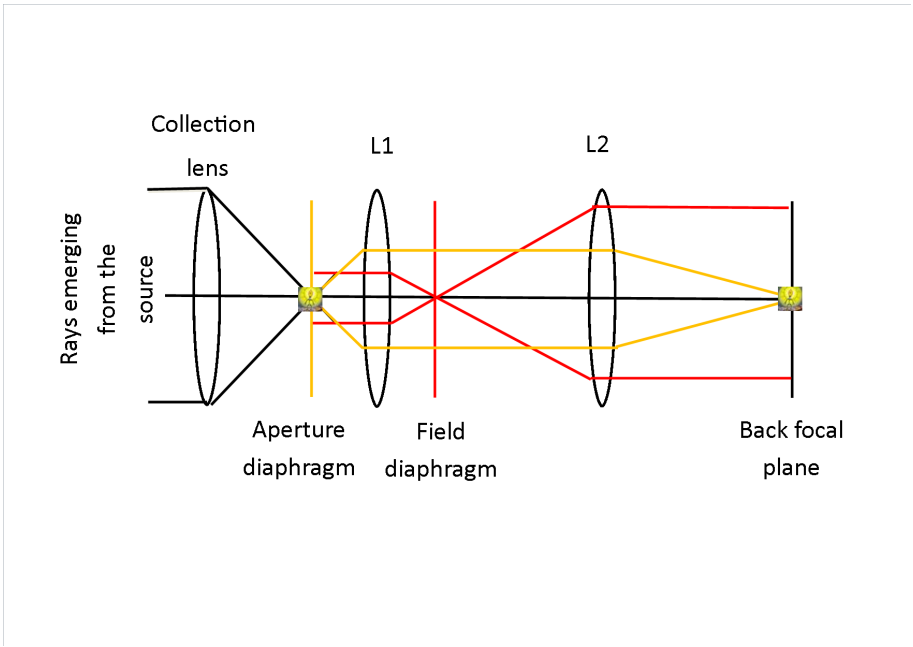

Figure 2.2: Classical scheme for a Köhler illumination. The light source is focused in both the aperture diaphragm and the back focal plane of the objective

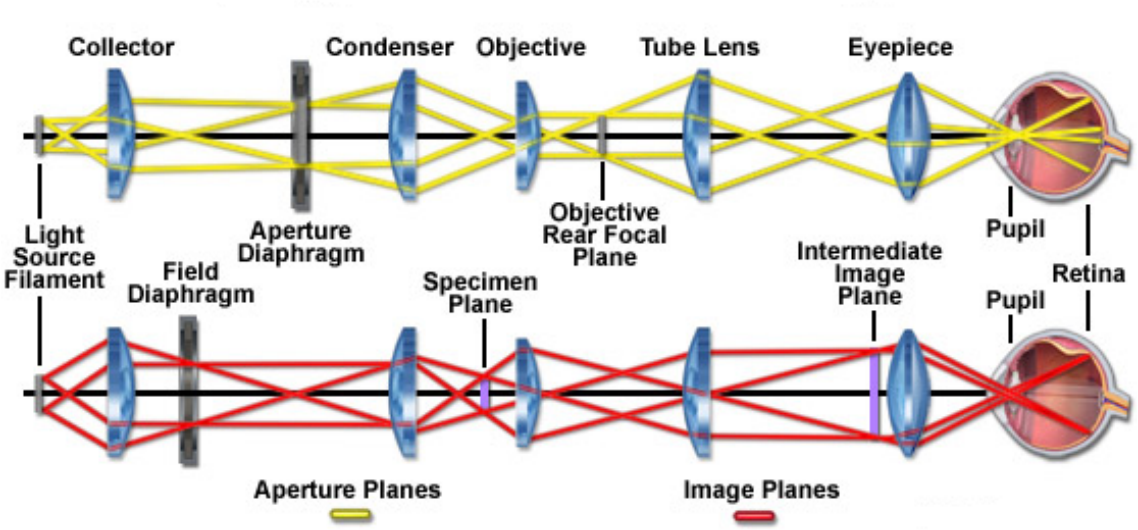

Figure 2.1: Sets of conjugate planes in Köhler illumination, courtesy of Carl Zeiss, Inc

The aperture diaphragm is used as a secondary source. However, the Köhler illumination images the light source in the back focal plane of the condenser (in the epi-illumination case, the objective). In classical microscopy (i.e. trans-illumination and imaging in the real space), this design is optimal because the sample is evenly enlightened and the light source is not imaged at the same time as the sample (see fig. 2.2). We want thus to create some kind of Köhler illumination designed for the Fourier space imaging where the sets of conjugate planes should be inverted.

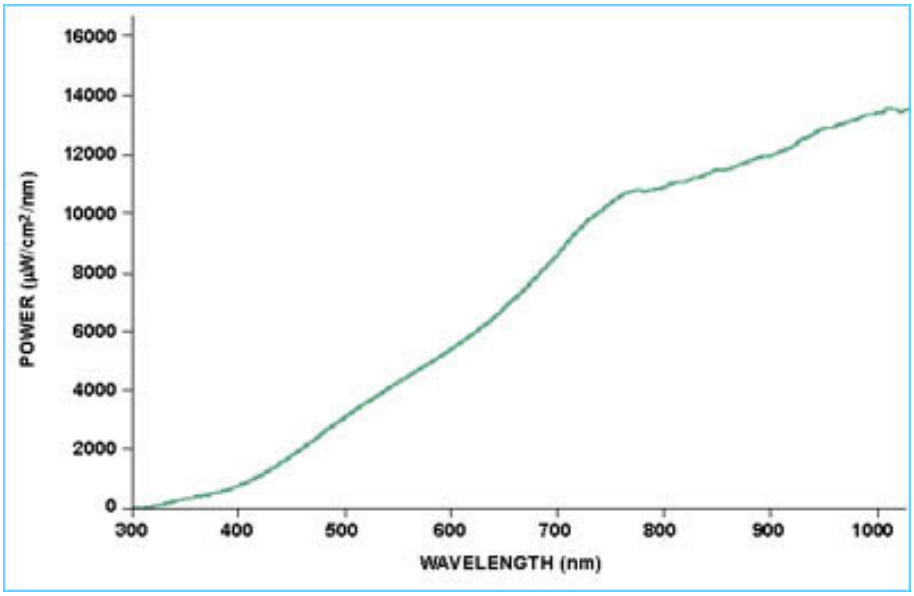

Figure 2.3: Output spectrum of the light source

Nevertheless, we specified as a key feature of our device its versatility with respect to the imaging modes it offers: the illumination will be a trade-off between the real space and the Fourier in order to have a good illumination quality no matter what the imaging mode is. We then chose to slightly defocus the light source (Ocean Optics HL2000 HP, 20W output which emission spectrum can be found in fig. 2.3) so it is not directly imaged neither in the back focal plane of the objective nor in the sample plane. This defocus of the source does not hinder the decoupling of the field and the aperture, this property being granted by the arrangement of the lenses and the diaphragms. The light emerges from the source through an optical fiber (diameter $\Phi = 600\mu m$, numerical aperture $NA = 0.34$). The lens L_1 is said to be telecentric both in the image and the object space. All lenses are commercially available lenses from Edmund Optics. We chose the inked lenses so the reflection on the edges are limited.

> "Telecentricity is a special property of certain lens designs in which the chief rays for all points across the object or image are collimated. For example, telecentricity occurs when the chief rays are parallel to the optical axis, in object and/or image space. Another way of describing telecentricity is to state that the entrance pupil and/or exit pupil of the system is located at infinity." (definition by Edmund Optics, Inc).

By inserting a diaphragm in the front focal plane of the lens, we are imposing the exit pupil to be located at infinity, and by placing a diaphragm in the back focal plane, we are imposing the entrance pupil to be located at infinity too [39]. One should be careful when dealing with the concept of telecentricity because the same term may describe a lot of different things. Throughout this manuscript we will use the term telecentric as previously defined. Let us notice that the pair of lenses L_1 and L_2 is sometimes called a telecentric system or a telescope instead of a afocal system, we will try to avoid ambiguous denominations when possible.

Figure 2.4 shows the images in the back focal plane of the objective: (a) with a good focus of the light source and (b) with a slight defocus. One can notice that the back focal

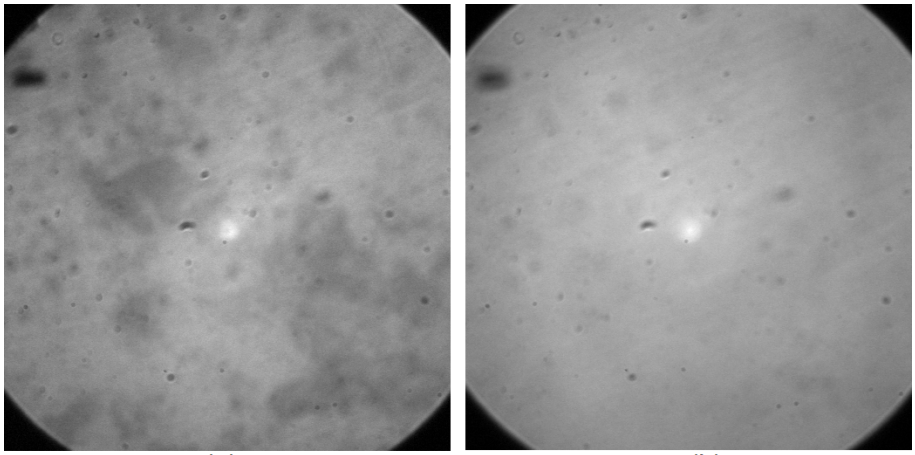

Figure 2.4: (a) : image of the source in the back focal plane when well focused - (b) : image of the source in the back focal plane when slightly out of focus

Wavelength (nm)	T_s	T_p	$T_s - T_p$
454	45,881049	44,208247	1,672802
532	45,381157	48,103459	-2,722302
633	46,292081	46,639766	-0,347685

Table 2.1: Transmission factors of the non-polarizing cube beam-splitter for the wavelengths used during measurements

plane is then more evenly illuminated with the slight defocus, all the inhomogeneities of the source not being imaged.

Figure 2.5 points out the changes brought to the classical Köhler illumination set-up.

It is to be noticed that not all lens alignments are critical in the illumination system. The first lens L_{Coll} only serves as a light collector and thus does not need to be very accurately positioned whereas the lenses L_1 and L_2 should be positioned with extreme caution: it is very important that the back focal plane of L_1 is superimposed on the front focal plane of L_2 if we want the field and the aperture to really be decoupled.

The non-polarizing beam splitter

Although the system will be calibrated using a very powerful method, the choice of the beam-splitter we are using is critical because the light passes twice in it, once in the illumination part and once in the imaging part. We then use a broadband non-polarizing cube beam-splitter which transmission curves are given in fig. 2.6. For our measurements, we specifically use three different wavelengths: 454nm, 532nm and 633nm. Table 2.1 gives the transmission factor of the cube beam-splitter for these three wavelengths.

This beam-splitter features a low polarization dependence of the dichroic coating allowing the transmission of the s- and p- polarizations to be within 6% of each other. It consists of a pair of precision high tolerance right angle prisms cemented together with a metallic dielectric coating. A broadband antireflective coating is applied to each face of the beam-splitter avoiding unwanted reflections. However, we notice during the

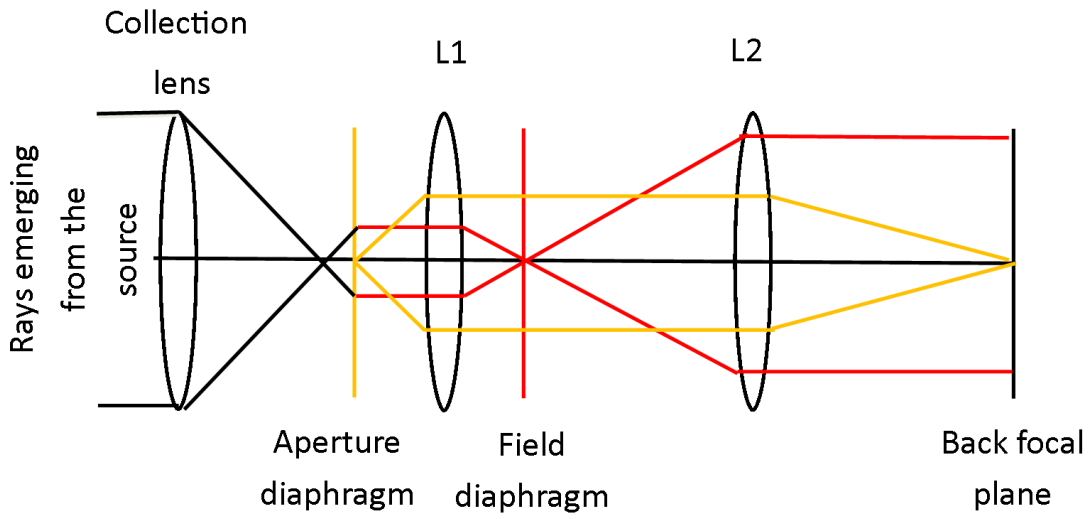

Figure 2.5: New illumination system with source slightly defocused

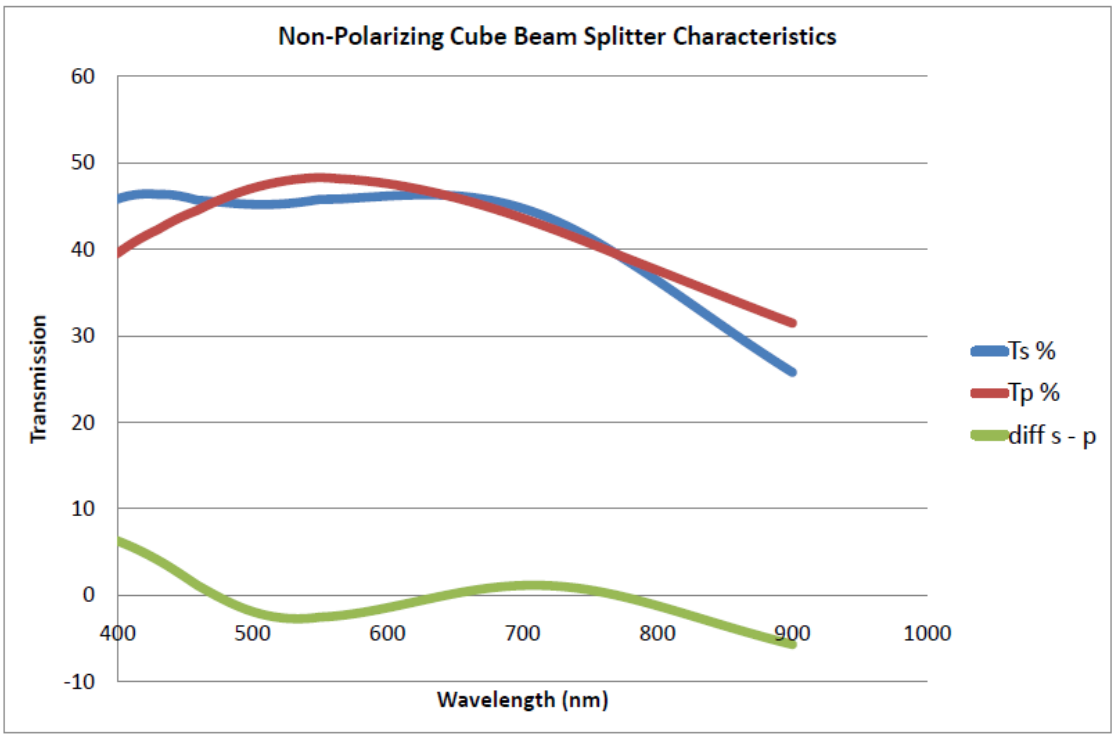

Figure 2.6: s- and p- polarization transmission curves of the non-polarizing beam-splitter versus wavelength.

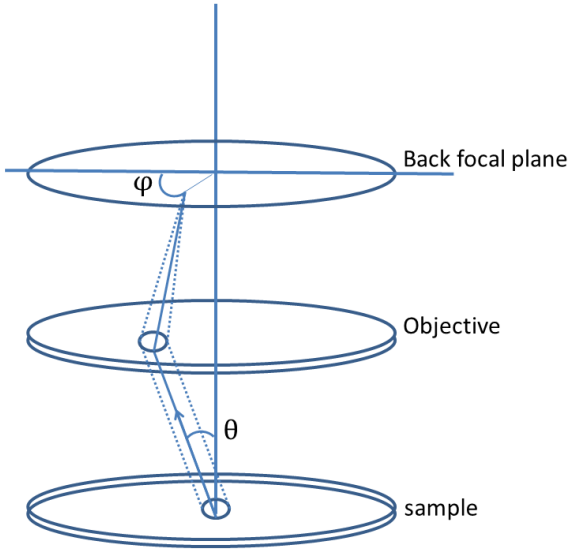

Figure 2.7: Principles of a conoscopic inspection: Parallel rays with inclination θ and azimuth φ, focused by the objective at a point with radius $r = \sin(\theta)$ and same azimuth.

alignment of the system that the antireflective coating is not perfect and dual images appear on the detector. Due to the incoherent superposition of two images on the detector, depolarization arises and should then be accurately calibrated.

2.1.2 Imaging part

Our device should have two modes of imaging: real space and its conjugate space, the Fourier space. Even though the measurements are performed in Fourier space, imaging in real space is essential to be able to find the right spot on the samples.

In real space, images are spatially resolved, for each pixel located by its cartesian coordinates (x,y), all angles defined by the aperture are averaged. This observation mode will also be referred to as orthoscopic mode.

In the Fourier space, images are angularly resolved, for each pixel then located by its cylindrical coordinates (θ,ϕ), all points defined by the field are averaged. This imaging mode is often referred in the bibliography as conoscopic mode: we analyse the light emitted (reflected, scattered or diffracted) in a cone of light which aperture is defined by the numerical aperture of the microscope objective. In fig.2.7, one can see that every collimated beam of light emitted with an angle θ at an azimuth φ exits the microscope objective in a pixel which cartesian coordinates are $(R\sin\theta\cos\varphi, R\sin\theta\sin\varphi)$. Conoscopic observation is nothing new to any microscopist, in a conventional microscope it can be made either by replacing the regular ocular with a telescope that brings the aperture plane into focus or by inserting a Bertrand lens (that serves as a telescope objective) in front of a regular ocular. These systems are commercially available and are still a part of fundamental research in microscopy [40].

The key point of the imaging part design is to keep it simple, especially how to switch from one space to the other. We chose to keep the general idea of the previous design, a removable lens to switch from real to Fourier space. However, when we previously had to add the lens to be in the Fourier space, we now have the simpler design for this space. The basics of the design are outlined in fig. 2.8. A very good introduc-

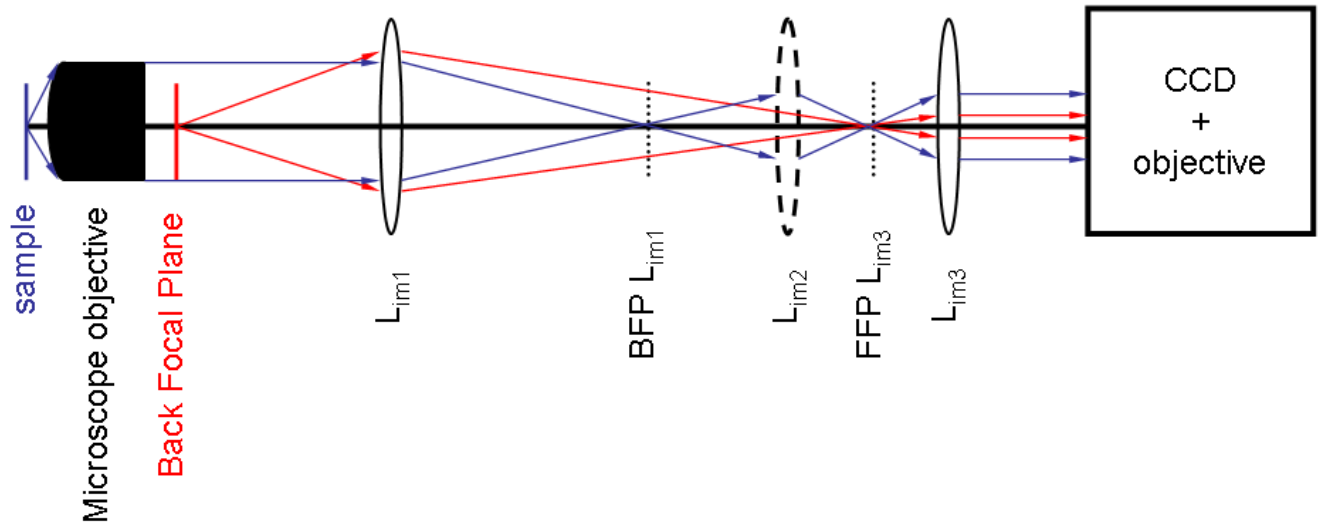

Figure 2.8: Layout of the imaging part of the system. BFP : Back Focal Plane, FFP : Front Focal Plane. In blue : ray tracing for the real image of the sample, in red : ray tracing for the imaging of the back focal plane of the objective

tion to imaging optical system and some examples of ad-hoc lens configurations used extensively during the design process can be found in [39].

Imaging the Fourier space means imaging the back focal plane of the microscope objective. The first lens L_{im1} is just performing a simple point-point conjugation between the back focal plane and an intermediate plane where, if needed, we can add an aperture diaphragm to select the imaged angles. The intermediate plane is then imaged on a CCD camera using an afocal system comprising a 25mm lens (L_{im3})and the CCD camera with its objective set at the infinity. This system enables us to change very easily the camera and its objective: we just have to match the global magnification of the imaging part by choosing the proper focal for the objective with respect to the size of the detector.

To image the sample (real space imaging), we just have to add a lens (L_{im2}) between L_{im1} and L_{im3}. This lens must conjugate the back focal plane of L_{im1} and the front focal plane of L_{im3}. By doing so, the sample and the Fourier plane can be both imaged using the same configuration and without major change in the set-up (just switching a retractable lens).

The detector

A badly chosen detector is the ruin of an imaging system The detector linearity, spatial and temporal stability are the key factors of a good image. We use a Hamamatsu Orca II BT LAG camera in our system. This is an air-cooled camera (cooling down to -60°C) with a 512×512 CCD detector (pixel size : $24\mu m$). The grayscale ranges from 0 to 4095 (12 bits). The quantum efficiency of the detector is given in fig.2.9

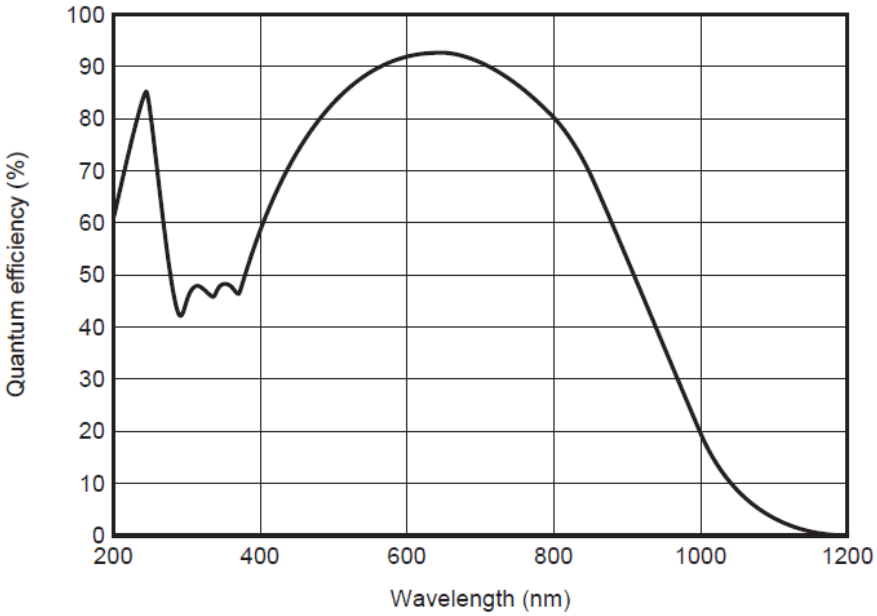

Figure 2.9: Quantum efficiency of the detector versus wavelength

The linearity of the detector has been tested in previous work [41]. The changes brought to the system especially the new light source impose a new study of the noise and stray light causing ghost images which results are summarized in table 2.2. From this study, it is pretty clear that the doors must be kept close during the experiments; however, once the doors are closed, all secondary sources (halogen source and neon lights in the experiment room) can remain switched on during measurement without affecting the results. One should remain careful when measuring low reflectivity samples: as we can see, even without any sample, the stray light can go up to 40 on the 4096 level grayscale with the doors closed which means that for a low reflecting sample some intensity images we acquire can be completely ruined by this stray light and then loose all their meaning.

For all measurements presented in this manuscript, we tried to keep the minimal average signal (on the 16 images required to compute the Mueller matrix) around 10 times the stray light level, i.e. around 400 on the grayscale, by varying the exposure time.

2.2 From a classical microscope to a polarization microscope

Using polarization in microscopy is quite common and enables to observe anisotropy of crystals for example. It is mostly used as a contrast enhancing method for birefringent materials. Used solely by geologists in mineralogy and petrographic research for some time, it has since been successfully used in biology, medicine, chemistry and material research. However, polarization is not very often used quantitatively but rather qualitatively. The best known application of quantitative polarized microscopy is the study of minerals in thin sections of rocks [42]. Although very similar to common bright-field microscopes, a polarized light microscope includes specific parts such as a strain free

Experimental conditions	Mean	Max
camera shutter closed	4.35	26
(C1): shutter auto, all sources off, doors open	36	67
(C2): shutter auto, all sources off, doors closed	34	65
(C1) + low halogen source	112	190
(C1) + medium halogen source	370	610
(C1) + high halogen source	990	1700
(C2) + low halogen source	35	65
(C2) + medium halogen source	35	65
(C2) + high halogen source	37	68
Source on, black paper before L_{coll}	37	70
Source on, black paper before PSG	37	70
Source on, black paper before NPBS	38	70
Source on, black paper between NPBS and objetive	42	75

Table 2.2: Noise signal during acquisition (Ti = 200ms) without sample respect to the different experimental conditions

objective, a strain free condenser and a polarizer / analyzer couple. Figure 2.10 gives an outlook of the different samples one can image using a polarized light microscope.

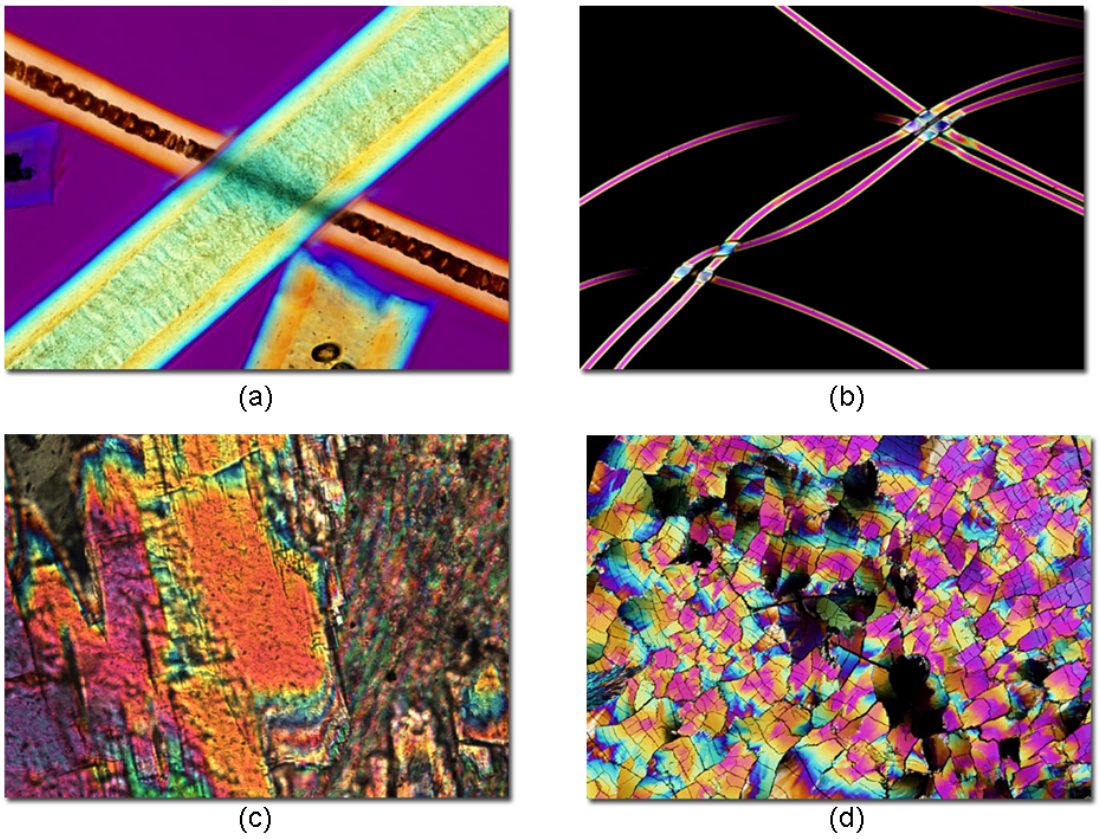

Figure 2.10: Examples of images acquired with a polarized light microscope (a) badger hair (b) nylon fiber (c) actinolite schist (d) cholesterol

2.2.1 Choice of the microscope objectives

During manufacturing of the objective, stress can be introduced into the glass which then produces spurious optical effects under polarized light like diattenuation or retardance which could compromise accuracy of the polarimeter. Objectives designed for polarized light observation are distinguished from ordinary objectives with the inscription P, PO, or Pol on the barrel. These objectives can be used in our polarimeter for inspection. We selected the CFI LU Plan Fluor EPI microscope from Nikon because they offer the best trade-off between high numerical aperture and high working distances. They also are compliant with the evolution of the system we had in mind when buying them: dark-field observations and UV illumination. It may seem difficult to understand all the subtle differences between microscope objectives but all the information needed are clearly listed on the barrel of the objective. Table 2.3 gives the most common specifications of microscope objectives.

The numerical aperture of the objective gives us the maximum angle we can reach [39] :

$$NA = n \cdot \sin(\theta_{max}) \tag{2.1}$$

The numerical aperture and the maximum angle being proportional, we will sometimes refer to them using indifferently the term aperture.

Due to technical difficulties, we are not using immersion objectives so the working medium is the air. In eq. 2.1, the refraction index n is then always equal to 1.

The CFI series of Nikon objectives use a tube length (TL) of 200mm contrary to some other manufacturers who use different tube lengths. We can for example cite Olympus who uses a 180mm tube length and Zeiss using a 165mm tube length. The tube length, also called the reference focal length, helps us calculate the focal length of the objective :

$$f_{obj} = \frac{TL}{Magnification} \tag{2.2}$$

The size of the exit pupil is then :

$$D_{pupil} = 2 \cdot NA \cdot f_{obj} \tag{2.3}$$

Table 2.4 summarizes the principle features of the chosen objectives.

As we will see in next sections, though these objectives are better suited for quantitative polarization, they are not free of polarization effects and then require either a proper modeling or calibration. Unfortunately, it has been impossible despite asking several times to gain access to more detailed information on the design of the objectives and especially their remaining polarization effects when used in conoscopic mode.

2.2.2 General considerations on polarimeters

The main limitation of a polarized light microscope is that only one polarization state is generated and only one polarization state is analyzed. We transformed the conventional microscope described in 2.1 into a polarimeter by adding a polarization state generator (PSG) and a polarization state analyser (PSA) in respectively the illumination and the imaging part of the microscope. We assume that the elements forming the PSG and PSA are thin enough and well-aligned so we can neglect the defocus and the change in position of the image when adding them in the light path. In some cases,

abbreviation	type
Plan	Flat Field optical correction
Apo	Apochromatic aberration correction
Fluor, Fl, Fluar, Neofluar, Fluotar	Fluorite aberration correction
Achro, Achromat	Achromatic aberration correction
LU	Nikon Luminous Universal (Brightfield, Darkfield, DIC, and Polarized L
L, LL, LD, LWD	Long Working Distance
ELWD	Extra Long Working Distance
Oil, Oel	Oil immersion
Water, W, Wasser	Water immersion
DIC, NIC	Differential or Nomarski Interference Contrast
CF, CFI	Chrome-Free, Chrome-Free Infinity-Corrected (Nikon)
P, Po, Pol, SF	Strain-Free, Low Birefringence, for polarized light
U, UV, Universal	UV transmitting (down to approximately 340 nm)
EPI	Epi illumination

Table 2.3: List of common abbreviations on microscope objectives

reference	Magnification	Numerical aperture	Working Distance	Exit pupil diameter
MUE10050	5X	0.15	23.5mm	12mm
MUE10200	20X	0.45	4.5mm	9mm
MUE10500	50X	0.80	1mm	6.4mm
MUE10901	100X	0.90	1mm	3.6mm

Table 2.4: Specifications of the chosen objectives

choosing some very well-suited polarization states can actually gives better results, either for degree of polarization imaging[43] or in Mueller polarimetry [44]. We see that the choice of the PSG (and the PSA) is a key point of the polarimeter. The upgraded layout of the microscope is given in fig. 2.11.

As stated previously, the polarization state of light changes when reflected, diffracted or scattered by a medium: the measurement of the Mueller matrix of the medium is called polarimetry. A polarimeter is generally made of a light source, a polarization state generator and a polarization state analyzer and a detector. To have a complete measurement of the Mueller matrix, it is mandatory to generate a basis of the Stokes vector space, which means that at least 4 independent Stokes vectors must be generated by the PSG and the same condition applies to the PSA. However, it is possible to overdetermine the system and generate more than four states if the benefits and costs of such change in the set-up have been fairly considered in terms of time and complexity.

Let us call $W_i, i \in [1,2,3,4]$ the Stokes vectors generated by the PSG, and $A_j, j \in [1,2,3,4]$, the Stokes vectors generated by the PSA. The interaction between the Stokes vector W_i generated by the PSG and the Mueller matrix of the sample $\mathbf{M}$ can be written as the product $\mathbf{M} \cdot W_i$. On the detector, we measure the intensity I_{ij} at the exit of the PSA characterized by the Stokes vector A_j.

$$I_{ij} = A_j \cdot \mathbf{M} \cdot W_i \tag{2.4}$$

We generate 4 independent states for the PSG and the PSA, we can summarize the 16 measurements using the matrix formalism.

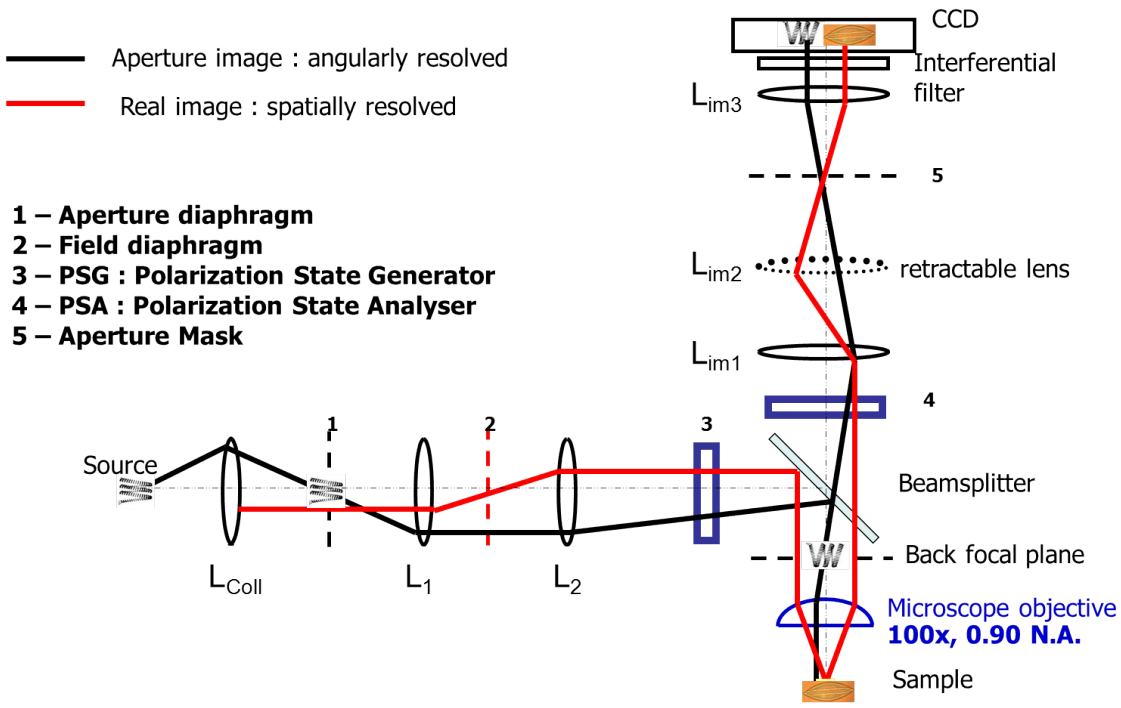

Figure 2.11: Upgraded layout of the microscope

$$\mathbf{B} = \mathbf{A} \cdot \mathbf{M} \cdot \mathbf{W} \tag{2.5}$$

with $\mathbf{B}$, a 4×4 matrix, matrix of the measured intensities, $\mathbf{A}$ and $\mathbf{W}$ matrices composed of the concatenation of the generated Stokes vectors.

The Mueller matrix $\mathbf{M}$ of the sample can be extracted from the measurement matrix $\mathbf{B}$ with a matrix inversion.

$$\mathbf{M} = \mathbf{A}^{-1} \cdot \mathbf{B} \cdot \mathbf{W}^{-1} \tag{2.6}$$

Though it may seem simple to invert the matrices $\mathbf{A}$ and $\mathbf{W}$, we have to check the invertibility. For a matrix to be invertible, its columns must be linearly independent which means in our case that the four states must be as linearly independent as possible. If we project the generated states on the Poincaré sphere, the states must be homogeneously scattered. A very simple guess clearly shows us that to be able to accurately measure the Mueller matrix of a linear polarizer, choosing four states very close to each others would propagate more errors [45].

The computation of the inverse matrix may propagate errors throughout the calculus of the Mueller matrix, we then have to define a criterium to check the quality of the matrix inversion. We then introduce the condition number associated to our matrix inversion problem. Let $\mathbf{A}$ and $\mathbf{B}$ be two matrices. We define the equation

$$\mathbf{A} \cdot \mathbf{X} = \mathbf{B} \tag{2.7}$$

We assume that all dimensions match so the equation exists and has a solution.

The condition can be roughly thought as the rate at which the solution of an equation will change with respect to the change in initial members. Thus, if the condition number is large, even a small change in $\mathbf{B}$ in our equation may cause a large error on $\mathbf{X}$. On the other hand, if the condition number is pretty small, the errors on $\mathbf{X}$ will not be bigger that the errors on $\mathbf{B}$.

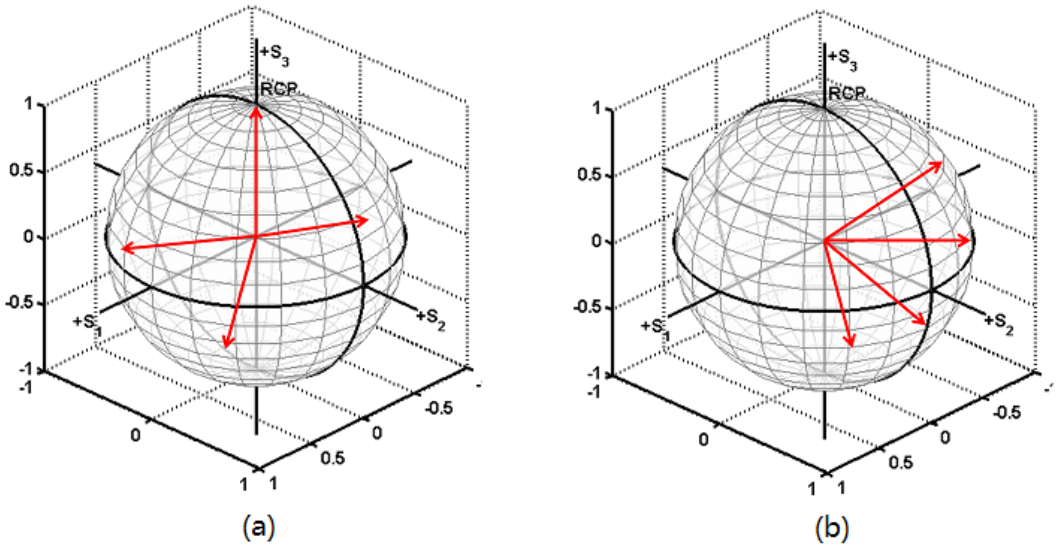

Figure 2.12: Examples of possible polarization states generated by the PSG (PSA) (a): best a priori choice for 4 linearly independent states. (b) bad choice: states are clearly not linearly independent

The condition number of a matrix **A** is defined as:

$$C(\mathbf{A}) = Norm(\mathbf{A}^{-1}) \cdot Norm(\mathbf{A}) \tag{2.8}$$

If we choose the L_2 norm, and if the matrix **A** is normal (i.e. $\mathbf{A}^{\dagger} \cdot \mathbf{A} = \mathbf{A} \cdot \mathbf{A}^{\dagger}$) then the condition number of the matrix **A** is defined as:

$$C_A = \left| \frac{\lambda_{max}}{\lambda_{min}} \right| \tag{2.9}$$

With λ_{max} and λ_{min}, the biggest and smallest (by moduli) eigenvalues of **A**.
In the case of our polarimeter, equation 2.6 can be rewritten as:

$$\mathbf{M} = \mathbf{Q}^{-1} \cdot \mathbf{B} \tag{2.10}$$

with **M** and **B**, written as 16 component vectors and **Q**, a 16 by 16 matrix defined as:

$$\mathbf{Q} = \mathbf{W}^t \bigotimes \mathbf{A} \tag{2.11}$$

The noise $\delta\mathbf{M}$ on the computed Mueller matrix is directly linked to the noise on the measurement $\delta\mathbf{B}$ by the following relationship:

$$\delta\mathbf{M} = \mathbf{Q}^{-1} \cdot \delta\mathbf{B} \tag{2.12}$$

By applying the norm on equations 2.12 and 2.10, supposing that the measurement noise comes primarily from the matrices **A** and **W**, the relative error on the Mueller matrix is bounded by:

$$\frac{\|\delta\mathbf{M}\|}{\|\mathbf{M}\|} \leq \|\mathbf{Q}^{-1}\| \cdot \|\mathbf{Q}\| \cdot \frac{\|\delta\mathbf{B}\|}{\|\mathbf{B}\|} \tag{2.13}$$

The condition number of the 16 by 16 matrix **Q** clearly arises in equation 2.13. To minimize the relative errors on **M**, we have to minimize the condition number of **Q**. Given that the condition number of the inverse of a matrix is equal to the condition number of the matrix and that the condition number of a product is the product of the condition number, it is straightforward that

$$C(\mathbf{Q}) = C(\mathbf{W}) \cdot C(\mathbf{A}) \tag{2.14}$$

We have to optimize both condition numbers of the PSG and the PSA [46]. The theoretical limit for the condition number of a matrix is 1 when the matrix is unitary. However, the matrices **A** and **W** are special matrices: their rows (or columns) are Stokes vectors representing totally polarized states which implies some theoretical bounds. The condition number of the matrix of the PSG and the PSA is bounded by $\sqrt{3}$.

2.2.3 Design and optimization of the PSG (PSA)

The idea is to be able to generate 4 independent polarization states. The illumination is provided by an unpolarized light source (Ocean Optics HL2000 HP, 20W output). To generate our polarization states, we use a linear polarizer and two nematic liquid crystals (LC) which are linear retarders. This is one of the many designs we could have chosen for the PSG [43, 47, 48, 49, 50, 51].

We assume that all polarization elements are perfect which means that the linear polarizer (resp. retarder) does not exhibit retardance (resp. diattenuation).

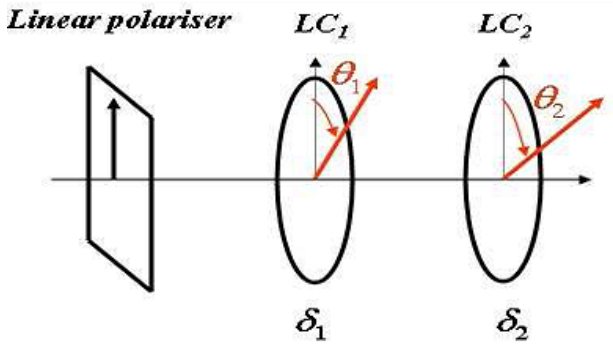

Figure 2.13: General layout of a PSG made of a linear polarizer followed by two nematic liquid crystals

The PSG is then fully characterized by 4 parameters: the orientations of the fast axis of the LCs with respect to the orientation of the linear polarizer (θ_1 and θ_2) and their retardance (δ_1 and δ_2).

We can calculate the Stokes vector generated by this PSG.

$$S = M_{\theta_2,\delta_2} \cdot M_{\theta_1,\delta_1} \cdot \frac{1}{2} \cdot \begin{bmatrix} 1 & 1 & 0 & 0 \\ 1 & 1 & 0 & 0 \\ 0 & 0 & 0 & 0 \\ 0 & 0 & 0 & 0 \end{bmatrix} \tag{2.15}$$

As seen in the appendixes, the Mueller matrices of a linear retarder is:

$$M_{\theta,\delta} = \begin{bmatrix} 1 & 1 & 0 & 0 \\ 1 & c^2 + s^2 \cos\delta & cs(1-\cos\delta) & s \cdot \sin\delta \\ 0 & cs(1-\cos\delta) & c^2 + s^2 \cdot \cos\delta & -c \cdot \sin\delta \\ 0 & -s \cdot \sin\delta & -c \cdot \sin\delta & \cos\delta \end{bmatrix} \tag{2.16}$$

with $c = \cos 2\theta$ and $s = \sin 2\theta$

The output Stokes vector is given by:

$$S = \begin{bmatrix} 1 \\ (c_2^2 + s_2^2 \cos\delta_2)(c_1^2 + s_1^2 \cos\delta_1) + c_1 c_2 s_1 s_2 (1-\cos\delta_1)(1-\cos\delta_2) - s_1 s_2 \sin\delta_1 \sin\delta_2 \\ c_2 s_2 (1-\cos\delta_2)(c_1^2 + s_1^2 \cos\delta_1) + c_1 s_1 (1-\cos\delta_1)(s_2^2 + c_2^2 \cos\delta_2) - s_1 c_2 \sin\delta_1 \sin\delta_2 \\ s_2 \sin\delta_2 (c_1^2 + s_1^2 \cos\delta_1) - c_2 \sin\delta_2 c_1 s_1 (1-\cos\delta_1) + s_1 \sin\delta_1 \cos\delta_2 \end{bmatrix} \tag{2.17}$$

The columns of the matrix **W** are the four Stokes vectors generated by switching the retardations of the liquid crystals. Optimizing **W** is equivalent to optimizing the orientations and retardations of the LCs.

A previous work by Blandine Laude-Boulesteix [52] using numerical optimization demonstrated that this maximum of the condition number of **W** can be reached by switching the liquid crystals between two well-chosen states in the following sequence:

$$(\delta_1, \delta_2) = (\Delta_1, \Delta_1); (\Delta_2, \Delta_1); (\Delta_1, \Delta_2); (\Delta_2, \Delta_2) \tag{2.18}$$

where the first value is the retardation applied to the first liquid crystal and the second value is applied to the second liquid crystal. For this configuration, it has been demonstrated that the following values of the retardations (Δ_1, Δ_2) are optimal.

$$\Delta_1 = 315^\circ + p \cdot 90^\circ \quad \Delta_2 = 135^\circ + p \cdot 90^\circ \tag{2.19}$$

with p an integer having the same value for Δ_1 and Δ_2.

and the orientations of the liquid crystals are given by:

$$\theta_1 = \varepsilon 27.4^\circ + q \cdot 90^\circ \quad \theta_2 = \varepsilon 72.4^\circ + r \cdot 90^\circ \tag{2.20}$$

with q and r two integers and $\varepsilon \pm 1$

The evolution of the condition number with respect to Δ_i and θ_i can be found in the manuscript of Blandine Laude-Boulesteix [52]. The optimization presented here is by no means the only one, it is one of the possibility to generate 4 polarization states distributed along a tetrahedron but we can not choose the states generated and thus optimize the input states by mapping the whole Poincaré sphere. To do so, one should choose $\theta_1 = 45^\circ$ and $\theta_2 = 0^\circ$ and choose the retardation accordingly to the application.

We optimize the PSA with exactly the same method: we switch the LC between two well-chosen retardations Δ_1 and Δ_2. We take $\mathbf{A} = \mathbf{W}^t$ and therefore, **A** and **W** have the same condition number.

About the liquid crystals

The selected nematic liquid crystals are liquid crystal variable retarders (LVR100) from Meadowlark Optics. The principles of liquid crystals are outlined in fig. 2.14. With

no voltage applied, the molecules lie parallel to the glass and the retardation is maximal. When the voltage is applied, the orientation of the molecules change and they begin to tip perpendicular to the glass. The more the molecules tip, the smaller the retardation. However, the molecules closer to the substrate are pinned at the alignment layer and then unable to rotate freely which causes a residual retardation that can be compensated if needed.

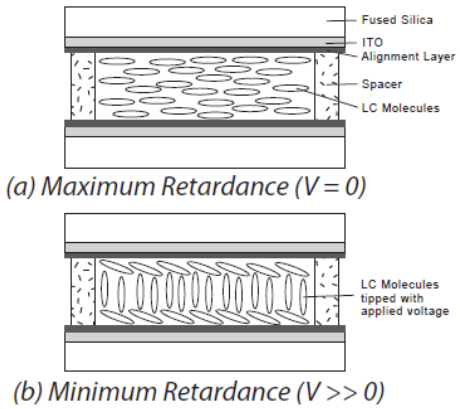

Figure 2.14: Liquid Crystal Variable retarder construction showing molecular alignment (a) without and (b) with applied voltage.

The retardation of the liquid crystal strongly depends on the operating wavelength and the temperature. According to the manufacturer, the overall retardation of the liquid crystal decreases of approximately 0.4% / °C. Though we have a good control on the wavelength with the use of interferometric filters with a 10nm bandwidth, we have to add a temperature regulation system on the LCs. The room temperature is kept quite constant around 22°C with the air conditioning but this is not sufficient to ensure that the retardation of the LCs is constant. Figure 2.15 gives the raw intensities measured during almost 40 hours. The dependency of the intensity with respect to the retardation of the LCs is outlined by eq. 2.4.

The same experiment has been carried out with a thermal regulation of the LCs. An heating ribbon is inserted between the liquid crystals and the mount. A thermal probe is introduced in the mount to control the temperature. We assume that the thermal resistance of the mount is small enough so we have access to the temperature of the liquid crystals. The curves obtained with these new experimental conditions are given in fig. 2.16.

We can see that it is quite impossible experimentally to be sure that the retardations used are exactly the ones we specify due to the very steep slope of the characteristics of the liquid crystals (cf fig. 2.17). We then optimize "blindly" by varying the control voltages of the liquid crystals to achieve the highest condition number.

2.3 Calibration of the system

As we have seen in eq. 2.6, the actual Mueller matrix of the sample can be characterized by 16 measurements only if the polarimeter is calibrated, which means that we are able to accurately know the matrices **A** and **W** and thus invert them to gain access to the Mueller matrix M. We will shortly present the chosen calibration method we used to calibrate our polarimeter.

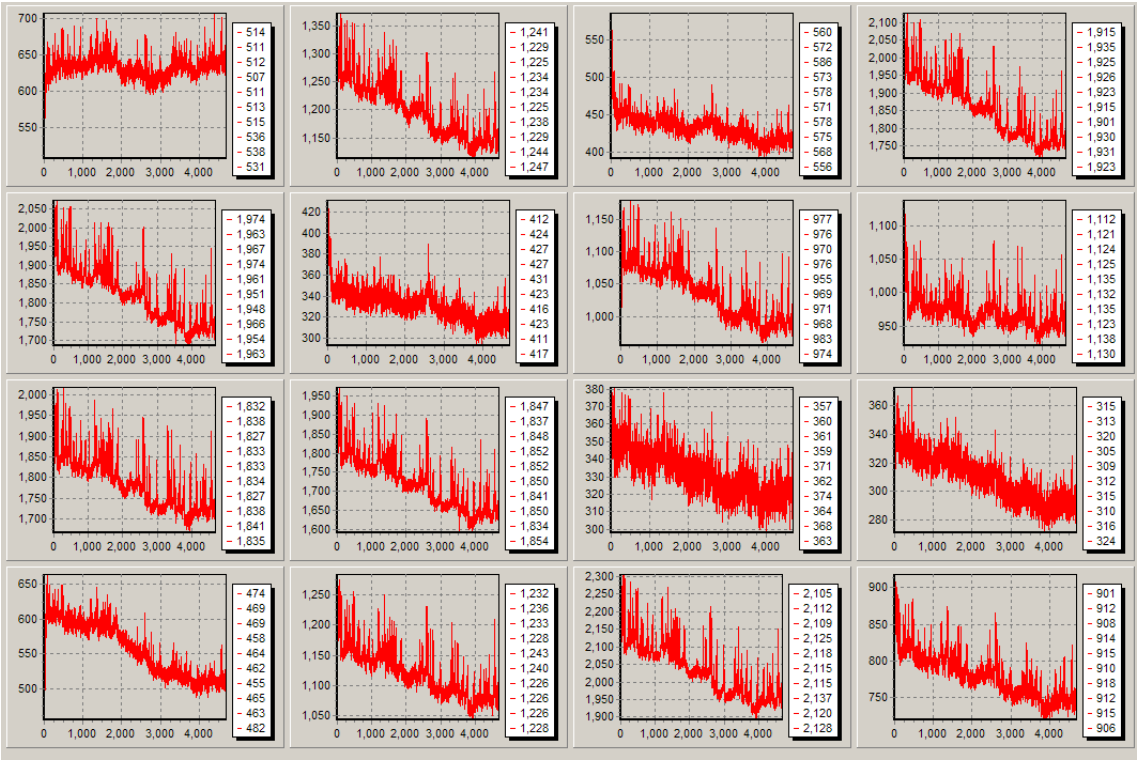

Figure 2.15: Evolution of the 16 raw intensities measured on the same sample, with the same integration time, without thermal regulation of the liquid crystals.

2.3.1 Eigen Value Calibration Method

Introduced by Eric Compain in [53], the eigen value calibration method (later referred as ECM) is a very powerful tool to calibrate any polarimeter without any prior modeling of the polarimeter itself. Using only linear dichroic retarders whose characteristics don't need to be accurately known, we calibrate the instrument and assess the quality and validity of the calibration.

Choice of the reference samples

As mentioned above, the reference samples are supposed to be linear dichroic retarders whose Mueller matrix can be expressed by:

$$M(\tau,\Psi,\Delta,\varphi) = \tau R(-\varphi)\begin{bmatrix} 1 & -\cos 2\Psi & 0 & 0 \\ \cos 2\Psi & 1 & 0 & 0 \\ 0 & 0 & \sin 2\Psi\cos\Delta & \sin 2\Psi\sin\Delta \\ 0 & 0 & -\sin 2\Psi\sin\Delta & \sin 2\Psi\cos\Delta \end{bmatrix} R(\varphi) \tag{2.21}$$

with τ the transmission factor, Ψ the dichroism angle, Δ the retardation and φ the orientation of the fast axis. $R(\varphi)$ is the rotation matrix defined in 1.30. The key point of the procedure is that the eigenvalues of the matrix $M(\tau,\Psi,\Delta,\varphi)$ are actually independent of the parameter φ. This matrix has two real eigenvalues and two complex conjugate.

$$\lambda_{R1} = 2\tau\cos^2\Psi \quad \lambda_{R2} = 2\tau\sin^2\Psi \quad \lambda_{C\pm} = \tau\sin(2\Psi)e^{\pm i\Delta} \tag{2.22}$$

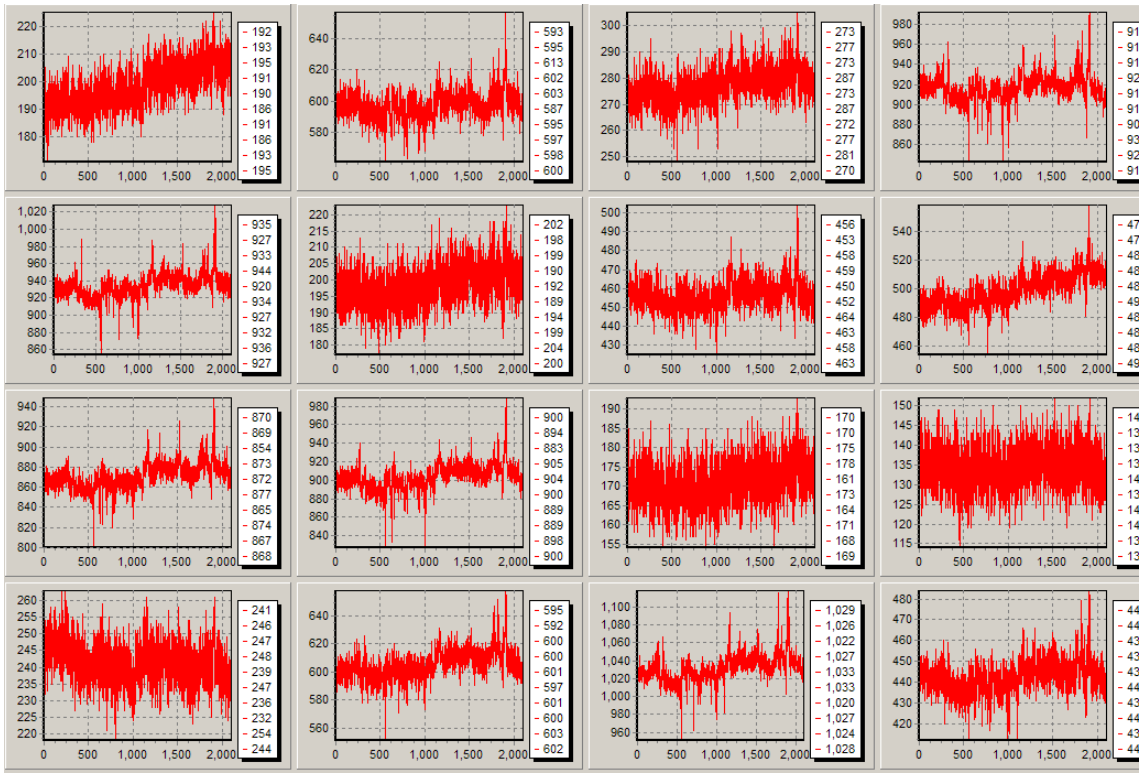

Figure 2.16: Evolution of the 16 raw intensities measured on the same sample, with the same integration time, with thermal regulation of the liquid crystals.

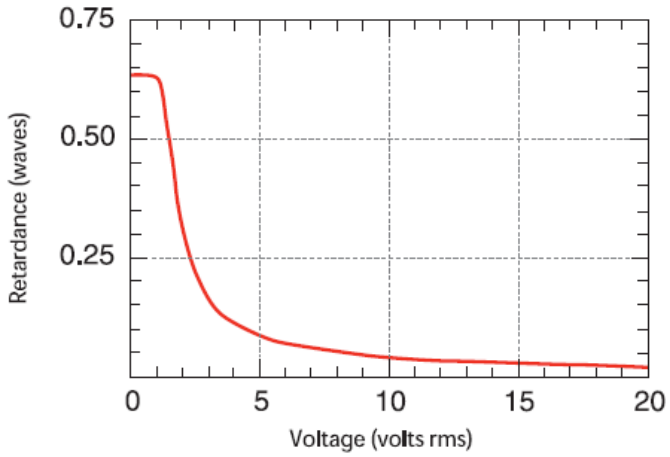

Figure 2.17: Liquid Crystal Variable Retarder performance versus applied voltage at 632.8 nm, 21°C.

The first estimator we can extract to assess the quality of the calibration is:

$$\frac{\lambda_{R1}\lambda_{R2}}{\lambda_{C+}\lambda_{C-}} = 1 \tag{2.23}$$

From the eq. 2.22, it clearly arises that knowing the eigen values of the Mueller matrix we have just measured, it is fairly easy to recover the polarimetric properties

τ, Ψ and Δ with the following equations.

$$\tau = \frac{1}{2}(\lambda_{R1} + \lambda_{R2}) \tag{2.24}$$

$$\cos(2\Psi) = \frac{\lambda_{R1} - \lambda_{R2}}{\lambda_{R1} + \lambda_{R2}} \tag{2.25}$$

$$\sin(2\Psi)\cos(\Delta) = \frac{\lambda_{C+} + \lambda_{C-}}{\lambda_{R1} + \lambda_{R2}} \tag{2.26}$$

$$\sin(2\Psi)\sin(\Delta) = -i\frac{\lambda_{C+} + \lambda_{C-}}{\lambda_{R1} + \lambda_{R2}} \tag{2.27}$$

Experimental Procedure

The first step of the procedure is to measure without any sample,

$$\mathbf{B}_0 = \mathbf{AW} \tag{2.28}$$

We then measure our reference samples. Each sample gives us an experimental matrix

$$\mathbf{B}_i = \mathbf{AM}_i\mathbf{W} \tag{2.29}$$

with $\mathbf{M}_i$, the Mueller matrix of the sample which is of the form defined in 2.21.

The next step is to compute the matrix $\mathbf{C}_i$ defined by:

$$\mathbf{C}_i = \mathbf{B}_0^{-1}\mathbf{B}_i = \mathbf{W}^{-1}\mathbf{M}_i\mathbf{W} \tag{2.30}$$

The interesting point and the key point of this method is that the matrix $\mathbf{C}_i$ has the same eigenvalues as $\mathbf{M}_i$ which enables us to completely characterize it except for the azimuth φ. For each reference sample, we can rewrite 2.30 as:

$$\mathbf{M}_i\mathbf{W} - \mathbf{WC}_i = 0 \tag{2.31}$$

We have a system of equations whose size is defined by the number of reference samples we have measured. The indeterminacy of the azimuth angle φ will be treated later so we assume that the matrix $\mathbf{M}_i$ is fully characterized. In eq. 2.31, $\mathbf{M}_i$ and $\mathbf{C}_i$ are known, the only unknown is $\mathbf{W}$. For any real 4×4 matrix, we define the linear mapping T_i defined by:

$$T_i : \mathbf{X} \longmapsto \mathbf{M}_i\mathbf{X} - \mathbf{XC}_i \tag{2.32}$$

It is obvious that the matrix $\mathbf{W}$ belongs to the kernel (Ker) of T_i, which is true no matter the value of i. We then have to wisely choose the n reference samples so

$$\bigcap Ker(T_i), i \in [1...n] = \{\mathbf{W}\} \tag{2.33}$$

If this equation is satisfied, $\mathbf{W}$ is uniquely defined by our set of reference samples.

Using the proper renumbering of the elements [53], a 4×4 matrix $\mathbf{X}$ can be rewritten as a 16 element vector X^{16} and the linear mapping T_i can be rewritten as 16×16 matrix H_i. Equation 2.32 can then be rewritten as:

$$H_iX^{16} = 0, i \in [1...n] \tag{2.34}$$

This overdetermined system can be resolved with a least-square method using the well-known relation:

$$\mathbf{K}X^{16} = 0 \tag{2.35}$$

with

$$\mathbf{K} = \begin{bmatrix} H_1 & H_1 \\ \vdots & \vdots \\ H_n & H_n \end{bmatrix}^T = \sum_i H_i^T \cdot H_i \tag{2.36}$$

K is symmetrical and semidefinite positive so it can be diagonalized. Given eq. 2.33, it has 15 non-null eigenvalues and 1 null eigenvalue and **W** is the eigenvector associated to the null eigenvalue.

Now that we have found **W**, **A** is easily found using eq. 2.28.

We can now deal with the indeterminacy in the azimuth of the reference samples. The matrices H_i are indeed φ dependent. **K** is then also a function of φ and its spectrum also depends on φ. However, if the azimuth value was not correct, the system of equations would have no solution because **K** would have only non-null eigenvalues. The correct azimuths of the reference samples can be determined if we minimize the smallest eigenvalue of **K**.

This optimization of the smallest eigenvalue is well-suited for our experimental calibration given that measurements are never free of noise which prevents the smallest eigenvalue to be equal to zero. If we sort the eigenvalues of **K** in decreasing order (λ_1 highest eigenvalue and λ_{16} smallest eigenvalue), we can derive another estimator of the quality of the calibration by computing:

$$R_\lambda = log_{10}(\frac{\lambda_{16}}{\lambda_{15}}) \tag{2.37}$$

The estimator R_λ will typically range from -2 to -3, which means that the smallest eigenvalue is two or three orders of magnitude smaller than the second smallest eigenvalue.

Optimal parameters for the reference samples

As seen in 2.3.1, the reference samples are linear dichroic retarders. We now have to optimize the parameters of these reference samples so the calibration method is as accurate as possible. The set of samples must fulfill two conditions:

- K must have only one null eigenvalue
- The other eigenvalues must be as different from zero as possible. This condition is summarized by the maximization of the ration $\frac{\lambda_{15}}{\lambda_1}$ which is always smaller than 1.

To simplify even more the calibration method, we limit ourself to components commercially available, i.e. polarizers and waveplates which are supposed to be perfect (no retardation for the polarizers and no dichroism for the waveplates). The degrees of freedom are the orientations of these components and the retardation of the waveplates. We futhermore assume that the generation and analysis matrices **A** and **W** are close to the optimized ones described previously in 2.2.3.

The conditions enounced previously are fulfilled for the following set of measurements:

- measurement of B_0, without any sample, just the product of $\mathbf{A} \cdot \mathbf{W}$
- polarizer alone, set at two different azimuths φ_1 and φ_2. φ_1 azimuth will be considered as the zero afterwards without any loss of generality
- waveplate with a retardation Δ and azimuth φ_{wp}

We then optimize the ratio $R = \frac{\lambda_{15}}{\lambda_1}$ by varying the parameters of the samples. Though a pretty long numerical trial and error procedure, we obtain a maximum ratio R=0.0105 which is apparently a global maximum. This value is reached for the values of the parameters in table 2.3.1

φ_1	φ_2	φ_{wp}	Δ
$0°$	$90°$	$30.5°$	$109°$

Table 2.5: Optimal values of the parameters of the samples used fir calibration

A study of the variations of the ratio R with the different parameters can be found in [52]. We will only remark that the retardation value is not very critical if the waveplate is well oriented. As a consequence, we can afford to be less careful when choosing the waveplate and the same waveplate can be used for calibrations at different wavelengths although the retardation is not optimal.

2.3.2 Discussions on the Eigen Value Calibration Method and experimental implementation

Though the ECM is a very versatile and powerful calibration method, it can not be directly applied to fully calibrate our angle-resolved Mueller polarimeter. We have to insert the calibration samples between the front lens of the objective and the mirror. However due to the very short working distance of the 100X objective (1mm) it is impossible to do so. And even if samples sufficiently thin could be found, they should be inserted perpendicular to the beam propagation direction which can not be defined for highly convergent beam. We have to use a low numerical aperture objective (Nikon MUE10050 NA 0.15 5X WD 23.5mm) to calibrate the system. The long working distance of this objective enables us to easily insert our calibration samples.

Even though the system is calibrated in reflection, with the conditions enounced in 1.3.2, the Mueller matrix of a mirror at normal incidence is the identity matrix. We also previously stated that the objectives used in the set-up are supposed to be strain-free and should have a Mueller matrix very close to the identity matrix. This assumption is fairly reasonable for the low aperture ones because the curvature radius of the lens is small enough to neglect the dichroism induced by a reflection or a transmission on a surface. Except for a transmission factor we neglect for now, the Mueller matrix of the 5X objective can be considered equal to the identity matrix too.

Given that the system operates in reflection, light passes through the calibration samples twice which means that their transmissions must be squared and the retardation of the waveplate is doubled. The eigenvalue calibration provides us the characteristics of the samples in double-pass just like the system was calibrated in transmission.

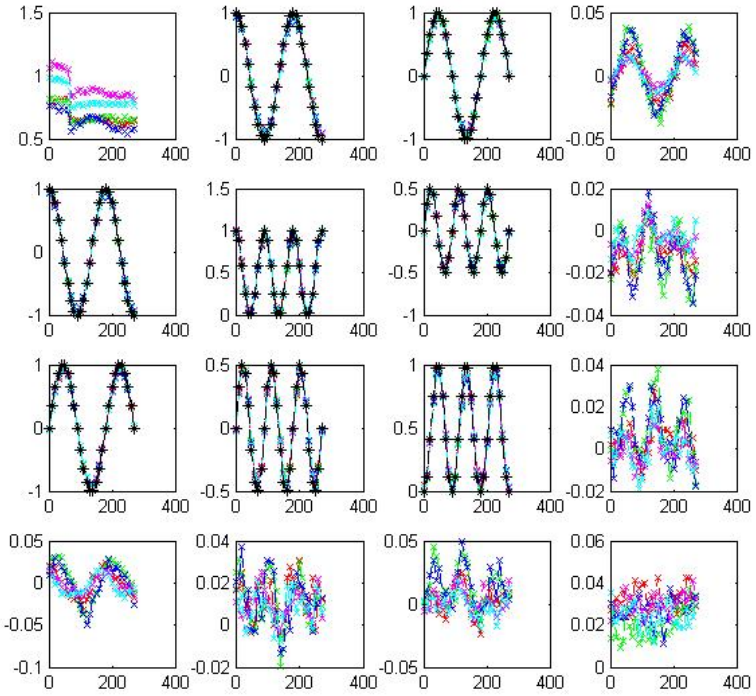

Figure 2.18: Mueller matrix of a polarizer set at different azimuths versus its orientation. Each curve corresponds to a different measurement pixel. Black curve: simulation of the sample

Besides looking at the criteria provided by the calibration method itself, we can assess the validity of the calibration by measuring a standard polarization element. We measured with the low numerical aperture a polarizer / retarder at different orientations with 10°increments. The measured Mueller matrices should be homogeneous given that the maximal angle of collection is very small (below 5°). We select 5 pixels on the intensity image and plot the Mueller matrix elements for these 5 pixels versus the orientation of the polarizer / retarder. The results are given in fig.s 2.18 and 2.19.

As one can see on the figures, the remaining error on the normalized matrix is about 2% (4% maximum). One can also see that the errors are not random and in fact display a clear tendency which can be attributed by some mistakes in the **A** and **W** matrices. These errors could be corrected using a perturbation method assuming the corrections are small. By fitting the previous measurements on the polarizer and the retarder, on can adjust the matrices $\mathbf{W} \rightarrow \mathbf{W} + \delta\ \mathbf{W}$ and $\mathbf{A} \rightarrow \mathbf{A} + \delta\ \mathbf{A}$

This procedure has not been implemented yet and should be demonstrated on real samples.

2.3.3 Objective calibration

Once the quality of the calibration with the low NA objective has been verified, we have to calibrate the high NA objective because most of our measurements are carried out with this objective. Though all the other optical components of the set-up have been calibrated during the ECM, the high NA objective cannot be calibrated with the same method for the reasons previously stated. Instead of introducing calibration samples

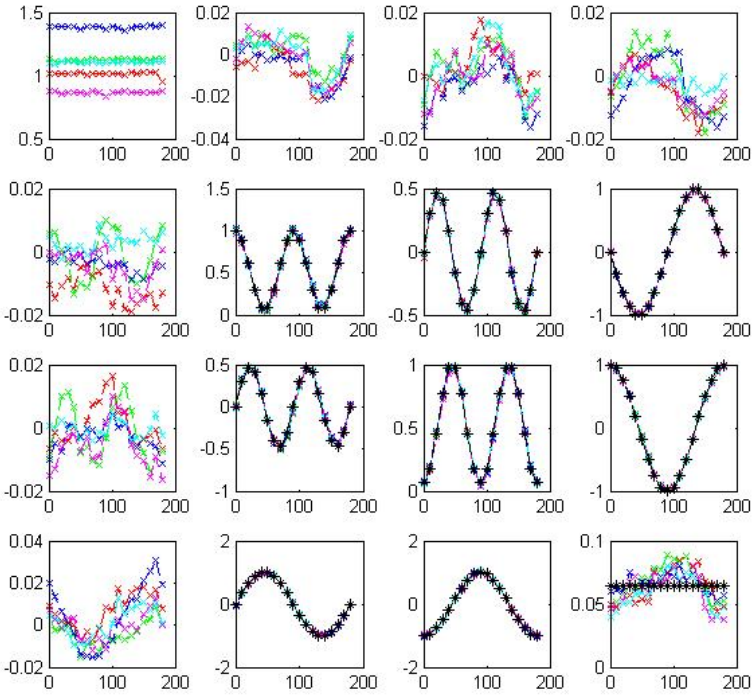

Figure 2.19: Mueller matrix of a retarder set at different azimuths versus its orientation. Each curve corresponds to a different measurement pixel. Black curve: simulation of the sample

between the front lens of the objective and the mirror, we are measuring very well-known (holy) samples in reflection.

Principles

The problem we have to resolve is quite similar to the ECM.

$$B = M_{objbackward} \cdot M \cdot M_{objforward} \tag{2.38}$$

with B, the measured Mueller matrix; M, the "true" Mueller matrix of the sample; $M_{objbackward}$ (resp. $M_{objforward}$), the Mueller matrix of the objective in single-pass in the backward (resp. forward) direction.

The problem is that we don't have the same liberty of choice for the "holy" samples as we had in the ECM. We choose to measure isotropic linear dichroic retarders whose Mueller matrix for each pixel is given by 2.21 $M(\tau_M, \Psi_M, \Delta_M, \varphi)$ with φ is the azimuth of the ray. The simulated Mueller matrix of a crystalline silicon wafer is given in fig 2.20.

We can see that the sample being isotropic, the dichroism and the retardance are radially oriented and only depend on the polar angle θ.

We are assuming that the objective satisfies the following conditions:

- The Mueller matrices in the forward and the backward directions are equal. $M_{objbackward} = M_{objforward} = M_{obj}$

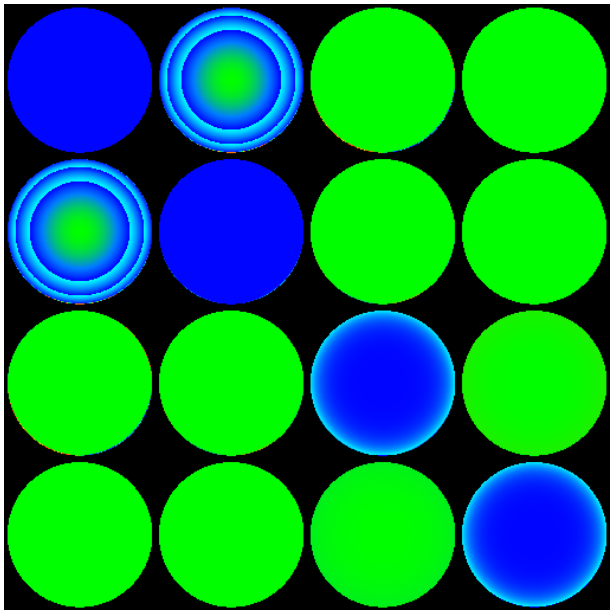

Figure 2.20: Normalized angle-resolved Mueller matrix of a crystalline silicon wafer. Maximum aperture angle: 62°. scale [-0.2 .02]

- The Mueller matrix of the objective in single pass is the one of an isotropic linear dichroic retarder $M_{obj}(\tau_o, \Psi_o, \Delta_o, \varphi)$ given in 2.21.

It should be notice that in Sami Ben Hatit's manuscript, only the first assumption is made. Its seems that we are a bit more restrictive and then may lose some generality but though the second assumption was not valid in Sami ben Hatit's thesis, the choice of the new objectives has been made so they are strain-free and thus do not exhibit uniaxial birefringence.

In eq. 2.38, all the terms we multiply are Mueller matrices of isotropic linear dichroic retarders so B is also a linear dichroic retarder Mueller matrix. Besides, two Mueller matrices of linear dichroic retarders commute so we can rewrite eq. 2.38 as follows:

$$\begin{aligned} B &= M \cdot M_{obj}^2 \\ &= M_{obj}^2 \cdot M \end{aligned} \tag{2.39}$$

For each pixel, we extract the parameters Ψ_B, Δ_B, Ψ_M and Δ_M through a Lu-Chipman decomposition (cf eq. 1.51).

We have a very simple relation between the dichroism and retardance of the matrices B,M and M_{obj}.

$$\begin{aligned} \tan \Psi_B &= \tan \Psi_M \cdot \tan^2 \Psi_o \\ \Delta_B &= \Delta_M + 2\Delta_o \end{aligned} \tag{2.40}$$

The **A** and **W** determined using the ECM can now be replaced by **W'** = $M_{obj}\cdot$ **W** and **A'** = **A** $\cdot M_{obj}$. These new generation and analysis matrices take into account the contribution of the objective in the measurements.

Experimental realization

Given that the objective calibration only uses one reference sample, the obtained Mueller matrix may depend on the selected sample. We choose a crystalline silicon wafer (c-Si)

covered with 1.5nm of native oxyde and a 92nm layer of thermal silica on a crystalline silicon wafer ($SiO2$) as reference samples. Using the formula in eqs. 2.40 for both samples we calculate the objective Mueller matrix. Fig. 2.21 displays the dichroism and retardance of the objective for both samples.

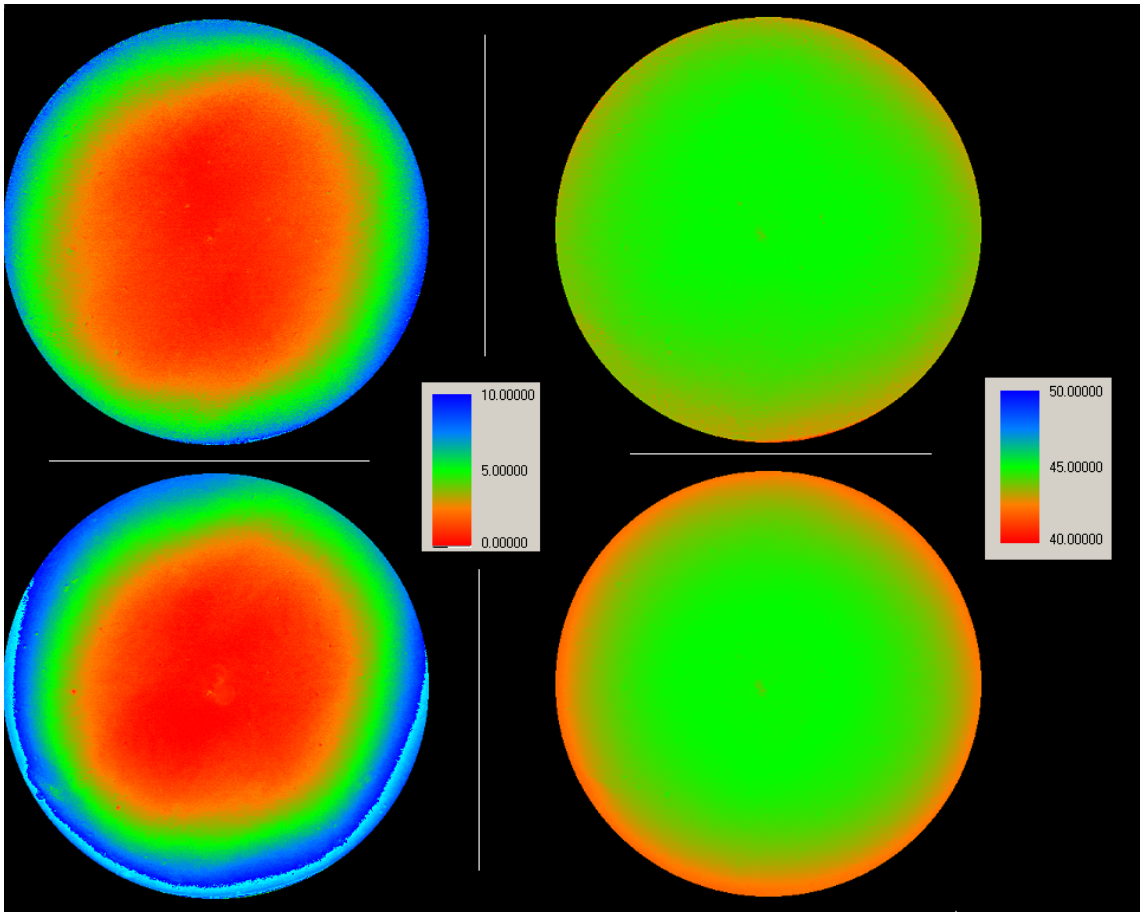

Figure 2.21: Dichroism and retardance of the Mueller matrix of the objective calculated for two different reference samples. First row: c-Si, second row: SiO_2. First column: retardance, second column: dichroism

One can observe some small discrepancies between the computed matrices. The main reason is that these so-called "holy" samples are not precisely characterized. The thicknesses and refraction indexes of the layers of silica on both samples should be more accurately characterized in order to increase the convergence of results.

The limitations of this method appear on fig. 2.22. The errors in the raw measurement affecting the elements normally null (elements in the red squares on the figure) in the Mueller matrix of a linear dichroic retarder cannot be corrected. These elements, however, remain small and are typically smaller than 5% on normalized elements and the (Ψ, Δ) elements exhibit errors close to the precision of the measurement which is around 2%.

2.3.4 Intensity Calibration

In the procedure described before, **W** is obtained as the eigenvector corresponding to the only null eigenvalue. **W** is defined up to the transmission factor. Because the

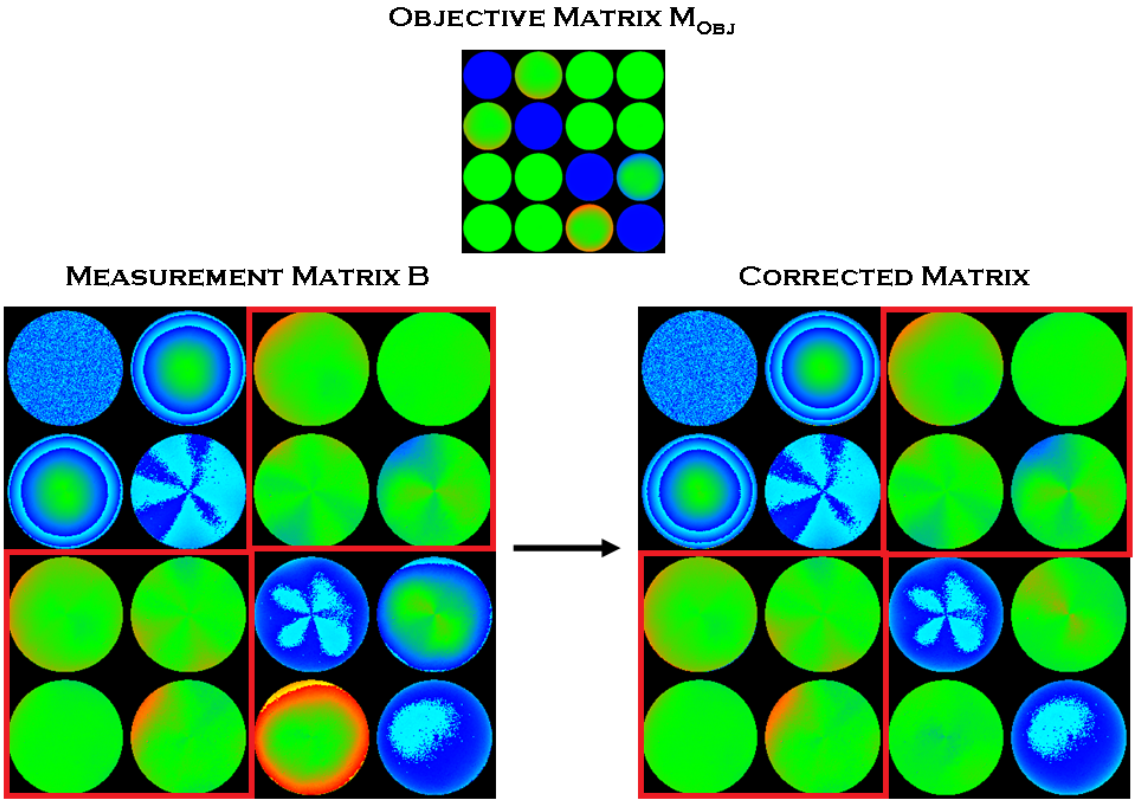

Figure 2.22: Mueller matrix of c-Si. Left: raw measurement; Right: Corrected measurement using the Mueller matrix of the objective (top)

Mueller matrix is extracted through intensity measurements (cf eq. 2.6), only the product of the transmission factors of **A** and **W** really matters.

Principles

We adjust the first element of the **A** and **W** matrices so $\mathbf{A}_{11} = \mathbf{W}_{11} = 1$. We can now express the intensity matrix **B**

$$\mathbf{B} = \tau \cdot \mathbf{A}' \cdot M \cdot \mathbf{W}' \cdot I_{source} \tag{2.41}$$

with τ the transmission factor of the system, **A**′ and **W**′ the matrices defined before, M unnormalized Mueller matrix of the sample, I_{source} intensity of the source.

We introduce the coefficient $c = \tau I_{source}$.

We can rewrite 2.41:

$$M = \frac{1}{c} \cdot \mathbf{A'}^{-1} \cdot \mathbf{B} \cdot \mathbf{W'}^{-1} \tag{2.42}$$

We can deduce the factor c from the measurements of the matrices **A**′, **W**′ and **B** for a known sample (M is then known). We also define the reflectance matrix $R = \frac{1}{c} \cdot \mathbf{B}$.

Experimental implementation

We combine our simulation of the normalized Mueller matrices of our reference samples (c-Si and SiO_2) which first element is not calibrated and the simulation of the re-

flectance of reference samples versus the angle of incidence (fig. 2.23).

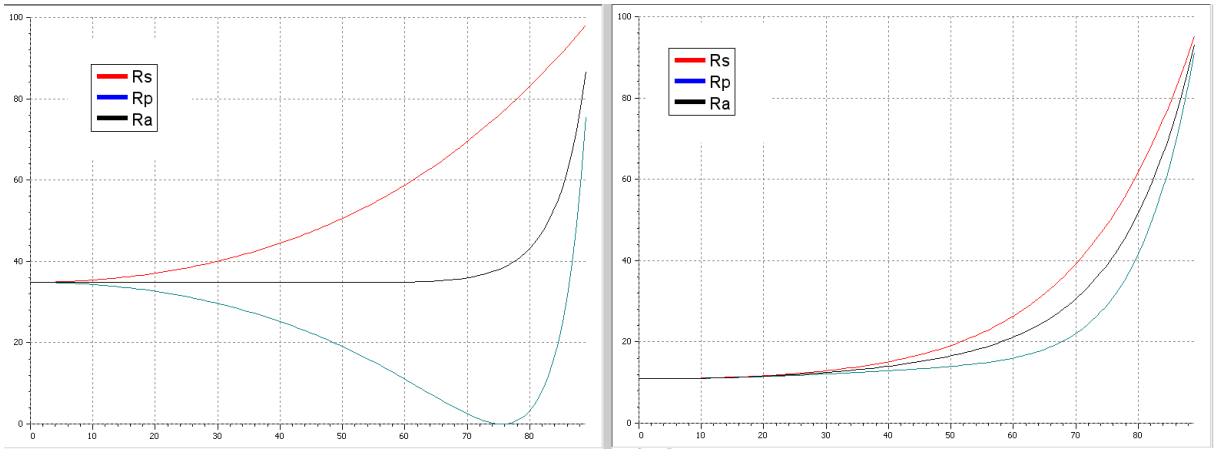

Figure 2.23: Simulation @633nm of the reflectance of reference samples. Left: c-Si; Right: SiO_2.

The fig. 2.24 shows the transmission factor c obtained for two reference samples.

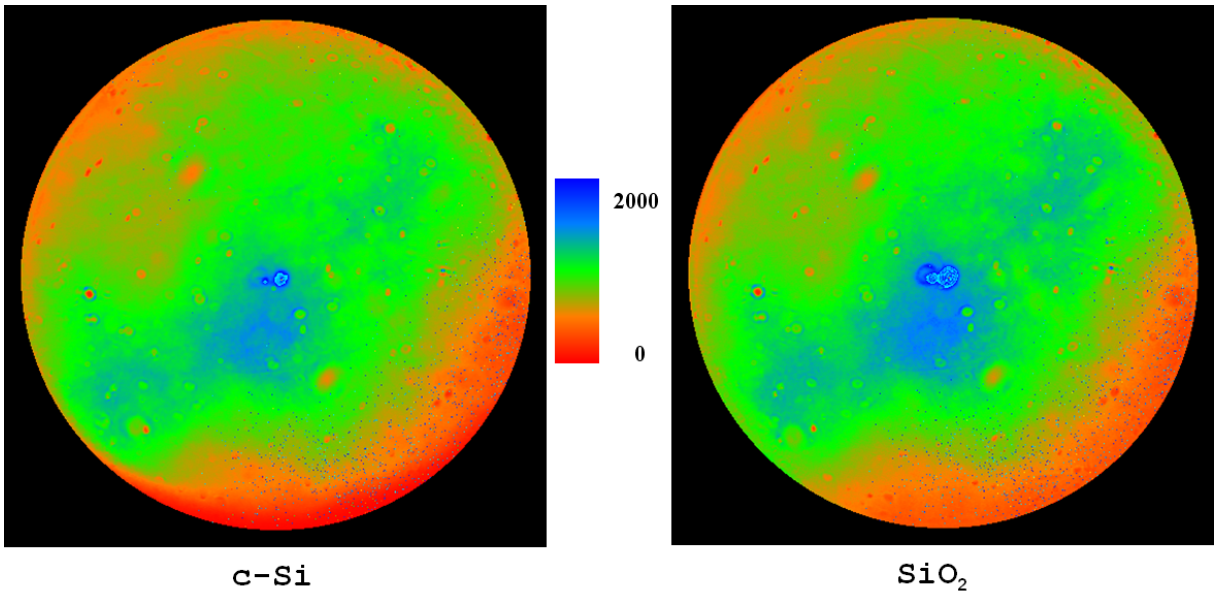

Figure 2.24: Transmission factors calculated using two different reference samples.

The calibration of the M11 element of the Mueller matrix is then complete and the M11 can be used to fitting purpose although we never tried. The calibration procedure should nevertheless improved, especially regarding its repeatability. As we can see in fig.2.24, the errors between the calibration with two different samples can reach 10% of the total scale of M11.

2.4 Description of the measurements

After the calibration of the system (objective and intensity included), we are able to measure the Mueller matrix of our sample. It is interesting to focus on the measurement itself to have a better and deeper understanding of how to extract the information. The

imaging part images the back focal plane of the objective on our 512×512 pixel CCD detector. Our measurement is a $512 \times 512 \times 16$ matrix (512×512 images, each image being an element of the Mueller matrix). The measurement of a silicon wafer with a thin layer of native oxide is given in fig. 2.25.

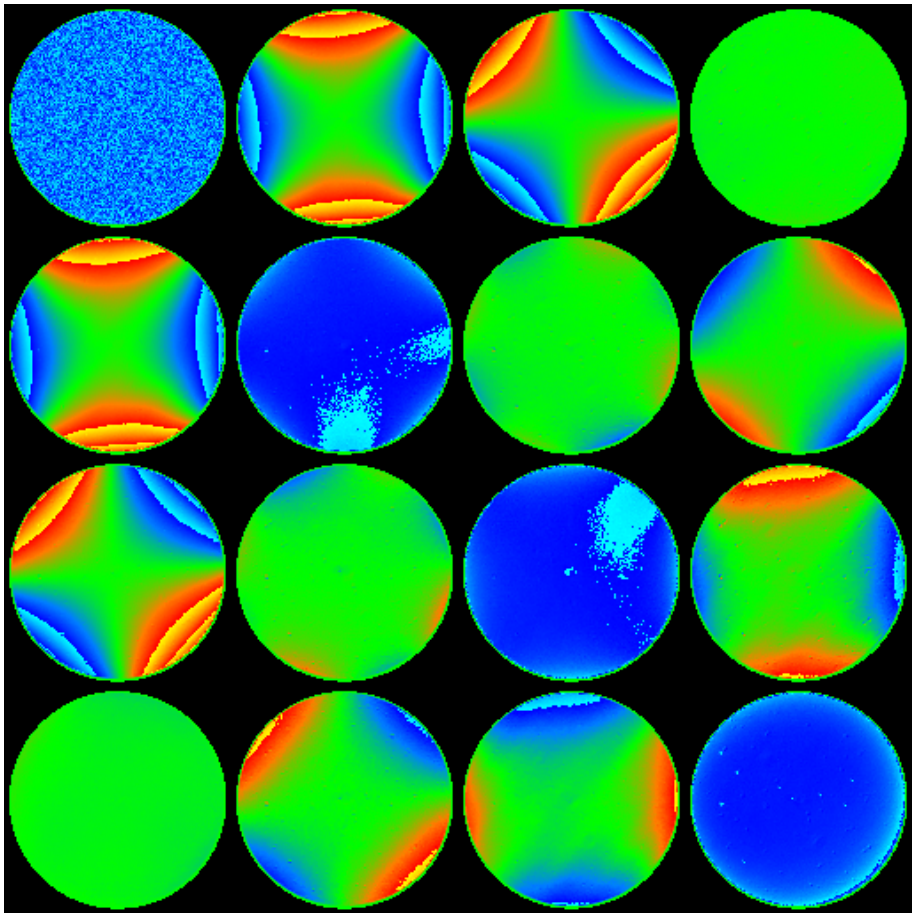

Figure 2.25: Measurement of c-Si. Scale [-0.2 0.2]

This figure is very different from what we have previously shown in fig. 2.20. The elements of the two Mueller matrices are not expressed in the same axis: in fig. 2.20 the elements are expressed in the variable axis defined by the polarizations s- and p- whereas in fig. 2.25 the elements are expressed in the fixed axis x and y defined by the orientations of the first polarizer during the calibration of the system and all the azimuths are measured in the same axis which is rotated with respect to the incident and scattered light. This rotation can be numerically corrected by a point-by-point rotation of the axis to obtain the matrix in fig. 2.20. We will try throughout this manuscript to always specify the axis the Mueller matrices are expressed in.

To be able to use the data for fit purposes, we need to be sure that the numerical aperture specified for the different objectives is fully imaged on the CCD. Several factors may decrease the numerical aperture in the system. We use gratings whose pitches are very-well characterized.

The position of the diffraction orders in the Fourier plane with respect to the zero order enables us to calibrate the angular scale of the images. Let R_{max} be the radius of the image corresponding to the maximum aperture θ_{max}, d the shift (in pixels) between the orders, λ the working distance and Λ the pitch of the grating.

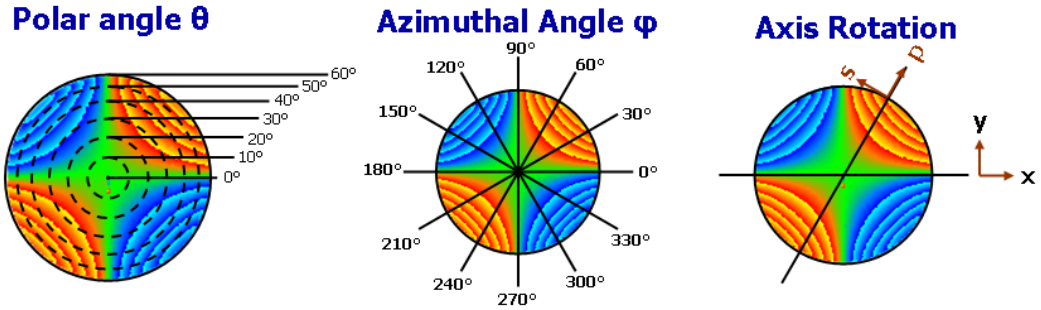

Figure 2.26: Description of the measurements and rotation of the axis

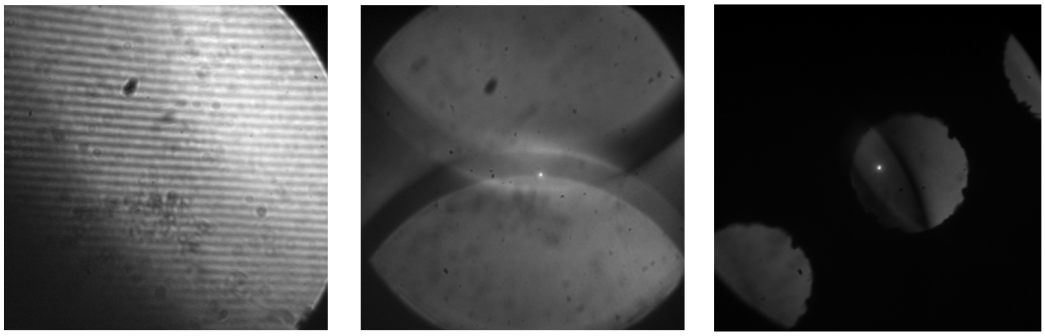

Figure 2.27: From left to right: real image of a 700nm pitch grating imaged with the 50x objective; Full aperture imaged in the Fourier plane; image of the Fourier plane with a mask placed in the aperture plane. $\lambda = 633nm$

The maximum radius is given by:

$$R = \alpha \sin(\theta_{max}) \tag{2.43}$$

The shift between the orders k and $k + n$ is given by:

$$d = \alpha n \frac{\lambda}{\Lambda} \tag{2.44}$$

By combining eq. 2.43 and eq. 2.44,

$$\theta_{max} = \arcsin(n \frac{\lambda \cdot R}{\Lambda \cdot d}) \tag{2.45}$$

Wavelength (nm)	Pitch of the grating (nm)	Maximum angle (°)	Maximum aperture
633	700	62.25	0.8850
633	700	63.21	0.8927
633	500	62.46	0.8867
633	600	64.21	0.9004
633	800	63.40	0.8942
633	700	63.76	0.8970
532	900	63.30	0.8934
532	500	63.81	0.8973

Table 2.6: Maximum aperture (θ_{max}) obtained using eq. 2.45

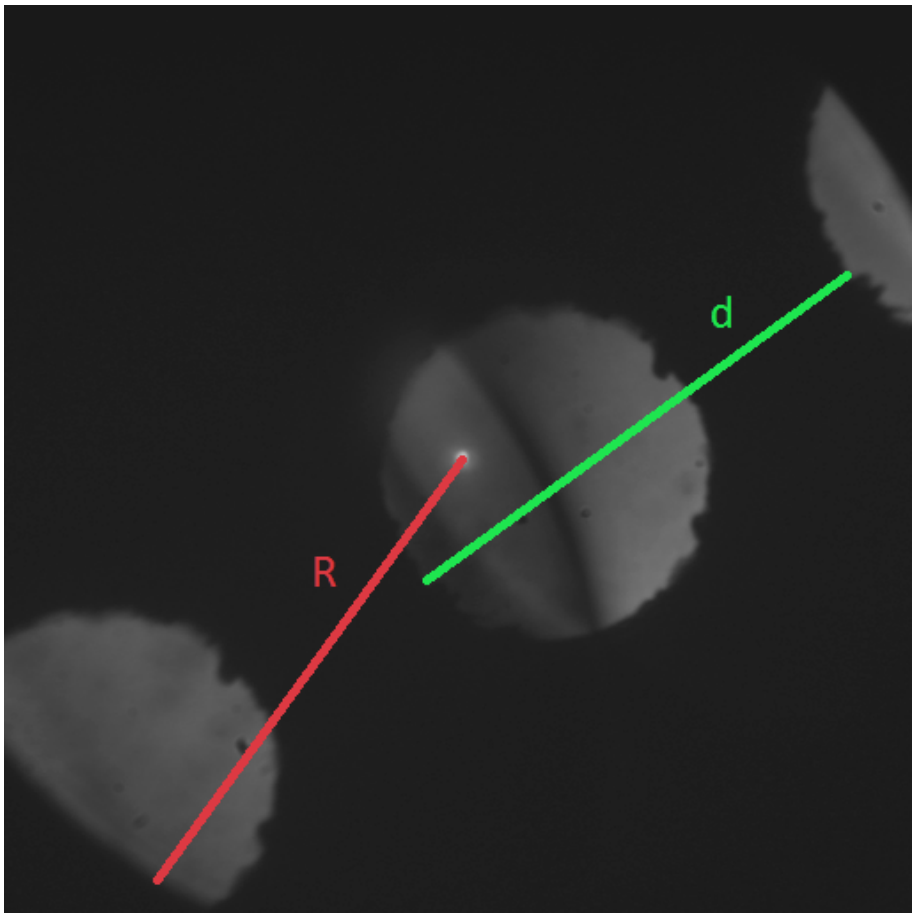

Figure 2.28: 700nm pitch grating with a mask in the aperture plane. λ=633nm Three diffraction orders are visible: -1, 0 and 1.

It is very important to measure the distance d between the same points of the aperture for both diffraction orders to avoid systematic errors on the aperture. Table 2.6 summarizes results obtained for different gratings.

The apertures we find in table 2.6 are very close to each others and are typically equal to the maximum numerical aperture specified for the microscope objective. However, one should be careful with this apparent perfect adequation between the specifications of the objective and our results. The sample must be perfectly aligned to have the maximum aperture and the center of the pupil must coincide with the center of the image. Though, it may be difficult to check the quality of the alignment of the objective

and the sample by looking at the intensity images, a small misalignment can easily be discovered with the polar decomposition of the measurement. Figure 2.29 displays the polar decomposition images of a misaligned sample.

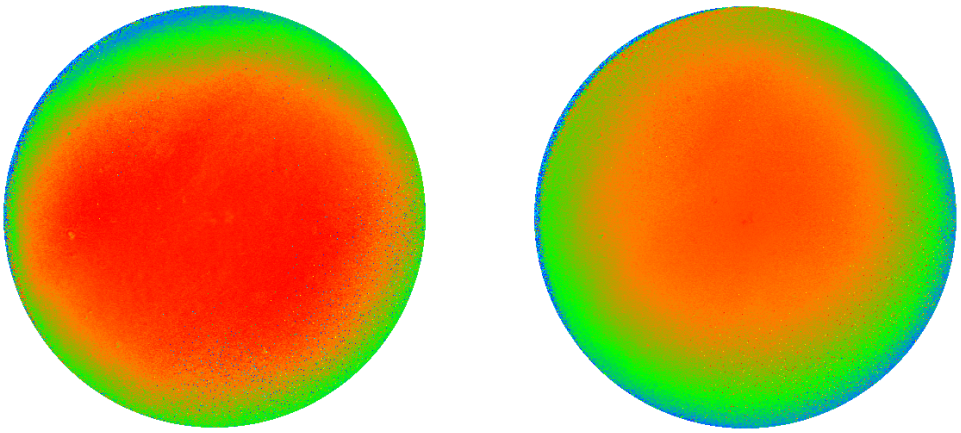

Figure 2.29: Polar decomposition images of a misaligned sample. (a): retardation Δ, (b) Dichroism ψ

2.5 Conclusions

In this section, we have presented the new configuration of the angle resolved Mueller polarimeter. The illumination part of the system has been re-engineered to accurately decouple the field and the aperture thanks to a modified Köhler scheme. The classical scheme for a Köhler illumination has the drawback of conjugating the light source in the back focal plane of the objective which is optimal for classical applications of bright-field microscopes but will increase noise and errors when imaging the back focal plane. We proposed to slightly defocus the light source so its inhomogeneities don't appear in the back focal plane. By doing so we proposed a trade-off for the illumination arm so it is both working for real and reciprocal imaging.

We also presented the new calibration method for the objective. When previously an a-priori model and a heavy fitting procedure were required, now only a measurement of a very accurately characterized sample is needed. The only assumption is that the Mueller matrix of the objective can be regarded as a linear dichroic retarder. This assumption seems acceptable given the new set of strain-free microscope objectives we used for our applications. It is also confirmed by the results of the calibration itself.

The quality of the design of the set-up and its accurate calibration thanks to the eigenvalue calibration method and the additional procedures that have been developed during my thesis improved the overall performances of the polarimeter and the stability of the measurements. The maximal aperture has been increased up to $62°$ for a 240pixel radius of the exit pupil of the 100x objective and the errors are found to be smaller than 2%.

This set-up is now ready to be used for quantitative applications. In the following, we will see various possible applications of our apparatus both in the real and the reciprocal space.

Chapter 3

Real space measurements on Entomological structures

As we have previously described in chapter 2, the real space imaging configuration can been used to align the samples we want to measure with the Fourier configuration. But it would be a limitation of the possibilities of our system not to acquire Mueller matrices in the real space too. Due to the versatility of our set-up, we can use our system as a microscope with the polarization information added. Both theory and measurements stated that using the same calibration, we can measure both in the Fourier and the real space by just switching a retractable lens L_{im2} (cf fig.2.8). However, this lens is not taken into account in the calibration of the system (calibration in the Fourier space).

In this chapter, we will present our work in collaboration with the group of Prof. Hans Arwin at the University of Linköping, Sweden about the characterization of the polarization effects of the cuticle of some species of beetles. This work is the direct continuation of what Sami Ben Hatit started at the end of his thesis (see [41]).

3.1 Experimental validation of the measurements in real space

3.1.1 Mueller matrices of known elements

The first step of this validation is to measure well-known samples with classical Mueller matrices like polarizers. Figures 3.1 and 3.2 give the measured Mueller matrices of circular polarizers. We remind that with the convention used here, the last two rows of the Mueller matrix are the opposite of what normally would be expected and thus should be multiplied by -1 to be compared with measurements carried out outside the laboratory with other instruments. The matrices displayed with the corrected signs will be explicitly identified.

In order to calibrate the handedness of the circular dichroism, we measured circular polarizers. The results are given in fig.3.1 and fig.3.2. Thanks to these measurements, we can unambiguously determine the handedness of the chirality of the beetles.

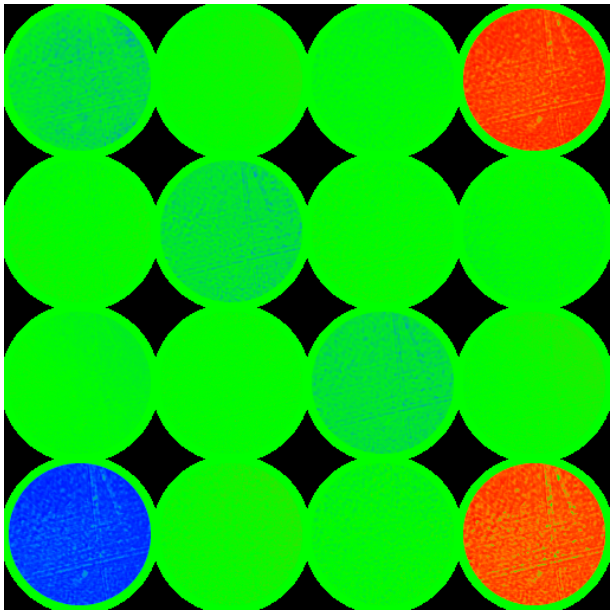

Figure 3.1: Left circular polarizer measured in the real space with the 5X objective

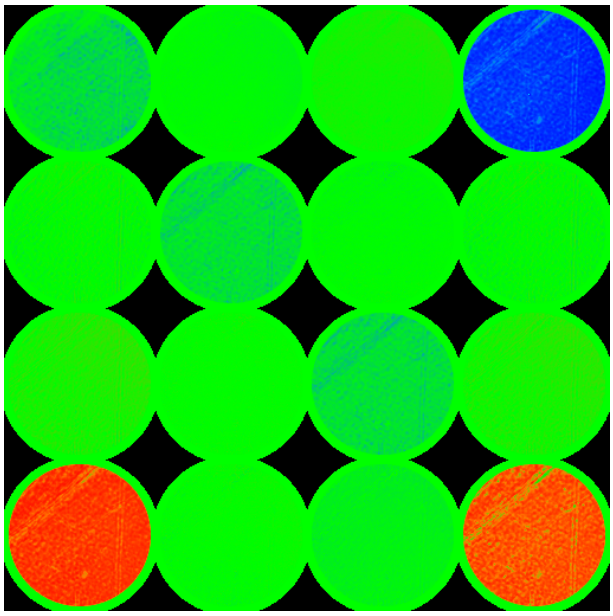

Figure 3.2: Right circular polarizer measured in the real space with the 5X objective

3.1.2 Calibration of the imaged area

To be able to use the system as a microscope, we need to have access to the lateral resolution. However, the positioning of the lens L_{im2} is so critical that it is hard to be able to know accurately the global magnification of the system therefore we image very-well characterized gratings with our real space microscope configuration which enables us to calibrate the area imaged by the different microscope objectives. Some characteristic images are shown in fig.3.3. Using these images, we find the total imaged areas shown in table 3.1.

Commercial magnification	Diameter of the imaged area
5X	$360\mu m$
20X	$90\mu m$
50X	$36\mu m$
100X	$18\mu m$

Table 3.1: Total imaged fields for different objectives

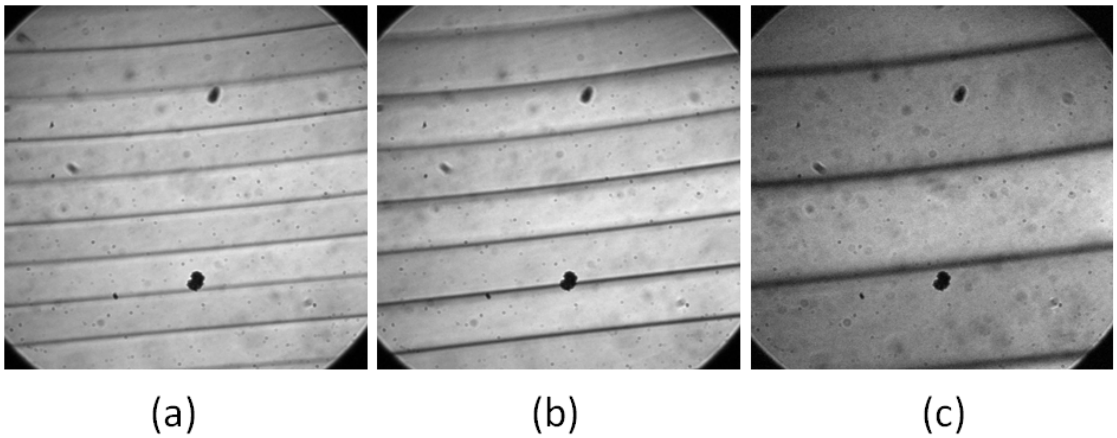

Figure 3.3: Real images of diffraction gratings with well-known pitches. (a): $15\mu m$ grating imaged with the 20x objective. (b): $10\mu m$ grating imaged with the 50x objective. (c): $5\mu m$ grating imaged with the 100x objective

These areas can be decreased by varying the field diaphragm in the illumination part (cf fig.2.11). Fig.3.4 gives an outlook of the smallest area yet achievable with the current pinhole.

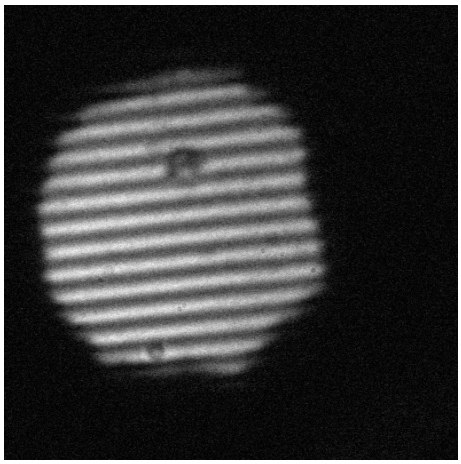

Figure 3.4: Real image of a 900nm pitch grating with the smallest area yet achievable ($diameter \sim 11.7\mu m$)

3.2 Measurements on entomological samples: Iridescence and structural colors

Entomology (from greek $\varepsilon\nu\tau o\mu o\varsigma$, entomos "that which is cut in pieces", referring to the three main constituent parts of the body, hence "insect" and $\lambda o\gamma\iota\alpha$, logia "the study of") is the science that studies insects. This is a branch of the arthropodology, the study of arthropods, the phylum of animals including insects, arachnids and crustaceans. We focus on a specific group of insects, the coleoptera species (from greek, $\kappa o\lambda\varepsilon o\varsigma$, koleos "sheath" and $\pi\tau\varepsilon\rho o\nu$, pteron "wing" thus sheathed wing), often referred to as beetles. The coleoptera contains more species than any other order in the animal kingdom and constitutes around 25% of all known life-forms. The beetles can be found in almost all habitats. They are generally characterized by a particularly hard exoskeleton and hard forewings (elytra). This elytra separates them from most other insect species except for a few hemiptera species. This exoskeleton is made up of several plates called sclerites, the precise shape and arrangement of the sclerites are used as features when reconstructing the phylogenetic relationships between different lineages. The beetles undergo a complete metamorphosis during their life, they physically develop after birth and their body structure changes quite abruptly (see fig.3.5).

Figure 3.5: Chromatogenesis of a *Cetonia aurata*. 60hours span between the first and the last pictures

Iridescence (also known as goniochromism) is the property of surfaces which appear to change color with the angle of view or the angle of incidence [54]. This property must be clearly separated from the pigmentary colors of the sample, the iridescence only comes from the structure of the sample. The structural colors of certain beetles and their specific polarization properties had already been observed in 1911 by A.A Michelson [55] who stated that *"the effect must be due to some screw structure of ultramicroscopic dimension."* although references of studies about the creation of structural colors can be tracked down to scientists such as Newton or Lord Rayleigh just to name a few. Iridescent colors can be found on the bodies and wings of many birds, butterflies [56] and all kinds of insects from moths to beetles [57, 58] (see fig.3.6). This has been studied for centuries now and Newton was the first to suggest that these colors might be due to the presence of thin film structures. The latter advances of the wave theory

of light demonstrated that the interference phenomenon plays a key role in the generation of structural colors. Artists have always been attracted by this kind of structures to create some new effects for their work of art [59] like Jan Fabre (see fig.3.7) did in the Louvre Museum in the exhibition *L'Ange de la métamorphose* in 2008. The study of structural colors enables to create bio-inspired structures that can be used for applications ranging from anti-counterfeiting of banknotes [60] to anti-reflecting coatings.

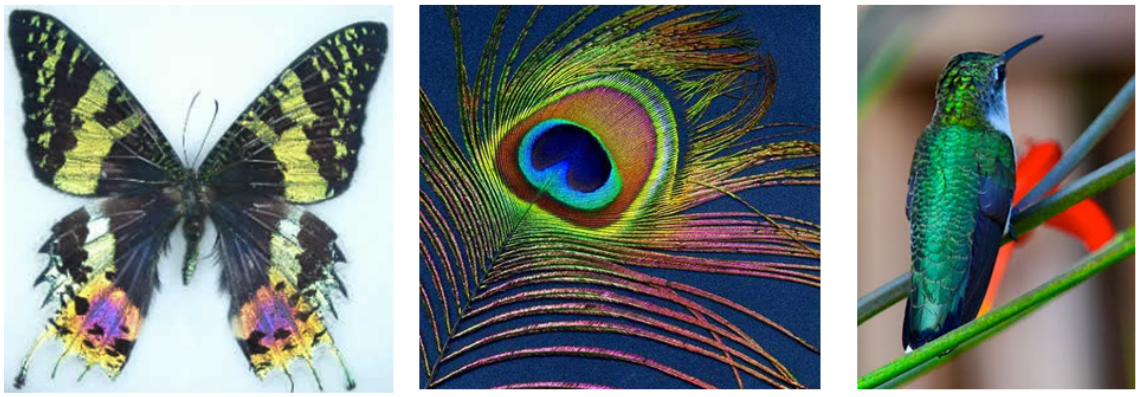

Figure 3.6: Examples of structural colors in nature. From left to right: Urania riphaeus; peacock feather; Red Humming bird

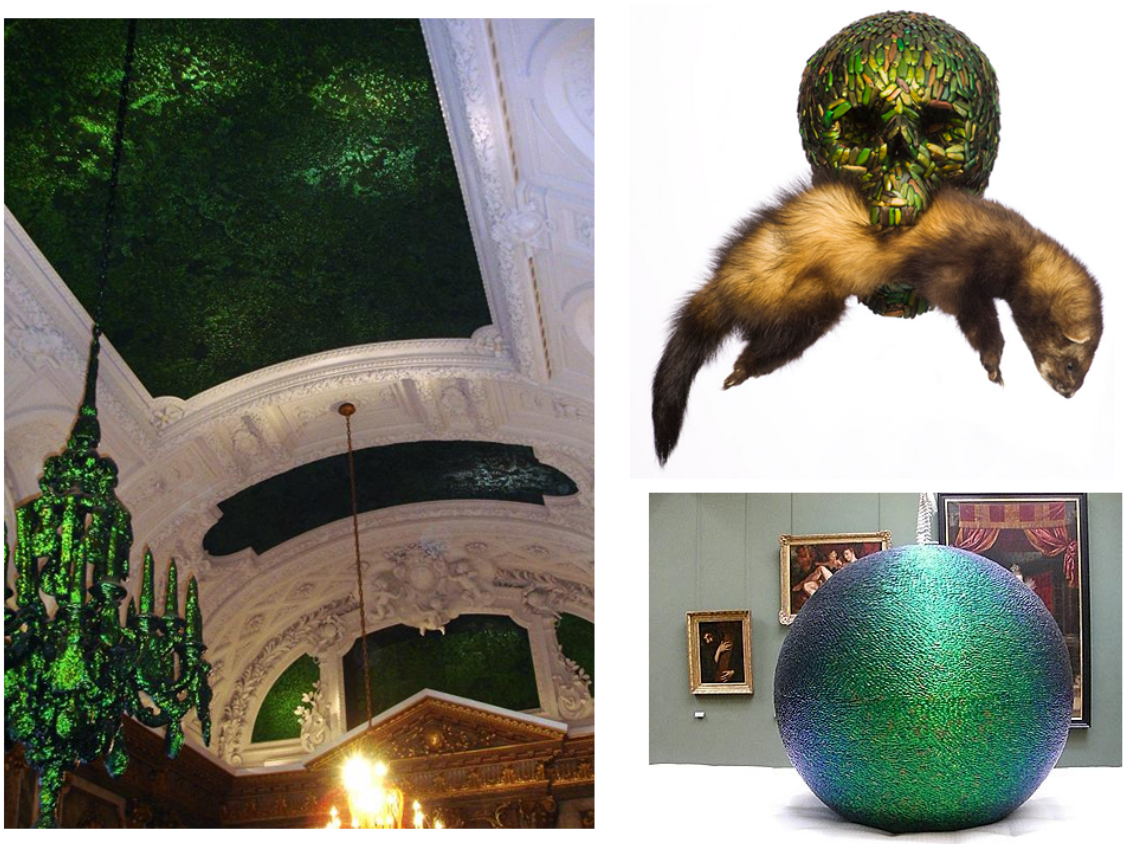

Figure 3.7: Some art pieces of Jan Fabre. Left: His decoration of the ceiling of the Royal Palace in Brussels Heaven of Delight (made out of one million six hundred thousand jewel-scarab wing cases), Top right: Skull, Bottom Right: Installation at the Louvre Museum

In this chapter, we will focus on the structural colors generated by some beetles.

3.3 Entomological description of the chosen beetles

Thanks to our collaboration with the group of Hans Arwin from the Department of Physics, Chemistry and Biology, of the University of Linköping, we gained access to various species of beetles. During our measurement sessions, we focused on 5 species whose characteristics will be given in this section. They belong to different subfamilies of the Scarabaeidae family but have common features all presenting a high optical activity and very bright metallic colors. A sixth species, *Cyphochilus insulatus* was also measured, not for the metallic colors it exhibits, but for the total lack of it since it is a completely white bug (see fig.3.8). Cyphochilus is a genus of beetle with an unusually bright white body, occurring in Southeast Asia. The white beetle scales are brighter than milk, tooth enamel and most white materials we find in nature. According to a new study, they are also a number of times thinner than white plastic [61]. Unlike other colors, white is relatively rare in animals because the substance must be able to scatter all the visible wavelengths in order to appear white. Researchers can learn from the structure of these scales to increase the whiteness of synthetic objects such as light emitting devices. In an article published in Science [62], Pete Vukusic and his colleagues in the UK describe the flat and overlapping scales covering the body, head and legs of the beetle.

Figure 3.8: *Cyphochilus insulatus*, left: in our measurement system, right: in its natural habitat

To clearly identify the species and their connections, we are using the full name of the species with details of the phylogenetic tree starting from the coleoptera order, even if it may seem unnatural and quite heavy. The focus will be put on two subfamilies, the rutelinae and the cetoniinae.

3.3.1 Cetoniinae

We will study three beetles from this subfamily, *Cetonia aurata*, *Pseudochalcothea auripes*. and *Potosia cuprea*

Cetonia aurata (also known as the rose chafer) is common in its area of distribution which is particularly wide from Western Europe (Portugal, France, Great Britain) as far as Eastern Russia and China. This species has a large color change: usually metallic green often more or less vivid, it is sometimes tinged with red, rarely blue, violet or black.

Figure 3.9: *Cetonia aurata*, left: in our measurement system, right: in its natural habitat

The appearance of *Potosia cuprea* is quite similar to *Cetonia aurata*. The taxon cuprea is very variable, especially in the chromatism, and generally the specimens can be divided in 2 large groups according to the punctuation of the posterior part of the elytra which can be either very finely, superficially and sparsely punctuated, almost smooth, or densely and deeply punctuated as on the pronotum. Its chromatic forms were the subject of various descriptions.

Figure 3.10: *Potosia cuprea*, left: in our measurement system, right: in its natural habitat

The *Pseudochalcothea auripes* is a very shiny green beetle from the Southeastern Asia, especially from Borneo.

Figure 3.11: *Pseudochalcothea auripes*

3.3.2 Rutelinae

From this subfamily, we will investigate the polarimetric response of *Chrysina argenteola*.

This beetle is quite rare and can only be found in tropical areas. Common spots to find them include Honduras and Costa Rica. Its color is green with golden reflects.

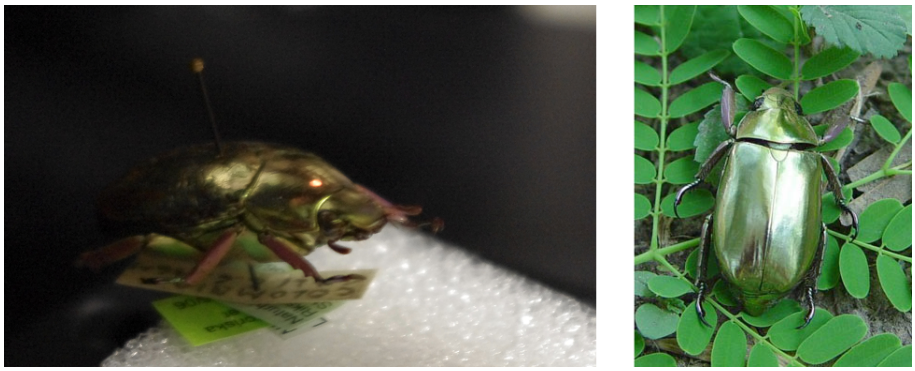

Figure 3.12: *Chrysina argenteola*, left: in our measurement system, right: in its natural habitat

3.4 Study of the exoskeleton structure

3.4.1 Previous studies and state of the art

In [63], Neville stated that the structure of the cuticle of some beetles is analoguous to cholesteric crystals (see fig. 3.13). These helicoidal structures (also called Bouligand structures) are twisted multilayer structures and induce optical activity: they highly reflect circularly polarized light. Each layer consisting of a chitin structure have uniaxial anisotropy. The study of the structures of these beetles is a very active domain where we can cite in very recent years the work of Jewell and Vukusic [64] (University of Exeter) for study of the *Plusiotis boucardi* with confocal microscopy, the contributions of Hodgkinson [65] (University of Otago) and Arwin [66] and Järrendahl [67] (University of Linköping) who studied the optical activity of different beetles using spectroscopic ellipsometry, and the qualitative study of the localization of circularly polarizing effects of some species of the Cetoniinae and Rutelinae carried out by Hegedus [68].

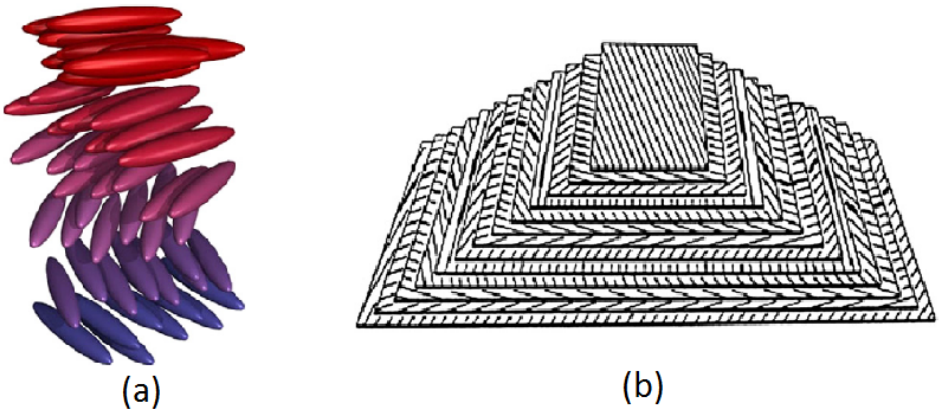

Figure 3.13: (a): The helical structure of cholesteric liquid crystal. Elongated molecules with an orientational order and positional disorder with twist in a direction perpendicular to their long axis. (b): Cholesteric representation in the form of the 'twisted' plywood model (from [69])

However, these studies always focus on the spectral response of the beetles and barely look at the localization of these effects on a microscopic scale. Jewell and Vukusic presented some very interesting images in [64] which challenged us to combine

the spatial resolution of a microscope and the polarization information brought by a polarimeter.

The left-circular polarization of these beetles can easily be demonstrated by observing them through a right circular polarizer. This property already highlighted by Michelson [55] for the *Chrysina resplendens* led to the widely accepted idea that beetles reflect left circular polarization and Können [70] and Kattawar [71] even stated that this was the common feature of the beetles but maybe that a right circular polarization mutant species may be found although it had not been documented so far. However, in [68], Hegedus et al showed that the handedness of the polarization reflected by beetles was a much more complex matter given the wavelength dependency.

Using our system, we can both image the sample with a high magnification, seeing the very fine structures of the beetles' cuticle, and have access to the localization of the polarization effects. Besides, the use of a white source and interferential filters also enables us to use discrete wavelengths for our study. Three wavelengths were selected: 454nm, 532nm, 633nm. Whenever it is possible, we measured the beetles on the scutellum, the triangular plate on the dorsal side of the thorax, usually where the wings attach (see fig.3.14). A picture of the sample was taken for every measurement showing exactly the localization of the spot.

Figure 3.14: Picture of a *Cetonia aurata* and localization of its scutellum (circled in red)

In the following of this manuscript, we will focus on the selected beetles we have previously described and compare them with the existing examples in the literature. The taxons of the beetles studied and cited in this manuscript can be found in a very exaustive article by Bouchard *& al* [72] and by Smith in [73, 74] for a more concise version. Fig. 3.15 gives an overview of the phylogenetic tree of scarabs.

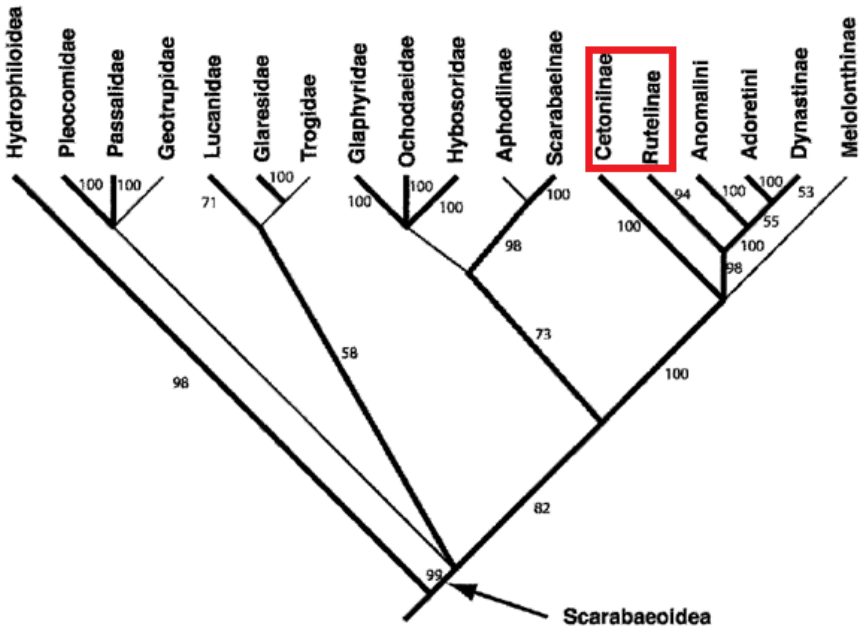

Figure 3.15: phylogenetic tree of scarabs from Smith [73]. Circled in red are the two subfamilies considered for this study.

3.4.2 Spatially resolved Mueller matrix measurements

In [75], Sharma *& al* showed that the cuticle of *Chrysina gloriosa* is a mosaic of mainly hexagonal tiles but also 5 and 7-sized polygons which are more frequent on more curved areas (see fig. 3.16). Fig. 3.17 shows an image of the exoskeleton of *Chrysina argenteola* acquired with our system using the 20x microscope objective. The imaged area is about $90\mu m$ showing the hexagonal and pentagonal structures on the cuticle of the *Chrysina argenteola*. This image should be compared with the structures published by Sharma *& al* [75] which are presented in fig.3.16.

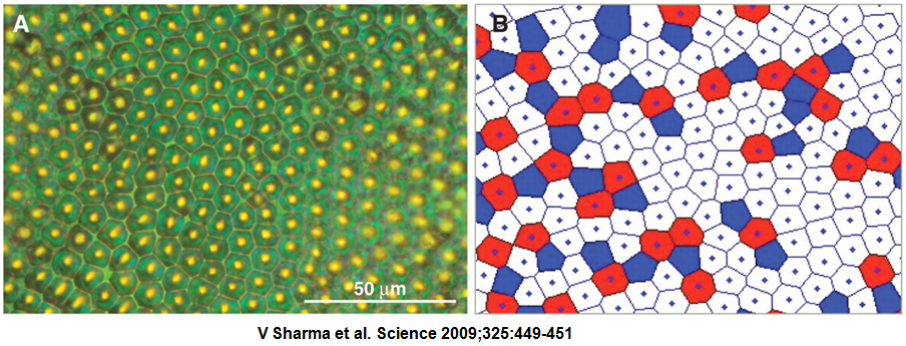

Figure 3.16: (a) Optical micrograph of the exoskeleton of *Chrysina gloriosa*. (b) Voronoi analysis of the corresponding image. Pentagons are colored blue, heptagons are red and hexagons white.

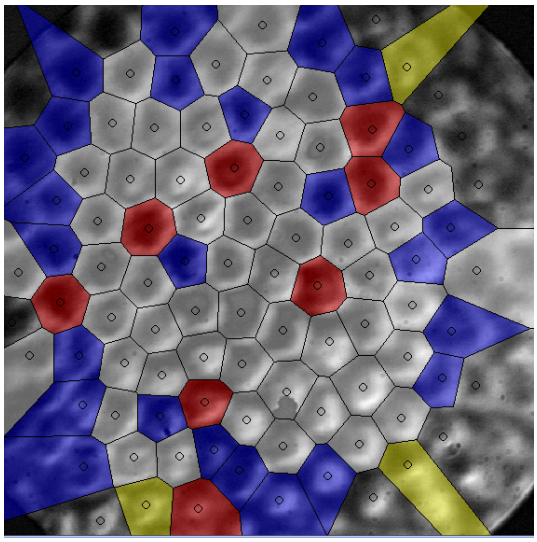

Figure 3.17: Voronoi diagram (pentagons: blue, heptagons: red, hexagons: white) superimposed to the intensity image of the exoskeleton of *Chrysina argenteola* acquired with our system using 20X objective. The imaged area is approximately $90\mu m$

We find a good agreement between the size of the cells of the exoskeleton extracted for both our images and Sharma's ($\sim 10\mu m$). We can also compare these images to the ones presented by Jewell and Vukusic [64]. They found the same structures on the exoskeleton of the *Chrysina boucardi* (formerly known as *Plusiotis boucardi*). It should then be noticed that this beetle belongs to the same branch of the phylogenetic tree (see fig. 3.15), the Chrysina genus of the rutelinae subfamily, and it is not very surprising that they share the same exoskeleton structures with a similar parameters.

We present here the structures of the exoskeleton of species belonging to cetoniinae subfamily, *Potosia cuprea* and *Pseudochalcothea auripes*. The structure of their exoskeleton look very alike the one of the Rutelinae with hexagonal and pentagonal tiles. These features are often listed as characteristic of the iridescent beetles.

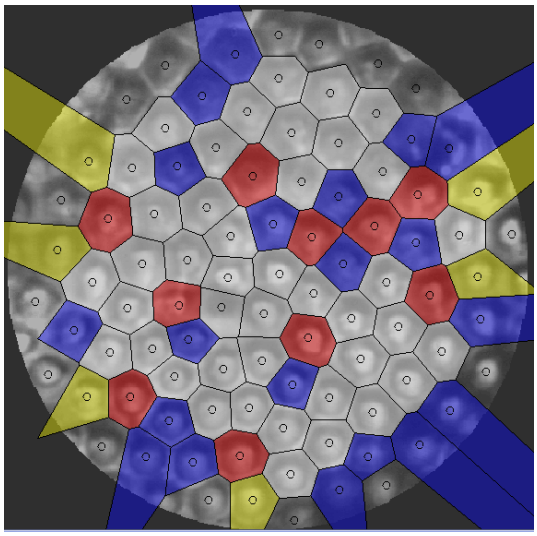

Figure 3.18: Voronoi diagram (pentagons: blue, heptagons: red, hexagons: white) superimposed to the intensity image of the exoskeleton of *Pseudochalcothea auripes* acquired with our system using 20X objective. The imaged area is approximately $90\mu m$

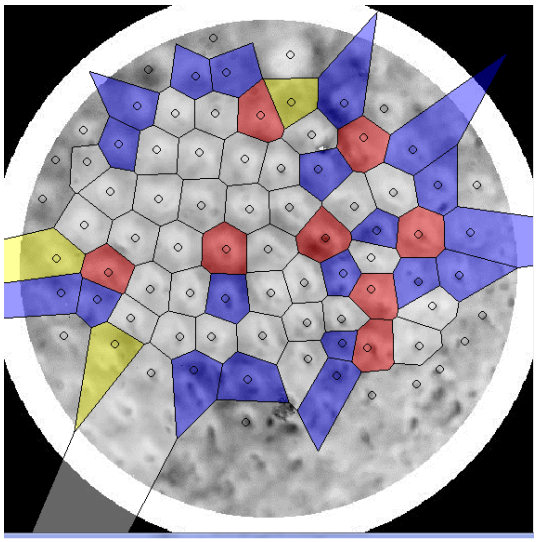

Figure 3.19: Voronoi diagram (pentagons: blue, heptagons: red, hexagons: white) superimposed to the intensity image of the exoskeleton of *Potosia cuprea* acquired with our system using 20X objective. The imaged area is approximately $90\mu m$

However, all the species of beetles do not share the same structural characteristics. Although we find similar hexagonal structures on the cuticle of *Cetonia aurata*, we notice that the sizes of the tiles may vary a lot.

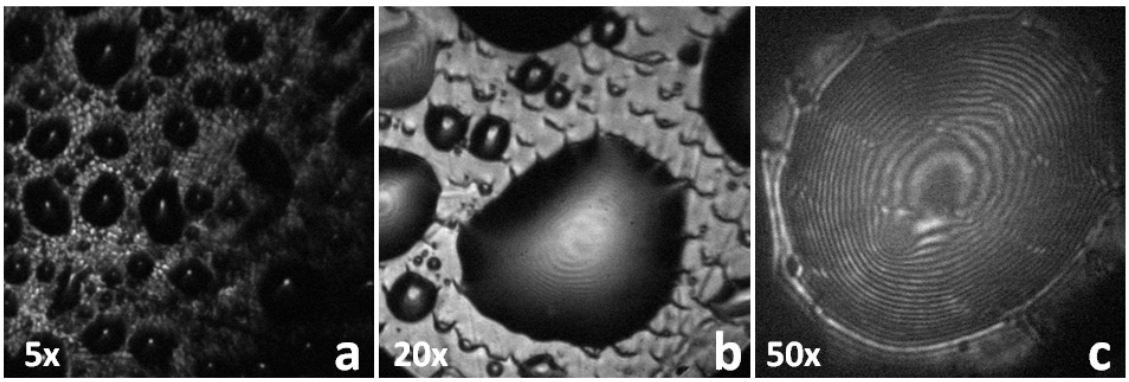

Figure 3.20: Images of the *Cetonia aurata*'s exoskeleton. (a) 5x image, field $\sim 360\mu m$. Size of the characteristic features (wells) varies a lot. (b) 20x image, $\sim 90\mu m$. The size of some wells can reach $50\mu m$. (c) 50x image, one can see very clearly the bouligand structures inside the well.

The image on the right of fig. 3.20 is very interesting because one can clearly see the Bouligand structures inside the well on *Cetonia aurata*'s exoskeleton. Though the origin of these bowls is still unknown, it is a common feature among beetles and their study can bring a lot to the understanding of the structure as a whole.

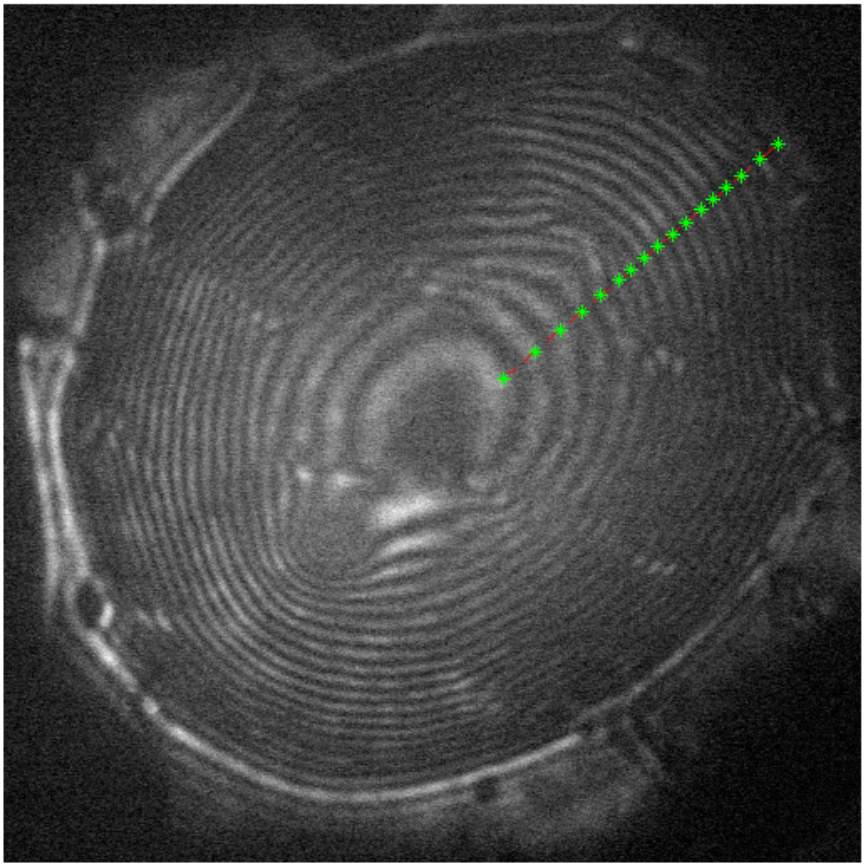

Figure 3.21: 50x image of the exoskeleton of *Cetonia aurata*. In red dashed line, selected cross-section for analysis. In green dots, detected layers of fibrous chitin

To study the Bouligand structures, we select a cross-section (in red dashed line on fig. 3.21), thanks to an automated procedure in Matlab®, we smooth the signal, filter it and automatically detect the peaks with a adaptative threshold filter (see fig. 3.22); we are then able to locate the layers of fibrous chitin on the image.

As we can see in fig.3.21, the layers seem to be thicker at the center of the bowls which probably comes from higher curvature whereas the layers are equally spaced at the edges.

Having calibrated the size of the imaged area for all the microscope objectives, we can measure the apparent thickness of the fibrous chitin. The 512 $\times$ 512 image images a 36μm area which means that each pixel represents a 70 nm $\times$ 70nm area. From the graph in fig. 3.22, we extract the distance in pixels between peaks and thus we find an apparent thickness ranging from 500nm to 1,3μm. This value has to be compared with the pitch used for simulation. In the literature, we found that the value of 370nm seems to arise very often [64, 67, 76]. Assuming this value of the pitch, we define θ the angle of curvature with respect to the normal according to fig. 3.23.

Knowing the curvature angle, we can easily reconstruct the profile of the bowl. Figure 3.24 gives an outlook of what the bowl looks like according to our measurements of the apparent thickness of the layers of fibrous chitin and assuming an even pitch of 370nm.

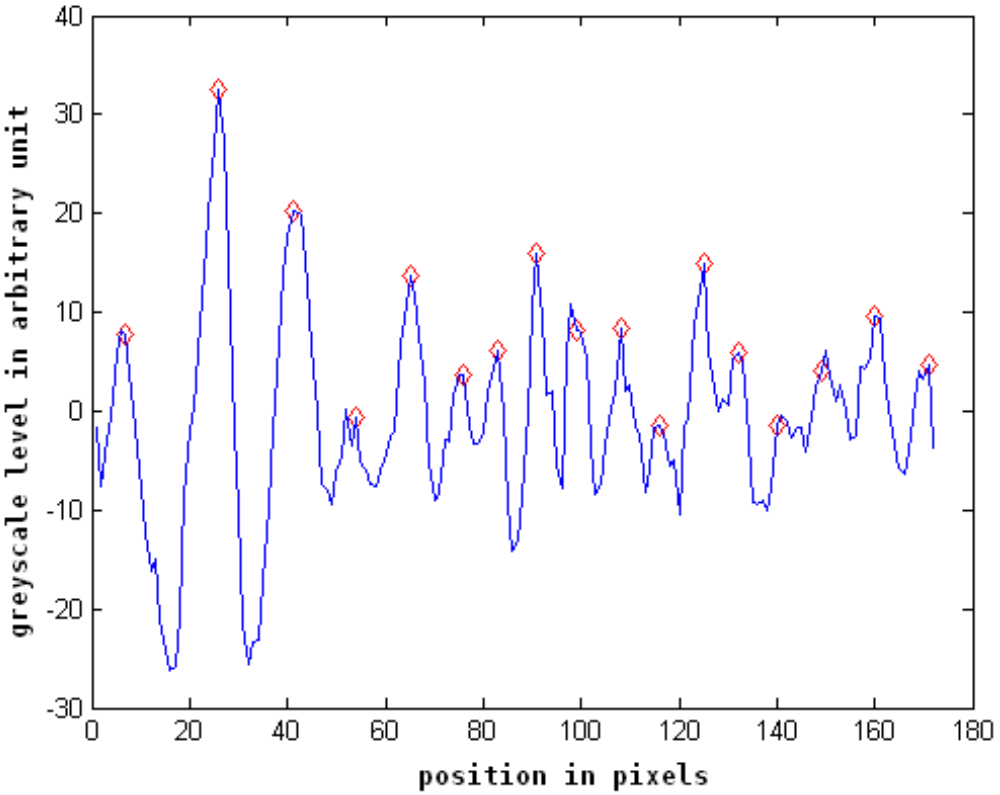

Figure 3.22: Smoothed and filtered signal. In red diamonds, the detected peaks corresponding to the chitin layers

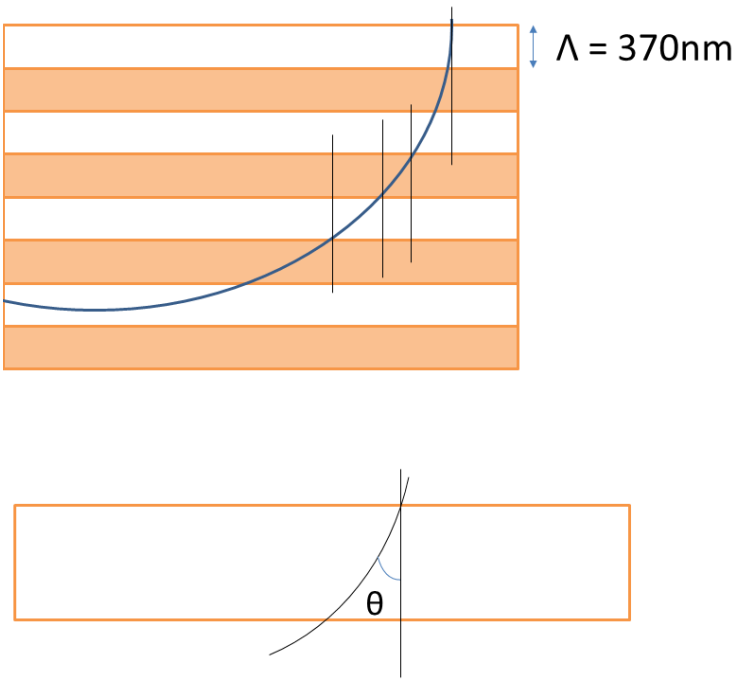

Figure 3.23: Definition of θ, the angle of curvature with respect to the normal

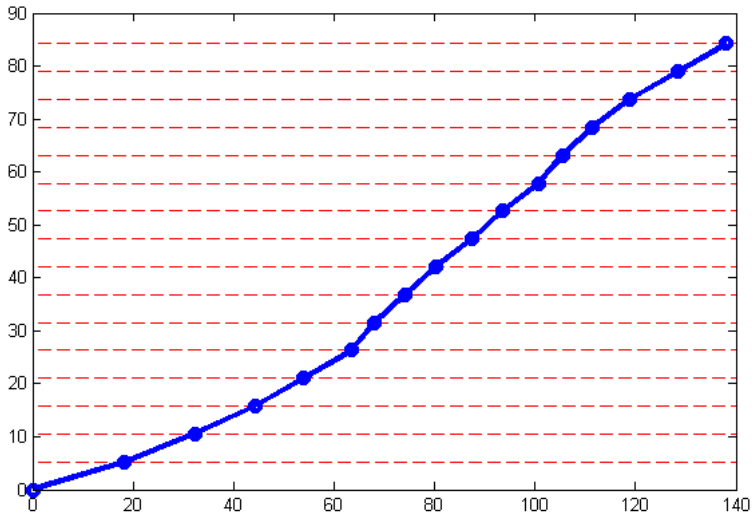

Figure 3.24: Reconstruction of the profile of the bowl according to the 50X image

3.4.3 Comparison of the Mueller matrices of selected beetles

We will compare the Mueller matrices obtained with our system which could be described as a polarimetric microscope with the ones obtained with a variable angle spectroscopic ellipsometer (VASE) (fig. 3.25, RC2 J.A. Wollam Co. Inc.). The measurements on the dual rotating compensator system were carried out by Hans Arwin and his team at Linköping University, Sweden. The spectroscopic measurements are acquired at a discrete angle between $20°$ and $75°$ with $5°$ increment. The wavelength range of interest is 400-800nm, the system can however provide data in a much broader wavelength region.

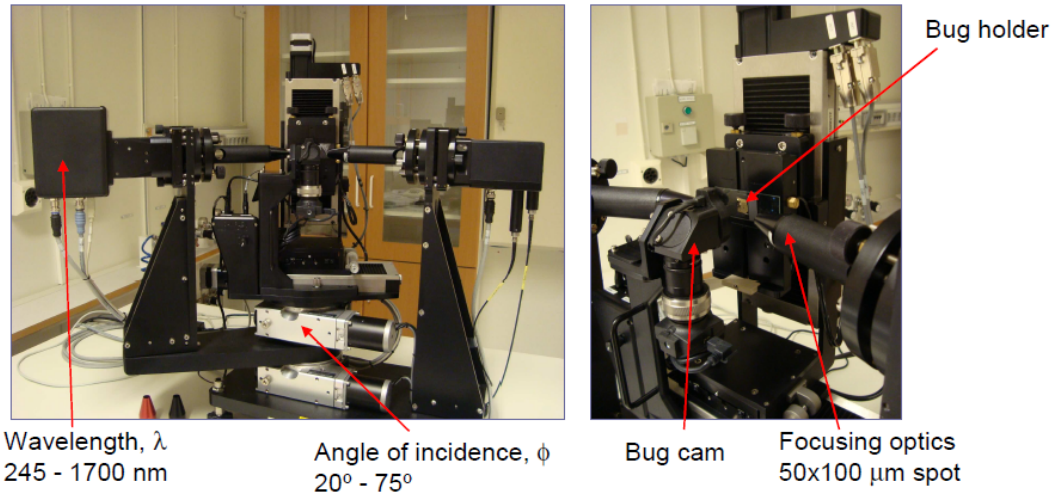

Figure 3.25: Variable Angle Spectroscopic ellipsometer RC2. Picture courtesy of Hans Arwin, LiU

For the sake of comparison, all the measurements were carried on the scutellum (see fig.3.14 for the location of the scutellum on the beetle and fig.3.26 for the spot on the scutellum).

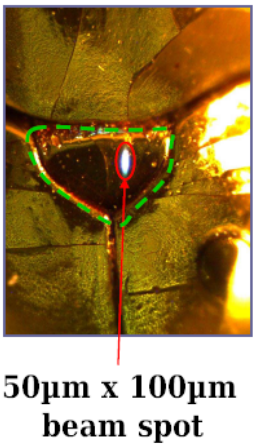

Figure 3.26: Location of the $50\mu m \times 100\mu m$ beam spot of the VASE on the scutellum

We remind here that the selected wavelengths for our system are 454nm, 532nm and 633nm and that the numerical aperture and imaged areas of the microscope objective are given in tab. 3.2.

Magnification	Aperture (0-θ°_{max}	Imaged area
5X	$0-8^{\circ}$	$360\mu m$
20X	$0-26^{\circ}$	$90\mu m$
50X	$0-53^{\circ}$	$36\mu m$
100X	$0-64^{\circ}$	$18\mu m$

Table 3.2: Numerical apertures and imaged areas on the microscope objective used for this study.

The angular range we have to average the spectroscopic data on vary a lot with respect to the chosen objective. Figures 3.27, 3.28, 3.29 show the Mueller matrices with corrected signs obtained for various beetles with the 20X objective of our system and the spectra acquired with RC2.

However, the smallest angle of the RC2 measurements is almost the limit of the angular range of our 20X objective ($20^{\circ} vs. 26^{\circ}$) which means that the comparisons could be difficult. Moreover, the illumination method is not the same. In the Mueller polarimeter we are sending a cone of light which aperture is θ_{max} (given in tab.3.2) on the sample. We gather the light scattered in the same cone of light, whereas the spectroscopic measurements are instead carried out using a 2θ configuration. That is, the light is emitted at a single incidence angle and the collection angle is equal to the incidence angle thus only measuring the specular reflection.

To highlight the discrepancies in the polarimetric response due to the illumination and collection methods we compare the RC2 measurements with a Fourier space Mueller matrix. We remind here that the Fourier space imaging, also referred to as conoscopic mode, gives us an angle-resolved image of the light emitted by the sample. The fig. 3.30 shows the M14 element of the angularly resolved Mueller matrix of *Cetonia aurata* and a cross-section of this element; we can clearly see the angular dependency of the circular dichroism.

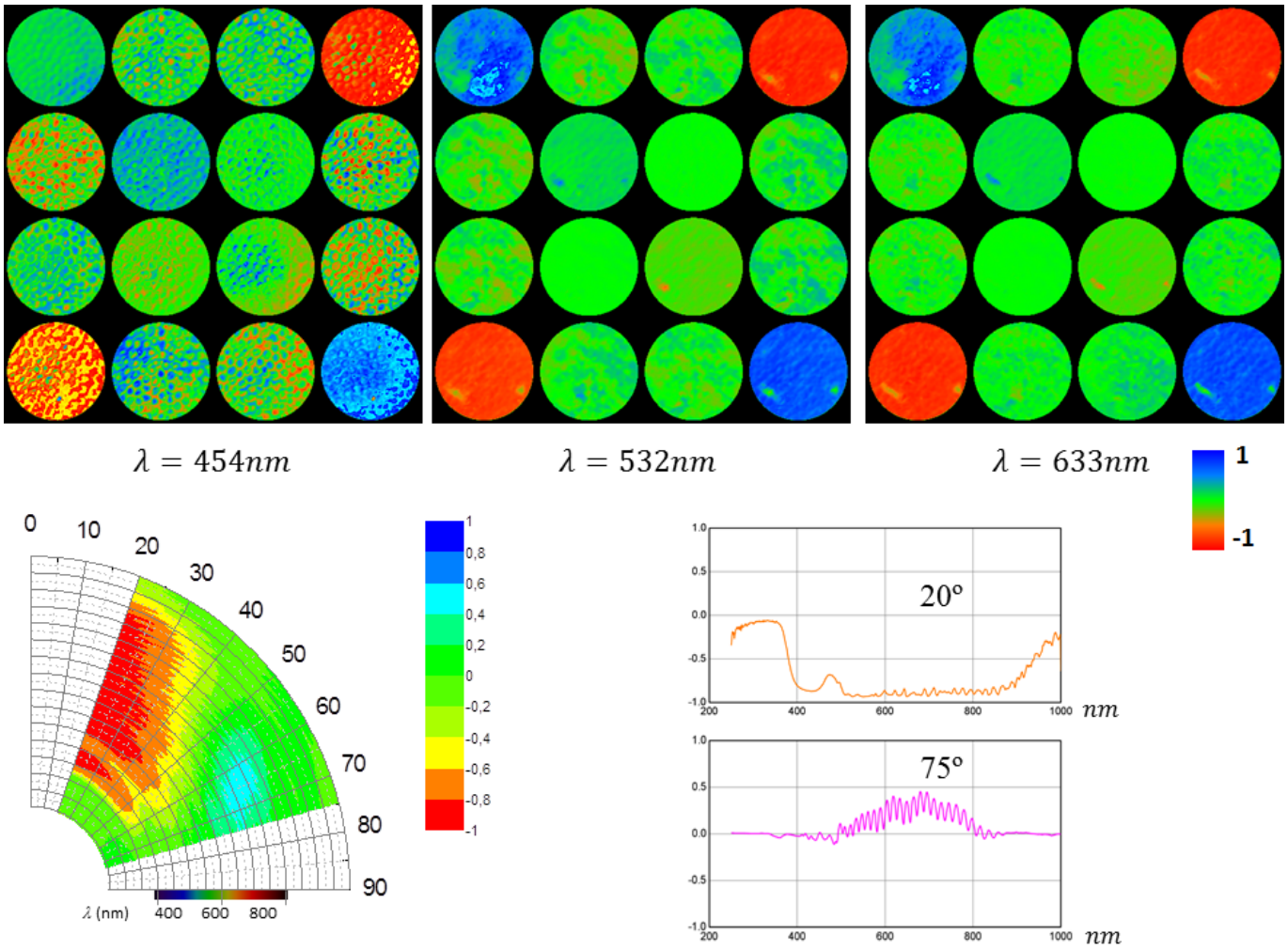

Figure 3.27: Top: Mueller matrix of a *Chrysina argenteola* acquired with a 20X microscope objective for 3 different wavelengths. Bottom: Polar plot (λ, ϕ) of Mueller matrix element M14 with $\lambda \in [245 - 1000]$ and $\phi \in [20 - 75°]$ and spectra at specific incident angles of 20° and 75°

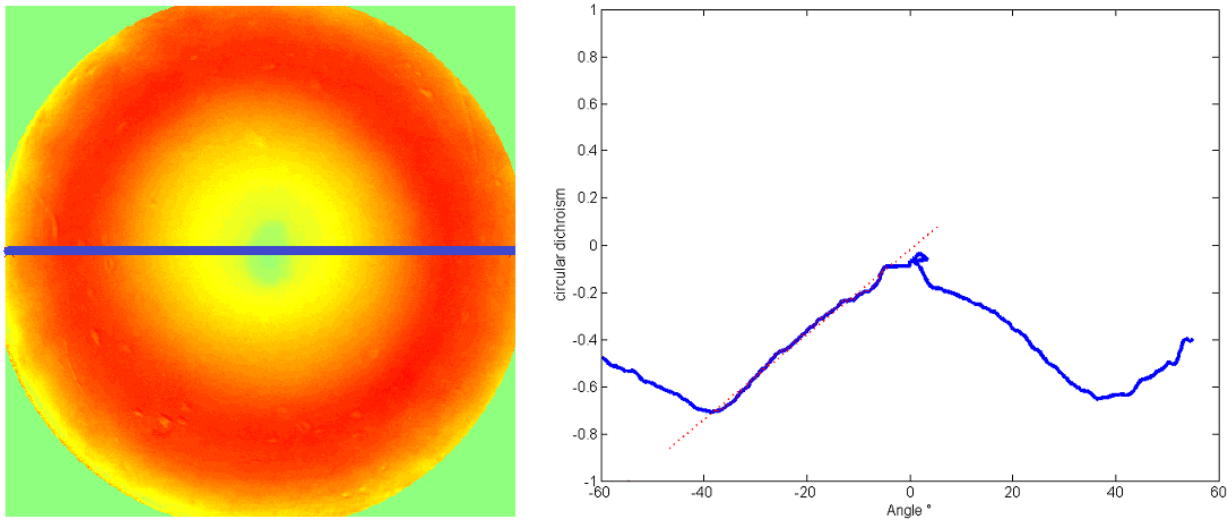

Figure 3.30: Left: M14 element of the Mueller matrix in the Fourier space at 532nm, scale [-1 1] and direction of the cross-section in blue. Right: cross-section of the M14 element along the blue line

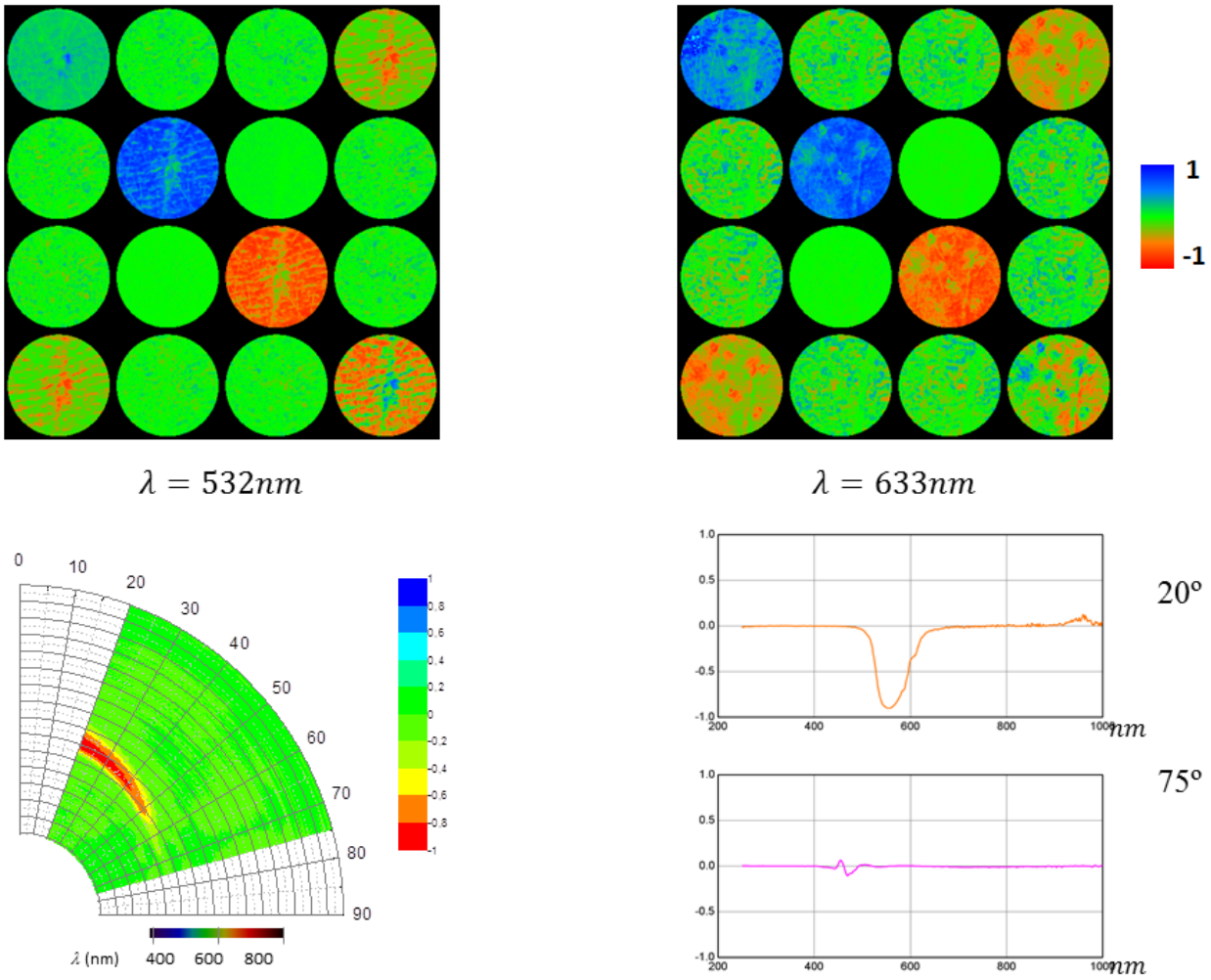

Figure 3.28: Top: Mueller matrix of a *Cetonia aurata* acquired with a 20X microscope objective for 2 different wavelengths. Bottom: Polar plot (λ, ϕ) of Mueller matrix element M14 with $\lambda \in [245 - 1000]$ and $\phi \in [20 - 75°]$ and spectra at specific incident angles of $20°$ and $75°$

That is, a direct comparison of this result with the polar plot presented in fig. 3.28 is impossible. The resulting Mueller matrix is the integral of the Mueller matrix for each incident beam weighted by the reflectance for this angle which explains the increase in the circular dichroism with the angle. Given that we send a cone of light, each pixel whose cylindric coordinates are $(r.\sin\theta_{out}, \varphi_{out})$ corresponding to the cartesian coordinates (x, y) in the Fourier space will measure a polarimetric response m_{xy} equal to:

$$m_{xy} = A_{xy}^{-1} \int_0^{\theta_{max}} \int_0^{360°} B_{xy}(\theta_{in}, \varphi_{in}) W_{\theta_{in}\varphi_{in}} d\theta_{in} d\varphi_{in} \tag{3.1}$$

where

- A_{xy} is the analysis matrix corresponding to pixel (x,y)
- $W_{\theta_{in}\varphi_{in}}$ is the modulation matrix corresponding to the ray of light illuminating the sample with angles $(\theta_{in}, \varphi_{in})$

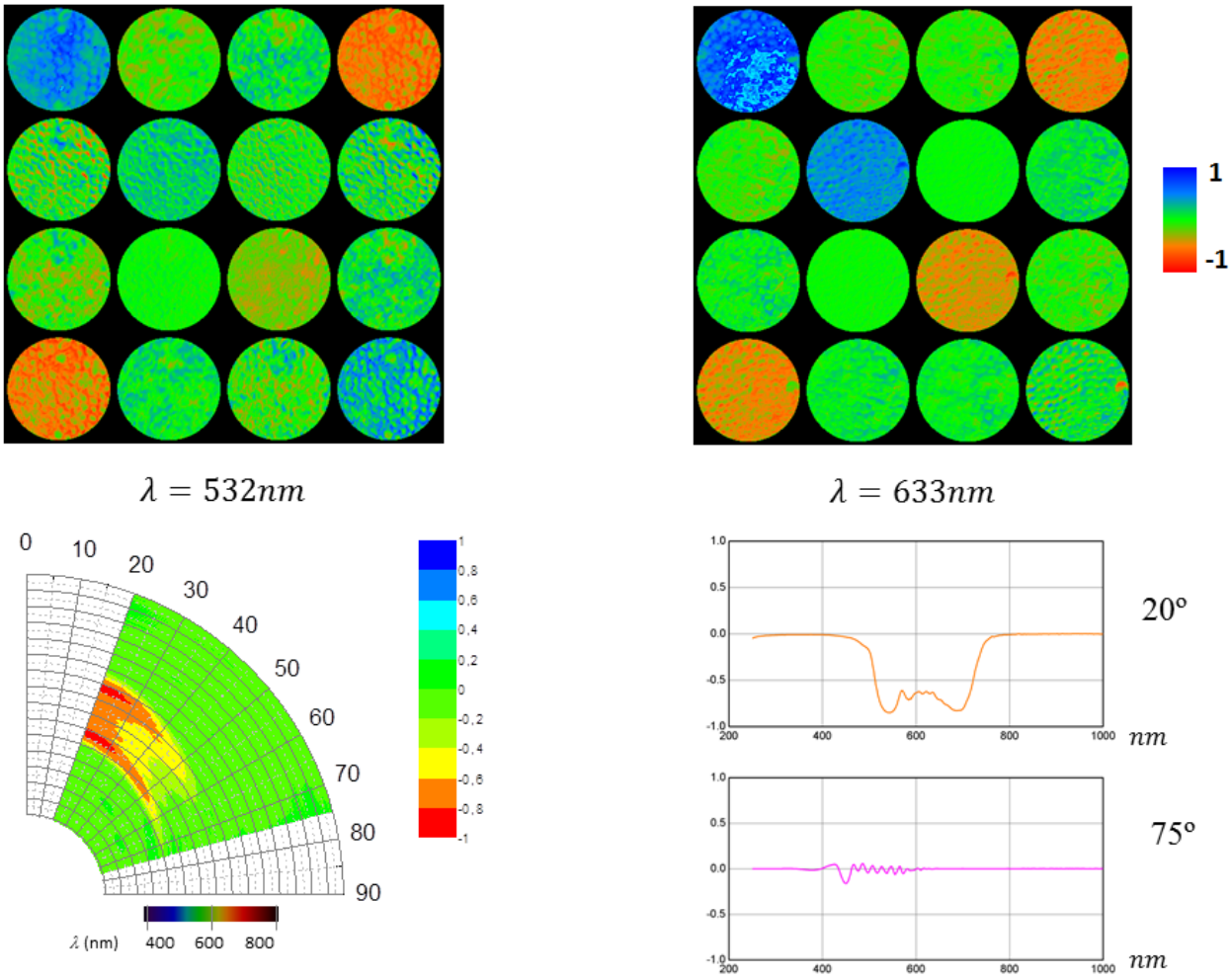

Figure 3.29: Top: Mueller matrix of a *Potosia cuprea* acquired with a 20X microscope objective for 2 different wavelengths. Bottom: Polar plot (λ, ϕ) of Mueller matrix element M14 with $\lambda \in [245 - 1000]$ and $\phi \in [20 - 75°]$ and spectra at specific incident angles of $20°$ and $75°$

- $B_{xy}(\theta_{in}, \varphi_{in})$ is the intensity matrix emitted by the sample in the pixel (x,y) from an illumination coming from $(\theta_{in}, \varphi_{in})$

The intensity matrix B actually consists of two parts: the intensity reflectance and the polarization information itself. In this case, it is some sort of generalization of the notion of Bidirectional Reflectance Density Function (BRDF) for polarized light.

The cross-section of the M14 element also shows that the polarization effect on the cuticle of beetle happens even for small incidence angles, the circular dichroism increases linearly with the incidence angle (see fig. 3.30).

The discrepancies in the acquisition method of both systems will only enable to qualitatively compare the measurements. The spectroscopic measurements will be used for fitting purposes while spatial measurements will be used to precisely localize the polarization effects on the cuticle.

The measurements presented here prove that our system can be used to measure the circular dichroism in the real space. The results are consistent with the spectroscopic measurements carried out at Linköping even though a thorough comparison is impossible.

3.4.4 Study of the localization of circular dichroism

Ossikovski *& al* stated in [32] that beetles are natural occurrences of Stokes non diagonalizable Mueller matrices (see 1.4 for a description of Stokes non diagonalizable Mueller matrices). This study was carried out on the *Cetonia aurata* but the results can be generalized to any species exhibiting circular dichroism. In fact, large areas of the cuticle of the *Cetonia aurata* can be seen as the incoherent superposition (ie weighted average) of a circular polarizer, a mirror and a half-wave plate rotated at $45°$.

$$M_{cuticle} = \alpha \cdot \begin{bmatrix} 1 & 0 & 0 & -1 \\ 0 & 1 & 0 & 0 \\ 0 & 0 & 0 & 0 \\ -1 & 0 & 0 & 1 \end{bmatrix} + \beta \cdot \begin{bmatrix} 1 & 0 & 0 & 0 \\ 0 & 1 & 0 & 0 \\ 0 & 0 & -1 & 0 \\ 0 & 0 & 0 & -1 \end{bmatrix} + \gamma \cdot \begin{bmatrix} 1 & 0 & 0 & 0 \\ 0 & -1 & 0 & 0 \\ 0 & 0 & 1 & 0 \\ 0 & 0 & 0 & -1 \end{bmatrix} \tag{3.2}$$

with α, β, γ, the respective weights.

The coefficient α directly gives us an outlook of the circular dichroism on the cuticle. We compute the sum decomposition of the Mueller matrix introduced in eq. 3.2 for all our measurements. 6 images are indeed generated by our Matlab® code: α, β and γ, the coefficients of the sum decomposition; a false color image where each channel represents a coefficient of the sum decomposition ($R = \alpha, G = \beta, B = \gamma$) which gives us a direct interpretation of the localization of the different contributions; ε, the ellipticity angle and p, the degree of polarization. Those 6 images for the *Cetonia aurata* can be found in fig. 3.31

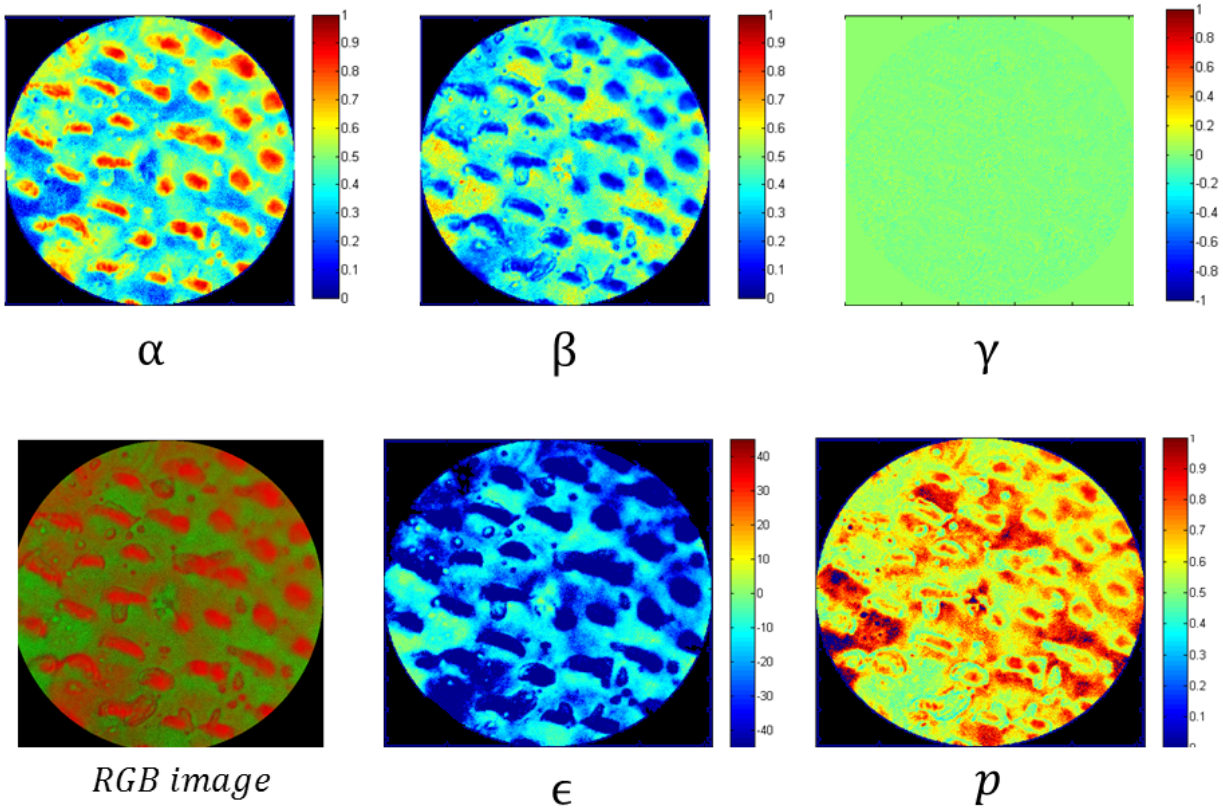

Figure 3.31: Output images of the sum decomposition of the Mueller matrix. Color scales for each image are given in colorbars. Background pixels are set to black. Sample: *Cetonia aurata* imaged at 20X, $\lambda = 532nm$

One can typically distinguish two kinds of polarimetric responses on the cuticle:

- $\alpha \sim 1, \varepsilon \sim -45°$ and $\beta \sim 0$. Red areas on the RGB image.

- $\alpha \sim \beta \sim 0.5$ and $\varepsilon \ll 45°$. Green areas on the RGB image.

For both areas, $\gamma \sim 0$.

Pixels from the first area behave like an highly-elliptical (close to circular) polarizer whereas the pixels from the second area behave more like a non-diagonal depolarizers. This is confirmed by the image of the degree of polarization which is lower in these areas compared to the centers of the elliptical spots with a high-ellipticity. Figure 3.32 shows the DOP ellipsoid (how the Poincaré sphere is transformed by the sample) for the different areas.

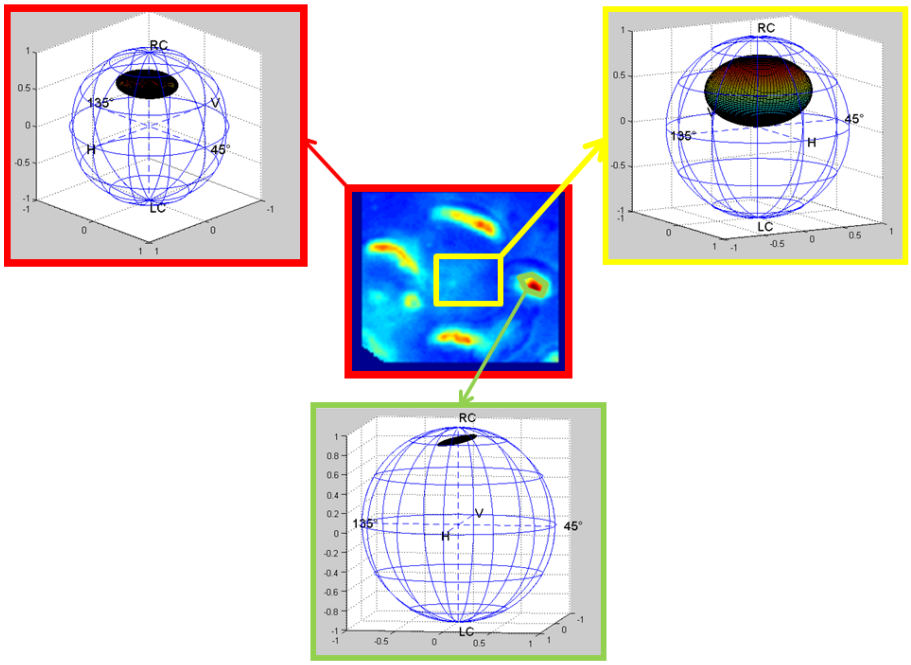

Figure 3.32: DOP ellipsoid for different areas of the cuticle of *Cetonia aurata*

3.5 Toward a better understanding of the exoskeleton's structure?

Up to now, simulations of the exoskeleton have always been carried spectroscopically using a simple 1D multi-layer optics model, assuming an homogeneous cuticle (see fig.3.33). The first layer of the cuticle, called the epicuticle, is modeled as a dielectric layer (Cauchy dispersion) with a thickness of $d_{epi}nm$. The second and most important layer, the exocuticle, is modeled as a uniaxial dielectric layer (Cauchy dispersion and Urbach absorption), the chirality of this layer has a pitch p with a pitch distribution Δp. Some variations of this model have been presented in the literature, we will here note the contribution of Jewel [64] who split the exocuticle in two parts: an helicoidal region with short pitch (310nm) followed by a region with long pitch (370nm). We assume that the azimuth (in the x–y-plane) of the fast-axis of the anisotropic media in the helicoidal layers varies linearly as a function of distance. The refraction indexes of the different layers and model results can be found in [64] for Chrysina *boucardi* and in [67] for *Cetonia aurata*. We present in fig.3.34 the results of the fit for the spectroscopic Mueller matrix of *Cetonia aurata* by K.Järrendahl.

However, our real space measurements show that the cuticle of the beetles cannot be regarded as homogeneous. To our knowledge, no simulation has ever taken into account the different polarimetric behaviors of the center of the hexagonal structures. As shown in [75] and as confirmed by our intensity images, the Bouligand structures play a very important role in the circular dichroism. Jewell *et al.* published some very interesting images of the cuticle of *Chrysina boucardi* using microscopy in both bright-field and dark-field configuration as well as confocal microscopy [64] showing the localization of the reflected light depending on the wavelength. However, the absence of use of polarization makes it hard to compare these results with our images.

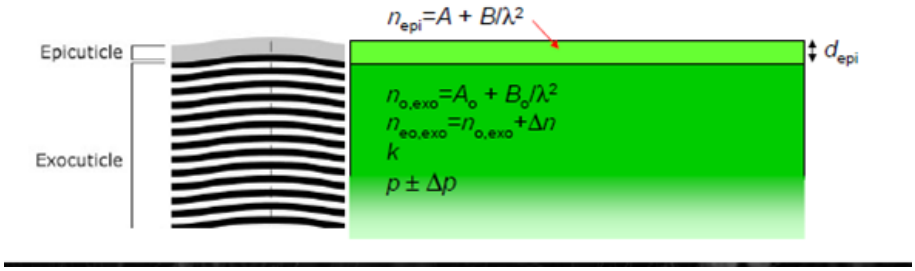

Figure 3.33: Model used to simulate the optical response of studied beetles. Image courtesy of K.Järrendahl [67]

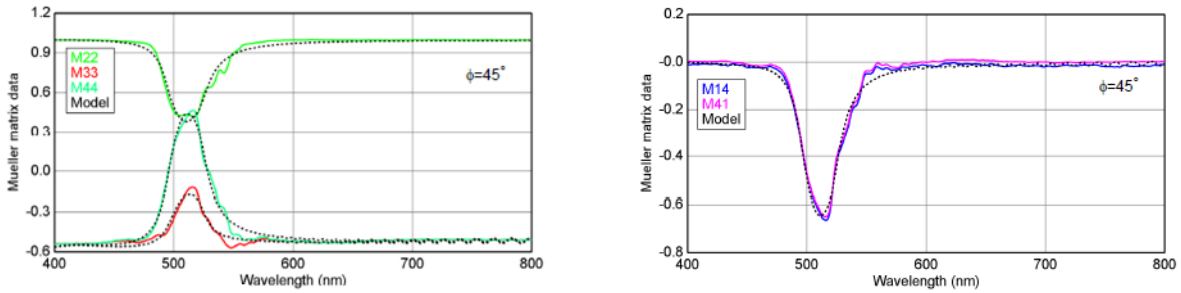

Figure 3.34: Results of the fit of the Mueller matrix of *Cetonia aurata*. Model and fit by K.Järrendahl [67]

By using our spatially resolved Mueller polarimeter, we can also improve the model by measuring the actual variation of the orientation of the fast-axis of the uniaxial layer by measuring the orientation of the polarimetric properties of the sample such as the diattenuation or the retardance. Some results on *Cetonia aurata* measured with a 50x microscope objective are given in fig. 3.35. We performed a Lu-Chipman decomposition of the Mueller matrix of this sample and extract the scalar values of the retardance and the dichroism as well as their respective orientations.

The Mueller matrix images presented in this chapter are qualitative measurements and cannot be interpreted directly. We find a good agreement between the observations made in other publications and our conclusions regarding the localization of the polarimetric effects on the cuticle.

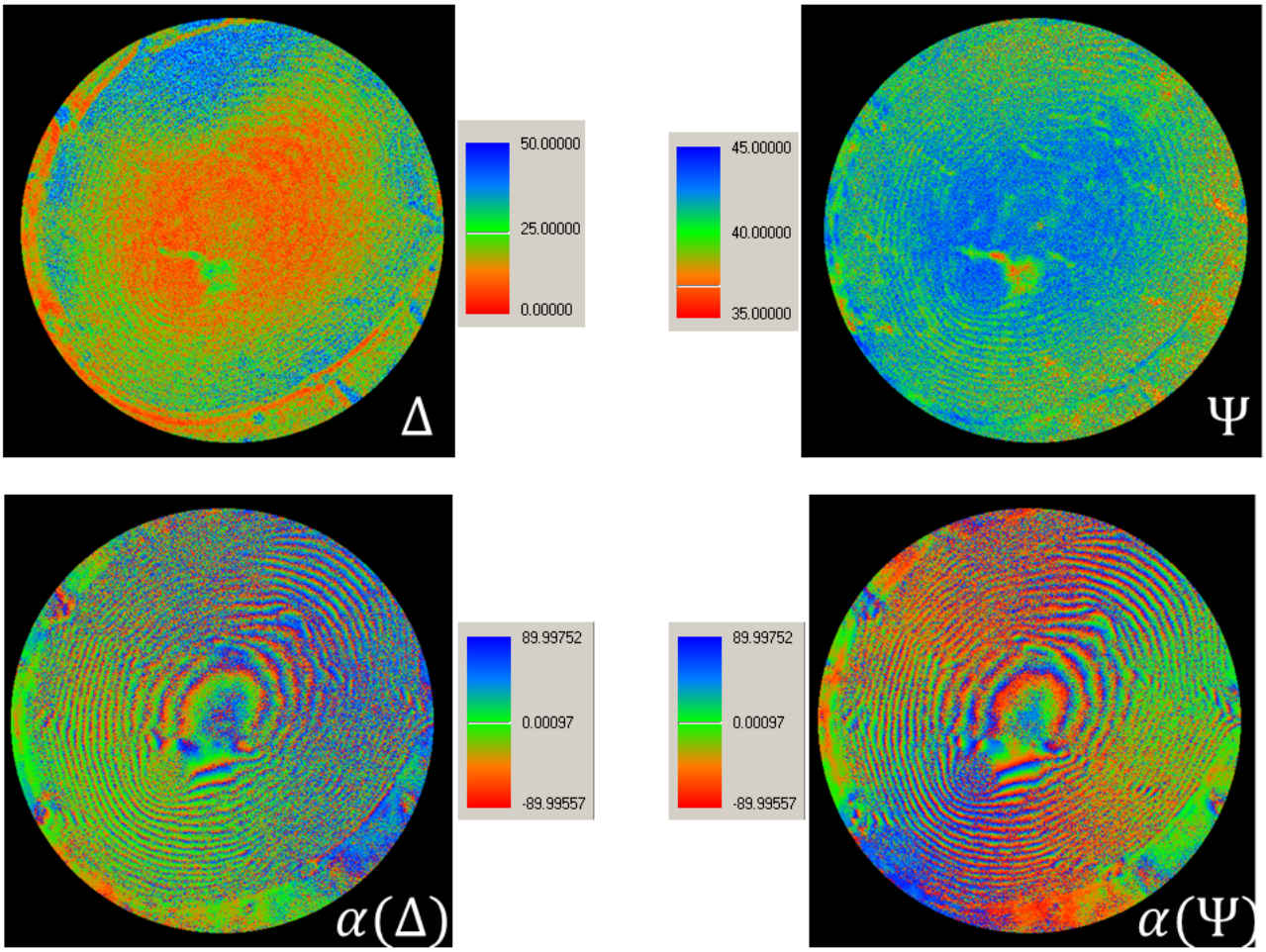

Figure 3.35: Results of the Lu-Chipman decomposition on the Muller matrix of a Bouligand structure imaged on *Cetonia aurata* with a 50x objective. From top left to bottom right: scalar retardance, scalar dichroism, orientation of retardance, orientation of dichroism

Chapter 4

Fourier space measurements: Applications to overlay characterization in Microelectronics

4.1 Generalities and motivations

4.1.1 Generalities about the semiconductor industry

Even though people are not always aware of it, microelectronics and semiconductors have invaded our everyday life. The technology is always evolving, making the past generation completely obsolete and old-fashioned. The Moore's law introduced as early as 1975 [77] describes the long-term evolution of microelectronics and predicts that the number of transistors that can be placed inexpensively on an integrated circuit doubles approximately every two years (though originally predicted every year). Figure 4.1 displays the actual evolution of the number of transistors per surface unit. This trend has continued for more than half a century and is expected to continue until 2015 or 2020 or later. However, an increase in the number of transistors per surface unit also means a decrease in their size. Table 4.1 gives an outlook of the drastic decrease in size of the features.

The fabrication of transistors is a very complex process as we can see on fig. 4.2: it includes a large number (actually hundreds) of steps alternating thin film deposition (metal or resist), lithography (including insolation of resist by UV or electron beam in a predefined pattern) and etching. We will focus on the different metrology challenges of the lithography. A more detailed scheme of this process can be found in fig.4.3.

year	1971	1975	1982	1985	1989	1994	1995	1998	1999
Technology Node	$10\mu m$	$3\mu m$	$1.5\mu m$	$1\mu m$	$800nm$	$600nm$	$350nm$	$250nm$	$180nm$
	2000	2002	2006	2008	2010	2011	2013	2015	
	$130nm$	$90nm$	$65nm$	$45nm$	$32nm$	$22nm$	$16nm$	$11nm$	

Table 4.1: Semiconductors manufacturing processes: typical feature size (from the ITRS)

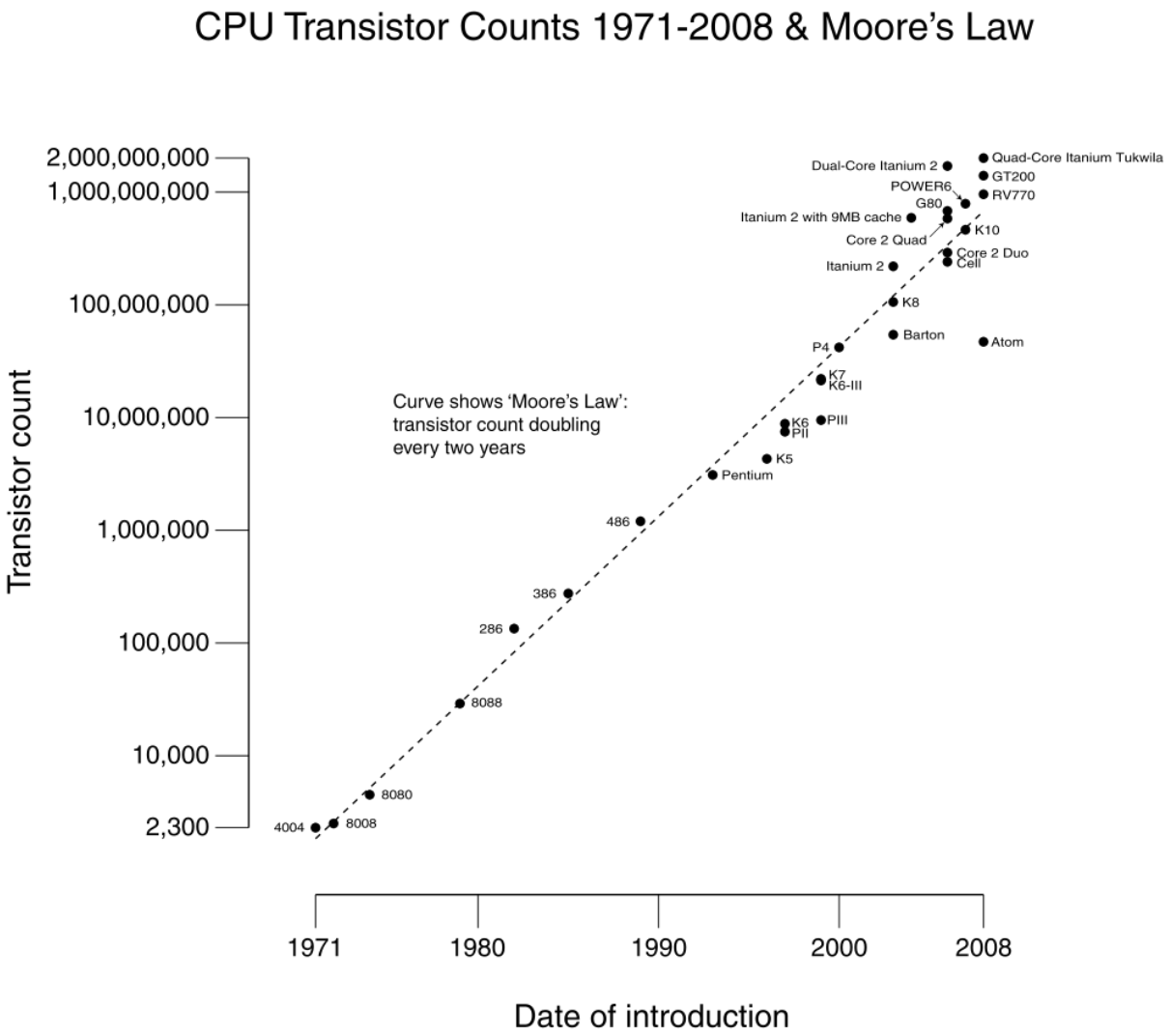

Figure 4.1: evolution of the number of transistors on an integrated circuit

4.1.2 Challenges for the metrology

With new technology nodes, lithography tools and metrology tools have to evolve to meet the standards required and are now highly entwined in what we call Integrated Metrology (IM) which is now a rising trend in the field of Advanced Process Control (APC). This problematic emerged a few years ago when the metrology requirements became so demanding that a new vision was needed. Integrated Metrology is basically the coupling of a metrology tool to a process / fabrication tool, the metrology providing the measurements to correct the output of the process.

In a perfect integration scheme, the same instrument should be able to measure various parameters such as the critical dimensions. However, along with the characterization of the profile itself (referred to as Critical Dimension (CD) metrology), a very precise relative positioning of the layers of a stack, called overlay, is needed. The overlay is defined as the misalignment between two layers of a stack. The influence of this error could lead to defective transistors for example if there is no electrical contact between the different constitutive layers (see fig.4.4 for a cross-section of a transistor and the importance of alignment between layers).

This feature is more and more challenging with the shrinking of the technology

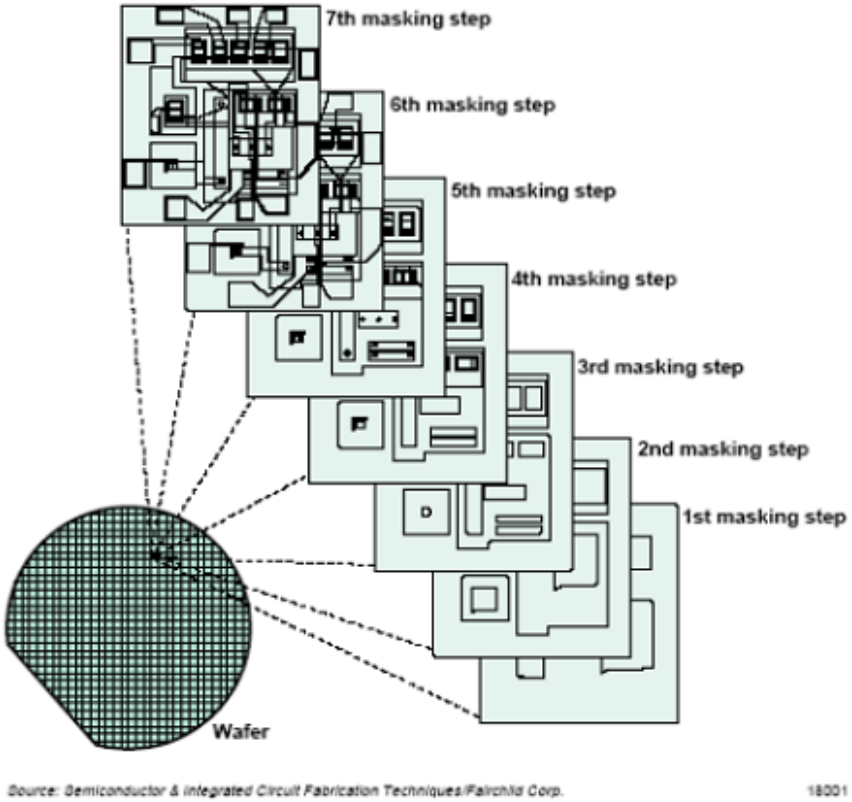

Figure 4.2: Different steps in the fabrication of semiconductors

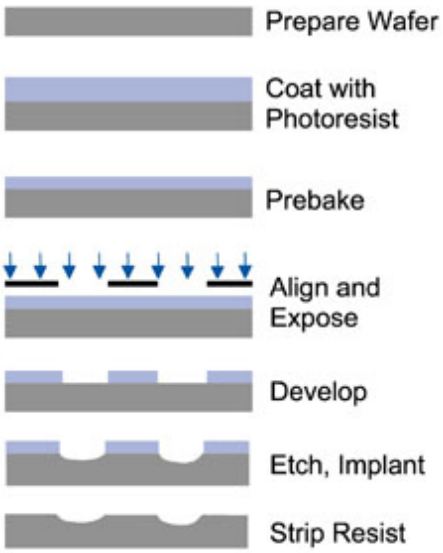

Figure 4.3: Different steps in the lithography process for the fabrication of semiconductors

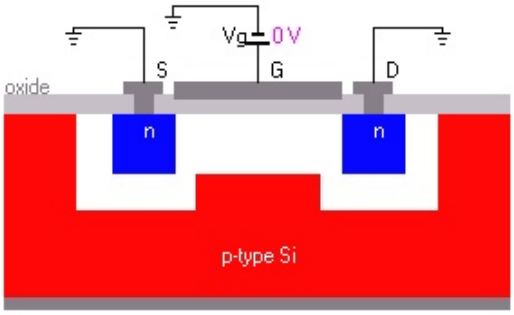

Figure 4.4: cross-section of a transistor. In the case of a misalignment between layers, there could be no electrical contact between the source and the doped region.

node (TN) and used to be of no interest at all when its effect was neglected compared to the defect in critical dimension. Nowadays the overlay error must not exceed one quarter of the CD and the measurement uncertainty is now around the nanometer range (cf fig.4.5). Moreover, the overlay is not uniform on the wafer, it clearly depends on the position on the wafer. To have an accurate characterization of the overlay on the wafer, we need to measure a large number of calibrated targets spread on the wafer thus imposing a very fast technique. Ausschnitt [78] introduced a utopian metrology target called MOXIE (Metrology Of eXtremely Irrational Exuberance) to both measure CD and overlay. This is the ultimate goal of the metrology and we are going to demonstrate that our technique could approach the MOXIE.

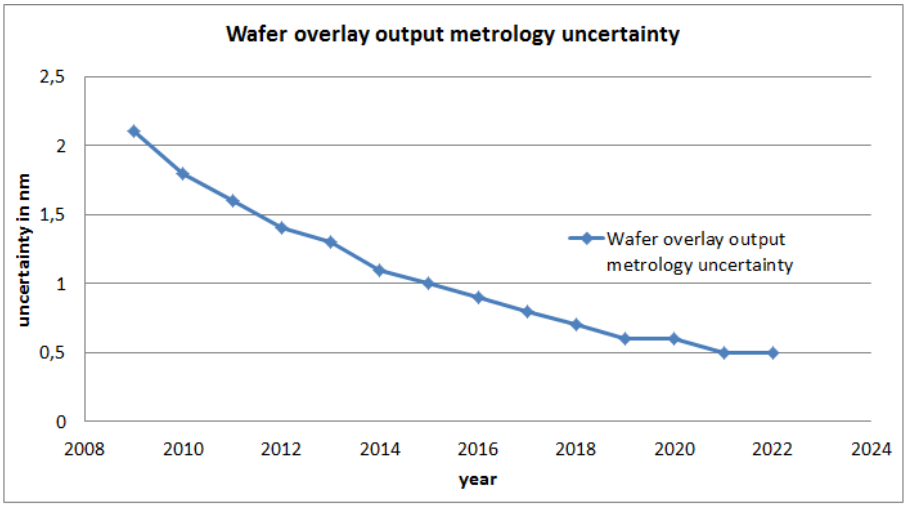

Figure 4.5: Evolution of the output overlay uncertainty versus the year (source: ITRS 2010)

The problematic of CD metrology using Mueller polarimetry has already been reviewed in details and was the focus of the thesis of Sami Ben Hatit [41]. We will not insist more on the benefits and disadvantages of this method for CD measurements and we will only focus on the use of Mueller polarimetry for overlay characterization. If this overlay is higher than a set threshold, the whole batch cannot be processed to the new step, this results in a rework, the wafer returns to the previous lithography step and the resist is stripped. This means that the overlay metrology must be done right after developing which could be difficult so the overlay is sometimes only measured after etching. In this case, rework is not an option and the wafer just goes to scrap.

4.2 Overview of the metrology techniques for microelectronics

In this section, we will present the different techniques used for overlay characterization in the microelectronics industry. We can separate them into two categories: the non-optical techniques and the optical techniques, the latter being non-destructive in contrary to the first. It is important to notice that **there is no overlay standard** and there is no systematic way to verify and compare the accuracy of overlay metrology. The programmed overlay offsets we introduce are very hard to control as we will see in the following of this chapter.

4.2.1 Non-optical techniques

Electron microscopy

So far, scanning electron microscopy (SEM) has been the gold standard for CD measurements because it provides real images of the wafer and the structures engraved in the scribe lines. As SEM cannot see buried layers, it is then not a candidate for overlay measurements. Only in very special cases it can be used but we have to use Cross Sectional SEM (X-SEM), these images are easily processed and give a direct characterization of our sample. However, this technique is destructive, very very slow and requires sample preparation which alters the profile of structure and then increase the uncertainty of the measurements.

Atomic Force Microscopy (AFM)

The bottleneck of AFM measurements for overlay and critical dimensions (CD) metrology is their tips. AFM can provide good measurements as long as the tip can reach the bottom of the trench and as long as its asymmetry can be calibrated. However, AFM is unable to access the buried layers of the structure and then cannot provide information about the positioning of the layers. Moreover, for characterization of small patterns, commercially available tips are too large and cannot grant reliable results. The other disadvantage of both non-optical techniques is their very poor throughput. Both methods are very lengthy and it is very hard to inspect the surface of a wafer fast enough.

4.2.2 Optical techniques

A fast and non-destructive method to characterize overlay is required. Optical techniques are very good candidates for this metrology. The main appeal of these techniques is that light can penetrate several "layers" of the sample and then is sensitive to the bulk structure of the sample even though structures are buried and are so inaccessible to other non-destructive techniques.

Image-based techniques

Image-Based Overlay (IBO) techniques rely on box in box (BiB) or bar in bar marks imaged with a bright-field optical microscope and has been adopted as the standard for overlay metrology for years. However, IBO is not free of artifacts [79] and the size

of the marks it requires (at least $18\mu m \times 18\mu m$ boxes repeated in the scribe lines) may become a limitation in the future. New designs for the targets used are still a part of research and help always push further the limits, the grating based AIM methods introduced is a good example and provides better results than traditionnal BiB or FiF targets [80].

Conventional BiB metrology has been the standard for many years but the global overlay budget shrinking and the resolution of a bright field microscope being limited by aberrations, we can see that the cost of such device will increase with new technology nodes. The fundamental limitations of BiB metrology are listed in [81].

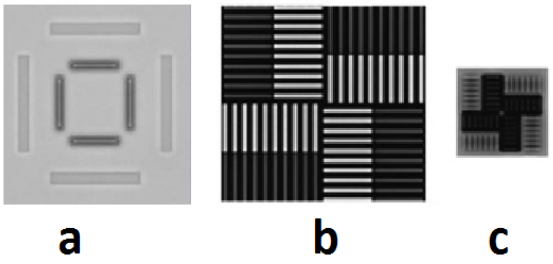

Figure 4.6: (a): Standard BiB mark. (b): AIM mark $30 \times 30\mu m^2$. (c): μAIM mark $15 \times 15\mu m^2$

Diffraction-based techniques

Diffraction based overlay (DBO) techniques, also called scatterometry, are spreading very fast in the microelectronics industry. The instrument collects the light diffracted, scattered and reflected by the sample and analyzes it as a function of a variable which can be the angle of incidence or the wavelength, the latter being referred to as spectroscopic scatterometry. The signature of the sample is very rich and detailed, enabling very accurate fits. The most widespread DBO technique for overlay measurements is the so-called Scatterometry for Overlay (or SCOL), which involves spectrally resolved ellipsometric measurements in planar diffraction geometry, i.e. with the incidence plane perpendicular to the grating lines. This technique is quite fast and non-destructive, the measurements can be done in situ, however a fit of the experimental data by multiparemeter models is often required and the final results are model-dependent. However, the signature of the measured samples and the use of dense structures instead of isolated ones allow a rigorous modeling [82].

In the case of standard scatterometry, the spectra from pads with same overlay magnitude but opposite directions are identical due to symmetry. In the case of empirical DBO (e-DBO), no modeling of the structure is required and the measurement accuracy can be increased by adding some reference structures. Model-based DBO (m-DBO) adds the overlay in the parameters of the fit and provides both overlay and structure profile information [83].

While a single pad of 3D structures should be enough to completely characterize the overlay, actual DBO methods rely on measurements of 2D linear gratings, thus having at least one test structure per axis. 2 pads are then sufficient for m-DBO while at least 4 pads are required for e-DBO while 6 or 8 are typically used [79, 82, 83, 84]. Standard boxes for measurement of overlay using scatterometry are typically $40\mu m \times 160\mu m$ but new targets developed by ASML for their YieldStar device [85] of only $30\mu m \times 60\mu m$ (containing two x gratings of different biases and two y gratings of different biases)

have been introduced recently [86]. However, this technique still requires specially designed and dedicated structures that use too much space on the wafer and don't reflect exactly the actual in-chip overlay. DBO techniques typically provide better short term reproducibility than direct optical imaging of BIB, AIM or "blossom" targets for overlay measurements. This improvements of the reproducibility is the main advantage of the DBO technique compared with IBO which will be soon limited especially in the case of double patterning which requires a reproducibility better than 0.2nm [82, 84].

4.3 Intrinsic properties of Mueller matrices in conical diffraction and simulations

Mueller polarimeters have already proved to be excellent candidates for the metrology of CD in microelectronics either in spectroscopic [87, 88, 89, 90] or in conoscopic mode [41, 37, 91]. This is the most general polarimetry technique and although Mueller polarimetry is way less wide-spread than classical ellipsometry, the development of such instruments is a very active field [37, 48, 51, 92, 93, 94, 95]. In the first part of this section we will introduce the fundamental and intrinsic properties of a Mueller matrix which enables us to use this formalism for the characterization of overlay. We will then focus on the Mueller matrices of simulated structures of interest which will lead to the definition of linear estimators for overlay.

We here remind that we use a complete Mueller polarimeter mode which means that the measurements are 4×4 matrices contrary to other systems used for the same purpose but that are only able to measure a partial Mueller matrix (3×4 matrix [96, 97]). Moreover, the measurements are performed at a single wavelength in a conoscopic mode which means that we can access all the angle of incidence (AOI) and azimuth whereas traditionally measurements are spectroscopically resolved at discrete AOI and azimuth (see fig 4.7).

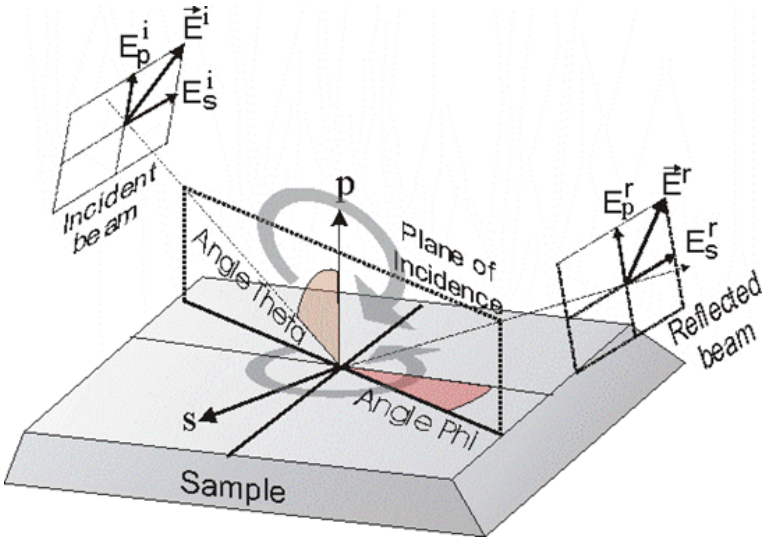

Figure 4.7: Geometry of conical light incidence in traditional ellipsometry for 1D grating

4.3.1 Intrinsic properties of Mueller matrices

In the Stokes-Mueller formalism, light can be described by a 4-dimension vector called the Stokes vector (see 1.1.2 for more details about Stokes vectors). The light-matter interaction is then summarized by the 4×4 matrix called Mueller Matrix. In the absence of depolarization, as it is the case in many microelectronics measurements, the Mueller matrix can directly be derived from the Jones matrix [28] (see eq. 4.1) $\mathbf{J} = \begin{bmatrix} r_{pp} & r_{ps} \\ r_{sp} & r_{ss} \end{bmatrix}$ which depends on the azimuth, AOI, wavelength and also on the structure details on the sample. The diagonal elements of the matrix describe the reflection coefficients for parallel (p) and perpendicular (s) light. The off-diagonal elements of the matrix describe the polarization conversion between s- and p- polarizations that occurs when the sample is anisotropic. Li demonstrated in [98] that the Jones cross-polarization reflection coefficients are anti-symmetric for symmetric structures as a result of the electromagnetic reciprocity theorem for the 0th-order diffraction of symmetrical gratings and that this condition is not fulfilled when asymmetry occurs in the structure and then can be used for overlay metrology. This result is generalized when the wave vector of the incident plane wave and the negative of the wave vector of the m^{th} reflected order are symmetrical with respect to the plane perpendicular to the grating grooves. However, we will limit our study to the 0^{th} order of diffraction (specular reflection) so we are not limited by the period-wavelength ratio.

$$\mathbf{M} = \left\langle \begin{bmatrix} \frac{1}{2}(|r_{pp}|^2 + |r_{ss}|^2 + |r_{ps}|^2 + |r_{sp}|^2) & \frac{1}{2}(|r_{pp}|^2 - |r_{ss}|^2 - |r_{ps}|^2 + |r_{sp}|^2) & & \\ \frac{1}{2}(|r_{pp}|^2 - |r_{ss}|^2 + |r_{ps}|^2 - |r_{sp}|^2) & \frac{1}{2}(|r_{pp}|^2 + |r_{ss}|^2 - |r_{ps}|^2 - |r_{sp}|^2) & & \\ re(r_{pp}^* r_{sp} + r_{ps}^* r_{ss}) & re(r_{pp}^* r_{sp} - r_{ps}^* r_{ss}) & & \\ im(r_{pp}^* r_{sp} + r_{ps}^* r_{ss}) & im(r_{pp}^* r_{sp} - r_{ps}^* r_{ss}) & & \end{bmatrix} \right.$$
$$\left. \begin{bmatrix} re(r_{pp}^* r_{ps} + r_{sp}^* r_{ss}) & -im(r_{pp}^* r_{ps} + r_{sp}^* r_{ss}) \\ re(r_{pp}^* r_{ps} - r_{sp}^* r_{ss}) & -im(r_{pp}^* r_{ps} - r_{sp}^* r_{ss}) \\ re(r_{pp}^* r_{ss} + r_{ps}^* r_{sp}) & -im(r_{pp}^* r_{ss} - r_{ps}^* r_{sp}) \\ im(r_{pp}^* r_{ss} + r_{ps}^* r_{sp}) & re(r_{pp}^* r_{ss} - r_{ps}^* r_{sp}) \end{bmatrix} \right\rangle, \quad (4.1)$$

By writing $\mathbf{M}$ has a 2×2 block matrix, $\mathbf{M} = \begin{bmatrix} \mathbf{M}_1^{(2\times2)} & \mathbf{M}_2^{(2\times2)} \\ \mathbf{M}_3^{(2\times2)} & \mathbf{M}_4^{(2\times2)} \end{bmatrix}$, one can easily see that in the case of a symmetric structure, we have the following relationships between the elements of the off-diagonal blocks $\mathbf{M}_2^{(2\times2)}$ and $\mathbf{M}_3^{(2\times2)}$

$$\mathbf{M}_2^{(2\times2)}(i) \pm \mathbf{M}_3^{(2\times2)}(i) = 0 \quad \text{with } i \in [1,4], \text{ and the sign depending on i} \quad (4.2)$$

In the regime of small overlays, there is a linear relationship between the elements of the off-diagonal blocks and the overlay ∇ [96, 97, 99, 100, 101].

$$\mathbf{M}_2^{(2\times2)}(i) \pm \mathbf{M}_3^{(2\times2)}(i) = C_i \cdot \nabla \quad \text{with } i \in [1,4], C_i \text{ a constant} \quad (4.3)$$

It has been shown that the choice of proper azimuthal configuration for the measurements with spectroscopic polarimetry is extremely important for the overlay characterization [96, 99]. Given that our apparatus gives an angular signature, we can also exploit the fundamental symmetries of the grating to enhance our knowledge of its angle-resolved signature. The sign of the off-diagonal blocks changes when the azimuth φ is changed into $-\varphi$. If the profile is symmetric, the signature is invariant when $\varphi \to \varphi + 180°$ and for the special case of $\varphi = 90°$ the previous two conditions can only be fulfilled if the off-diagonal blocks are zero. A rupture of symmetry in the structure will violate the above conditions and the off-diagonal blocks will take non-zero values for $\varphi = 90°$. Moreover, given that these blocks change sign upon a mirror symmetry,

the information about the sign of the overlay can be unambiguously extracted. In order to decrease the experimental artifacts due to noise, the information at φ should be compared to $-\varphi$.

4.3.2 Simulation of structures of interest

The simulation method used for our purpose is inspired by the work of Novikova *et al.* [99] but we replaced the spectral Mueller polarimetry for the sample characterization by the angle-resolved Mueller polarimetry. The main difference is that with the measurements in the Fourier space we measure all the angles at once at one fixed wavelength whereas with spectral Mueller polarimetry the entire spectrum is measured at fixed angle of incidence and azimuthal angle. We defined for the simulations the periodic structure with the pitch $\Lambda = 1000nm$ and filling factor of 0.5 (see fig. 4.8). We simulated the same structure with overlay ranging from 0 to 25nm.

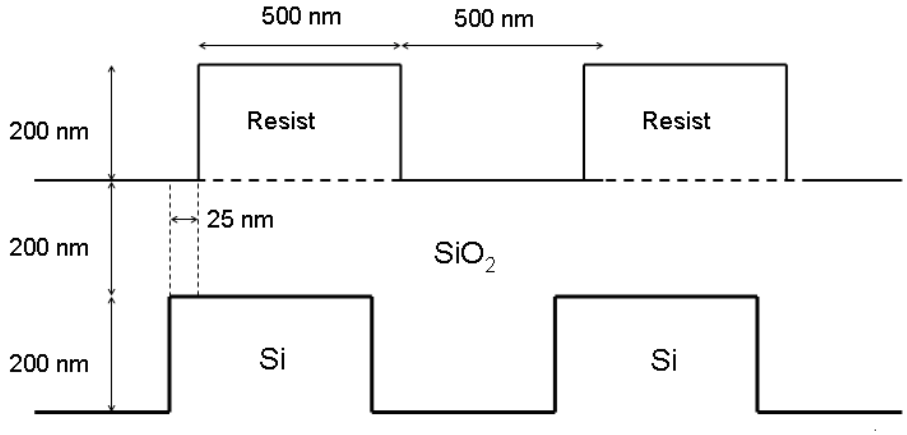

Figure 4.8: Simulated 1D periodic structure for the overlay characterization. Overlay: 25nm

RCWA simulations

This section is dedicated to a brief description of the most widely used digital method to solve the problem of direct diffraction and commonly referred to by its acronym RCWA (for *Rigourous Coupled Wave Analysis*) [102, 103, 104, 105, 106, 107]. This method was used for the interpretation of all polarimetric measurements on gratings carried out in LPICM, from CD metrology [41] to the work presented here, using codes developed in the laboratory by Tatiana Novikova first and then by Martin Foldyna.

We assume the grating to be invariant along y and periodic x (1D structure). Inside the structure, the complex permittivity ϵ_x and the field amplitudes are developed in Fourier series, whose coefficients are functions of z. This development transforms Maxwell's equations into a system of coupled differential equations, which can be directly solve by differential methods. In addition, these equations separate according to polarizations x and y if plane of incidence is in either of these two directions.

RCWA method, initially introduced by Knop [102] and Moharam and Gaylord [105] is a modal method perfectly adapted to the case of lamellar gratings. Indeed, in this case, the coefficients of the coupled equations are constant, and it suffices to diagonalize the matrix describing the coupling to find the natural modes of propagation, which

are a superposition of the incident wave and diffracted waves, propagating without distortion, with just a phase shift and attenuation.

However, in practice this diagonalization presupposes a truncation of the Fourier basis, corresponding to a physical limitation to a given value N of the total number of waves (propagating and evanescent) taken into account in the calculation. The method only converges to the exact solution when N tends to infinity, and this convergence is much slower for the TM mode (polarization p) than for the TE mode (s polarization). This problem was solved by Lalanne and Morris [103, 104] with a modification of the rule of multiplication of functions developed in Fourier series (here the permittivity and electric field).

Figure 4.9: Slicing of a one-dimensional grating, invariant following y in a superposition of lamellar gratings.

If we now want to calculate the optical response of a grating of any a priori form (but preferably reasonably close to a lamellar network), we can consider the structure as a superposition of M lamellar gratings approaching the real profile with a "staircase structure" as shown in fig. 4.9.We then need to solve the problem for each lamellar grating, then connect the solutions by the right continuity conditions at the interfaces.

4.3.3 Definition of the criteria for the overlay characterization

It is possible to determine the direction of the resist grating displacement with respect to the Si grating. To highlight these effects we simulated the Mueller matrix M of the structure depicted in fig. 4.8. We computed then the difference $\mathbf{E} = |\mathbf{M}| - |\mathbf{M}|^t$ where the superscript t denotes the transposed matrix. The grating is oriented and aligned along the y-axis (vertical axis on the figure), the displacement is along the x-axis. The resulting matrix is shown in fig. 4.10.

The elements of this matrix can reach the value of 0.25 (m_{14} and m_{41}), ie 1/8 of the total scale for a 25 nm overlay (however, as we will see in the following of this chapter, the slope of the estimator versus the overlay highly depends on the structure profile). In [96], the authors showed that their estimator (based on m_{13} and m_{31}) was linear with the overlay error up to $\pm$ 15nm. Linearity curve of this estimator calculated for the structures with different overlays can be found in fig. 4.11. The linear regression is excellent and these results can be extended to negative overlays, the sign of the estimator becoming negative. So we can expect that the overlay errors can be accurately determined provided that we are able to design an apparatus with small enough errors. For this particular case, an error of 1% of an element of the matrix is associated to a 1nm overlay. Another important feature is highlighted by this simulation: only some incidence angles are sensitive to the x-overlay. We can see that the response for the x-overlay is mainly located in the octants located near the y-axis. The limitation on the location of the response enables us to decouple the overlay in x and y directions; the last one should appear in the octants located near the x-axis. Thus we may suggest a new way to measure overlay by analyzing the location of the maximal response

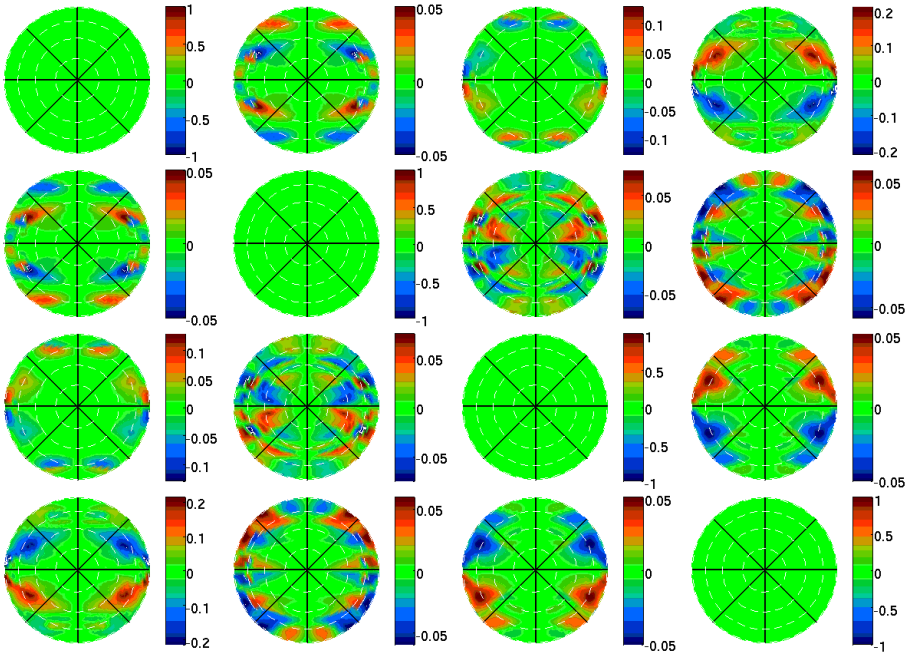

Figure 4.10: Difference for the simulated structure (see fig. 4.8) displayed in (s,p) axis. All elements m_{ij} (i,j $\neq 1$) are normalized by m_{11}, consequently $0 < |m_{ij}| < 1$.

of the estimator and thus obtain the orientation of the overlay directly from only one measurement. This possibility has not been investigated yet.

One of the drawbacks of this estimator is that it clearly suppresses the signal at the configuration where it should be more sensitive, namely, along the grooves of the grating. As it is specified in [99] and highlighted previously, when the plane of incident light is parallel to the grooves, the off-diagonal elements of the matrix should vanish if the profile is symmetrical while they will take non-zero value otherwise.

We have $m(\varphi) = m(\varphi + \pi)$ for the symmetrical grating profile and the off-diagonal 2×2 blocks are anti-symmetrical. So we can define another estimator for the overlay measurements as $m_{ij}(\varphi) - m_{ij}(\varphi + 180°)$. The values of this estimator are shown in fig. 4.12.

The second estimator seems to give better results, as the elements of this matrix can reach the value of 0.5 (m_{14} and m_{41}) for a 25 nm overlay. But given the uncertainty in our measurements it could be difficult to find the image pixel corresponding to azimuthal angle $\varphi + 180°$. Since even a small error in the estimator calculation could generate the important artifacts in the overlay images, we have decided to use the first estimator $\mathbf{E} = |\mathbf{M}| - |\mathbf{M}|^t$. No experimental validation of the second estimator has been carried out up to this date.

The second step of the definition of our estimator is to be able to extract a scalar value to characterize the overlay. We focus on the m_{14} and m_{41} elements of the Mueller matrix for several reasons: they show the best sensitivity to the overlay defects and they are not mixed with the objective contribution given that the objective is circular-dichroism free. If we only focus on these two elements, we don't even need to characterize the objective and we don't need to subtract its contribution to our measurements. We now have a 512×512 image, we call it the image estimator, representing $E_{14} = |m_{14}| - |m_{41}|$. The use of the E_{14} estimator enables us to use both (s,p) and (x,y) axis matrices given that the m_{14} and m_{41} are invariant by this transformation.

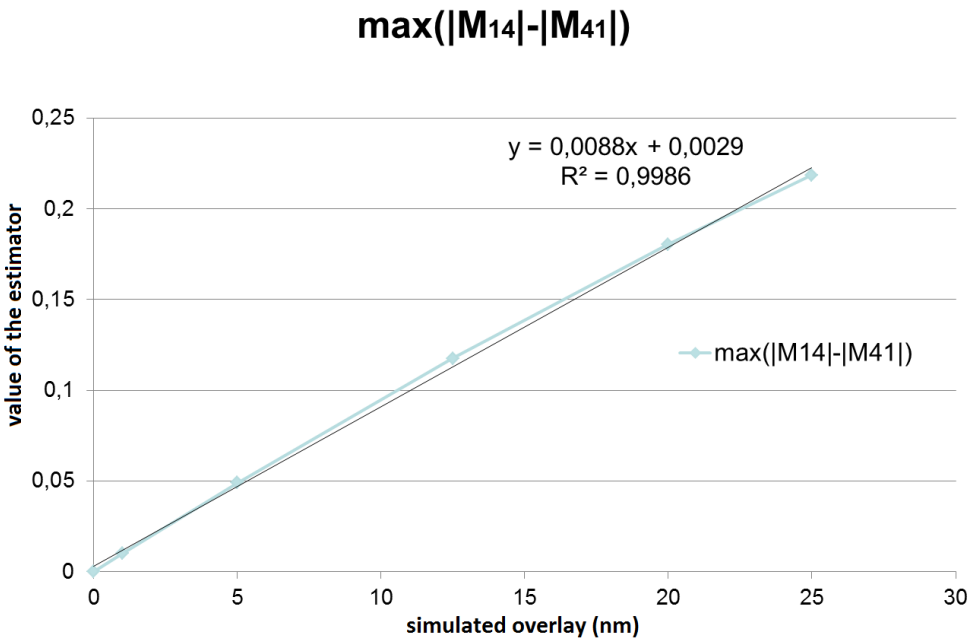

Figure 4.11: Scalar estimator calculated for the simulated structures with different overlays.

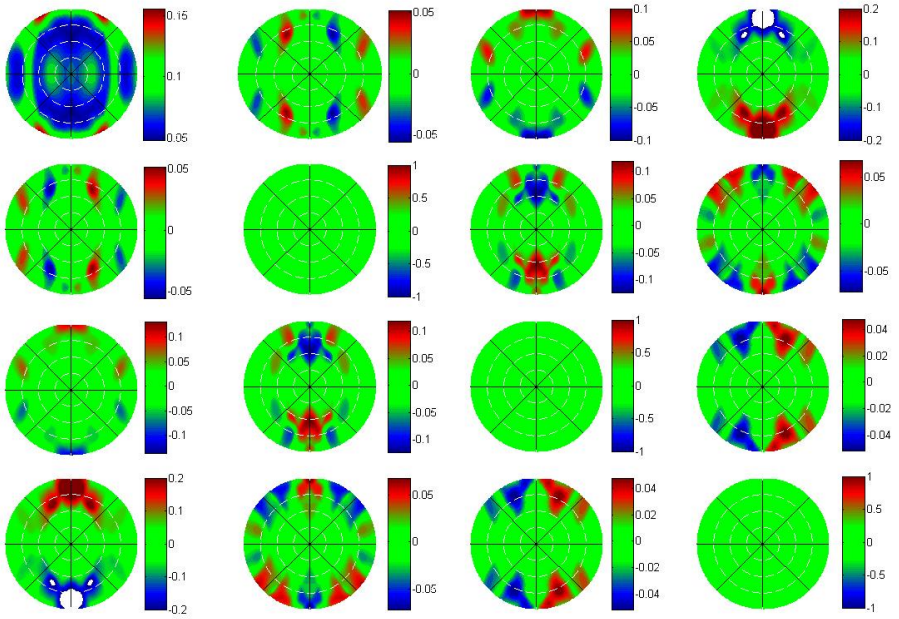

Figure 4.12: Difference $m_{ij}(\varphi) - m_{ij}(\varphi + 180°)$ for the simulated structure (see fig. 4.8) displayed in (s,p) axis. The scale is defined to match the one in fig.4.10 so pixels out of scale appear white.

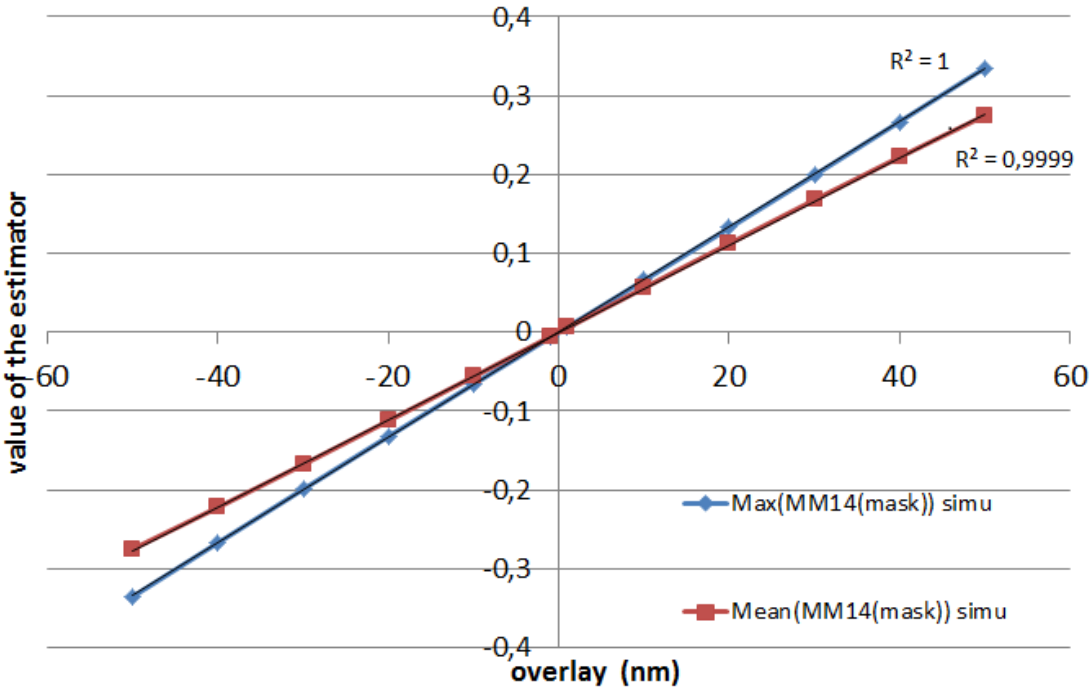

Figure 4.13: Effect of the chosen statistic on the estimator. We show here only two statistics: mean and max.

We select in this image the region of interest (ROI) by defining a mask (manual selection). This mask should only contain pixels belonging to the zero order and we try to select the region around the maximum. The figure 4.13 shows the difference between two statistics applied to the same mask of a simulated structure. We can see that the slope is slightly different, the max gives higher value. However, it is impossible to use the maximum for our experimental estimator due to the noise which alter it. The estimator on the ROI is averaged and attributed to the scalar estimator E. Several other statistics including standard deviation, median, different percentiles and linear combinations of percentiles have also be investigated but none of them combines the same robustness and sensitivity as the mean. Figure 4.14 summarizes all the processing steps to extract the scalar estimator E from the Mueller matrix **M**.

4.4 Validation of the estimator and description of the test structures

4.4.1 Validation of the estimator on real samples

Before using our estimator on structures specially designed for the metrology of overlay, we validated it on real samples. In the following of this manuscript, we will use the notation ∇ for the overlay.

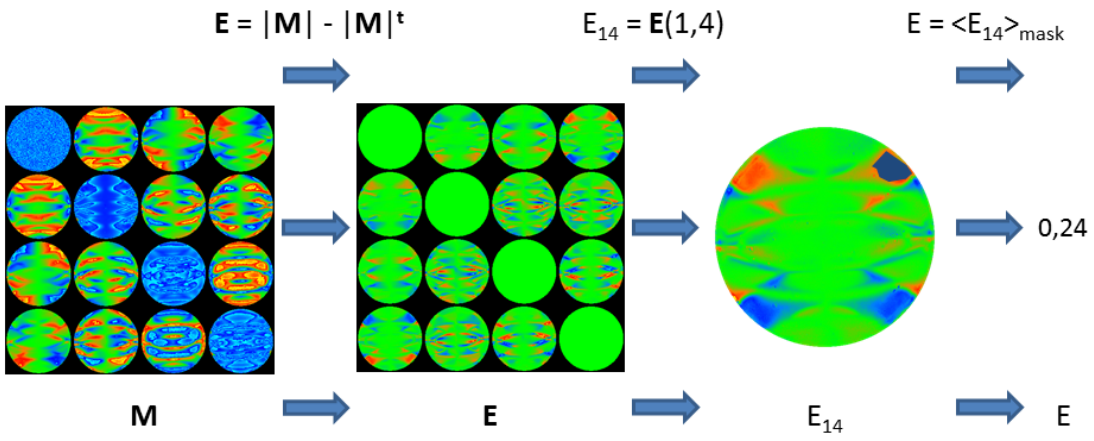

Figure 4.14: Processing steps to extract the scalar estimator E from the Mueller matrix **M**

Isotropic samples

The first two samples we tested were isotropic samples namely a crystalline silicon wafer and a 89nm layer of silica on a c-Si substrate. These samples are the same used for the calibration of the objective or the calibration of the reflectivity. Their matrices are well-known and the samples being isotropic, the image estimator and the scalar estimator should be both equal to zero. The results obtained are displayed in fig. 4.15 and 4.16. Because the samples are isotropic and thus should have a zero estimator on the whole pupil, the selected ROI is the complete pupil.

Both scalar estimator are very close to zero and the remaining error is due to the noise (up to 0.02 on each element). However, averaging on the ROI decreases the errors on the scalar estimator. By measuring these isotropic samples, we confirm that our estimator has a null bias and thus a non zero value of the estimator directly reflect a rupture of symmetry in the structure.

Symmetric and asymmetric gratings

This estimator is meant to be used for gratings. As seen in [97], the asymmetry of the structure profile also affects the value of the estimator. We compare the estimators obtained for two types of gratings: resist gratings whose profiles are supposed to be symmetric and a blazed grating whose profile is by definition asymmetric. The pitches of the resist gratings are chosen so they are around the pitch of the blazed grating and then are easily comparable. The estimator is only defined for the zero order so we crop the images in order to keep only the zero order visible.

The asymmetry of the blazed grating profile can easily be spotted in the image estimator. The resist grating profiles are symmetric as we can see by the very small value of their estimators. We must nevertheless be careful because we limit the aperture and the azimuths of the collection angles by cropping the images so only the zero order is displayed. We could correct this by using a sliding aperture in the Fourier space whose size is well adjusted with respect to the angular distance between the diffraction orders, the full zero order of the grating can then be reconstructed.

We experimentally showed that this estimator has a null bias for the asymmetry and so that the selected estimator can be used for the characterization of gratings provided

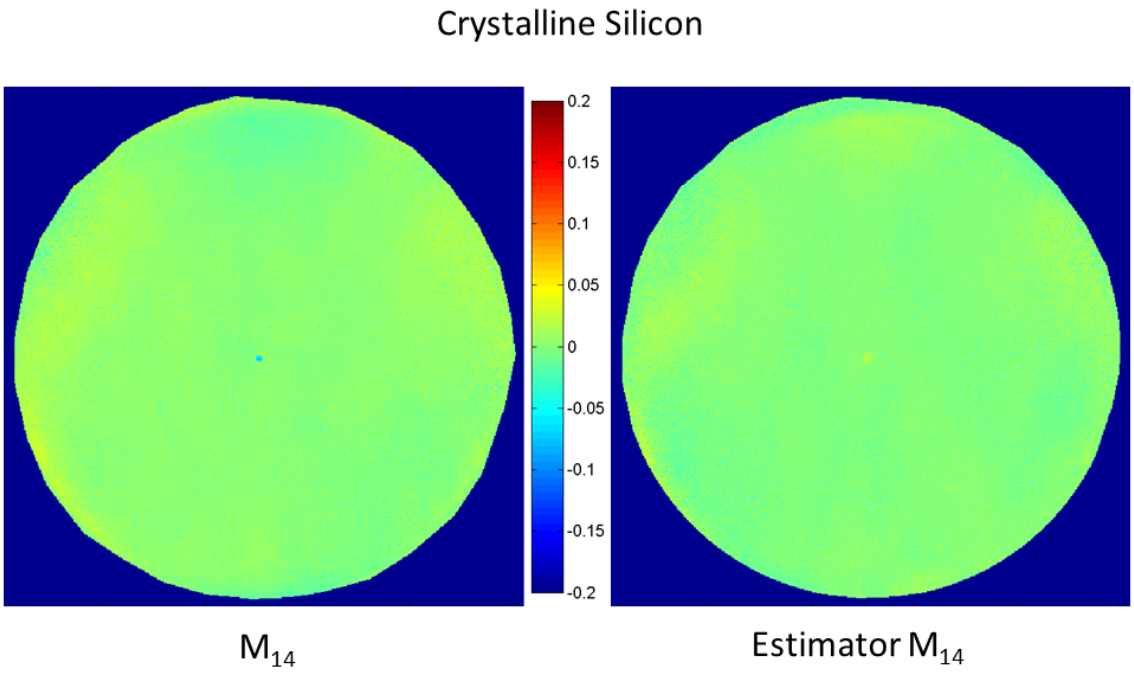

Figure 4.15: Left:m_{14} Mueller matrix element. Right: Image estimator. Scalar estimator E = 0.001

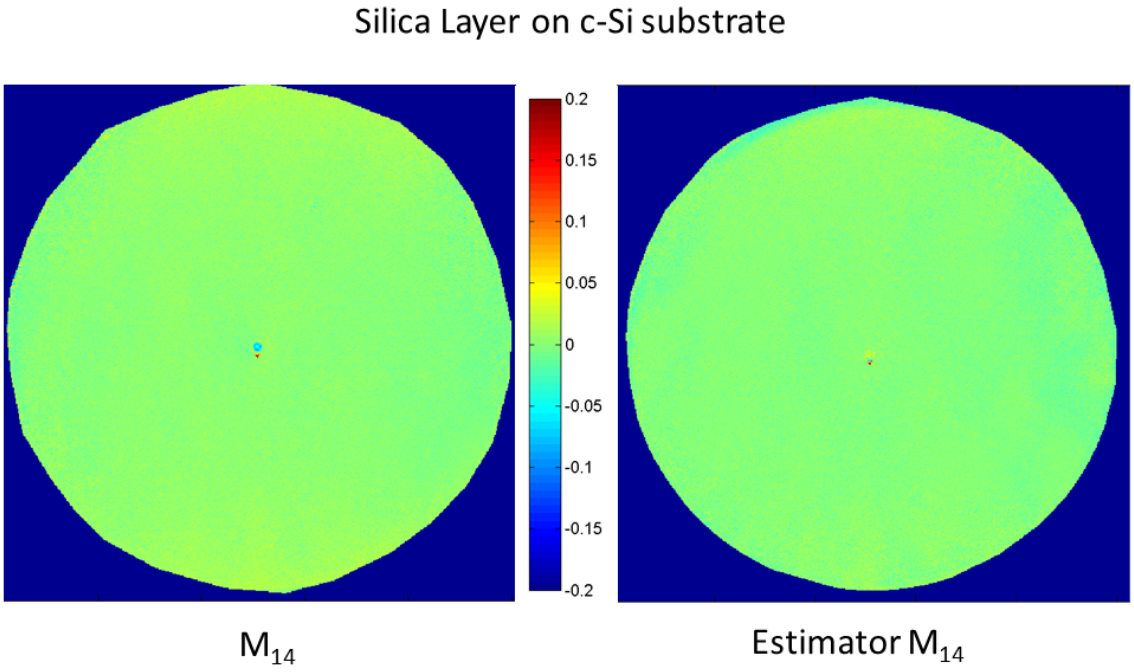

Figure 4.16: Left: m_{14} Mueller matrix element. Right: Image estimator. Scalar estimator E = 0.0035

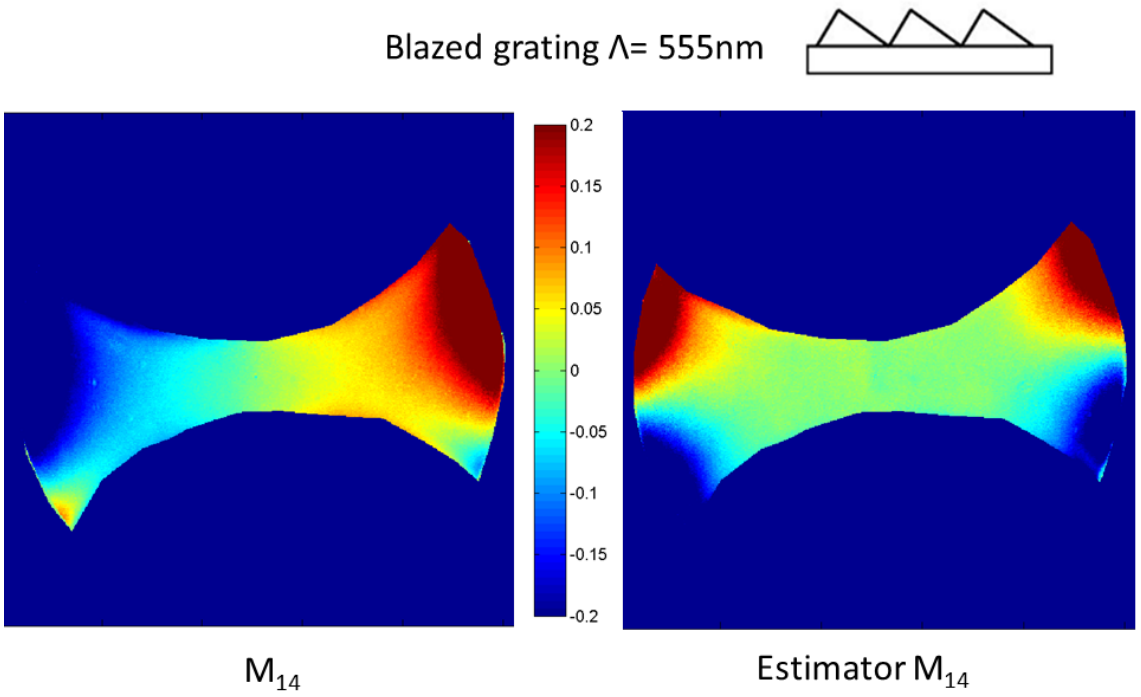

Figure 4.17: Left: m_{14} Mueller matrix element. Right: Image estimator. Scalar estimator E = 0.2578

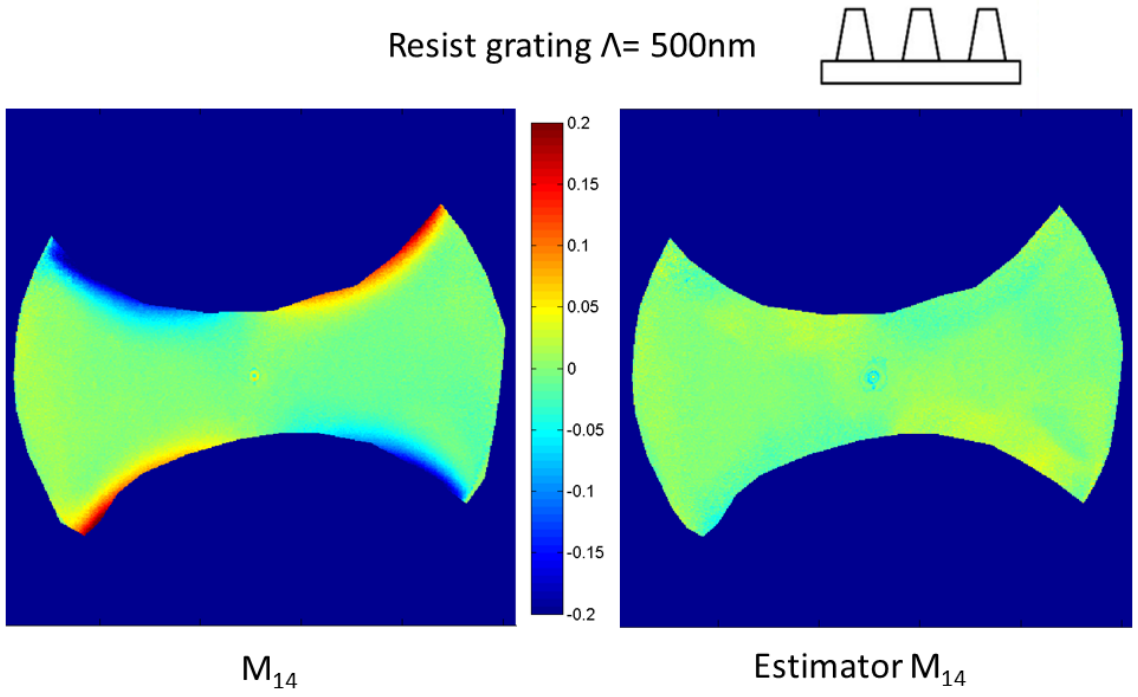

Figure 4.18: Left: m_{14} Mueller matrix element. Right: Image estimator. Scalar estimator E = 0.0127

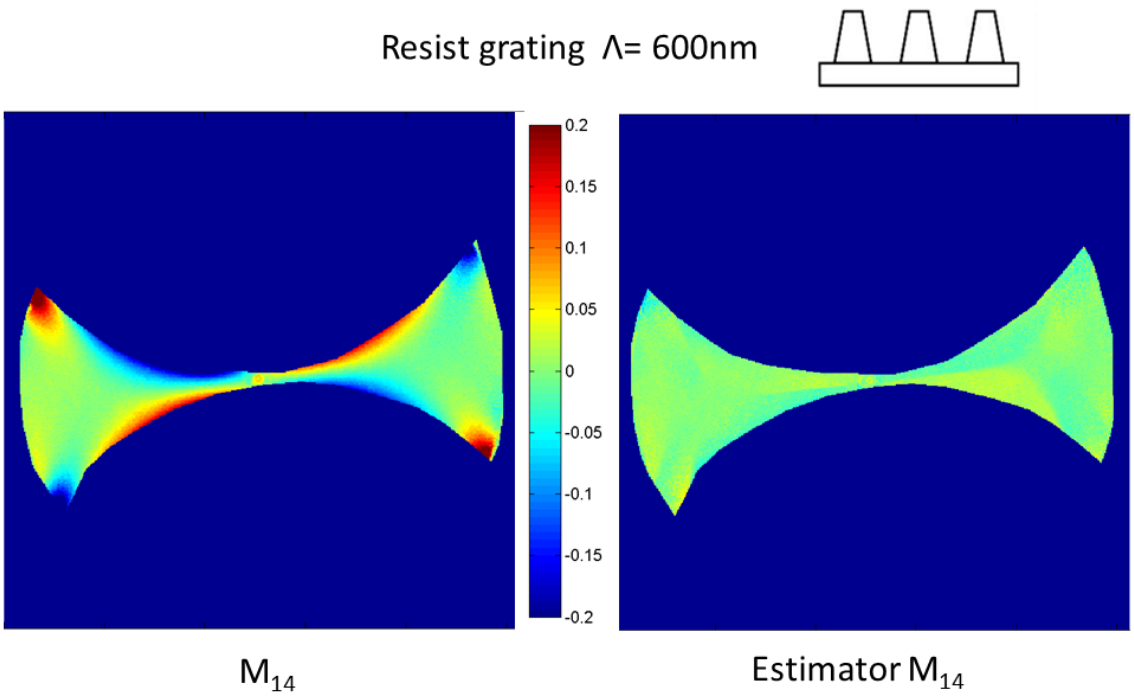

Figure 4.19: Left: m_{14} Mueller matrix element. Right: Image estimator. Scalar estimator E = -0.0014

that the profile is symmetric and that only the zero order of diffraction is gathered by the microscope objective thus imposing a relationship between the measurement wavelength and the pitch of the measured grating to avoid the use of a sliding aperture. At the end of chapter 2, we defined the relationships between the aperture, the pitch of the grating and the positions of the orders of diffraction (see eq.2.43 and eq.2.44). From these two equations, we deduce that in order to only image the zero order of diffraction, the pitch of the grating must satisfy the following equation:

$$\Lambda \leq \frac{\lambda}{2 \cdot NA} \tag{4.4}$$

where:

- Λ is the pitch of the grating
- λ is the working wavelength
- NA is the working numerical aperture of the selected microscope objective

In our case, for a wavelength $\lambda = 633nm$ and a numerical aperture $NA = 0.9$, we find that the pitch of the grating can not exceed $\Lambda_{max} = 350nm$.

4.4.2 Description of the targets for overlay measurements

The test samples of superimposed gratings with intentional and controlled overlay errors have been designed and manufactured at CEA/LETI (Grenoble, FRANCE), bottom (1st) level Si grating and top (2nd) level resist grating with common pitch of 400 nm are separated by a silicon nitride layer. The bottom grating is placed on top of SiO_2

	N mod	1	2	3	4	5	6	7	8	9	10	11	12
CD0	Level 2	150	150	200	200	200	250	250	250	300	300	300	300
	Level 1	250	300	100	200	300	100	200	300	100	150	200	250
CD1	Level 2	150	150	200	200	200	250	250	250	300	300	300	300
	Level 1	280	330	110	220	330	110	220	330	110	170	220	280
CD2	Level 2	170	170	220	220	220	280	280	280	330	330	330	330
	Level 1	250	300	100	200	300	100	200	300	100	150	200	250
CD3	Level 2	170	170	220	220	220	280	280	280	330	330	330	330
	Level 1	280	330	110	220	330	110	220	330	110	170	220	280
CD4	Level 2	150	150	200	200	200	250	250	250	300	300	300	300
	Level 1	220	270	90	180	270	90	180	270	90	130	180	220
CD5	Level 2	130	130	180	180	180	220	220	220	270	270	270	270
	Level 1	250	300	100	200	300	100	200	300	100	150	200	250
CD6	Level 2	130	130	180	180	180	220	220	220	270	270	270	270
	Level 1	220	270	90	180	270	90	180	270	90	130	180	220

Table 4.2: Nominal values of CDs (nm) for different fabricated modules; level 1- Si grating, level 2 - resist grating.

layer on Si substrate (see fig. 4.20). The pitch of this structure is slighly higher than what we defined in eq.4.4 which means that we will gather a fraction of higher orders of diffraction (-1 and 1).

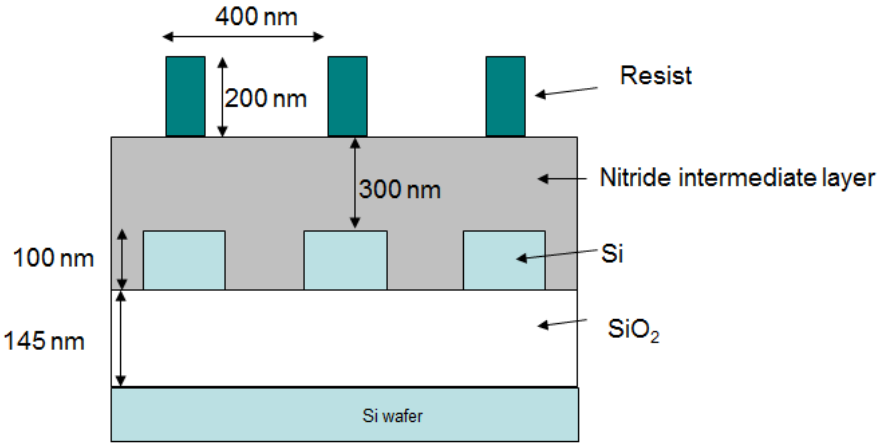

Figure 4.20: Cross section of the layer stack of the designed target for overlay measurement.

A large panel of critical dimensions (CD) for the top and bottom gratings have been investigated. The nominal values of CD are given in table 4.2.

Each test module includes 2 test structures whose cross sections have been presented in fig. 4.20. The test structures have perpendicular orientations with respect to each other so we measure x-overlay on the y-oriented structure and y-overlay on the x-oriented structure. AIM marks and other specific marks complete the reticule. A schematic of the reticule is shown in fig. 4.21 and an intensity image acquired with our device in real space is shown in fig. 4.22. The AIM marks are in red. For our purpose of overlay characterization, two test structures are actually engraved, one in a $20 \times 20 \mu m^2$ box and one in a $5 \times 5 \mu m^2$ box. In order to sufficiently decrease the room dedicated

to metrology on the wafer, if the results were good enough, only the $5 \times 5\mu m^2$ box could be engraved on the sample as the metrology target. However, due to the current limitations of our device, investigations were carried out using the $20 \times 20\mu m^2$.

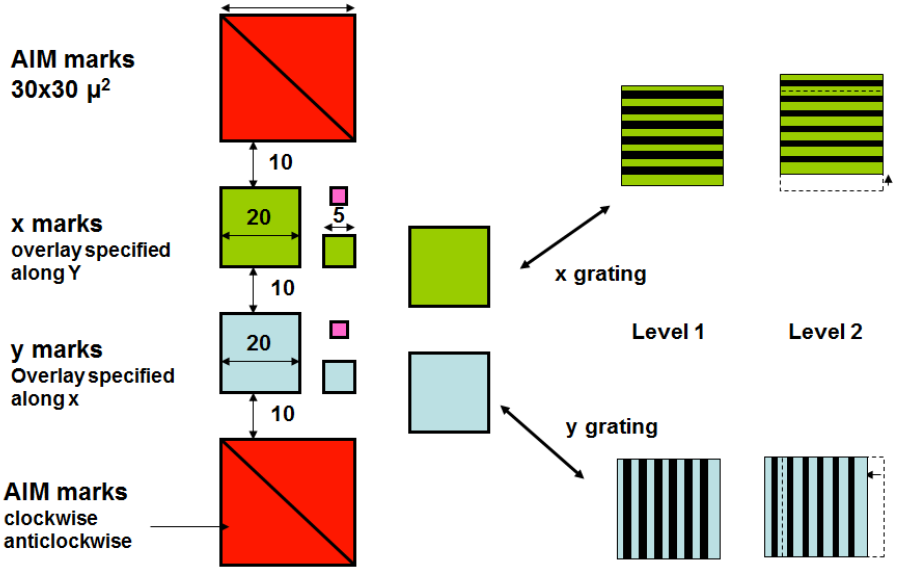

Figure 4.21: Schematic of the reticule. AIM: red. Mueller Polarimetry: blue (x-overlay) and green (y-overlay). All dimensions in μm

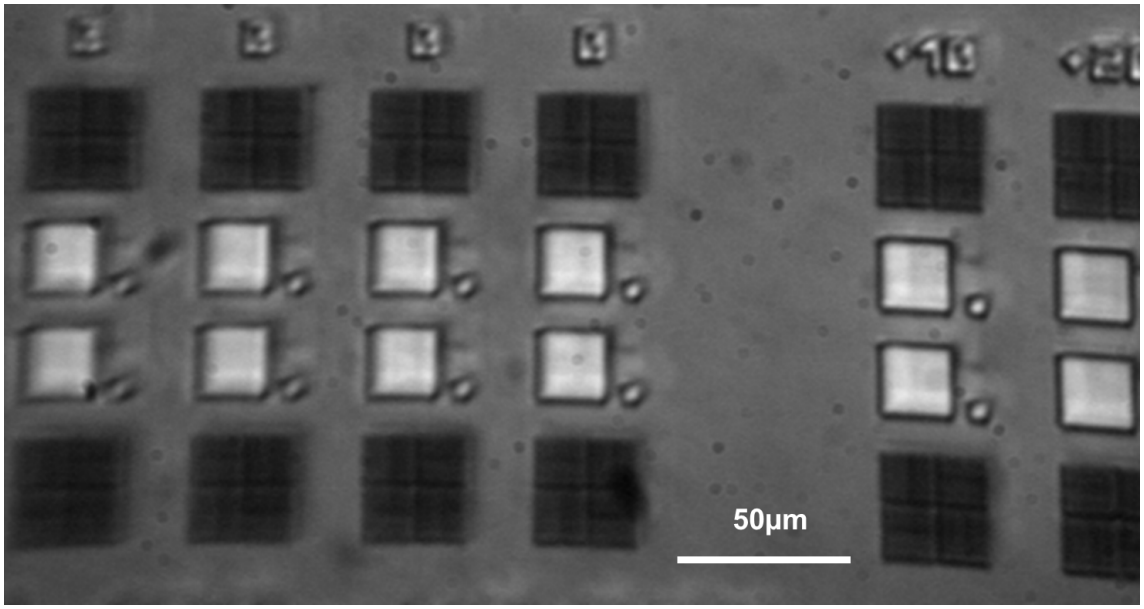

Figure 4.22: Real image of the wafer. Magnification: 5X.

Each test structure (see tab. 4.2) was fabricated with different nominal overlay values (0, $\pm$10, $\pm$20, $\pm$30, $\pm$40, $\pm$50, $\pm$100, $\pm$150nm). The structures with different nominal overlays are arranged row-wise whereas the variations in CD is column-wise. A schematic of the complete measurement module can be found in fig. 4.23.

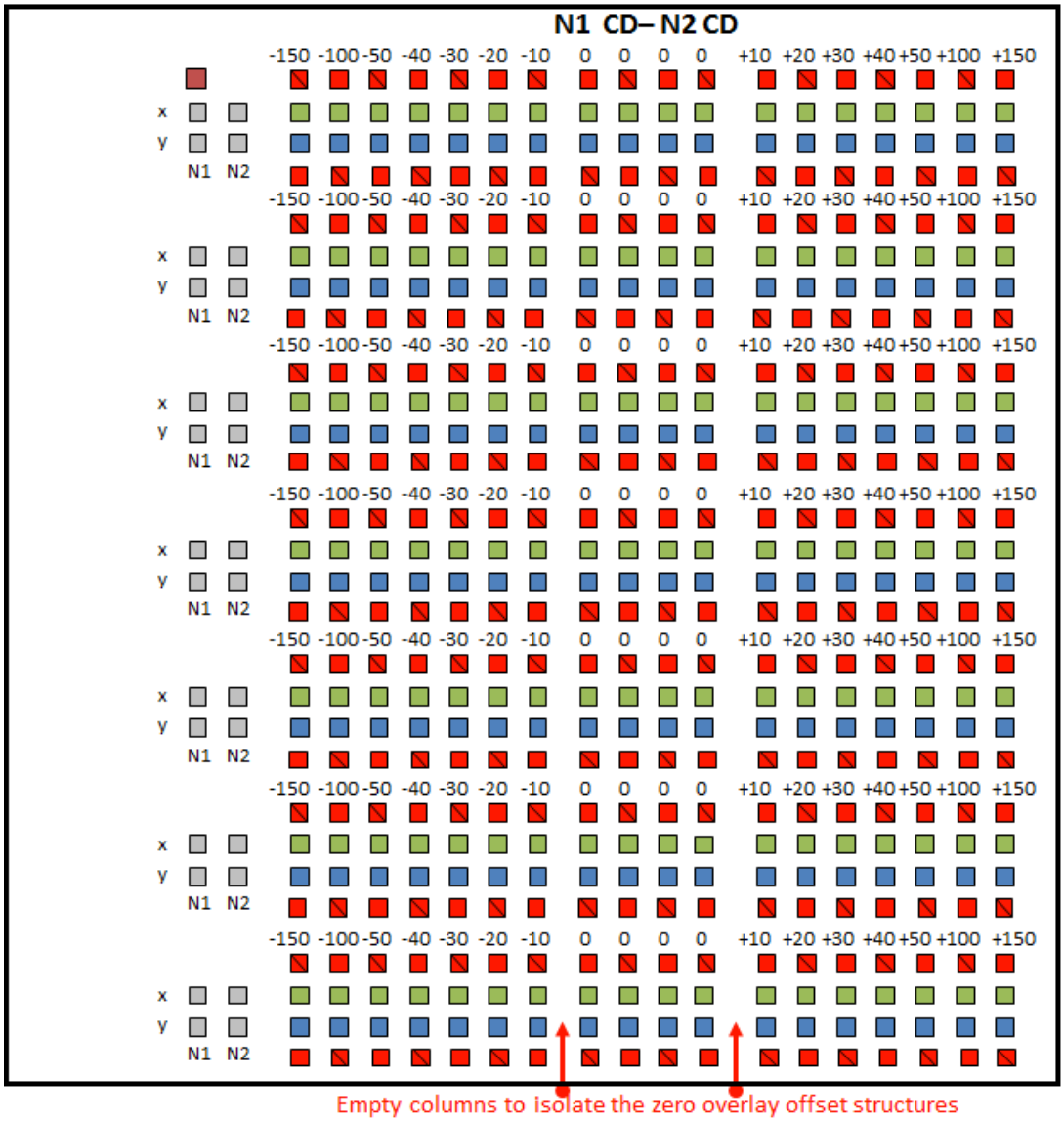

Figure 4.23: Schematic of a complete module. The values of the CDs can be found in tab. 4.2.

4.5 Validation of the linearity of the estimator on test structures

4.5.1 Experimental procedure

We use our Mueller polarimeter in the back focal plane for our inspection. The 200mm wafer specially designed by CEA-LETI with 12 modules in a field, repeated five times over the wafer is placed on a XYZ translation stage (see fig.**??**). The X and Y axis enable us to accurately position the spot in the measurement box (positioning precision around $1\mu m$). The Z axis is used for focusing purpose.

The ability of our device to acquire both angularly-resolved and spatially-resolved images enables a fine positioning of the sample and a visual control of the illuminated spot on the sample. The distance between two measurement boxes is $50\mu m$ along the

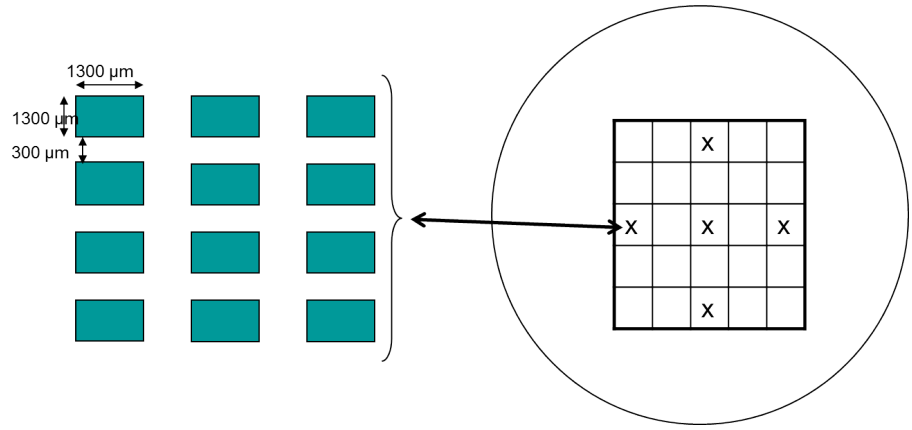

Figure 4.24: 12 modules in a field, repeated five times over the wafer on a 200mm silicon wafer.

x-axis and $100\mu m$ along the y-axis. The automatization of the measurements for a complete module has not been implemented due to lack of time and insufficient repeatability in the positioning on the stage of the sample itself. The positioning of the sample has been done manually for each measurement, thus ensuring that the measurements are done in the correct boxes.

If no other indication, the working wavelength is set at 633nm.

We carried out intensive measurement campaign of the test wafer. 12 modules are engraved on the wafer, each with seven different combinations of critical dimensions for the top and bottom layers thus grating us 84 different measurement lines to characterize the linearity of our estimator. We measured 19 lines, 10 were measured for both x and y-overlay whereas the 9 remaining were only measured for y-overlay.

The Mueller matrix, the matrix estimator and the image estimator for one of our measurements are summarized in fig. 4.25.

4.5.2 Use of AIM measurements

Each measurement box has also been measured using the KLA-TENCOR Archer 100 which has a total measurement uncertainty below 2nm [108]. We can thus compare the results obtained with AIM technique and our Mueller polarimetry technique. The results obtained with the Archer 100 are taken as the gold standard in the rest of this section; we will rely on them and regard them as "true" overlay. We will then distinguish between the AIM overlay ∇_{AIM} (Archer 100) and the nominal overlay (given on the wafer) ∇_{nom}. The measurement targets for Mueller polarimetry and AIM are sufficiently close to each other to safely assume that the overlay is the same for both targets.

We measured complete lines of x-oriented gratings with a specified overlay along the y-axis and plotted our estimator versus the overlay measured by AIM at CEA-LETI.

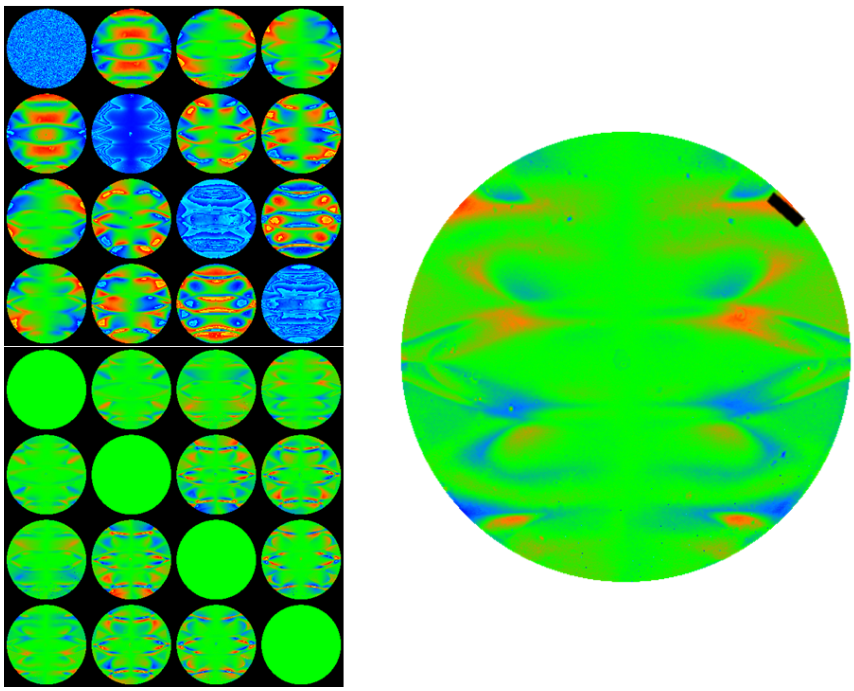

Figure 4.25: Measurement for the y-overlay box of module 7 N1 220 N2 280, Nominal overlay +50nm. Matrices are displayed in (x,y) axis. Top left: Mueller matrix measurement. Bottom left: matrix estimator. Right: Image estimator (MM14) with the manually selected mask for averaging in black

Overlay on the module 10

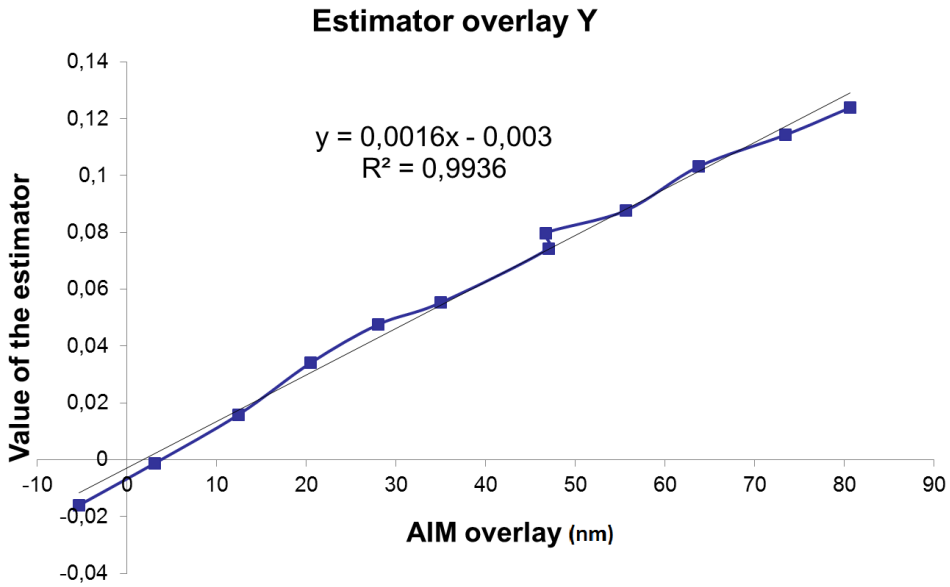

Figure 4.26: Linearity curve for y-overlay in module 10 N1 150 N2 300. Scalar estimator versus AIM overlay

These data confirm the excellent linearity of the estimator E versus the "true" (AIM) overlay. The linear relationship between these two quantities can be rewritten as:

$$E = S(\nabla_{AIM} - \nabla_0) \tag{4.5}$$

where the sensitivity factor S is equal to 0.0016 and the offset ∇_0 is as small as 2nm.

However, these values are lower than what is predicted by the simulations as seen in fig. 4.27. The sensitivity factor S is smaller for experimental data which hinders the precision of our measurements. The origins of this decrease in sensitivity with respect to simulations has yet not been explained.

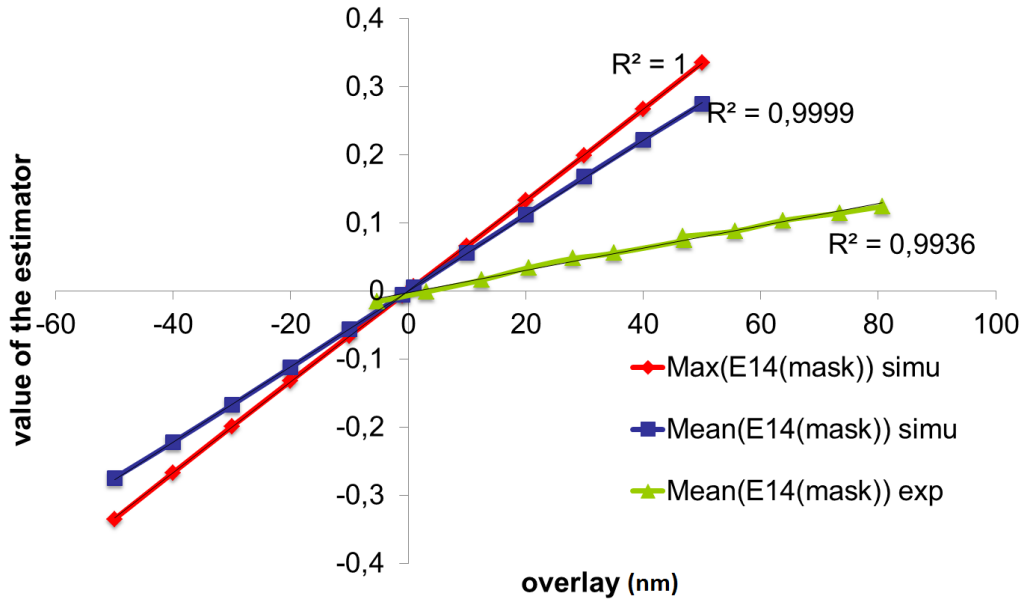

Figure 4.27: Comparison between simulations and experimental data for module 10 N1 150 N2 300.

The results presented for y-overlay can be generalized to x-overlay with the same linearity and small offsets as shown on the figures below.

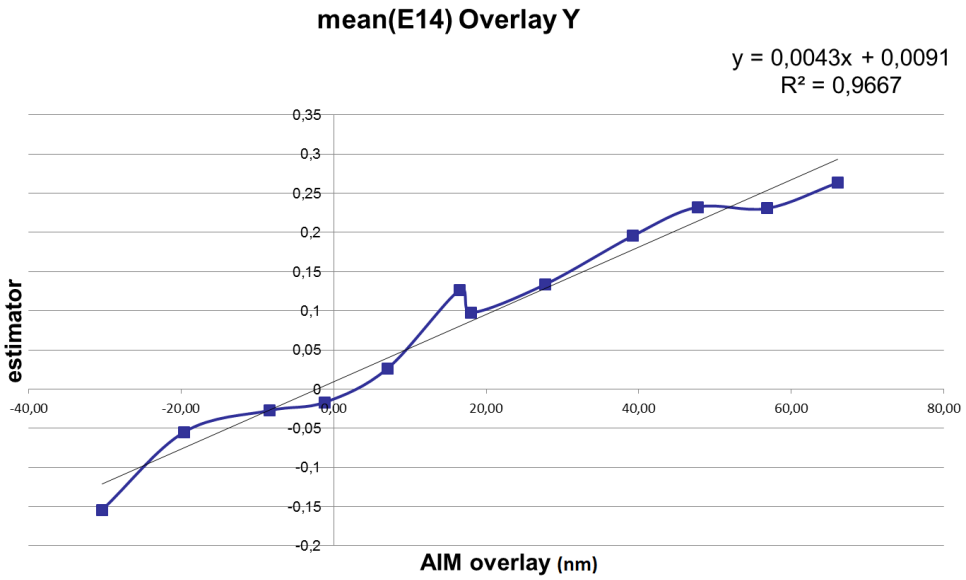

Figure 4.28: Linearity curve for y-overlay in module 10 N1 130 N2 300. Scalar estimator versus AIM overlay

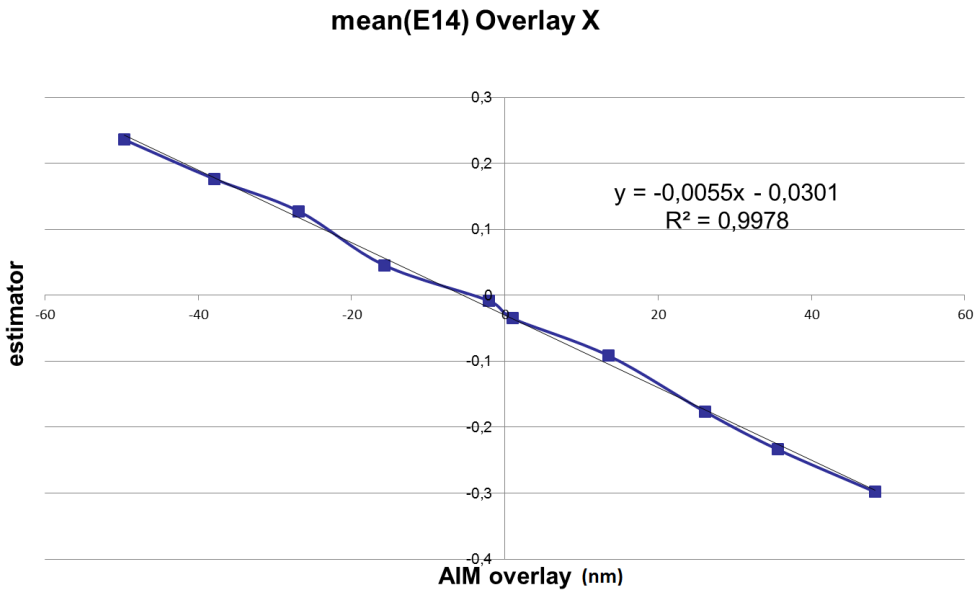

Figure 4.29: Linearity curve for x-overlay in module 10 N1 130 N2 300. Scalar estimator versus AIM overlay

Overlay on the module 1

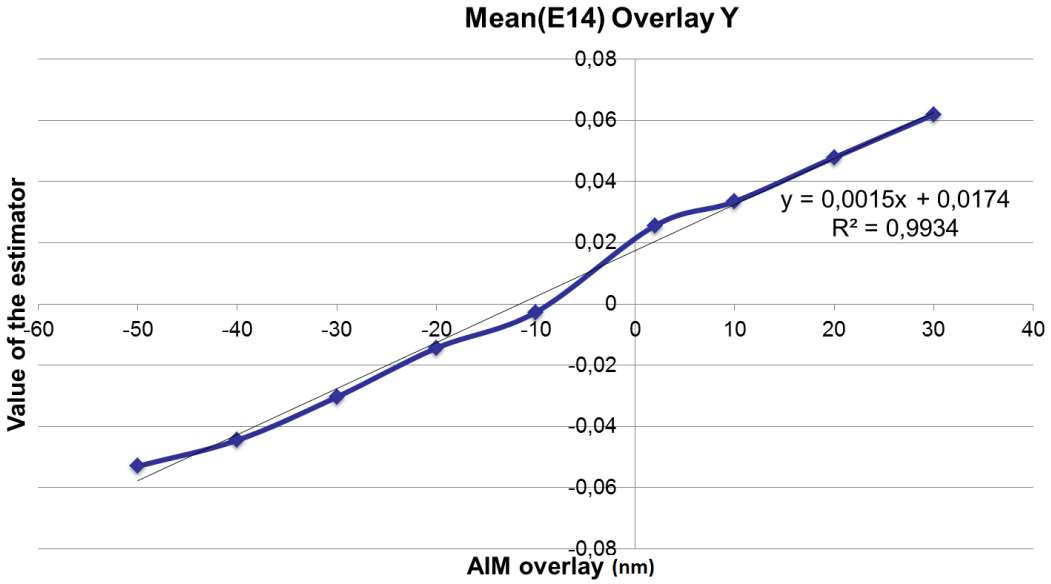

Figure 4.30: Linearity curve for y-overlay in module 1 N1 250 N2 130. Scalar estimator versus AIM overlay

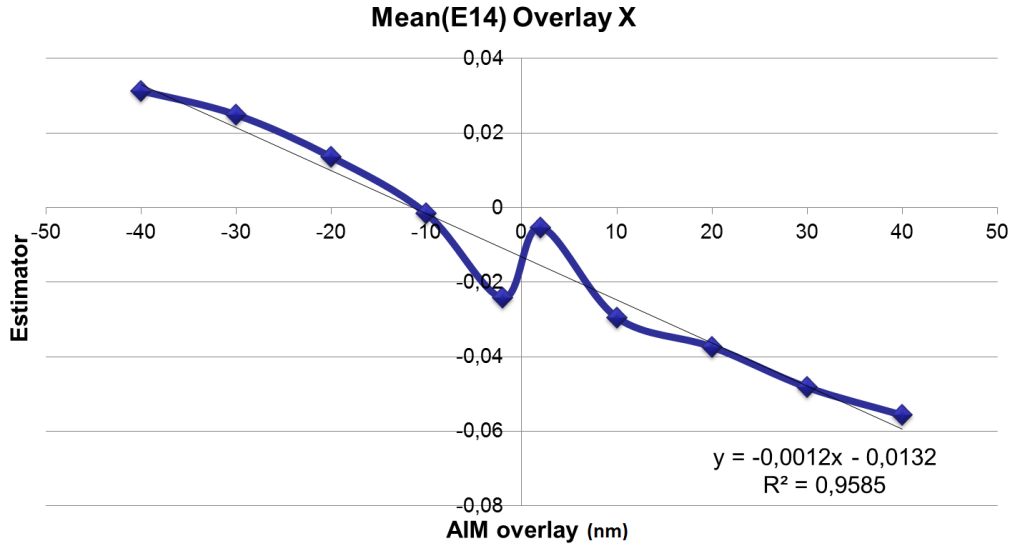

Figure 4.31: Linearity curve for x-overlay in module 1 N1 250 N2 130. Scalar estimator versus AIM overlay

4.5.3 Use of nominal overlays

Provided S is known, we can define the Mueller overlay ∇_M as:

$$\nabla_M = E/S \tag{4.6}$$

where E is the measured value of the estimator. Eq. 4.6 is thus derived from eq. 4.5 by neglecting the offset ∇_0, which is quite small and should be zero from first princi-

ples, as mentioned above. However, to experimentally determine S we need at least a pair of neighboring targets with accurately known different overlays. In practice, what is always available is the nominal overlay ∇_{nom}, as defined by the process. This nominal overlay may be rather different from the actual one, as shown below. As a result, at least two "gold standard" measurements are needed to determine S. Of course, to qualify our technique as a possible alternative to established techniques in real world, it is desirable to use as few AIM measurements as possible. As nominal overlays ∇_{nom} are always available, we now explore the link between theses nominal values and the AIM ones, to determine to what extent the nominal overlays ∇_{nom} can be used to determine S and then ∇_M.

Process characterization: nominal overlay versus AIM overlay

A typical plot of ∇_{nom} versus ∇_{AIM} obtained for module 9 (CD1 90 nm, CD2 300nm) is shown in fig. 4.32. This plot, which includes the data for ∇_{nom} between -50 nm and 50 nm, is almost linear, with a slope practically equal to 1 and an offset close to 20 nm. We can then conclude that the process is accurate for overlay variations, with however a large offset which is uncontrolled though constant, that we call excess overlay contribution ∇. Of course, if S is to be determined from two points only, then the best choice is obviously the two extreme points.

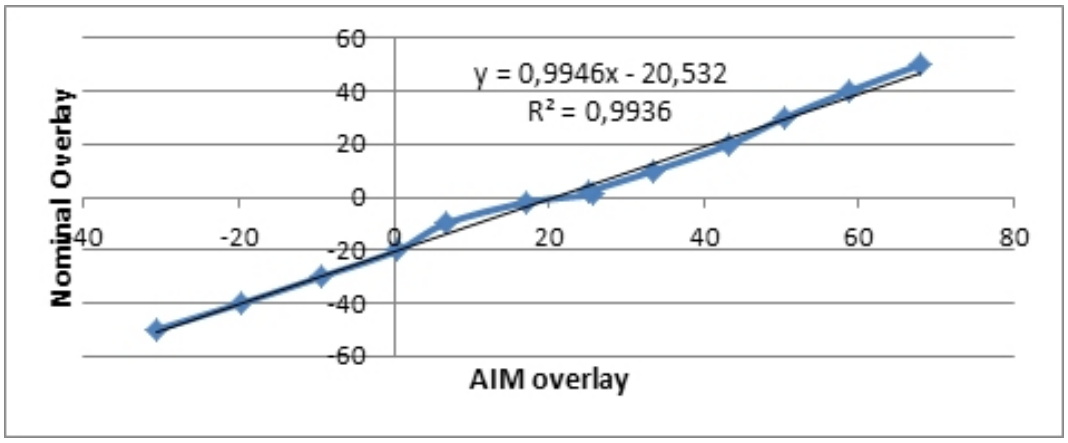

Figure 4.32: Correlation between AIM and nominal overlay values for module 9 (CD1 90 nm, CD2 300 nm)

4.5.4 Discussion

From the curves showed above, we can point out several important remarks. First, the linearity of the estimator on our test structures is confirmed by the plots for the "true" overlay. The correlation ratio is excellent and the offset is close to zero (a few nanometers at most). However, we notice that our estimator has a non-null value for the zero nominal overlay pad, indicating either an offset in our estimator or a process-based offset. The first option can be ruled out by the simulation and the second one is actually confirmed by the overlay data acquired by other techniques as shown by the plot for "true" overlay. The difference between the "true" overlay and the nominal overlay will be called the excess overlay. This is the overlay that matters the most because it is not controlled and is process-based. Measuring this excess will be the core of our method.

Second, as one can clearly see on the curves, the values of the estimator highly depends on the CDs of the different layers of the test structures. In the first case (module 10 N1 130 N2 300), the slope of the linearity curve is three times the one in the second case (module 10 N1 150 N2 300). This clearly indicates that the CDs really matter when designing the target for overlay metrology. The direct consequences of the smaller value in the second case is that the signal to noise ratio (SNR) is smaller (the noise is supposed to be constant). However, the linearity of the curve described by the correlation ratio (R^2) is still very good despite the smaller SNR. This trend is also confirmed by other measurement couples like in fig. 4.33.

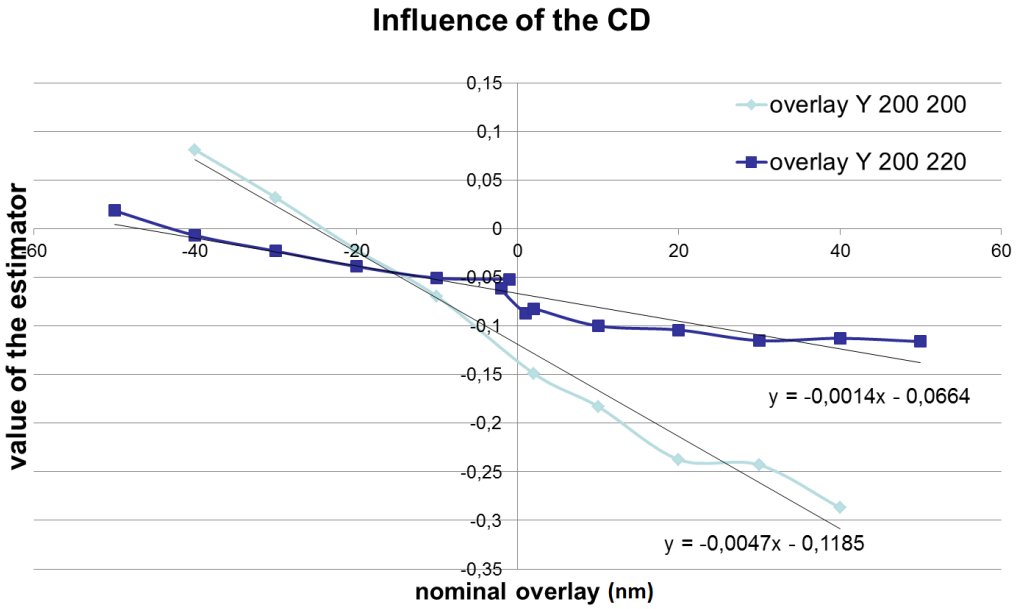

Figure 4.33: Influence of the CD on the slope of the estimator

We have proven in this section that our estimator is linear to the overlay in the regime of overlay up to 50nm in both directions. We showed that the slope of the curve highly depends on the CDs of the constitutive layers of the target but that the linearity remains excellent even for non-optimized structures.

4.6 Experimental characterization of the overlay

4.6.1 Comparison with AIM data

In [84], the authors introduced a formula to extract the excess overlay from two measurements with opposite misalignments d and $-d$. Assuming a linear response to the total overlay error,

$$E(-d) = S(-d + \nabla) \tag{4.7}$$

$$E(d) = S(d + \nabla) \tag{4.8}$$

where the sensitivity S is the same as that defined in eq. 4.5, because the slope of the plot of ∇_{nom} versus ∇_{AIM} is practically unity.

By simply adding or subtracting eq.4.7 and eq. 4.8

$$\begin{array}{ll} \text{(4.8) + (4.7):} & E(d) + E(-d) \propto 2\nabla \\ \text{(4.8) - (4.7):} & E(d) - E(-d) \propto 2d \end{array} \tag{4.9}$$

The excess overlay ∇ can then be found using the simple formula below:

$$\nabla = \frac{E(d) + E(-d)}{E(d) - E(-d)} \cdot d \tag{4.10}$$

and the sensitivity factor can also be recovered with this method by:

$$S = \frac{E(d) - E(-d)}{2d} \tag{4.11}$$

Of course, this method is only valid if the excess is the same for both d and $-d$ pads, a condition not always satisfied on our test structures. The clear advantage of this method is that it only requires two measurements points. For each measurement couple (d,-d), we compute the excess overlay ∇ according to eq.4.10 and add this value to the nominal overlay specified on the wafer. The corrected measurements will be referred to as 'Jie Li corrected' measurements.

This method could be very noise dependent because it only uses two measurement points. To reduce this noise we prefer to determine S and ∇ by using all available measurement points via a linear regression

$$\text{linear model: } E = S \cdot \nabla_{nominal} + E_0 \tag{4.12}$$

$$E_0 = S \cdot \nabla \tag{4.13}$$

The ∇_M being just linked to the nominal overlay by linear relationship, the correlation between ∇_M and ∇_{AIM} is the same as the correlation between ∇_{nom} and ∇_{AIM}, the only difference is the offset between them.

Figure 4.34 shows typical plots of the Mueller overlay ∇_M, determined with the value of S obtained by the linear regression and the Jie-Li corrected overlay versus the AIM gold standard. The Mueller overlay ∇_M again exhibits a very good linearity, with a slope very close to 1 and an offset as small as 2 nm. On the other hand, the 'Jie Li corrected' values are very close to the Mueller ones except for the central nominal overlays (-10 nm, 10 nm). These discrepancies are obviously due the smaller value of the 2d denominator in the expression of S when calculated from two points only and the difference in excess overlay: the deviations from linearity observed in the central region of the plot shown in fig. 4.32 are thus amplified with respect to the other ones.

However, some other modules have a quasi constant excess overlay ∇ like module 3. The result is a possible characterization for all the data included (-10,10) nominal overlays.

To assess the validity of our measurements on a broader scale, we compare a large number of measurement points with the standard AIM overlay measurements. We take the measurements from several modules and plot the correlation between the AIM overlay and our measured overlay for all these values (see figs. 4.36 and 4.37).

Both directions X and Y show a very good correlation with a slope very close to 1. However, we found an offset of nearly 1.5nm which should not be regarded as a limitation and a lack of accuracy of our device. As previously stated, there is no systematic

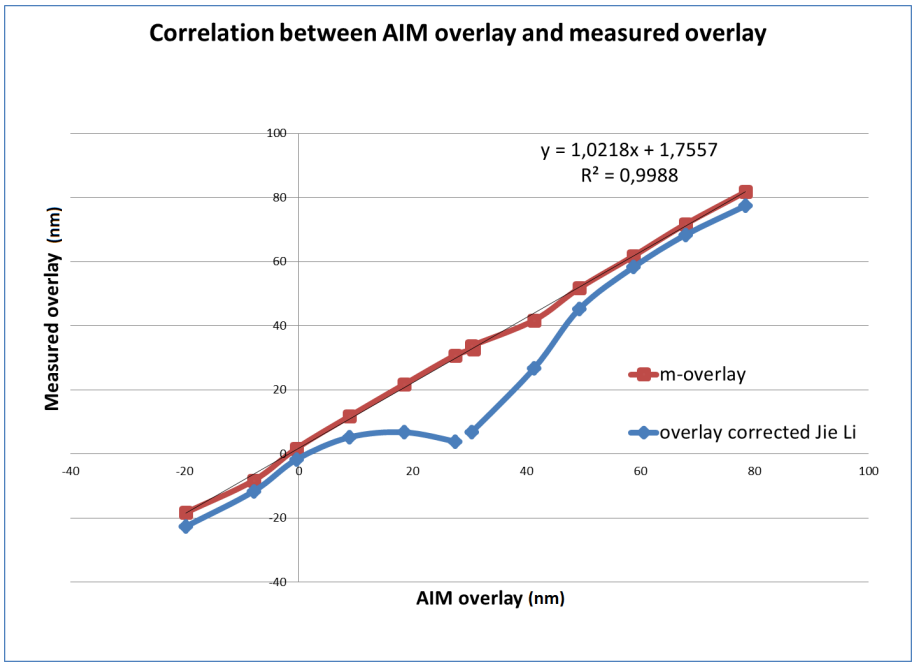

Figure 4.34: Module 10 N1 170 N2 300, Correlation between measured and AIM overlays

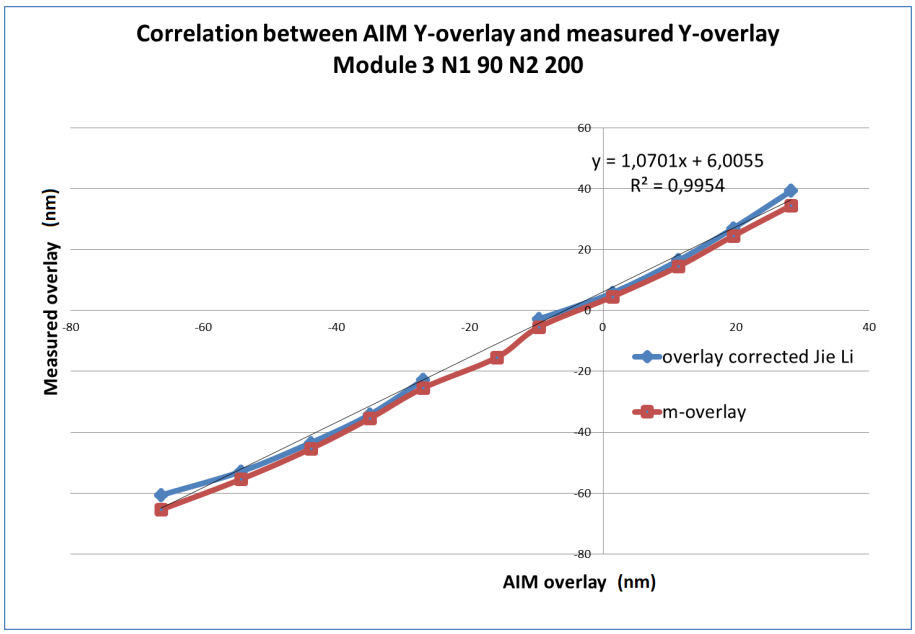

Figure 4.35: Module 3 N1 90 N2 200, Correlation between measured and AIM overlays

way to verify and compare the accuracy of overlay metrology. We have here made the assumption that overlays measured by AIM are the true overlay without considering the tool induced shift and the precision of the measurements carried out with AIM. The remaining error after the tool induced shift correction can be estimated by looking at the linearity curve we plotted in fig. 4.26 for example. We pointed that $\nabla_0 = 2nm$ which is approximately the value of our offset as well. Given the lack of a gold standard for overlay, it is very complicated to compare two different methods: here, we can only notice that the two measurement methods have an excellent correlation and a very small offset.

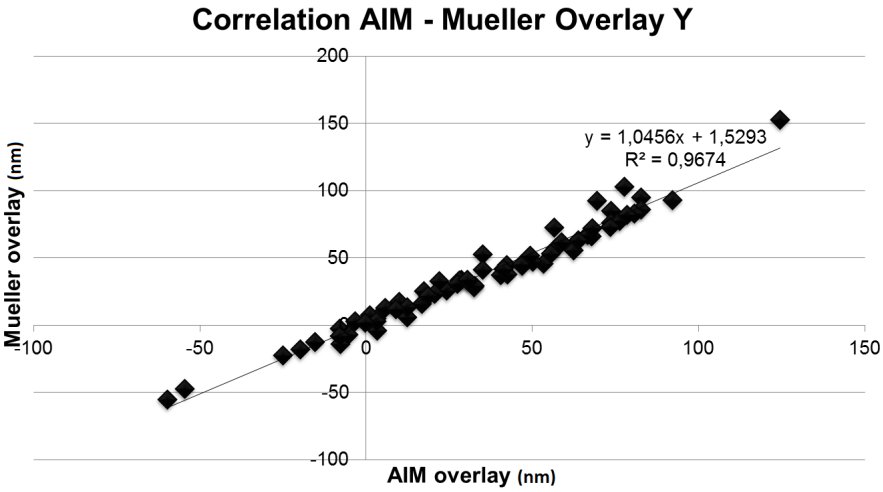

Figure 4.36: Correlation between measured and AIM Y-overlay for 6 modules.

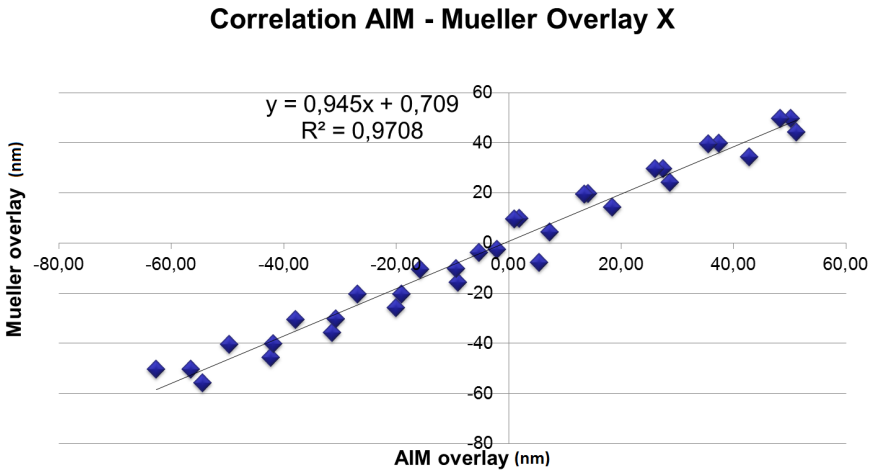

Figure 4.37: Correlation between measured and AIM X-overlay for 3 modules.

4.6.2 Map of the overlay over a complete field

As we have stated at the beginning of this chapter, the overlay error is not constant on the wafer, we have to measure a large number of targets to get an idea of the spatial distribution of the overlay error. We have access to 12 modules spread out in a field (see fig.4.24). Each module (except module 11) has been measured, some have even been measured several times, the final overlay being the average of the overlay measured for each line of this module. Table 4.3 gives the number of times each module has been measured.

Module Id	1	2	3	4	5	6	7	8	9	10	11	12
Number of lines measured	1	1	1	1	1	1	4	2	2	3	0	2

Table 4.3: Repartition of the measurements on the Mueller Fourier targets

Modules 1,2,4,5,6,7,8,10 and 12 have been measured for both x and y-overlays. We are then able to measure the overlay vector . Modules 3,and 9 have only been measured

for y-overlay. Only the overlay error along this direction will be included.

We plot the overlay vector on a map of the modules. The result is a map of the overlay error over a complete field (see fig. 4.38). The scale is the same for all the overlay errors so results can be compared for different modules.

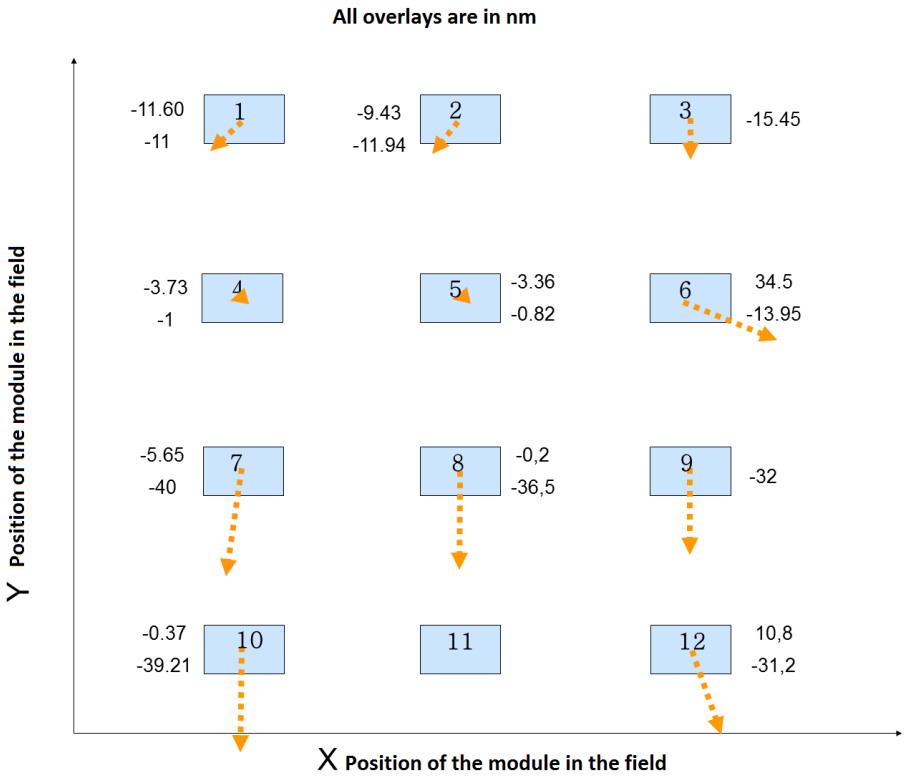

Figure 4.38: Map of the overlay vector on a complete field. Only y-overlay is available for some modules.

The results seem consistent, with all vectors pointing down which means that the overlay error always has the same sign along the y direction. Two modules are found to have very small overlay errors (module 4 and 5). Modules 6 and 12 have a different sign on their x component which is consistent with a zero overlay error for module 5.

4.6.3 Measure of the quality of the overlay measurements

The standard measure of system quality is the Total Measurement Uncertainty (TMU) defined as [82, 109]:

$$TMU = \sqrt{(TIS^2 + \sigma_{TIS}^2 + \sigma_{meas}^2 + \sigma_{match}^2)} \tag{4.14}$$

where

- TIS is the average Tool Induced Shift
- σ_{TIS} is the variation of the Tool Induced Shift (TIS).
- σ_{meas} is the measurement precision.

Design Rule (DRAM half-pitch)	45nm	36nm
Overlay specification	9.0nm	7.1nm
Expected TMU (10% of specification)	0.9nm	0.7nmn
On-product TMU	2.1nm	1nm

Table 4.4: Lithography technology requirements from ITRS 2008 and expected TMU. Table from [109]

- σ_{match} is the site-by-site variation in tool-to-tool matching (not measurable in our case).

The corrected formula for the TMU is then:

$$TMU = \sqrt{(TIS^2 + \sigma_{TIS}^2 + \sigma_{meas}^2)} \tag{4.15}$$

Table. 4.4 from [109] gives the TMU required by ITRS 2008 (not up to date).

Precision

The typical error on a pixel of the Mueller matrix measurement can be modeled by a gaussian noise with a null mean and a standard deviation $\sigma = 2/3\%$. Most of the errors on the pixels of the Mueller matrix elements are below $3\sigma = 2\%$. Our estimator being the difference between two elements of this Mueller matrix, the errors on the estimator are bounded by $2 \cdot \sqrt{2} \simeq 2.82\%$. Yet the scalar estimator of the overlay is the average of the image estimator for the pixels on a mask manually selected. The average number of pixels in the mask is around 500 (20×25 pixels selection). In the case of a well distributed gaussian noise (totally uncorrelated pixels), the averaging on the mask would decrease the standard deviation of a factor of $\sqrt{500} \sim 22$. In the case of totally correlated pixels, averaging on the mask would not change the standard deviation. Fig. 4.39 shows the actual histogram of the pixels in the selected mask of the image estimator E14.

Standard Deviation	Excess Kurtosis	Skewness
0.0294	0.0514	-0.0848

Table 4.5: Estimators for the pixels of E14 in the selected mask

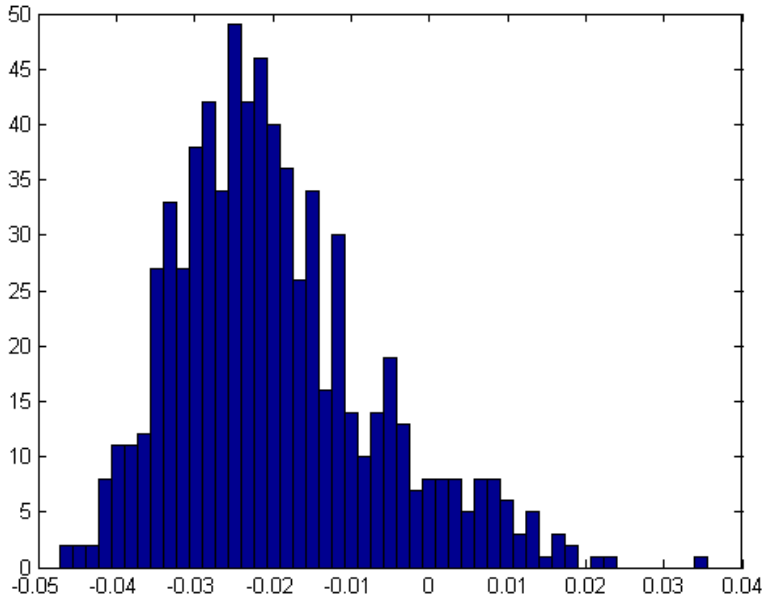

Figure 4.39: Histogram of the pixels in the selected mask for the estimator E14 along X. Module 10 N1 130 N2 300, Nominal overlay -50nm

The histogram confirms that the distribution is close to a normal one. To have a better comparison of our distribution with a normal one, we calculate 3 basic statistical estimators: the standard deviation σ, the excess kurtosis γ_2, the skewness γ_1. The formulas below recall the usual definitions of these estimators.

$$\gamma_1 = \mathrm{E}\left[\left(\frac{X-\mu}{\sigma}\right)^3\right] = \frac{\mu_3}{\sigma^3} = \frac{\mathrm{E}\left[(X-\mu)^3\right]}{(\mathrm{E}\left[(X-\mu)^2\right])^{3/2}} = \frac{\kappa_3}{\kappa_2^{3/2}} \tag{4.16}$$

where μ_3 is the third moment about the mean μ, σ is the standard deviation, and E is the expectation operator. The skewness is a measure of the asymmetry of a distribution.

The last equality expresses skewness in terms of the ratio of the third cumulant κ_3 and the 1.5th power of the second cumulant κ_2. This is analogous to the definition of kurtosis as the fourth cumulant normalized by the square of the second cumulant.

$$\gamma_2 = \frac{\kappa_4}{\kappa_2^2} = \frac{\mu_4}{\sigma^4} - 3 \tag{4.17}$$

The kurtosis is a measure of the "peakedness" of the distribution.

One should be careful when using the kurtosis. We clearly specified here that we are using the excess kurtosis defined in eq. 4.17 whereas some scientific software (e.g. Matlab®) gives the kurtosis $\beta_2 = \frac{\mu_4}{\sigma^4} = \gamma_2 + 3$.

We also remind that the skewness and excess kurtosis of a normal distribution are both null.

The values of the excess kurtosis and the skewness confirm that the distribution is close to a normal one. On the selected mask, the standard deviation reaches 3%, however this value should not be mistaken as the error on the pixels given that nothing states that the mask should be homogeneous.

The error of the estimator is very hard to quantify and we are only able to give a decent approximation of this error. Given the statistic error on a single pixel (2,82%) and given the quasi-normal distribution of the noise on the selected mask, we can fairly assess that the noise on the estimator should not be higher than 0.5%.

To obtain the error on the overlay, we just have to look at the slope of the estimator. Depending on the selected module, the slope of the estimator ranges from 0.001 to 0.007. The resulting error on the overlay then ranges from 0.7nm to 5nm. The upper bound of this error is unacceptable, the module exhibiting such a small slope should not be taken as a reference. The different modules give us a good exploration of the parameter space for the critical dimensions to use for the gratings. The module 5 N1 300 N2 180 gives the best sensibility for both x and y-overlay with respective slopes of 0.0069 and 0.0057.

Given that the purpose of this study is to define the best parameters for the overlay characterization, we keep as precision value the error on the module 5.

$$precisionX = 0.72nm \tag{4.18}$$

$$precisionY = 0.88nm \tag{4.19}$$

Tool Induced Shift

To calculate TIS, we assume that the AIM measurements provide us the true overlay (same assumption as before). For each measurement, we can then calculate the difference between the overlay measured by our system and the true overlay. This difference is the TIS for one measurement. The average is taken over a sample of N=55 measurements to find the mean TIS.

$$TIS = \frac{1}{N}\sum_{1}^{N} \nabla_{true} - \nabla_{m} \tag{4.20}$$

Average TIS is -1.12nm. The contribution of precision has been removed from the standard deviation of TIS, the standard deviation of TIS is 1.1nm. The relatively small value of TIS indicates that on average AIM and Mueller polarimetry give the same result but the high value of the standard deviation with respect to the average also shows some large discrepancies between the two methods.

Resulting TMU

We recall here the three components of the TMU and their values:

- TIS = 1.12nm
- σ_{TIS} = 1.1nm
- precision = 0.88nm

The resulting TMU is:

$$TMU = 1.80nm \tag{4.21}$$

This value is below the specifications for the 45nm DRAM half-pitch (2.1nm) but remains very high with respect to the 36nm DRAM half-pitch design rule (1nm). It is very important to note that the TMU for our method is equal to the TMU given by the authors in [108]. Throughout this manuscript we have considered as gold standard a method which may have the same uncertainty as the one we are trying to validate.

Nevertheless, this value should also be compared to previously published results and commercial set-ups.

In [86], the author claims to reach a 0.2nm TMU through angle-resolved scatterometry platform developed by ASML and Nanometrics recently published a very thorough study about the TMU of their instruments [82]. Most data of the TMU are under 0.4nm even though some may reach 0.6nm for eDBO, mDBO results being slighly higher. In chip overlay tool for DRAM has proven to give better results than what we are currently proposing [83].

4.7 Conclusion

The microelectronic industry is a very fast evolving one. When the MuellerFourier started, the current technological node was the 45nm node and the required uncertainty was around 2nm. In 2011, the current technological node is down to 22nm and the output uncertainty on the overlay measurement down to 1.5nm. The requirements imposed by IRTS become more and more challenging and bring the instruments to their very limits. The main purpose of this chapter was to demonstrate the capability of Mueller polarimetry to meet these requirements.

In this chapter, we assessed the validity of our image estimator E14 based on the difference of two elements of the Mueller matrix. We showed that the correct choice of statistic on a manually chosen mask leads to a linear relationship between the total overlay and the estimator. This linear relationship has been demonstrated for both x and y-overlay. We saw that the sensitivity of the chosen estimator depends a lot on the choice of the critical dimensions of the two superimposed gratings in the target. We found the signal on the most sensitive target to be sevenfold higher than the least sensitive one. This huge difference may even lead to further optimization of the test structure to improve the method sensitivity and accuracy.

We see that the lack of an international standard for overlay measurements severely hinder any comparison between different methods. We chose in this work to rely on the measurements provided by CEA-LETI using an Archer-100 system from KLA-Tencor as well as rely on the nominal overlays written on the wafer. These values are supposed to be the overlay intentionally introduced in the test structures in addition to the excess overlay due to the misalignment of the lithography tools between two steps. However, the AIM measurements proved that these values could not be exactly trusted: the 10nm increment is not respected and the four so-called zero overlay measurement pads show highly different overlay even though the excess overlay should be similar for close pad.

This work is a first step toward the definition of a new metrology tool for overlay. To measure overlay we used very often around 10 measurements on different pads to extract the linear fit of the estimator. In the best case scenario, only two measurements on pads with symmetric controlled overlays are sufficient to extract the excess overlay.

We proved that the use of only two pads for the linear fit does not severely increase the uncertainty of the estimator.

The next step for the project is the first prototype by Horiba Jobin Yvon and run the first tests with the CEA-LETI on production lines.

Chapter 5

Conclusions and perspectives

5.1 Improvements and perspectives on presented work

In this manuscript, we presented a new apparatus, the angle resolved Mueller polarimeter, and its potential applications. The development of the set-up itself and its optimization has been a long process and may even be a never-ending one depending on the latter applications chosen. The set-up is now as close as possible to a classical microscope and offer the user the possibility to measure Mueller matrices in both real and reciprocal spaces thus making it a very versatile measurement tool. However, as seen in chapter 2, only the imaging part of the set-up has been designed to work in both spaces, not the illumination part. A possible upgrade would be to have a switchable Köhler illumination optimized for both real and reciprocal space. The classical Köhler illumination scheme is optimized for imaging in real space so only illumination for the Fourier space should be changed. This could be achieved by adding a lens in the light collection part that would collimate the beam in the aperture diaphragm instead of focusing it. By doing so, we could expect more homogeneous modulation and analysis matrices $\mathbf{A}$ and $\mathbf{W}$ which could improve the repeatability of the measurements and their overall quality.

The second possible upgrade of the system would be to change the PSG configuration. As described in chapter 2, the PSG does not map the Poincaré sphere, some polarization states cannot be generated which could be a limitation of our system. To be able to generate any Stokes vector without major changes in the PSG design, we just have to change the orientation of the liquid crystals: by setting the first LC orientation to 45°with respect to the orientation of the polarizer and the second LC aligned with the polarizer, any Stokes vector can be generated. In addition to this change in configuration of the PSG, we should also accurately characterize the response of the liquid crystals depending on the control voltage to be able to accurately control the retardation of each LC and then the output Stokes vector. These two upgrades are the key components to succeed in sending controlled and optimized Stokes vectors on the sample to increase the measured signal which would decrease measurement time and increase sensitivity.

Another possible way of decreasing measurement time would be to change the light source. As shown in fig. 2.3 in chapter 2, the output power of the source almost varies linearly with respect to the wavelength and the total power is relatively low. A more powerful light source would decrease integration time thus decreasing artifacts and noise, would allow us to decrease the size of the field we can measure in and would

enable us to measure less reflective samples. A possible solution would be to use LED source which are compact, powerful, customable and can be fibered to comply with the current illumination scheme.

In chapter 4, we saw that the total measurement uncertainty achieved with this technique is close to the commercial systems and the ITRS roadmap specifications. For this study, only the $20 \times 20 \mu m$ boxes were measured due to the size of the spot. With the use of proper pinholes, we could decrease the spot size down to $5 \mu m$ and then measure in the $5 \times 5 \mu m$ boxes.

We also noticed in chapter 4 that the estimator highly depends on the selected mask. During this thesis, the mask has always been manually selected and no automatic procedure has been tested. The introduction of such procedure would be a critical step in the development of a commercial set-up able to measure wafers with a sufficient throughput compatible with actual industry requirements. By combining the work carried by Sami Ben Hatit [41] and the work presented in this thesis, we can approach Ausschnitt's concept of MOXIE (see introduction of chapter 4). The metrology of the groove profile and overlay could be measured by the same instrument, namely our angle resolved Mueller polarimeter. Further investigations would be required to compare the direct measurement of overlay without modeling of the structure (as presented in chapter 4) associated to a fitting procedure to recover the groove profile (as described in Sami Ben Hatit's thesis) and the addition of overlay defect as a parameter of the fitting procedure for CD reconstruction.

5.2 Perspectives for new applications

At the beginning of my thesis, I have developed and optimized a very versatile measurement tool, with the constant will to be able to measure samples as diverse as possible to check the possibility of the instrument. During these three years, a lot of samples have been measured by our Mueller polarimeter. A few examples are listed below.

5.2.1 Characterization of auto-organized and periodic structures

Periodic structures can be analyzed by electron microscopy, AFM or X-Ray diffraction to characterize their periodicity. Our set-up could also bring a lot of valuable information as we will see in a snapshot measurement both in real and reciprocal space. In the reciprocal space, the symmetries of the Mueller matrix reveal the pattern of the structure. Periodic structures developed in other laboratories have been measured with our angle resolved Mueller polarimeter. Some preliminary results and discussions are gathered below.

Example of sol-gel deposited silica spheres

Samples of sol-gel deposited silica spheres have been prepared by Dr. Sabine Portal Marco from the Department of Applied Physics and Optics of the University of Barcelona. Two samples with different degrees of self-organization have been studied, they will be referred to as S42a and S42b. We will only show the experimental Mueller matrices obtained in reciprocal space as well as the intensity images. No modeling of the structures has been investigated to compare with our measurements. We can see

on figures 5.1 and 5.3 clusters where the silica spheres are self-organized in hexagonal structures. This hexagonal pattern is also clearly visible both in Mueller matrices (cf figs. 5.1 and 5.3) and Lu-Chipman decompositions (cf figs. 5.2 and 5.4). The difference between the two samples is clearly the degree of auto-organization characterized by the size of the clusters. Given the lack of light reflected by the sample, limiting the field has proved difficult and the Mueller matrices displayed here should be regarded as averaged for several clusters. This averaging effect explains both the difference in Mueller matrices and in decompositions. However, common six fold features arise.

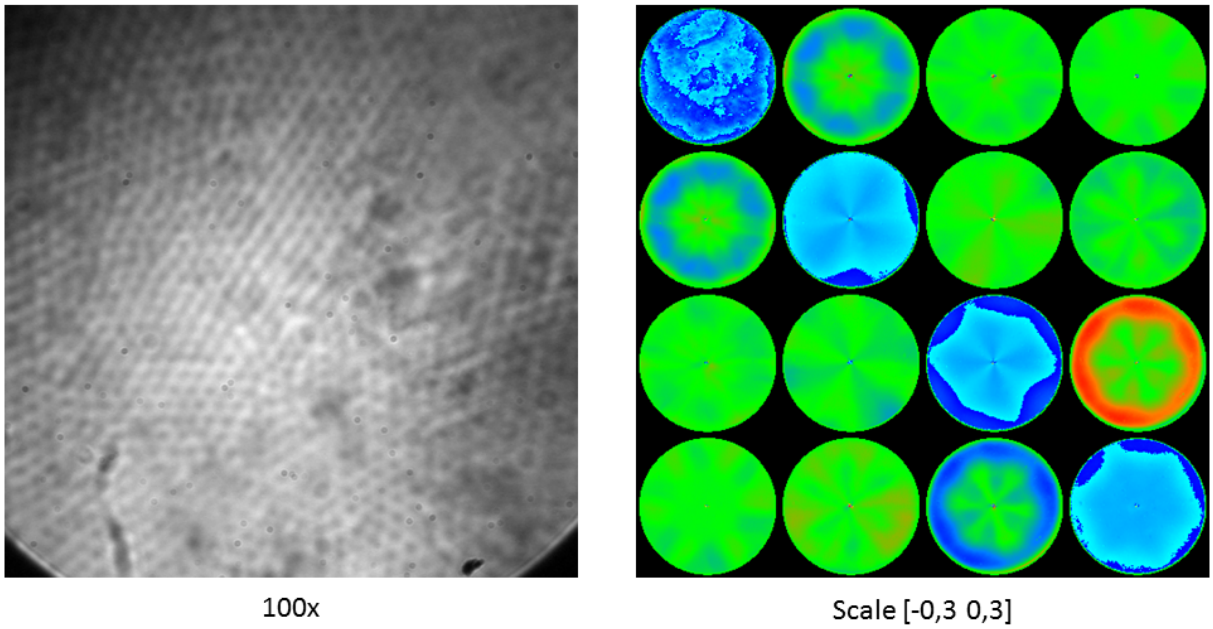

Figure 5.1: Left: 100X intensity image of sample S42a. Right: Mueller matrix in reciprocal space, scale [-0.3 0.3] $\lambda = 633nm$

Example of periodic holes for photonic crystals

Dr. Gaelle Lehoucq provided us a GaAs photonic crystal fabricated at Thales Research and Technology (Palaiseau). (cf fig. 5.5). Membrane photonic crystals are thin layers of semiconductor suspended in a low index medium (e.g. air) with a two-dimensional periodic pattern of holes [110].

Our instrument enables us to study the light scattered by the sample and thus to retrieve the pattern parameters (just like with any scatterometer image) but we can also analyze the polarimetric properties of such structures. The study of theses structures is very important because the quality of the photonic crystals highly depends on the periodicity of the holes [111]. The challenge is to be able to spot periodicity defects in the structure. Imaging in the real space is mandatory for this application because we are looking for localized spatial defects, it is then impossible to use Fourier space imaging because the polarimetric properties would be spatially averaged preventing any spatial characterization (though the angle resolved Mueller matrix and its decomposition may be very interesting for other purposes, see fig. 5.6 and 5.7). In the Fourier space, one can only check that the average periodicity is the right one.

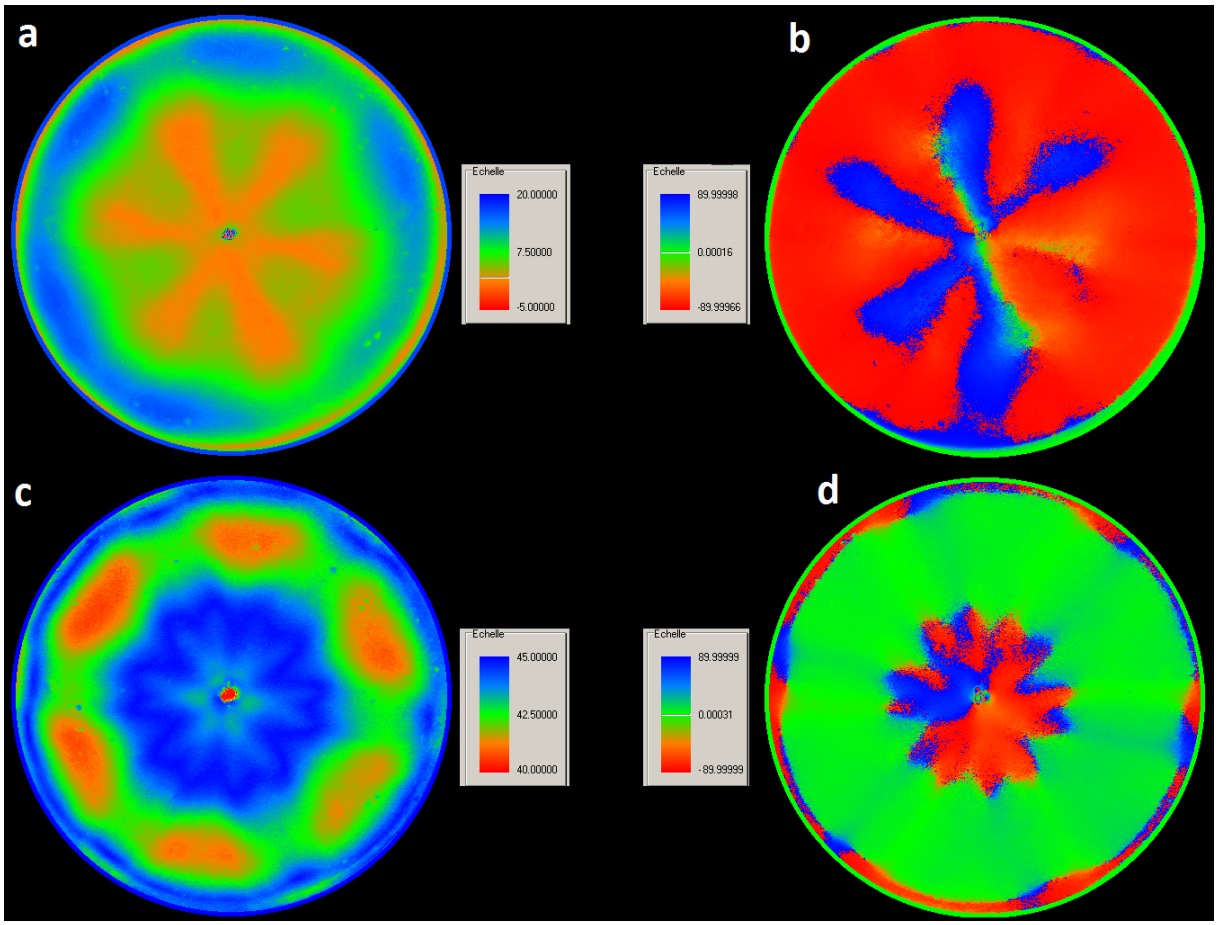

Figure 5.2: Lu-Chipman of the Mueller matrix of S42a. (a): Scalar retardance. (b): Orientation of the scalar retardance. (c) Scalar dichroism. (d): Orientation of the scalar dichroism

The poor quality of the real space measurements on this sample makes them impossible to interpret: the next measurements should be done more carefully in a real space oriented purpose not Fourier space oriented as we have previously done. However, the need for good spatial resolution (directly linked to the magnification of the microscope) and the need to scan large areas to detect periodicity defects seem hard to fulfill at the same time.

The next step for this potential application is to be able to define a periodicity quality estimator. For the overlay characterization, we defined an alignment estimator, we have to study the spatial polarimetric response of these structures and the effects of a small defect in periodicity on the Mueller matrix to maybe be able to define this estimator.

5.2.2 Characterization of chiral nanorods

Samples of chiral nanorods of $Al_{1-x}In_xN$ have been prepared by Dr. Jens Birch from University of Linköping (LiU) according to method described in [112] and illustrated in fig. 5.8. These structures enable us to make a step toward the understanding of the relationship between heloical structures and circular dichroism and mimic biological phenomena. The nanorods have been measured by spectroscopic ellipsometry (RC2 from J.A. Wollam CO. Inc.) by Roger Magnusson from LiU [113]. Spectroscopic Mueller matrices of left-handed and right-handed films clearly exhibit circular dichroism contrary

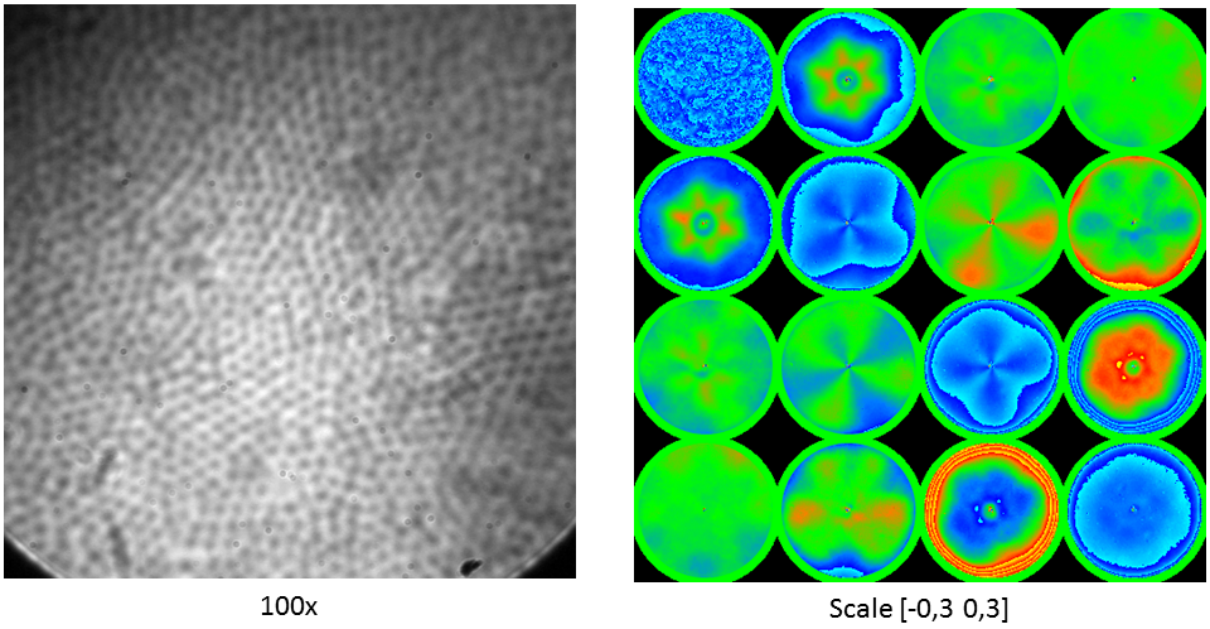

Figure 5.3: Left: 100X intensity image of sample S42b. Right: Mueller matrix in reciprocal space, scale [-0.3 0.3] $\lambda = 633nm$

to non-chiral films. The handedness of the chiral structures can be recovered from the sign of the M41 element of the Mueller matrix.

One of these structures has been measured by our angle resolved Mueller polarimeter at 454nm. However, as shown on the spectra in fig.5.9, even measuring this structure at 454nm is not sufficient to see a strong circular dichroism.Nevertheless, a circular dichroism around 10% appear on our measurement which is consistent with the spectra. Design and fabrication of structures optimized for circular dichroism in the visible range is currently discussed at LiU and could be characterized during fall 2011. The next step would be to quantitatively interpret the angle resolved measurements to accurately describe the sample structures.

5.3 General conclusions

We believe that the work presented in this manuscript and the perspectives for the instrument clearly demonstrate the potential of angle resolved Mueller polarimetry and Mueller polarimetry in general as a very general characterization tool with applications ranging from semiconductor industry to research laboratories studying exoskeletons of beetles. Some further improvements have to be done on the design of the instrument itself to make it even more reliable and accurate, new applications have been presented but are not limited to these ones.

The new implementation of the set-up with all the improvements suggested by Sami Ben Hatit has been presented in chapter 2. This polarimeter works both in the real and reciprocal space to keep it very versatile though we can clearly see the limitations of

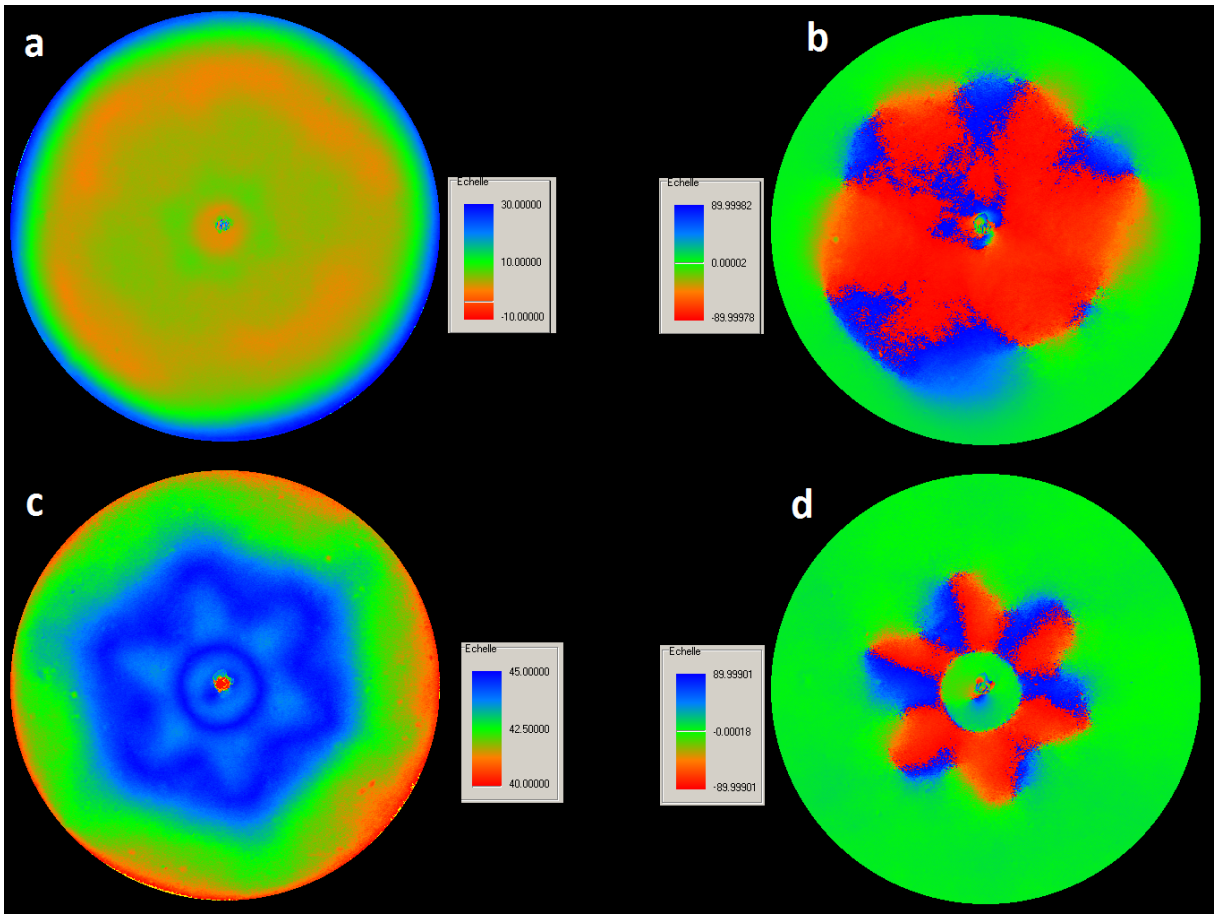

Figure 5.4: Lu-Chipman of the Mueller matrix of S42b. (a): Scalar retardance. (b): Orientation of the scalar retardance. (c) Scalar dichroism. (d): Orientation of the scalar dichroism

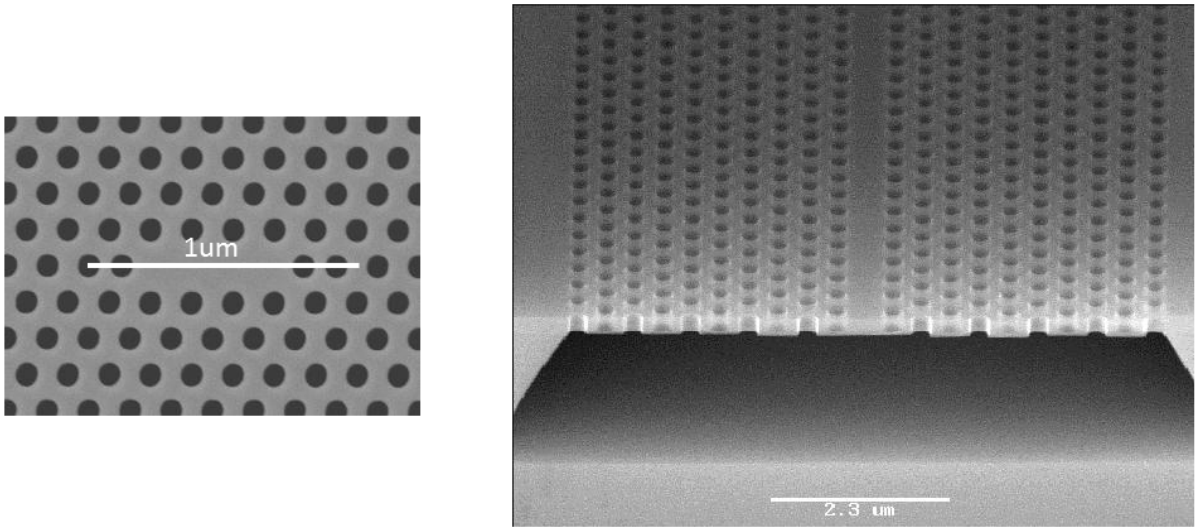

Figure 5.5: Electron microscopy images of the periodic holes. 200 nm holes spaced 400 nm (courtesy of S.Combrié & G.Lehoucq, Thales R&T)

working in two reciprocal spaces. The set-up currently enables us to measure the polarimetric response of samples for all azimuth angles (from 0 to 360°) for incidence an-

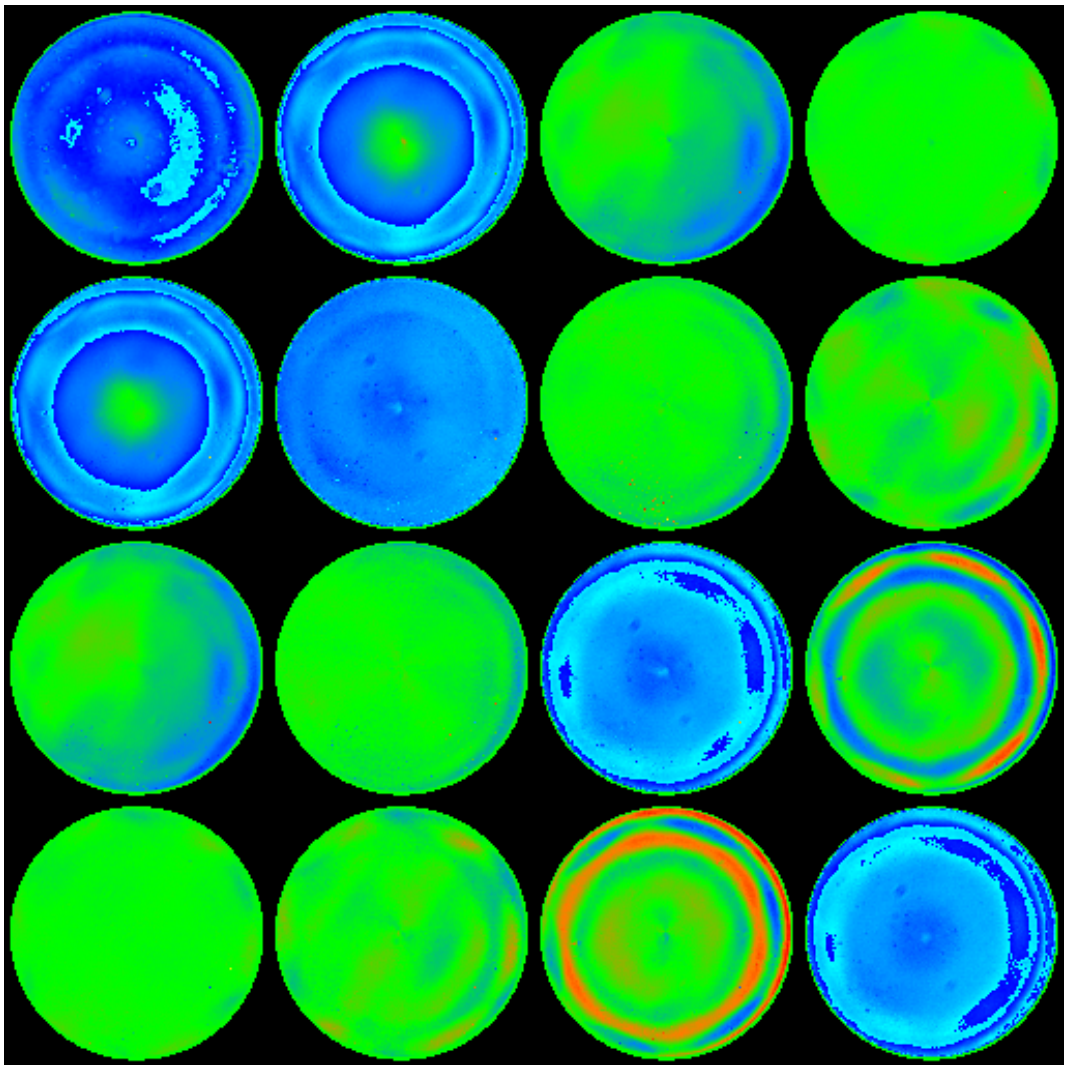

Figure 5.6: Mueller matrix of XXL 659. Scale [-0.3 0.3]

gles from 0 to 62°. We notice that although we decrease the numerical aperture of the microscope objective from 0.95 to 0.90, the actual numerical aperture of the complete system actually increased from 60°to 62°. The smallest spot achievable on the sample has been decreased from $30\mu m$ to $10\mu m$ and will be decreased even more (down to $5\mu m$) with the use of smaller pinholes and more powerful light sources. We have presented a new optimized illumination system for our Mueller microscope inspired by the Köhler illumination scheme used in classical bright-field microscopy. This system allows us to decouple the field and the aperture, thus varying one without altering the other. However, given the desired versatility of the apparatus, this system is a trade-off between the best illumination for measurements in the real space and measurements in the reciprocal space.

We also introduced an optimized detection arm with a retractable lens to easily switch from real space to reciprocal space without any major change in the set-up. Though this feature was also available in Ben Hatit's design, we improved it by adding a intermediate plane in which we can introduce more diaphragm in order for example to move toward dark-field microscopy.

The general design of our Mueller polarimeter is now very close to a conventional

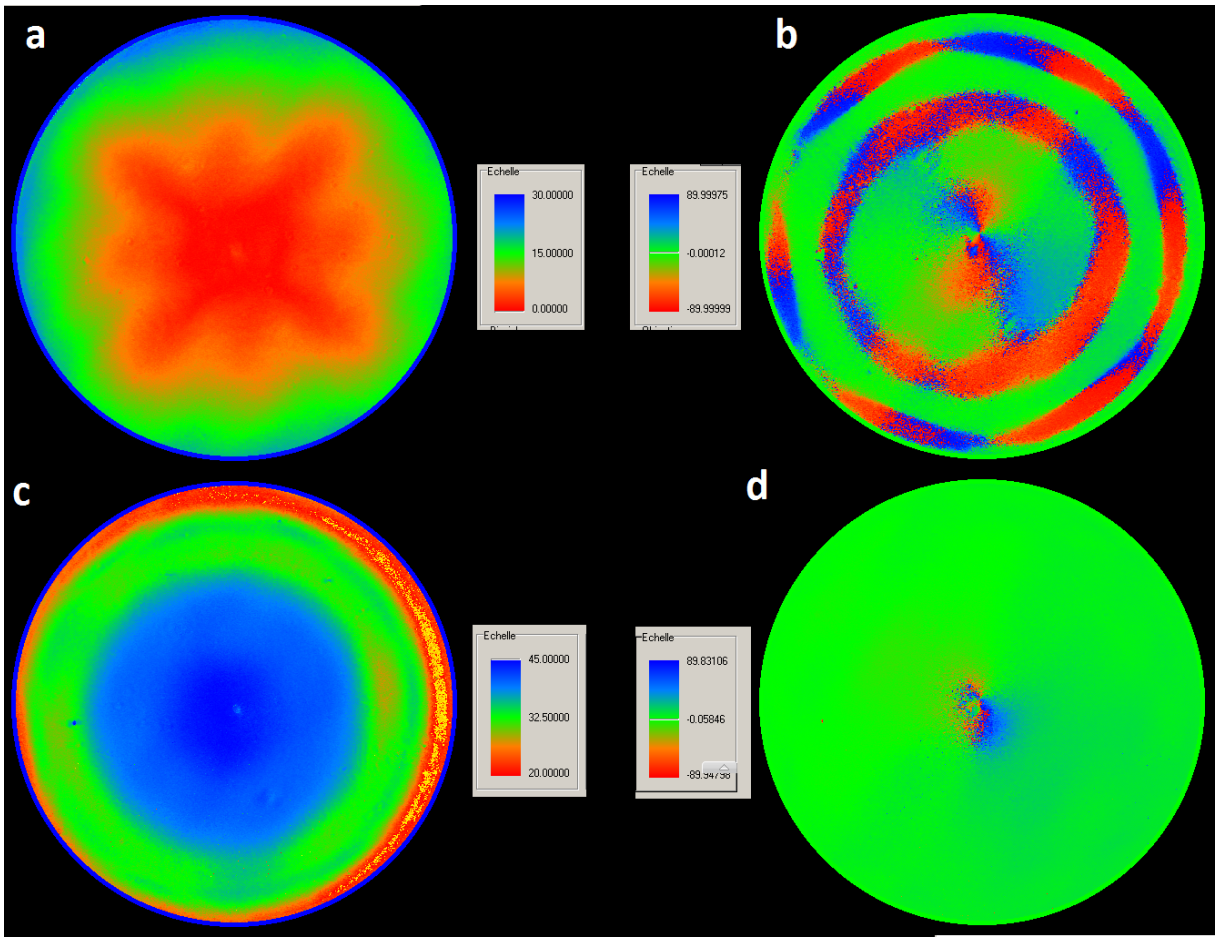

Figure 5.7: Lu-Chipman decomposition of XXL 659 sample. (a): Scalar retardance. (b): Orientation of the scalar retardance. (c) Scalar dichroism. (d): Orientation of the scalar dichroism

microscope and also offers different magnifications and apertures thanks to a set of strain-free microscope objectives mounted on a rotating turret.

In chapter 3, we presented the first and preliminary results obtained on the spatial characterization of the polarimetric response of the exoskeleton of some beetles. These results, though not conclusive on their own, will hopefully shed some light on the complex and yet neglected problem of the modeling and the understanding of the cuticle of beetles exhibiting circular dichroism. We proved that circular dichroism only occurs on some specific areas of the exoskeleton. Scientists have always studied beetles either with classical microscope (bright-field, dark-field, confocal) or with spectroscopic ellipsometry. To our knowledge, the only attempt to mix polarization and imaging to characterize the localization of circular dichroism on beetles only gave qualitative results on macroscopic images. We believe that our instrument brings a lot of value to the scientific community through the possibility to study the Mueller matrix of our sample under high magnification. We compared our first results with the ones from the group of Prof. Hans Arwin from the University of Linköping, Sweden and common features have been extracted. We proved thanks to our spatially resolved Mueller matrices that the cuticle of these beetles can not be modeled by a homogeneous medium but need to take into account some spatial variations. We also showed that our system can accurately image the constitutive structures (namely the Bouligand structures) of

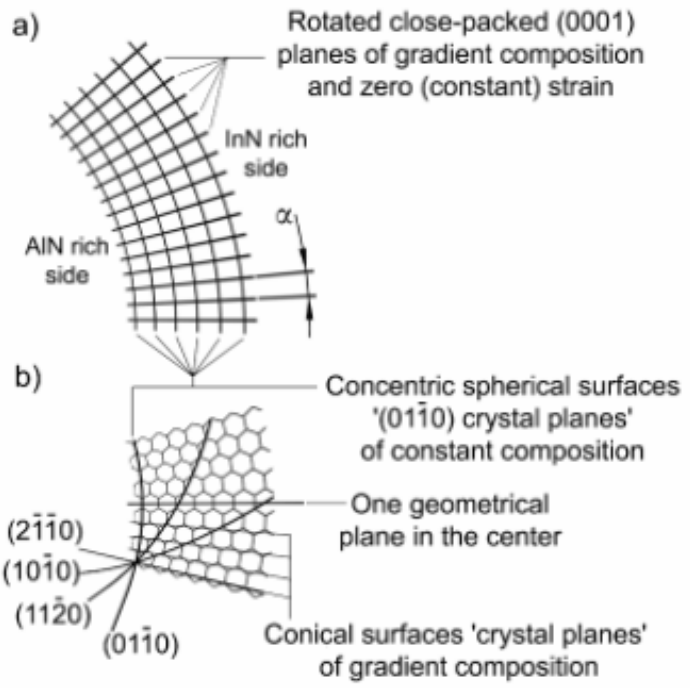

Figure 5.8: Growth method of chiral nanorods of $Al_{1-x}In_xN$. figure from [112]

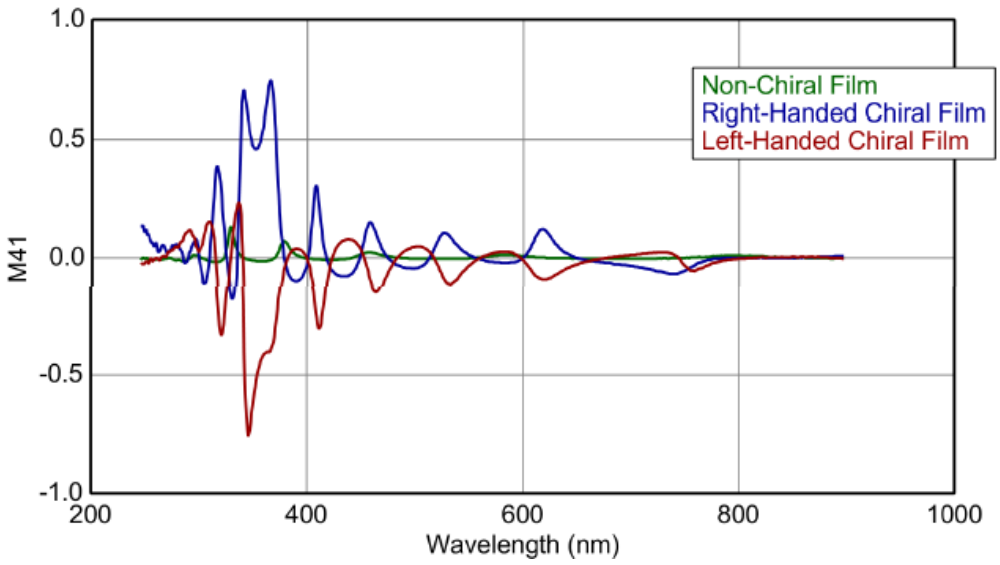

Figure 5.9: M41 element of the Mueller matrix for non-chiral, left-handed and right-handed films versus wavelength

the exocuticle. However, as stated in chapter 3, further investigations should be carried out to check the agreement of our measurements with previously published spectra.

The last part of this manuscript has been dedicated to the main project of this thesis. We introduced the new emerging challenges of semiconductor metrology and the current state of the art techniques to address this problem. Based on RCWA simulations, we clearly demonstrated the potential of angle resolved Mueller polarimetry for

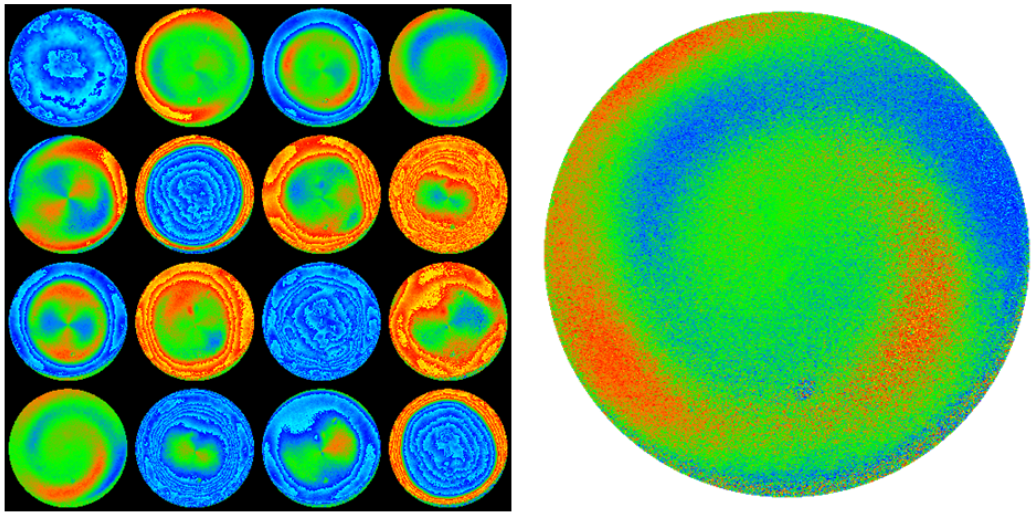

Figure 5.10: Left: Mueller matrix of VAI 5 ($Al_{1-x}In_xN$ nanorods),scale [-0.3 0.3]. Right: M14 element of the Mueller matrix.

overlay characterization and defined an estimator for the overlay. Through our collaboration with the CEA-LETI, we developed new metrology marks to be engraved in scribe lines to accurately measure the overlay on wafers. Though the smallest pinhole can not be used for now to measure the $5 \times 5\mu m^2$ targets, the $20 \times 20\mu m^2$ measurement boxes designed by CEA-LETI are among the smallest commercial metrology tools work with which is a major advantages of our method. We proved that our estimator has an excellent linearity with the overlay measured by the technique regarded as the current gold standard, the Advanced Imaging Method (AIM) by KLA-Tencor. The Mueller measurements are very well correlated to the AIM measurements with an offset close to the uncertainty of AIM. The other very promising advantage of Mueller polarimetry is that the overlay measurements are direct and do not require a modeling step of the structure which eradicates all model dependency and errors which may derive from that. The only requirement for our method is to dispose of two very-well characterized marks to calibrate our estimator. The resulting total measurement uncertainty is around 2nm which is almost compatible with the current requirements of the semiconductor industry. The current drawback of the setup is the measurement time: with the current light source, pinholes and filters, we need a 1s integration time per intensity measurement. Given that we need 16 intensity measurements to recover the full Mueller matrix, each Mueller matrix measurement takes around 16 seconds which is unacceptable in the industry. Possible ways to decrease the measurement time have been given at the beginning of this chapter.

Usual Jones & Stokes vectors, Usual Jones & Mueller matrices

Usual Jones vectors

H	V	45°	-45°	RC	LC	Elliptic
$\begin{bmatrix}1\\0\end{bmatrix}$	$\begin{bmatrix}0\\1\end{bmatrix}$	$\frac{1}{\sqrt{2}}\begin{bmatrix}1\\1\end{bmatrix}$	$\frac{1}{\sqrt{2}}\begin{bmatrix}1\\-1\end{bmatrix}$	$\frac{1}{\sqrt{2}}\begin{bmatrix}1\\-i\end{bmatrix}$	$\frac{1}{\sqrt{2}}\begin{bmatrix}1\\i\end{bmatrix}$	$\begin{bmatrix}\cos\theta\cos\varepsilon - i\sin\theta\sin\varepsilon\\ \sin\theta\cos\varepsilon + i\cos\theta\sin\varepsilon\end{bmatrix}$

Table 5.1: Jones vectors of classical polarization states. From left to right : linear 0°(horizontal), linear 90°(vertical), linear 45°, linear -45°, right circular, left circular gauche and the elliptic general case.

Usual Stokes vectors

H	V	45°	-45°	RC	LC	Elliptic
$\begin{bmatrix}1\\1\\0\\0\end{bmatrix}$	$\begin{bmatrix}1\\-1\\0\\0\end{bmatrix}$	$\begin{bmatrix}1\\0\\1\\0\end{bmatrix}$	$\begin{bmatrix}1\\0\\-1\\0\end{bmatrix}$	$\begin{bmatrix}1\\0\\0\\-1\end{bmatrix}$	$\begin{bmatrix}1\\0\\0\\1\end{bmatrix}$	$\begin{bmatrix}1\\ \cos 2\theta\cos 2\varepsilon\\ \sin 2\theta\cos 2\varepsilon\\ \sin 2\varepsilon\end{bmatrix}$

Table 5.2: Stokes vectors of classical polarization states. From left to right : linear 0°(horizontal), linear 90°(vertical), linear 45°, linear -45°, right circular, left circular gauche and the elliptic general case.

Usual Jones matrices

polarizer 0°	polarizer 90°	retarder Δ 0°
$\begin{bmatrix} 1 & 0 \\ 0 & 0 \end{bmatrix}$	$\begin{bmatrix} 0 & 0 \\ 0 & 1 \end{bmatrix}$	$\begin{bmatrix} e^{i\Delta} & 0 \\ 0 & 1 \end{bmatrix}$
reflection on an isotropic surface		
$\tau \begin{bmatrix} \tan\Psi e^{i\Delta} & 0 \\ 0 & 1 \end{bmatrix}$		

Table 5.3: Classical Jones matrices

Usual Mueller matrices

Air/vacuum	**Absorbing medium**
$\begin{bmatrix} 1 & 0 & 0 & 0 \\ 0 & 1 & 0 & 0 \\ 0 & 0 & 1 & 0 \\ 0 & 0 & 0 & 1 \end{bmatrix}$	$\begin{bmatrix} a & 0 & 0 & 0 \\ 0 & a & 0 & 0 \\ 0 & 0 & a & 0 \\ 0 & 0 & 0 & a \end{bmatrix}$

Table 5.4: Mueller Matrices of simple elements.

Linear Polarizer oriented at 0°	**Linear Polarizer oriented at 90°**
transmission factor τ	
$\frac{\tau}{2}\begin{bmatrix}1&1&0&0\\1&1&0&0\\0&0&0&0\\0&0&0&0\end{bmatrix}$	$\frac{\tau}{2}\begin{bmatrix}1&-1&0&0\\-1&1&0&0\\0&0&0&0\\0&0&0&0\end{bmatrix}$
Linear Polarizer oriented at 45°	**Circular Polarizer**
transmission factor τ	
$\frac{\tau}{2}\begin{bmatrix}1&0&1&0\\0&0&0&0\\1&0&1&0\\0&0&0&0\end{bmatrix}$	$\frac{\tau}{2}\begin{bmatrix}1&0&0&\pm1\\0&0&0&0\\0&0&0&0\\\pm1&0&0&1\end{bmatrix}$
Linear Dichroic at 0°	**Linear Dichroic at 45°**
transmission factor q, r	
$\frac{1}{2}\begin{bmatrix}q+r&q-r&0&0\\q-r&q+r&0&0\\0&0&2\sqrt{qr}&0\\0&0&0&2\sqrt{qr}\end{bmatrix}$	$\frac{1}{2}\begin{bmatrix}q+r&0&q-r&0\\0&2\sqrt{qr}&0&0\\q-r&0&q+r&0\\0&0&0&2\sqrt{qr}\end{bmatrix}$
Linear Dichroic at θ, transmission factor q, r	
$\frac{1}{2}\begin{bmatrix}q+r&(q-r)\cos 2\theta&(q-r)\sin 2\theta&0\\(q-r)\cos 2\theta&(q+r)\cos^2 2\theta+2\sqrt{qr}\sin^2 2\theta&(q+r-2\sqrt{qr})\sin 2\theta\cos 2\theta&0\\(q-r)\sin 2\theta&(q+r-2\sqrt{qr})\sin 2\theta\cos 2\theta&(q+r)\sin^2 2\theta+2\sqrt{qr}\cos^2 2\theta&0\\0&0&0&2\sqrt{qr}\end{bmatrix}$	

Table 5.5: Dichroics.

Ideal depolarizer	**Partial depolarizer**
$\begin{bmatrix}1&0&0&0\\0&0&0&0\\0&0&0&0\\0&0&0&0\end{bmatrix}$	$\begin{bmatrix}1&0&0&0\\0&a&0&0\\0&0&b&0\\0&0&0&c\end{bmatrix}$

Table 5.6: Depolarizers.

Ideal mirror or Half-wave plate

$$\begin{bmatrix} 1 & 0 & 0 & 0 \\ 0 & 1 & 0 & 0 \\ 0 & 0 & -1 & 0 \\ 0 & 0 & 0 & -1 \end{bmatrix}$$

Quarter-wave plate

$$\begin{bmatrix} 1 & 0 & 0 & 0 \\ 0 & 1 & 0 & 0 \\ 0 & 0 & 0 & 1 \\ 0 & 0 & -1 & 0 \end{bmatrix}$$

Linear retarder oriented at 0°

$$\begin{bmatrix} 1 & 0 & 0 & 0 \\ 0 & 1 & 0 & 0 \\ 0 & 0 & \cos\Delta & \sin\Delta \\ 0 & 0 & -\sin\Delta & \cos\Delta \end{bmatrix}$$

Linear retarder oriented at 90°

$$\begin{bmatrix} 1 & 0 & 0 & 0 \\ 0 & 1 & 0 & 0 \\ 0 & 0 & \cos\Delta & -\sin\Delta \\ 0 & 0 & \sin\Delta & \cos\Delta \end{bmatrix}$$

Linear retarder oriented at 45°

$$\begin{bmatrix} 1 & 0 & 0 & 0 \\ 0 & \cos\Delta & 0 & -\sin\Delta \\ 0 & 0 & 1 & 0 \\ 0 & \sin\Delta & 0 & \cos\Delta \end{bmatrix}$$

Circular retarder

$$\begin{bmatrix} 1 & 0 & 0 & 0 \\ 0 & \cos\Delta & \pm\sin\Delta & 0 \\ 0 & \mp\sin\Delta & \cos\Delta & 0 \\ 0 & 0 & 0 & 1 \end{bmatrix}$$

Linear retarder oriented at θ

$$\frac{1}{2}\begin{bmatrix} 1 & 0 & 0 & 0 \\ 0 & \cos^2 2\theta + \sin^2 2\theta\cos\Delta & \sin 2\theta\cos 2\theta(1-\cos\Delta) & -\sin 2\theta\sin\Delta \\ 0 & \sin 2\theta\cos 2\theta(1-\cos\Delta) & \sin^2 2\theta + \cos^2 2\theta\cos\Delta & \cos 2\theta\sin\Delta \\ 0 & \sin 2\theta\sin\Delta & -\cos 2\theta\sin\Delta & \cos\Delta \end{bmatrix}$$

Elliptic retarder oriented at θ and ellipticity $\tan\varepsilon$

$$\frac{1}{2}\begin{bmatrix} 1 & 0 & 0 & 0 \\ 0 & D^2 - E^2 - F^2 + G^2 & 2(DE+FG) & 2(DF-EG) \\ 0 & 2(DE-FG) & -D^2 + E^2 - F^2 + G^2 & 2(EF+DG) \\ 0 & 2(DF+EG) & 2(EF-DG) & -D^2 - E^2 + F^2 + G^2 \end{bmatrix}$$

$$D = \cos 2\varepsilon\cos 2\theta\sin\Delta/2$$
$$E = \cos 2\varepsilon\sin 2\theta\sin\Delta/2$$
$$F = \sin 2\varepsilon\sin\Delta/2$$
$$G = \cos\Delta/2$$

Table 5.7: Retarders.

Homogeneous linear dichroic retarder oriented at 0°

$$\begin{bmatrix} 1 & -\cos 2\Psi & 0 & 0 \\ \cos 2\Psi & 1 & 0 & 0 \\ 0 & 0 & \sin 2\Psi \cos \Delta & \sin 2\Psi \sin \Delta \\ 0 & 0 & -\sin 2\Psi \sin \Delta & \sin 2\Psi \cos \Delta \end{bmatrix}$$

Homogeneous linear dichroic retarder oriented at θ

$$\begin{bmatrix} 1 & -C_\theta \cos 2\Psi & -S_\theta \cos 2\Psi & 0 \\ C_\theta \cos 2\Psi & C_\theta^2 + S_\theta^2 \sin 2\Psi \cos \Delta & C_\theta S_\theta (1 - \sin 2\Psi \cos \Delta) & -S_\theta \sin 2\Psi \sin \Delta \\ -S_\theta \cos 2\Psi & C_\theta S_\theta (1 - \sin 2\Psi \cos \Delta) & S_\theta^2 + C_\theta^2 \sin 2\Psi \cos \Delta & C_\theta \sin 2\Psi \sin \Delta \\ 0 & S_\theta \sin 2\Psi \sin \Delta & -C_\theta \sin 2\Psi \sin \Delta & \sin 2\Psi \cos \Delta \end{bmatrix}$$

$$C_\theta = \cos 2\theta$$
$$S_\theta = \sin 2\theta$$

Table 5.8: Homogeneous linear dichroic retarders

List of publications and presentations

Publications in Peer review Journals

- Razvigor Ossikovski, **Clément Fallet**, Angelo Pierangelo, and Antonello De Martino, "Experimental implementation and properties of Stokes nondiagonalizable depolarizing Mueller matrices," Opt. Lett. 34, 974-976 (2009)

- Razvigor Ossikovski, Martin Foldyna, **Clément Fallet**, and Antonello De Martino, "Experimental evidence for naturally occurring nondiagonal depolarizers," Opt. Lett. 34, 2426-2428 (2009)

- **Clément Fallet**, Angelo Pierangelo, Razvigor Ossikovski, and Antonello De Martino, "Experimental validation of the symmetric decomposition of Mueller matrices," Opt. Express 18, 831-842 (2010)

- F. Ferrieu, T. Novikova, **C. Fallet**, S. Ben Hatit, C. Vannufel, A. De Martino, "Analysis of textured films and periodic Grating Structures with Mueller Matrices: A new Challenge in Instrumentation with the generation of angle-resolved SE polarimeters", Thin Solid Films, 519 2608–2612 (2011)

- **Clément Fallet**, Tatiana Novikov, Martin Foldyna, Sandeep Manhas, Bicher Haj Ibrahim, Antonello De Martino, Cyril Vannuffel, and Christophe Constancias, "Overlay Measurements by Mueller Polarimetry in Back Focal Plane", Journal of Micro/Nanolithography, MEMS, and MOEMS (2011)

Proceedings

- **Clement Fallet**, Sandeep Manhas, Antonello de Martino and Tatiana Novikova, "Applications of Mueller polarimetry in the Fourier space for overlay characterization in microelectronics", Proc. SPIE 7767, 77670N (2010)

- Tatiana Novikova, **Clément Fallet**, Martin Foldyna, Sandeep Manhas, Bicher Haj Ibrahim, Antonello De Martino, Cyril Vannuffel and Christophe Constancias, "Overlay measurement by Mueller polarimetry in the back focal plane", Proc. SPIE 7971, 797115 (2011)

- **Clément Fallet**, Tatiana Novikova, Aline Jolibois, Bicher Haj Ibrahim, Antonello De Martino, Cyril Vannuffel, "Overlay measurement by angle resolved Mueller polarimetry", Proc. SPIE (2011)

Posters and Presentations in Conferences

- Poster : **Clement Fallet**, "Design and optimization of an angle-resolved Mueller polarimeter, Applications to sub-wavelength structures metrology", Doctoriales 2009, Fréjus (FRANCE), September 2009.
- Poster : **Clément Fallet**, Antonello de Martino, Tatiana Novikova, "Applications of Mueller Polarimetry in the Fourier Space for overlay characterization in microelectronics", Journées de la Matière Condensée, Troyes (FRANCE), August 2010.
- Oral Presentation : **Clement Fallet**, Sandeep Manhas, Antonello de Martino and Tatiana Novikova, "Applications of Mueller polarimetry in the Fourier space for overlay characterization in microelectronics", Optics + Photonics 2010 - Instrumentation, Metrology, and Standards for Nanomanufacturing IV, San Diego (USA), August 2010
- Poster : **Clément Fallet**, Tatiana Novikova, Martin Foldyna, Bicher Haj Ibrahim, Sandeep Manhas, Antonello de Martino, Cyril Vannuffel, Frédéric Ferrieu, Christophe Constancias, Denis Cattelan, Cécile Lerondeau, "Mueller Imaging in Fourier space for overlay metrology", Journée Nationales en Nanosciences et Nanotechnologies (J3N), Lille (FRANCE), November 2010.
- Oral Presentation : **Clément Fallet**, Sandeep Manhas, Bicher Haj Ibrahim, Tatiana Novikova, Antonello De Martino, Cyril Vannuffel, Christophe Constancias, "Application of Mueller Polarimetry in the Fourier Space to semiconductor metrology", Workshop on Spectroscopic Ellipsometry 2011, Berlin (GERMANY), February 2011.
- Invited Oral Presentation : **Clément Fallet**, Tatiana Novikova, Aline Jolibois, Bicher Haj Ibrahim, Antonello De Martino, Cyril Vannuffel, "Overlay measurement by angle resolved Mueller polarimetry", Optics + Photonics 2011 - Polarization and Instrumentation, San Diego (USA), August 2011.

Bibliography

[1] S. Y. Lu and R. A. Chipman, "Mueller matrices and the degree of polarization," *Opt. Comm*, vol. 146, pp. 11–14, Jan. 1998.

[2] R. M. A. Azzam and N. M. Bashara, *Ellipsometry and polarized light*. North-Holland Pub. Co., 1977.

[3] J. J. Gil, J. M. Correas, P. A. Melero, and C. Ferreira, "Generalized Polarization Algebra," *Manographias del Seminario Matematico Garcia de Galdeano*, vol. 167, pp. 161–167, 2004.

[4] R. Schmieder, "Stokes-Algebra Formalism," *J. Opt. Soc. Am. A*, vol. 59, no. 3, 1969.

[5] J. Hovenier, "Structure of a general pure Mueller matrix," *Appl. Opt.*, no. 1, pp. 8318–8324.

[6] J. J. Gil, "Characteristic properties of Mueller matrices," *J. Opt. Soc. Am. A*, vol. 17, no. 2, pp. 328–334, 2000.

[7] B. N. Simon, S. Simon, N. Mukunda, F. Gori, M. Santarsiero, R. Borghi, and R. Simon, "A complete characterization of pre-Mueller and Mueller matrices in polarization optics," *J. Opt. Soc. Am. A*, vol. 27, no. 2, pp. 188–199, 2010.

[8] S. R. Cloude, "Conditions for physical realizability of matrix operators in polarimetry," in *SPIE Conference Series* (R. A. Chipman, ed.), vol. 1166 of *Society of Photo-Optical Instrumentation Engineers (SPIE) Conference Series*, pp. 177–185, 1990.

[9] S. Y. Lu and R. A. Chipman, "Interpretation of Mueller matrices based on polar decomposition," *J. Opt. Soc. Am. A*, vol. 13, no. 5, pp. 1106–1113, 1996.

[10] J. J. Gil and E. Bernabeu, "A Depolarization Criterion in Mueller Matrices," *Optica Acta: International Journal of Optics*, vol. 32, no. 3, pp. 259–261, 1985.

[11] R. Ossikovski, "Alternative depolarization criteria for Mueller matrices," *J. Opt. Soc. Am. A*, vol. 27, no. 4, pp. 808–814, 2010.

[12] R. Espinoso-Luna, G. Atondo-Rubio, E. Bernabeu, and S. Hinijosa-Ruiz, "Dealing depolarization of light in Mueller matrices with scalar metrics Â´," *Optik*, no. M, pp. 1–11, 2009.

[13] F. L. E. Roy-brehonnet and B. L. E. Jeune, "Utilization of Mueller matrix formalism to obtain optical targets depolarization and polarization properties," *Prog. Quant. Electr.*, vol. 21, no. 2, pp. 109–151, 1997.

[14] E. Bahar, "Road maps for the use of Mueller matrix measurements to detect and identify biological and chemical materials through their optical activity : potential applications in biomedicine , biochemistry , security , and industry," *J. Opt. Soc. Am. A*, vol. 26, no. 2, pp. 364–370, 2009.

[15] F. Boulvert, G. L. Brun, B. L. Jeune, J. Cariou, and L. Martin, "Decomposition algorithm of an experimental Mueller matrix," *Opt. Comm*, vol. 282, pp. 692–704, 2009.

[16] R. Ossikovski, M. Anastasiadou, S. Ben Hatit, and A. De Martino, "depolarizing Mueller matrices : How to decompose them?," *Physica status solidi a*, 2008.

[17] R. Ossikovski, M. Anastasiadou, and A. De Martino, "Product decompositions of depolarizing Mueller matrices with negative determinants," *Opt. Comm*, vol. 281, pp. 2406–2410, 2008.

[18] O. Arteaga and A. Canillas, "Pseudopolar decomposition of the Jones and Mueller - Jones exponential polarization matrices," *J. Opt. Soc. Am. A*, vol. 26, no. 4, pp. 783–793, 2009.

[19] J. Morio and F. Goudail, "Influence of the order of diattenuator , retarder , and polarizer in polar decomposition of Mueller matrices," *Opt. Lett.*, vol. 29, no. 19, pp. 2234–2236, 2004.

[20] R. Ossikovski, A. De Martino, and S. Guyot, "Forward and reverse product decompositions of depolarizing Mueller matrices," *Opt. Lett.*, vol. 32, no. 6, pp. 689–691, 2007.

[21] M. Anastasiadou, S. Ben Hatit, R. Ossikovski, S. Guyot, and A. De Martino, "Experimental validation of the reverse polar decomposition of depolarizing Mueller matrices," *Journal of the European Optical Society : RP*, pp. 1–7, 2007.

[22] N. Ghosh, M. F. G. Wood, and I. A. Vitkin, "Influence of the order of the constituent basis matrices on the Mueller matrix decomposition-derived polarization parameters in complex turbid media such as biological tissues," *Opt. Comm*, no. November, 2009.

[23] R. Ossikovski, "Interpretation of nondepolarizing Mueller matrices based on singular-value decomposition," *J. Opt. Soc. Am. A*, vol. 25, no. 2, pp. 473–482, 2008.

[24] R. Ossikovski, E. Garcia-caurel, and A. De Martino, "Product decompositions of experimentally determined non-depolarizing Mueller matrices," *Physica status solidii C*, 2008.

[25] Z. F. Xing, "On the deterministic and non-deterministic Mueller matrix," *Journal of modern optics*, vol. 39, no. 3, pp. 461–484.

[26] R. Sridhar and R. Simon, "Normal form for Mueller matrices in polarization optics," *Journal of modern optics*, vol. 41, no. 10, pp. 1903–1915.

[27] C. Fallet, A. Pierangelo, R. Ossikovski, and A. De Martino, "Experimental validation of the symmetric decomposition of Mueller matrices," *Opt. Express*, vol. 2832, no. 2004, 2009.

[28] K. Kim, L. Mandel, and E. Wolf, "Relationship between Jones and Mueller matrices for random media," *J. Opt. Soc. Am. A*, vol. 4, no. 3, pp. 1–5, 1987.

[29] A. V. G. Rao, K. Mallesh, and Sudha, "On the algebraic characterization of a Mueller matrix in polarization optics I. Identifying a Mueller matrix from its N matrix," *Journal of modern optics*, vol. 45, pp. 955–987, 1998.

[30] A. V. G. Rao, K. Mallesh, and Sudha, "On the algebraic characterization of a Mueller matrix in polarization optics II. Necessary and sufficient conditions for Jones-derived Mueller matrices," *Journal of modern optics*, vol. 45, pp. 989–999, 1998.

[31] Sudha and A. Gopala Rao, "Polarization elements : a group-theoretical study," *J. Opt. Soc. Am. A*, vol. 18, no. 12, pp. 3130–3134, 2001.

[32] R. Ossikovski, "Analysis of depolarizing Mueller matrices through a symmetric decomposition," *J. Opt. Soc. Am. A*, vol. 26, no. 5, pp. 1109–1118, 2009.

[33] Sudha, A. Gopala Rao, A. Usha Devi, and A. Rajagopal, "Positive-operator-valued-measure view of the ensemble approach to polarization optics," *J. Opt. Soc. Am. A*, vol. 25, no. 4, pp. 874–880, 2008.

[34] S. Y. Lu and R. A. Chipman, "Homogeneous and inhomogeneous Jones matrices," *J. Opt. Soc. Am. A*, vol. 11, pp. 766–773, 1994.

[35] S. Inoue and R. Oldenbourg, *Handbook of Optics Vol II*. McGraw-Hill, 1986.

[36] M. Françon, *Progress in Microscopy*. Row Peterson and Company, 1961.

[37] S. Ben Hatit and A. De Martino, "Angle-resolved Mueller polarimeter using a microscope objective," *Physica status solidi a*, vol. 5, pp. 1– 5, 2008.

[38] B. Haj Ibrahim, S. Ben Hatit, and A. De Martino, "Angle resolved Mueller polarimetry with a high numerical aperture and characterization of transparent biaxial samples," *Appl. Opt.*, vol. 48, pp. 5025–5034, Sept. 2009.

[39] M. Born and E. Wolf, *Priciples of Optics, 6th edition*. Pergamon Press, 1980.

[40] H. J. Patrick, R. Attota, B. M. Barnes, T. A. Germer, M. T. Stocker, R. M. Silver, and M. R. Bishop, "Scatterfield microscopy using back focal plane imaging with an engineered illumination field," vol. 6152, 2006.

[41] S. Ben Hatit, *Polarimétrie de Mueller résolue en angle*. PhD thesis, 2009.

[42] R. Oldenbourg, "A new view on polarization microscopy," *Nature*, vol. 381, pp. 811–812, 1996.

[43] A. Bénière, M. Alouini, F. Goudail, and D. Dolfi, "Design and experimental validation of a snapshot polarization contrast imager," *Appl. Opt.*, 2009.

[44] M. Richert, X. Orlik, and A. De Martino, "Adapted polarization state contrast image," *Opt. Express*, vol. 17, no. 16, pp. 608–610, 2009.

[45] H. Dong, Y. D. Gong, V. Paulose, P. Shum, and M. Olivo, "Optimum input states of polarization for Mueller matrix measurement in a system having finite polarization-dependent loss or gain," *Opt. Express*, vol. 17, no. 25, pp. 27–29, 2009.

[46] K. Twietmeyer and R. Chipman, "Condition Number as a Metric for the Effectiveness of Polarimetric Algorithms," *Optical Engineering*, vol. 25, no. 16, pp. 2493–2493, 2005.

[47] M. Shribak, "Complete polarization state generator with one variable retarder and its application for fast and sensitive measuring of two-dimensional birefringence distribution.," *J. Opt. Soc. Am. A*, vol. 28, pp. 410–9, Mar. 2011.

[48] R. S. Verma, M. K. Swami, S. S. Manhas, and P. K. Gupta, "Mueller matrix-base optimization of reflective type twisted nematic liquid crystal SLM at oblique incidences," *Opt. Comm*, no. February, 2010.

[49] M. Dubreuil, S. Rivet, B. L. Jeune, and L. Dupont, "Time-resolved switching analysis of a ferroelectric liquid crystal by snapshot Mueller matrix polarimetry," *Opt. Lett.*, vol. 35, no. 7, pp. 1019–1021, 2010.

[50] A. Peinado, A. Lizana, J. Vidal, C. Iemmi, and J. Campos, "Optimization and performance criteria of a Stokes polarimeter based on two variable retarders," *Opt. Express*, vol. 18, no. 8, pp. 9815–9830, 2010.

[51] S. Tripathi and K. C. Toussaint, "Rapid Mueller matrix polarimetry based on parallelized polarization state generation and detection," *Opt. Express*, vol. 17, no. 24, pp. 6676–6683, 2009.

[52] B. Laude-boulesteix, *Développements instrumentaux en imagerie tomographique et polarimétrique*. PhD thesis, 2004.

[53] E. Compain and B. Drevillon, "General and self-consistent method for the calibration of polarization modulators, polarimeters, and Mueller-matrix ellipsometers," *Appl. Opt.*, 1999.

[54] S. Berthier, *Iridescences, les couleurs physiques des insectes*. Springer, 2003.

[55] A. A. Michelson, "On metallic colouring in birds and insects," *Philos. Mag*, vol. 21, pp. 554–567, 1911.

[56] S. Berthier, *Photonique des Morphos*. Springer, 2010.

[57] M. Srinivasarao, "Nano-Optics in the Biological World: Beetles, Butterflies, Birds, and Moths.," *Chemical reviews*, vol. 99, pp. 1935–1962, July 1999.

[58] S. Kinoshita, S. Yoshioka, and J. Miyazaki, "Physics of structural colors," *Reports on Progress in Physics*, vol. 71, pp. 1–30, July 2008.

[59] S. Berthier, J. Boulenguez, M. Menu, and B. Mottin, "Butterfly inclusions in Van Schrieck masterpieces . Techniques and optical properties," *Appl. Opt.*, vol. 57, pp. 51–57, 2008.

[60] S. Berthier, J. Boulenguez, and Z. Balint, "Multiscaled polarization effects in Suneve coronata (Lepidoptera) and other insects : application to anti-counterfeiting of banknotes," *Appl. Opt.*, vol. 130, pp. 123–130, 2007.

[61] B. T. Hallam, A. G. Hiorns, and P. Vukusic, "Developing optical efficiency through optimized coating structure : biomimetic inspiration from white beetles," *Appl. Opt.*, 2009.

[62] P. Vukusic, B. T. Hallam, and J. Noyes, "Brilliant Whiteness in Ultrathin Beetle Scales," *Science*, vol. 315, no. January, p. 348, 2007.

[63] A. Neville and S. Caveney, "Scarabaeid beetle exocuticle as an optical analogue of cholesteric liquid crystals.," *Biol Rev Camb Philos Soc.*, vol. 44, pp. 531–562, 1969.

[64] S. A. Jewell, P. Vukusic, and N. W. Roberts, "Circularly polarized colour reflection from helecoidal structures in the beetle Plusiotis boucardi," *New Journal of Physics*, vol. 2630, no. 07, pp. 1–10, 2007.

[65] I. Hodgkinson, S. Lowrey, L. Bourke, A. Parker, and M. W. Mccall, "Mueller-matrix characterization of beetle cuticle : polarized and unpolarized reflections from representative architectures," *Appl. Opt.*, 2010.

[66] H. Arwin, "Application of ellipsometry techniques to biological materials," *Thin Solid Films*, vol. 519, no. 9, pp. 2589–2592, 2011.

[67] K. Järrendahl, J. Landin, and H. Arwin, "Mueller-matrix ellipsometry studies of optically active structures in scarab beetles," *EPJ Web of Conferences*, vol. 5, p. 3005, 2010.

[68] R. Hegedus, G. Szel, and G. Horwarth, "Imaging polarimetry of the circularly polarizing cuticle of scarab beetles (Coleoptera : Rutelidae , Cetoniidae)," *Vision Research*, vol. 46, pp. 2786–2797, 2006.

[69] L. Besseau and M.-M. Giraud-Guille, "Stabilization of fluid cholesteric phases of collagen to ordered gelated matrices," *J. Mol. Biol.*, no. 251, pp. 197–202, 1995.

[70] G. P. KoÌˆnnen, *Polarized light in nature*. Cambridge University Press, 1985.

[71] G. W. KATTAWAR, "A Search for Circular Polarization in Nature," *Opt. Photon. News*, vol. 5, pp. 42–43, Sept. 1994.

[72] P. Bouchard, Y. Bousquet, A. Davies, M. Alonso-Zarazaga, J. Lawrence, C. Lyal, A. Newton, C. Reid, M. Schmitt, A. Slipinski, and A. Smith, "Family-Group Names In Coleoptera (Insecta)," *ZooKeys*, vol. 88, pp. 1–972, Apr. 2011.

[73] A. B. T. Smith, D. C. Hawks, and J. M. Heraty, "An Overview of the Classification and Evolution of the Major Scarab Beetle Clades (Coleoptera: Scarabaeoidea) Based on Preliminary Molecular Analyses," *The Coleopterists Bulletin*, vol. 60, pp. 35–46, Dec. 2006.

[74] A. B. T. Smith, "A Review of the Family-group Names for the Superfamily Scarabaeoidea (Coleoptera) with Corrections to Nomenclature and a Current Classification," *The Coleopterists Bulletin*, vol. 60, pp. 144–204, Dec. 2006.

[75] V. Sharma, M. Crne, J. Park, and M. Srinivasarao, "Structural origin of circularly polarized iridescence in jeweled beetles," *Science*, vol. 325, pp. 449–451, 2009.

[76] H. Arwin, J. Landin, and K. Järrendahl, "Optical active cuticle structures in the beetle Cetonia aurata," *European Optical Society Meeting 2008*, 2008.

[77] B. G. E. Moore, "Cramming more components onto integrated circuits," *Electronics*, vol. 38, no. 8, 1975.

[78] C. P. Ausschnitt, "A new approach to pattern metrology," in *Metrology, Inspection, and Process Control for Microlithography XVIII* (R. M. Silver, ed.), vol. 5375, pp. 51–65, SPIE, 2004.

[79] C.-m. Ke, G.-t. Huang, J. Huang, R. Lee, L.-h. R. Hsinchu, and S. Park, "Accuracy of Diffraction-Based and Image-Based Overlay," in *Advanced Lithography*, no. Cd.

[80] P. L. Rigolli, L. Rozzoni, C. Turci, U. Iessi, M. Polli, E. Kassel, P. Izikson, and Y. Avrahamov, "AIM technology for non-volatile memories microelectronics devices," *Metrology, Inspection, and Process Control for Microlithography XX*, vol. 6152, no. Mi, pp. 61524C–61524C–13, 2006.

[81] M. Adel, M. Ghinovker, B. Golovanevsky, P. Izikson, E. Kassel, D. Yaffe, A. M. Bruckstein, R. Goldenberg, Y. Rubner, and M. Rudzsky, "Optimized Overlay Metrology Marks : Theory and Experiment," *IEEE Transactions on Semiconductor manufacturing*, vol. 17, no. 2, pp. 166–179, 2004.

[82] P. Dasari, N. Smith, G. Goelzer, Z. Liu, J. Li, A. Tan, and C. H. Koh, "A comparison of advanced overlay technologies," *Metrology, Inspection, and Process Control for Microlithography XXIV*, vol. 7638, no. 408, pp. 1–9, 2010.

[83] C.-h. Ko and Y.-s. Ku, "Overlay measurement using angular scatterometer for the capability of integrated metrology," *Opt. Express*, vol. 14, no. 13, 2006.

[84] J. Li, Y. Liu, P. Dasari, J. Hu, N. Smith, O. Kritsun, and C. Volkman, "Advanced Diffraction-Based Overlay for Double Patterning," *Metrology, Inspection, and Process Control for Microlithography XXIV*, vol. 7638, pp. 1–10, 2010.

[85] P. Vanoppen, T. Theeuves, H. Megens, H. Cramer, T. Fliervoet, M. Ebert, and D. Satriasaputra, "Lithographic scanner stability improvements through advanced metrology and control," *Optical microlithography XXIII*, 2010.

[86] K. Bhattacharyya, N. Wright, M. van der Schaar, A. den Boef, P. Hinnen, M. Sharjerdy, V. Wang, S. Lin, C. Wang, C.-M. Ke, J. Huang, and W. Wang, "New approaches for scatterometry-based metrology for critical distance and overlay measurement and," *J. Micro/Nanolith. MEMS MOEMS*, vol. 10, no. 1, pp. 1–8, 2011.

[87] A. De Martino, T. Novikova, S. BenHatit, B. Drevillon, and D. Cattelan, "Characterization of gratings by Mueller polarimetry in conical diffraction," in *Metrology, Inspection, and Process Control for Microlithography XIX* (R. M. Silver, ed.), vol. 5752, pp. 217–228, SPIE, 2005.

[88] A. De Martino, M. Foldyna, T. Novikova, D. Cattelan, P. Barritault, C. Licitra, J. Hazart, J. Foucher, and F. Bogeat, "Comparison of spectroscopic Mueller polarimetry, standard scatterometry, and real space imaging techniques (SEM and 3D-AFM) for dimensional characterization of periodic structures," in *Metrology, Inspection, and Process Control for Microlithography XXII* (J. A. Allgair and C. J. Raymond, eds.), vol. 6922, p. 69221P, SPIE, 2008.

[89] M. Foldyna, A. De Martino, D. Cattelan, F. Bogeat, C. Licitra, J. Foucher, P. Barritault, and J. Hazart, "Accurate dimensional characterization of periodic structures by spectroscopic Mueller polarimetry," in *Lithography Asia 2008* (A. C. Chen, B. Lin, and A. Yen, eds.), vol. 7140, p. 71400I, SPIE, 2008.

[90] T. Novikova, A. De Martino, S. Ben Hatit, and B. Drévillon, "Application of Mueller polarimetry in conical diffraction for critical dimension measurements in microelectronics," *Appl. Opt.*, 2006.

[91] A. De Martino, S. Ben Hatit, and M. Foldyna, "Mueller polarimetry in the back focal plane," in *Metrology, Inspection, and Process Control for Microlithography XXI* (C. N. Archie, ed.), vol. 6518, p. 65180X, SPIE, 2007.

[92] J. S. Tyo, Z. Wang, S. J. Johnson, and B. G. Hoover, "Design and optimization of partial Mueller matrix polarimeters," *Appl. Opt.*, 2010.

[93] D. Lara and C. Dainty, "Axially resolved complete Mueller matrix confocal microscopy," *Appl. Opt.*, vol. 45, no. 9, pp. 1917–1930, 2006.

[94] M. Dubreuil, S. Rivet, B. L. Jeune, and J. Cariou, "Two-channel snapshot Mueller matrix polarimeter," *Appl. Opt.*, vol. 48, no. 33, pp. 6501–6505, 2009.

[95] A. De Martino and B. Drevillon, "Spectroscopic Mueller polarimeter based on liquid crystal devices," *Thin Solid Films*, vol. 456, pp. 120–123, 2004.

[96] Y.-n. Kim, J.-s. Paek, S. Rabello, S. Lee, J. Hu, Z. Liu, Y. Hao, and W. Mcgahan, "Device based in-chip critical dimension and overlay metrology," *Opt. Express*, vol. 17, no. 23, pp. 21336–21343, 2009.

[97] J. Li and J. J. Hwu, "Mueller matrix measurement of asymmetric gratings," *J. Micro/Nanolith. MEMS MOEMS*, vol. 9, no. 4, pp. 1–8, 2010.

[98] L. Li, "Symmetries of cross-polarization diffraction," *J. Opt. Soc. Am. A*, vol. 17, no. 5, 2000.

[99] T. Novikova, A. De Martino, R. Ossikovski, and B. Drevillon, "Metrological applications of Mueller polarimetry in conical diffraction for overlay characterization in microelectronics," *European Physical Journal, Applied Physics*, vol. 69, pp. 63–69, 2005.

[100] T. Novikova, C. Fallet, M. Foldyna, S. Manhas, B. Haj Ibrahim, A. De Martino, C. Vannuffel, and C. Constancias, "Overlay Measurements by Mueller Polarimetry in Back Focal Plane," in *Advanced Lithography*, vol. 4, pp. 2–9, 2011.

[101] C. Fallet, S. Manhas, A. De Martino, and T. Novikova, "Applications of Mueller polarimetry in the Fourier space for overlay characterization in microelectronics," in *Instrumentation, Metrology, and Standards for Nanomanufacturing IV* (M. T. Postek, ed.), vol. 7767, p. 77670N, SPIE, 2010.

[102] K. Knop, "Rigorous diffraction theory for transmission phase gratings with deep rectangular grooves," *J. Opt. Soc. Am.*, vol. 68, pp. 1206–1210, Sept. 1978.

[103] P. Lalanne and G. M. Morris, "Highly improved convergence of the coupled-wave method for TM polarization," *J. Opt. Soc. Am. A*, vol. 13, no. 4, pp. 779–784, 1996.

[104] P. Lalanne, "Improved formulation of the coupled-wave method for two-dimensional gratings," *J. Opt. Soc. Am. A*, vol. 14, no. 7, pp. 1592–1598, 1997.

[105] M. G. Moharam and T. K. Gaylord, "Rigorous coupled-wave analysis of planar-grating diffraction," *J. Opt. Soc. Am.*, vol. 71, no. 7, pp. 811–818, 1981.

[106] M. G. Moharam, E. B. Grann, D. A. Pommet, and T. K. Gaylord, "Formulation for stable and efficient implementation of the rigorous coupled-wave analysis of binary gratings," *J. Opt. Soc. Am. A*, vol. 12, no. 5, pp. 1068–1076, 1995.

[107] S. Peng and G. M. Morris, "Efficient implementation of rigorous coupled-wave analysis for surface-relief gratings," *J. Opt. Soc. Am. A*, vol. 12, no. 5, pp. 1087–1096, 1995.

[108] Y. Li, A. Fan, G. Etheridge, G. Finken, and D. Louder, "Evaluation of AIM overlay mark for thin film head application," *Metrology, Inspection, and Process Control for Microlithography XXI*, vol. 6518, pp. 65182W–65182W–8, 2007.

[109] J. Shin, J. Yeo, Y.-s. Kang, and W. Han, "Impact of total measurement uncertainty," *J. Micro/Nanolith. MEMS MOEMS*, vol. 9, pp. 3–7, 2011.

[110] S. Combrié, *Etude et réalisation de structures en cristaux photoniques pour les applications de traitements du signal optique*. PhD thesis, Université Paris XI Orsay, 2006.

[111] M. Patterson, S. Hughes, S. Combrié, N.-V. Tran, N.-V. Quynh, A. De Rossi, R. Gabet, and Y. Jaouen, "Disorder-Induced Coherent Scattering in Slow-Light Photonic Crystal Waveguides," *Phys. Rev. Lett*, vol. 102, 2009.

[112] G. z. Radnoczi, T. Seppänen, B. Pecz, L. Hultman, and J. Birch, "Growth of highly curved Al1-xInxN nanocrystals," *Physica status solidi. A. Applied research*, vol. 202, no. 7, pp. R76–R78.

[113] R. Magnusson, "Mueller matrix ellipsometry studies of chiral nanorods Al1-xInxN films," in *WSE 2011*, 2011.

Abstract

With the constant decrease of the size of the transistors in microelectronics, the characterization tools have to be more and more accurate and have to provide higher and higher throughput. Semiconductor manufacturing being a layer-by-layer process, the fine positioning of the stack is crucial. The misalignment of the stack is called overlay and we here propose a new tool and method to accurately characterize overlay by measuring a single target built in the scribe lines. The method uses the fundamental symmetry properties of the Mueller matrix acquired in the back focal plane of a high-aperture microscope objective and enables a characterization of the overlay with a total measurement uncertainty of 2nm. After a brief introduction to polarization and the Mueller matrix, we describe the new design of the instrument and its complete calibration. The main body of this manuscript is dedicated to the overlay characterization but the applications of this instrument are very diverse so we also detail how our instrument can shed some light on the characterization and the understanding of the auto-organization of some scarab beetles' exoskeleton. These beetles exhibit a very strong circular dichroism and many research groups around the world try to mimic their exoskeleton. We conclude this manuscript with a brief overview of the main perspectives from our instrument.

Résumé

Avec la diminution constante de la taille des transistors dans la microélectronique, les outils de caractérisation doivent être de plus en plus précis et doivent fournir un débit de plus en plus élevé. La fabrication de semi-conducteurs étant un processus couche par couche, le positionnement précis de la pile est crucial. Le mauvais alignement de la pile est appelé overlay, et nous proposons ici un nouvel instrument et une nouvelle méthode pour caractériser avec précision l'overlay en mesurant une cible unique construite dans les lignes de découpe. La méthode utilise les propriétés fondamentales de symétrie de la matrice de Mueller mesurée dans le plan focal arrière d'un objectif de microscope à grande ouverture numérique et permet une caractérisation de l'overlay avec une incertitude de mesure totale de 2nm. Après une brève introduction à la polarisation et la matrice de Mueller, nous décrivons la nouvelle conception de l'instrument et son étalonnage complet. Le corps principal de ce manuscrit est dédié à la caractérisation de l'overlay, mais les applications de cet instrument sont très diverses aussi détaillerons nous comment notre instrument peut apporter des pistes pour la caractérisation et la compréhension de l'auto-organisation de l'exosquelette des scarabées. Ces coléoptères présentent un très fort dichroïsme circulaire et de nombreux groupes de recherche dans le monde entier essaient d'imiter leur exosquelette. Nous concluons ce manuscrit par un bref aperçu des principales perspectives pour notre instrument.